Thèse de Doctorat de l'Université de Lille

Spécialité:
Optique, lasers, physico-chimie, atmosphère

présentée par

Friederike HEMMER

pour obtenir le grade de

Docteur de l'Université de Lille

Characterization of Cirrus Clouds from Ground-Based Remote Sensing Using the Synergy of Lidar and Multi-Spectral Infrared Radiometry

(Caractérisation des cirrus à partir de mesures de surface en utilisant la synergie entre lidar et radiomètre infrarouge thermique)

Thèse soutenue le 7 Décembre 2018 devant le jury composé de:

Mme. Claudia STUBENRAUCH	*Rapporteur*
M. Jacques PELON	*Rapporteur*
M. Philippe KECKHUT	*Président du jury*
M. Johannes QUAAS	*Examinateur*
M. Frédéric PAROL	*Directeur de thèse*
M. Laurent C.-LABONNOTE	*Co-encadrant*
M. Gérard BROGNIEZ	*Co-encadrant*

Thèse effectuée au
Laboratoire d'Optique Atmosphérique
Faculté des Sciences et Technologies
Université de Lille
59655 Villeneuve d'Ascq, France

Abstract

There is a broad consensus that cirrus clouds strongly influence the energy budget of the Earth. However, their net radiative effect is still poorly quantified nowadays due to an insufficient knowledge of their microphysical properties. This thesis aims to improve our understanding of the complex microphysics of this cloud type which is mainly composed of irregularly shaped ice crystals. Thereby, we seek to improve estimates of the ice water content (IWC) of cirrus clouds. For this purpose, we developed an algorithm to retrieve the vertical profile of the IWC inside the cloud. The methodology combines the measurements of a ground-based micropulse lidar and a thermal infrared (TIR) radiometer in a common retrieval framework based on optimal estimation theory. It follows three main steps: (1) An algorithm to retrieve the vertically integrated amount of ice (ice water path, IWP) from the passive TIR measurements is established. (2) The information about the vertical distribution of the IWC inside the cloud is obtained from the active lidar measurements. The retrieved IWC profiles strongly depend on the so-called backscatter-to-extinction ratio of the ice crystals which has to be approximated when regarding simple micropulse lidar measurements alone. This is due to the intrinsic ambiguity between scattering and absorption processes in the atmosphere. In our case, the backscatter-to-extinction ratio of the ice crystals is obtained from a bulk ice microphysical model. The scattering phase function of this model used to define this parameter assumes a flat ending without backscattering peak. We show that this assumption is unrealistic since it results in the retrieval of IWC profiles which are inconsistent with the TIR measurements. (3) Consequently, both types of measurements are combined in a synergistic algorithm allowing to estimate together with the IWC profiles a correction factor for the phase function in backscattering direction. In the final chapter, the dependence of the retrieval results on different non-retrieved parameters is investigated and the main sources of uncertainty are discussed.

Key words: cirrus, instrument synergy, lidar, thermal infrared radiometer, remote sensing, inverse problems, radiative transfer, cloud microphysics

Résumé

Il est maintenant bien établi que les cirrus ont un impact important sur le climat. Cependant, l'estimation de cet effet est difficile car notre connaissance des propriétés microphysiques de ce type de nuage est encore incertaine. L'objectif de cette thèse est donc d'améliorer notre compréhension de la microphysique complexe du cirrus composé principalement de cristaux de glace de forme irrégulière et d'estimer ainsi un contenu en glace (ice water content, IWC) plus précis. Pour cela, nous avons développé un algorithme permettant de restituer le profil vertical d'IWC du cirrus. La méthodologie considère une synergie entre les mesures d'un micro-lidar et celles d'un radiomètre infrarouge thermique (IRT) effectuées depuis le sol, via une méthode d'estimation optimale. Ce travail s'est déroulé en trois étapes: (1) Le contenu en glace intégré verticalement (ice water path, IWP) est estimé à partir des mesures passives IRT. (2) L'information sur la distribution verticale d'IWC à l'intérieur du nuage est obtenue avec les mesures actives du lidar. Les profils d'IWC restitués dépendent fortement du rapport entre la rétrodiffusion et l'extinction des cristaux de glace qui doit être approximé dans le cas d'un micro-lidar simple comme celui-ci utilisé dans notre étude. Cela est dû à l'ambiguïté entre des processus de rétrodiffusion et d'absorption dans l'atmosphère. Nous obtenons le rapport entre la rétrodiffusion et l'extinction à partir d'un modèle microphysique du cirrus. La fonction de phase du modèle utilisée pour définir ce rapport ne prend pas en compte le pic de rétrodiffusion. Nous montrons que cette hypothèse aboutit à des résultats non réalistes par rapport aux mesures IRT. (3) Par conséquent, les deux types d'informations sont combinées en synergie pour estimer, lors de la restitution des profils verticaux d'IWC, un facteur correctif permettant de rendre compte de ce pic de rétrodiffusion. Finalement, la dépendance des résultats sur plusieurs paramètres non-restitués est analysés et les sources d'incertitude sont discutés.

Mots clés: cirrus, synergie multi-instrument, lidar, radiomètre infrarouge thermique, télédétection, problèmes inverses, transfert radiatif, microphysique des nuages

Remerciements

Il est enfin temps de rédiger la dernière partie de ce manuscrit qui n'est pas forcement la plus facile. Ces quelques paragraphes vont me permettre de remercier les personnes et les organismes qui ont contribué à la réussite de ce travail de thèse.

Avant tout, je tiens à remercier les co-financeurs de cette thèse, l'Université de Lille et le Conseil Régional Hauts-de-France.

Ensuite, je voudrais exprimer toute ma reconnaissance envers mes encadrants, Frédéric Parol, Laurent Labonnote et Gérard Brogniez, pour leur disponibilité, leur investissement et leurs conseils précieux. Je les remercie de m'avoir donné la possibilité de réaliser ce travail passionnant et de m'avoir guidée pendant ces trois années. Je leur suis extrêmement reconnaissante pour les connaissances, la méthodologie et la vision du travail scientifique qu'ils m'ont prodigué. Enfin, je les remercie pour leur confiance et la liberté d'initiative qu'ils m'ont laissé prendre durant ce travail.

Je tiens ensuite à remercier les membres du jury d'avoir accepté d'évaluer mon travail de thèse. Particulièrement, je remercie les deux rapporteurs, Claudia Stubenrauch et Jacques Pelon, pour leurs remarques détaillées et constructives qui ont grandement amélioré la qualité de ce manuscrit. Merci également aux examinateurs, Philippe Keckhut et Johannes Quaas, pour m'avoir fait l'honneur de participer à la soutenance de thèse et pour leurs conseils avisés.

J'adresse également mes remerciements à l'ensemble du LOA pour leur accueil chaleureux durant ces trois années. C'était un réel plaisir de travailler parmi vous. Je remercie plus spécifiquement Marie-Lyse Liévin et Anne Priem pour leur aide dans les questions administratives, ainsi que Christine Deroo et Romain De Filippi pour le soutien informatique. Un grand merci aussi à Isabelle Favier pour sa bonne humeur quotidienne et son coup de main dans l'organisation du pot de thèse. Je tiens également à remercier François Thieuleux et Fabrice Ducos qui m'ont aidé à résoudre de nombreux problèmes de programmation. Un grand merci à Bahy Damiri et Thierry Podvin pour leur participation aux étalonnages instrumentaux et à l'acquisition des données sans lesquelles cette thèse n'aurait pas été possible. Je pense ici aussi à Odran Sourdeval car c'est grâce à lui que j'ai fait la connaissance du LOA. Merci Odran de m'avoir encadré pendant mes stages de licence et de master, en coopération avec Johannes Quaas que je remercie également pour son soutien tout au long de mes études à Leipzig. Cela m'a ouvert la possibilité de faire cette thèse au LOA.

Une pensée particulière va vers les thésards, postdocs et autres qui ont participé à donner une ambiance si agréable durant ces trois années. Je salut ici mes premiers camarades de bureau, Ioana, Qiaoyun, Christian, Patrice et last but not least Danielle, bien évidemment, avec qui j'ai partagé mon bureau jusqu'à la fin et avec qui j'ai vécu les hauts et les bas de la thèse. Merci à Aurélien pour organiser les séances de footsal et aux sportifs qui y ont participé. Merci aussi à Fabien C. d'avoir pris régulièrement l'initiative de nous motiver d'aller boire un verre à la MDE après une longue journée de travail et merci à ceux qui ont suivi pour passer des bons moments de convivialité.

Enfin, je remercie ma famille: meinen Eltern, Marianne und Georg, meinen beiden Schwestern Katharina und Johanna, meinem Bruder Florian und seiner Frau Eva und meinem Neffen Felix. Danke für eure aufmunternden Worte und Unterstützung, nicht nur in den letzten drei Jahren. Pour finir, je souhaite dédier ce dernier merci à Jean-Christophe qui m'a accompagné et soutenu inconditionnellement et qui m'a toujours supportée et encouragée durant les moments difficiles, notamment dans la dernière phase de rédaction.

Contents

Introduction

Clouds have been a source of fascination for mankind since ancient times. Aristotle already poetically described the formation of clouds and rainfall in his treatise *Meteorologica* as early as around the year 350 BC. He explained that thanks to the sun "the finest and sweetest water is every day carried up and is dissolved into vapor and rises to the upper region, where it is condensed again by the cold and so returns to the earth" (Webster, 1931). However, it was not until the second half of the twentieth century with the invent of lidars and the availability of satellite data that our knowledge of clouds and their properties evolved significantly. Since then a large number of scientific studies has been conducted to improve our understanding of the global distribution and occurrence frequencies of clouds, their formation and dissolution processes, as well as their microphysical and radiative properties. Nevertheless, there still remain a lot of unresolved questions and the latest Intergovernmental Panel on Climate Change (IPCC) report states that clouds, together with aerosols, continue to contribute the largest uncertainty to estimates of the Earth's energy budget (Boucher et al., 2013).

In this context, especially the radiative impact of cirrus clouds is still poorly quantified although it has long been recognized to be of significant importance (e.g. Cox, 1971; Liou, 1986; Hartmann et al., 1992; McFarquhar et al., 2000; Dessler et al., 2006; Wang and Dessler, 2012; Hong et al., 2016; Lohmann and Gasparini, 2017; Järvinen et al., 2018). The main reason for this is the large range of different shapes and sizes of the ice crystals composing the cloud which interact in different ways with atmospheric radiation. Simply spoken, there are two each other opposing radiative effects: on the one hand, the cloud albedo effect which leads to a cooling of the atmosphere, and on the other hand, the cloud greenhouse effect which leads to a warming. Which one of these effects dominates depends on the cloud type. In case of cirrus, the net radiative effect is generally positive. However, this is not true for each individual cirrus cloud since the radiative effect depends not only on the macrophysical properties such as altitude, geometrical thickness, temperature, and the difference between the surface temperature and the cloud temperature (e.g. Stephens and Webster, 1981), but also on the microphysics of the cloud, especially the size, shape and number density of particles. Zhang et al. (1999) showed that the radiative effect of cirrus clouds can be positive or negative depending on their microphysics. Recently, Järvinen et al. (2018) confirmed that the optical properties of ice crystals strongly depend on their microphysical structure and that an increasing particle complexity can change the net radiative effect of cirrus.

The aim of this thesis is to contribute to a better characterization of the microphysical properties of this interesting but complex cloud type. There are different ways to perform observations of cirrus clouds which all have advantages and disadvantages. Airborne in situ measurements can provide detailed information about the particle size distribution, the ice crystal shape and their number concentration. However, these measurements are spatially and temporally limited and do not comprise all conceivable different variations of cirrus. To obtain a larger spatial and temporal coverage, remote sensing techniques are required which can be applied to spaceborne or ground-based measurements. Spaceborne remote sensing provides information about clouds on a global scale. In particular, the Cloud-Aerosol Lidar and Infrared Pathfinder Satellite Observations (CALIPSO) and CloudSat missions, which include active spaceborne sensors, significantly improved our knowledge about the global distribution and occurrence frequency of cirrus clouds in recent years. However, the spaceborne remote sensing of cirrus remains challenging because they are generally optically thin and often semi-transparent which complicates the accurate retrieval of their microphysical properties. In contrast to satellite observations, ground-based remote sensing does not provide global coverage but the cloud is situated much closer to the instrument and thus a higher accuracy can be achieved. Furthermore, the measurements allow the observation of the temporal evolution of individual cloud systems at a fixed location. In this thesis, we will focus on ground-based remote sensing. The instruments that will be used to study the properties of cirrus clouds are a micropulse lidar and a thermal infrared radiometer.

There are numerous studies that could be cited from the literature where ground-based lidar measurements have been used to study cirrus clouds (e.g. Ansmann et al., 1993; Sassen and Benson, 2001; Chen et al., 2002; Keckhut et al., 2006; Giannakaki et al., 2007; Seifert et al., 2007; Liu et al., 2015; Campbell et al., 2016). The advantage of these measurements is that even very tenuous layers can be detected (e.g. Sassen, 1991). The measured backscatter profiles provide information about the cloud base and top altitudes which can be related to temperature by using atmospheric temperature profiles from model reanalysis or radiosounding. Furthermore, these measurements yield the possibility to retrieve profiles of particle extinction which will be linked in our case to the ice water content (IWC) of cirrus clouds via a realistic bulk ice microphysical model. However, when using a simple micropulse lidar, strong assumptions about the so-called backscatter-to-extinction ratio have to be introduced. This is due to the intrinsic ambiguity between backscattering and extinction of atmospheric particles arising from simultaneous absorption and scattering processes. Even though more advanced lidar systems do not require such assumptions which lead to large uncertainties on the retrieved parameters, the lidar chosen in this thesis is a simple micropulse lidar. The reason for this is that most ground-based lidars operated at present are rather simple systems (Campbell et al., 2015) and the idea of this thesis is to develop a method that is applicable to a larger number of measurement sites. Furthermore, we aim to show the potential of this kind of measurements when combined with thermal infrared radiometer measurements.

Thermal infrared radiometer measurements provide valuable information about cirrus clouds as well because they are sensitive to the optical and integrated properties of the cloud, for example the ice water path (IWP). A well-known method for the exploitation of spaceborne measurements in the thermal infrared wavelength region is the split window technique. This method has been applied for decades to obtain the cloud top temperature and the effective emissivity of semi-transparent cirrus clouds from two channels centred around $11\,\mu$m and $12\,\mu$m, respectively (Inoue, 1985, 1987; Parol et al., 1991). The brightness temperature difference of these two channels is always more important for thin cirrus clouds than for thick clouds or under clear sky conditions. In addition, it is sensitive to the radiative and microphysical properties of the cirrus cloud (Dubuisson et al., 2008). Another method using spaceborne thermal infrared measurements is the weighted-χ^2 method of Stubenrauch et al. (1999) to retrieve cloud pressure and effective emissivity from measurements of five channels of the High-resolution Infrared Radiation Sounder (HIRS) aboard the National Oceanic and Atmospheric Administration (NOAA) polar orbiting satellites. This method has also been applied to the Atmospheric InfraRed Sounder (AIRS) (Stubenrauch et al., 2008, 2010; Guignard et al., 2012) situated aboard the Aqua satellite which is a part of the international satellite constellation known as A-Train (Stephens et al., 2002), as well as to the Infrared Atmospheric Sounding Interferometer (IASI) of which two instruments have been launched so far aboard the European platforms Metop-A and Metop-B (Stubenrauch et al., 2017).

However, in recent years there has been a growing awareness of the potential of using a maximum amount of available information from different sensors when retrieving cloud properties. Consequently, synergistic approaches combining independent sets of measurements in a common retrieval framework have become more and more popular. As an example, the raDAR/liDAR (DARDAR) algorithm (Delanoë and Hogan, 2008, 2010) should be mentioned here which is a variational algorithm to retrieve cirrus cloud properties from the synergy of spaceborne radar and lidar data obtained from the Cloud Profiling Radar (CPR) aboard CloudSat (Stephens et al., 2008) and the Cloud-Aerosol Lidar with Orthogonal Polarization (CALIOP) aboard CALIPSO (Winker et al., 2003, 2009, 2010) which are both members of the A-Train. Another example for a synergistic algorithm is the multilayer algorithm proposed by Sourdeval et al. (2015, 2016) which exploits the information from passive satellite sensors to retrieve ice and liquid water cloud properties simultaneously from three thermal infrared radiances measured by the Imaging Infrared Radiometer (IIR) aboard CALIPSO and the reflectances of two channels at $0.85\,\mu$m and $2.13\,\mu$m of the MODerate resolution Imaging Spectroradiometer (MODIS) aboard Aqua.

There are also a few methods which have been developed in the past that combine lidar and thermal infrared radiometer measurements. The first method using the synergy of these two instruments was the Lidar and Infrared Radiometric (LIRAD) method developed by Platt (1973, 1979) to retrieve optical properties of cirrus clouds. In this approach, the integrated attenuated lidar backscatter is related theoretically to the infrared absorption optical thickness which allows to obtain retrievals of the visible optical thickness and infrared emissivity which are coherent with both, lidar and thermal infrared radiometer measurements. This method has been applied and further developed in several following studies (e.g., Platt et al., 1987; Comstock and Sassen, 2001; Platt et al., 2002). Other studies focused on the combination of lidar measurements and the split-window technique to improve the retrievals of cloud properties from passive sensors alone by integrating the information provided by the active lidar measurements in the radiative transfer calculations. Chiriaco et al. (2004) showed the theoretical potential of this approach to improve the particle size retrieval from the instruments aboard CALIPSO, i.e. the IIR and CALIOP, and Garnier et al. (2012, 2013, 2015) developed an algorithm based on this idea to retrieve the effective emissivity, optical depth, effective diameter and IWP from CALIPSO measurements. Nevertheless, in their approach the retrieval is based on the split-window technique where the information about the scene identification and cloud altitude from the lidar has been integrated.

Recently, Saito et al. (2017) demonstrated a method to retrieve simultaneously the IWP, the cloud effective radius, the surface temperature and two morphological parameters, namely the fraction of plates and the surface roughness of ice crystal aggregates, from a synergistic approach. They used the layer-integrated total attenuated backscatter and the depolarization ratio at 532 nm from CALIOP as well as the brightness temperatures at 8.65, 10.6 and 12.0 μm from the IIR in a common retrieval framework to obtain the parameters cited above. As in case of the DARDAR algorithm (Delanoë and Hogan, 2008, 2010) and the multilayer algorithm (Sourdeval et al., 2015, 2016), the method of Saito et al. (2017) is based on optimal estimation theory introduced by Rodgers (1976, 1990, 2000). This approach allows the simultaneous inversion of measurements from different instruments in a robust mathematical framework. Furthermore, it directly provides an estimation of the uncertainties together with the retrieved quantities. Hence, it is a well-adapted tool to retrieve physical properties of the atmosphere and the particles within it from instrument synergies.

Since this thesis aims to exploit such a synergy, an optimal estimation framework has been chosen for the inversion of the ground-based lidar and thermal infrared radiometer measurements to retrieve microphysical properties of cirrus clouds. The development process of this synergy algorithm will be described in the course of this manuscript which has been subdivided into four main chapters for structuring purposes. The content of each of these chapters is briefly summarized in the following.

In the first chapter, the object of study is introduced. Firstly, some general information about the classification and definition of clouds, especially the different high level clouds, are provided. In a second step, the formation of cirrus clouds is described which includes the nucleation of ice crystals from the microphysical point of view as well as the meteorological conditions leading to the formation of cirrus in the atmosphere. Subsequently, definitions of the microphysical, optical and radiative properties which will be relevant in this work are provided before finally the state-of-the-art of the impact of cirrus clouds on the global climate is summarized.

The second chapter presents the measurement site, instruments and ancillary data used in this thesis. In a first step, the measurement platform of the Laboratoire d'Optique Atmosphérique in Lille and its climatological characteristics are introduced. Secondly, a technical description of the thermal infrared radiometer and its measurement principle are provided, before the same kind of information is given for the micropulse lidar. Subsequently, the cloud detection and the retrieval of the cloud optical thickness from the lidar measurements as well as the ancillary data used in the course of this thesis are described because this information is common in all steps of our methodology to study cirrus cloud properties.

This methodology is described in the third chapter on the basis of a case study. The development of the final synergy algorithm follows three main steps. All of these steps use the same microphysical bulk ice model as well as the same inversion method based on optimal estimation. Hence, these two concepts are described previously to the retrieval algorithms developed in this thesis. The first algorithm retrieves the IWP of cirrus clouds from the thermal infrared radiometer measurements alone. In a second step, the lidar measurements are used to integrate the information about the vertical distribution of the ice inside the cloud and a second algorithm to retrieve IWC profiles is demonstrated. These retrieved IWC profiles strongly depend on the so-called backscatter-to-extinction ratio which is discussed in detail before strategies to constrain this parameter are presented. In this context, it is demonstrated that thermal infrared radiometer measurements can be used to constrain the backscatter-to-extinction ratio of the bulk ice crystals. This finally leads to the establishment of the synergy algorithm combining the lidar and thermal infrared radiometer measurements in a common optimal estimation framework. The synergy algorithm allows to retrieve in addition to the IWC profile a correction factor for the backscatter intensity of the ice crystals composing the cirrus cloud.

Finally, the fourth chapter is dedicated to the discussion of the retrieval results obtained from this newly developed synergy algorithm. In this chapter, sensitivity studies for several non-retrieved parameters are presented and the sources of uncertainty for the retrieved quantities are pointed out. These sources of uncertainty are mainly related to an insufficient characterization of the surrounding atmosphere, in particular the amount of water vapour in the atmospheric column as well as the properties of atmospheric aerosols which may be present during the measurement. In this context, a second case study is introduced which illustrates the difficulties that may arise when applying the algorithm.

CHAPTER 1

Cirrus Clouds

The first chapter of this thesis aims to introduce the cloud type which is studied in this work. In a first step, some general information about clouds that can be found in the atmosphere and their classification is provided. In this context, special attention is drawn to cirrus clouds since they are the object of study here. Therefore, the definitions of different high level cloud types are given.

Secondly, the formation of cirrus clouds is described. This includes the nucleation of ice crystals from the microphysical point of view as well as the meteorological conditions leading to the formation of cirrus clouds in the atmosphere. Different processes connected with climatological and geographical characteristics are presented that produce different types of cirrus.

The third section of this chapter provides definitions of the microphysical, optical and radiative properties that may be used to describe cirrus clouds. It focuses on the properties relevant for this thesis and should not be understood as a complete description of all conceivable properties to characterize cirrus clouds.

In the last section, the global distribution of cirrus clouds and climatological statistics for mid-latitude cirrus are presented with regard to the cloud properties described in the previous section. Finally, the current understanding of the radiative impact of cirrus on the global climate is discussed and in this context open research questions are pointed out.

1.1 Definition of Clouds: Nomenclature and Classification

The first attempt to establish a cloud classification system dates back to the early nineteenth century and was proposed by Lamarck (1802) who defined five different cloud types including a category named *nuages en balayures* which means "broom-like clouds" and corresponds to what we call *cirrus* today. However, the nomenclature of Lamarck (1802) was not adopted by other scientists which is probably due to his choice of French names that were not understood in other countries. On the contrary, the classification of Howard (1803) published one year later in England was a huge success and constitutes the basis of the cloud classification system which is still used nowadays. Howard (1803) tried to establish a complete classification scheme suitable for all clouds and chose Latin names for the different cloud types in order to be understood internationally. He proposed three fundamental classes of clouds, namely *cirrus*, *stratus* and *cumulus*, from which all other clouds could be characterized by transition or association. For clouds that precipitate during observation he introduced the term *nimbus*.

Over the following years, other researchers proposed additional forms and the cloud altitude was recognized to be an important classification parameter. Finally, Hildebrandsson (1887) and Abercromby (1887) merged these propositions and came up with the classification system of ten cloud genera which was approved by the International Meteorological Conference held in Munich in 1891 and became the standard for cloud classification until today. It was published in the first International Cloud Atlas (ICA) in 1896 which contained 28 coloured pictures of clouds to illustrate the different types and was accompanied by definitions and descriptions in three languages (French, German and English). Since then, the ICA was updated several times. With progress in technology and an advanced understanding of the atmosphere new cloud types have been added. The latest version of the ICA is web-based and was published recently by the World Meteorological Organization (WMO, 2017). It provides the following definition of a cloud:

"A cloud is a hydrometeor consisting of minute particles of liquid water or ice, or of both, suspended in the atmosphere and usually not touching the ground. It may also include larger particles of liquid water or ice, as well as non-aqueous liquid or solid particles such as those present in fumes, smoke or dust." (WMO, 2017)

Level	Genera	Polar region	Mid-latitudes	Tropics
Low	Sc, St	0 - 2 km	0 - 2 km	0 - 2 km
Middle	As, Ac	2 - 4 km	2 - 7 km	2 - 8 km
High	Ci, Cs, Cc	3 - 8 km	5 - 13 km	6 - 18 km
Large vertical extent	Cu, Cb, Ns	0 - 8 km	0 - 13 km	0 - 18 km

Table 1.1: Approximate altitudes of the cloud levels and the cloud genera found within each level according to the International Cloud Atlas (WMO, 2017).

Every cloud appearing in the atmosphere is unique. However, there are some characteristic forms which are frequently observed all around the globe. The above-mentioned classification scheme is entirely based on morphology and groups clouds into these characteristic forms using the cloud altitude as classification criterion. In general, there are two different characters of clouds: stratiform and convective. As proposed by Howard (1803), from the three main types of clouds (namely *stratus* and *cumulus* for the stratiform and convective characters, respectively, as well as *cirrus* for high clouds) ten so-called cloud genera are derived which are sorted by altitude. The troposphere is divided into three levels: low, middle and high. These levels overlap and their limits depend on the geographical latitude. The approximate altitudes of each level are summarized in Table 1.1 for different geographical regions. Figure 1.1 illustrates the ten cloud genera and associates them to the levels in which they occur. In the low level *stratus* (St) and *stratocumulus* (Sc) can be found. Furthermore, the bases of clouds extending into higher levels (*cumulus* (Cu), *cumulonimbus* (Cb) and *nimbostratus* (Ns)) are located in the low level. The prefix *alto-* describes the clouds in the middle level, namely *altocumulus* (Ac) and *altostratus* (As).

In this thesis, we will focus on high level clouds that are generally composed of ice crystals, although some of them may contain patches of supercooled liquid water (Lynch et al., 2002). Figure 1.2 illustrates the three genera which can be found in the upper troposphere. According to the WMO (2017), they are defined as follows:

1. Cirrus (Ci): *"Detached clouds in the form of white, delicate filaments or white or mostly white patches or narrow bands. These clouds have a fibrous (hair-like) appearance, or a silky sheen, or both."*
2. Cirrocumulus (Cc): *"Thin, white patch, sheet or layer of cloud without shading, composed of very small elements in the form of grains, ripples, etc., merged*

or separate, and more or less regularly arranged; most of the elements have an apparent width of less than 1°."

3. Cirrostratus (Cs): *"Transparent, whitish cloud veil of fibrous (hair-like) or smooth appearance, totally or partly covering the sky, and generally producing halo phenomena."*

Hence, the genus *cirrus* can be distinguished from *cirrocumulus* due to its fibrous appearance and from *cirrostratus* due to its less continuous coverage. Since cirrus clouds are situated in high altitudes, they are often exposed to wind shear of horizontal winds leading to complex and unique cloud structures (Platt et al., 1994). Thus, it should be noted that the above-cited cloud genera are further subdivided into species and varieties to cover the large variability of cloud shapes and habits in the atmosphere. The most common type of cirrus is *cirrus fibratus* which describes *"nearly straight or more or less irregularly curved white filaments, which are always fine and do not terminate in hooks or tufts"* (WMO, 2017). Other species of this genus are *cirrus uncinus*, *spissatus*, *floccus* and *castellanus*. The genus *cirrocumulus* is subdivided into *stratiformis*, *lenticularis*, *castellanus* and *floccus*, and the genus *cirrostratus* into *fibratus* and *nebulosus*. All of these species are described in detail in the ICA (WMO, 2017) and will not be repeated here for brevity reasons. In the following, we will focus on the meteorological conditions and dynamical processes leading to the formation of clouds, especially high level clouds.

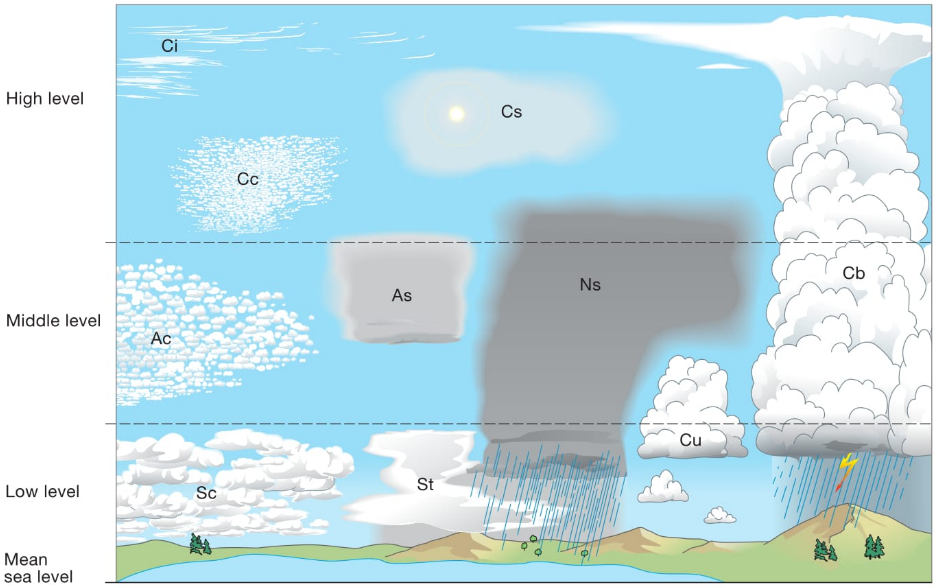

Figure 1.1: The ten cloud genera. Low level: stratocumulus (Sc), stratus (St). Middle level: altocumulus (Ac), altostratus (As). High level: cirrus (Ci), cirrostratus (Cs), cirrocumulus (Cc). Large vertical extent: cumulus (Cu), cumulonimbus (Cb), nimbostratus (Ns). Source: `https://cloudatlas.wmo.int/clouds-definitions.html`.

(a) Cirrus (Ci) **(b)** Cirrocumulus (Cc)

(c) Cirrostratus (Cs)

Figure 1.2: The three genera of high level clouds. Source: `https://cloudatlas.wmo.int/principles-of-cloud-classification-genera.html`.

1.2 Formation of Cirrus Clouds

In general, clouds can form in every air mass that becomes supersaturated and contains aerosol particles serving as cloud condensation nuclei (CCN) or ice nuclei (IN). Supersaturation means that the relative humidity exceeds 100 % and is reached when air is cooled by different atmospheric lifting mechanisms, for example convergence lifting, frontal lifting or orographic lifting. The lifted air contains water vapour and if it is cooled below the dew point, condensation or sublimation processes start on the CCN or IN, respectively. During condensation or sublimation, latent heat energy is released which increases the vertical motion, especially in convective clouds.

Once a droplet or ice crystal is formed, it can be modified by several different microphysical processes. For example, the droplet or ice crystal may continue growing by further condensation or sublimation. Another growth process for water droplets is the so-called coalescence which describes the fusion of colliding droplets. Similarly, collisions of ice crystals can lead to their aggregation. Other processes may provoke the break up of large droplets or crystals. Furthermore, the phase of water may change during the development process of the cloud between liquid water, water vapour and ice. Freezing, however, is complex and there are several different freezing mechanisms occurring in clouds which will be presented in the first paragraph of this section. Subsequently, different atmospheric conditions and processes leading to the formation of cirrus are described.

1.2.1 Freezing Processes in the Atmosphere

In the atmosphere, water droplets do not freeze instantaneously at a temperature of 0 °C. Supercooled liquid water exists down to a temperature as low as -38 °C (Pruppacher and Klett, 1997). Between 0 °C and -38 °C freezing processes are triggered by so-called *ice nuclei* (IN) which are aerosol particles facilitating the ice nucleation (heterogeneous freezing). For homogeneous freezing a temperature below -38 °C and a high supersaturation with respect to ice are required. Both types of freezing are introduced in the following.

Homogeneous freezing means that either pure water droplets or entirely dissolved solution droplets freeze spontaneously. This requires large saturation ratios with respect to ice of 1.4 to 1.7 and temperatures below -38 °C (Tabazadeh et al., 2000; Koop et al., 2000; Kärcher and Lohmann, 2002b). The first to describe the theory of homogeneous ice nucleation of supercooled liquid droplets in a coherent manner was McDonald (1953) who applied classical homogeneous nucleation theory for water droplets to the nucleation of ice in supercooled liquid water. From the molecular point of view the process of homogeneous ice nucleation can be described as follows: Due to the Brownian motion, the water molecules constantly change their position towards each other. As a result of random collisions, clusters of water molecules may form which have a similar structure as ice. These clusters are unstable and vanish as fast as they appear. However, sometimes they grow to a critical minimum size and form a stable ice embryo that acts as an ice nucleus. Subsequently, other water molecules within the droplet attach themselves to the nucleus and the droplet freezes. The formation of ice embryos starts at temperatures just below the freezing point, but at these temperatures the Brownian motion is large enough to weaken their structure. At lower temperatures, the thermal motion is reduced and thus bigger ice embryos may form more easily. Homogeneous freezing is therefore a stochastic process that becomes more likely with decreasing temperature. Since cirrus clouds form in the upper troposphere at low temperatures, homogeneous freezing is an important process during their formation (e.g. Pruppacher, 1995; Kärcher and Lohmann, 2002a).

However, heterogeneous ice nucleation at temperatures above -38 °C may also play an important role in the formation of certain cirrus clouds (Lynch et al., 2002). Heterogeneous freezing mechanisms require aerosol particles who act as IN. In contrast to CCN, IN are usually insoluble or only partially soluble aerosol particles (DeMott et al., 1997). The ability of a particle to act as an IN depends on its chemical composition and size. Suitable IN are for example mineral dust and fly ash or metallic particles which means both natural as well as anthropogenic (industrial or combustion) particles (DeMott et al., 2003).

There are at least four different heterogeneous ice nucleation mechanisms (Lynch et al., 2002). The direct deposition of water vapour on the surface of an IN is known as *deposition freezing*. This process requires supersaturation with respect to ice but not with respect to water. Suitable IN for deposition freezing are large particles with a hexagonal structure similar to the crystalline structure of ice.

Contact freezing describes the process when a supercooled droplet collides with an IN and the collision triggers freezing. Hence, this process depends on the collision rate between the supercooled droplets and the IN which in turn depends on the size

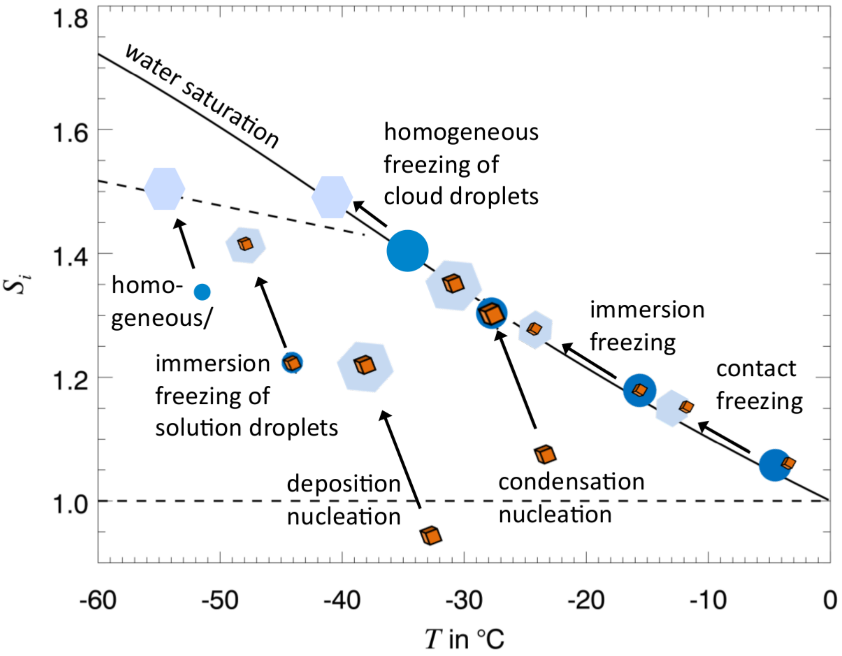

Figure 1.3: Freezing processes depending on temperature (T) and supersaturation with respect to ice (S_i) (Hoose and Möhler, 2012).

of the droplets and the aerosol particles. Contact freezing is an important process for the formation of ice in mixed-phase clouds.

Condensation freezing means that the aerosol particle first acts as CCN for a supercooled droplet. The water vapour condenses at the surface of the CCN at temperatures below 0 °C. Subsequently, the aerosol particle acts as IN and triggers freezing.

The fourth mechanism is denoted as *immersion freezing*. This process is similar to condensation freezing since the aerosol particle firstly acts as CCN and secondly as IN, but in contrast to condensation freezing, the aerosol particle is incorporated into the droplet at temperatures above 0 °C. When the temperature falls below 0 °C the aerosol particle becomes an IN and activates freezing.

Figure 1.3 borrowed from Hoose and Möhler (2012) summarizes the ice formation processes depending on temperature (T) and supersaturation with respect to ice (S_i) which are the determining factors for ice nucleation. Above the dashed line at $S_i = 1$, the environment is supersaturated with respect to ice. The solid diagonal line represents saturation with respect to water which means that supercooled water is in equilibrium with the vapour phase along this line. All freezing processes involving supercooled water droplets are arranged along that line. The heterogeneous freezing processes occur at warmer temperatures and lower supersaturation with respect to ice than homogeneous freezing. From warm to cold, firstly contact freezing takes place, followed by immersion and condensation freezing and finally homogeneous freezing of cloud droplets. For deposition freezing no supersaturation with respect to water is required because the water vapour deposits directly on the IN. This happens at temperatures lower than -30 °C. Similarly, for homogeneous and immersion freezing of solution droplets between -40 °C and -60 °C no supersaturation with respect to water is required. The following paragraph will focus on the meteorological conditions leading to the different ice nucleation processes described above and to the formation of cirrus clouds.

1.2.2 Meteorological Conditions and Dynamical Processes for the Formation of Cirrus

As mentioned above, the formation of clouds in the atmosphere is related to lifting processes of air masses. This is also true for cirrus clouds which are often of convective nature (Platt et al., 1994). One can think of several different meteorological conditions leading to the lifting of air masses in the atmosphere. The governing parameters for the generation of cirrus clouds are the ambient temperature, the strength of the updraught velocity and the characteristics of the available IN (Lynch et al., 2002). The most important natural cause for cirrus in the mid-latitudes are synoptic-scale disturbances, e.g. weather fronts or perturbations related to the jet stream, which are generally characterized by relatively weak updraughts. Other generation mechanisms are determined by larger updraught velocities, for example due to orographic lifting or in the case of anvil cirrus originating from a thunderstorm cloud (Cb). Special cases of cirrus clouds are tropical tropopause layer (TTL) cirrus as well as contrail cirrus initiated by aircraft emissions. In the following, we will have a closer look at the different cirrus generating processes and conditions.

Synoptic Cirrus

The term synoptic cirrus comprises the usual varieties of cirrus clouds formed in situ in the upper troposphere due to weather perturbations. These perturbations are often related to the jet stream or weather fronts (e.g. Liou, 1986; Lynch et al., 2002). Since the temperature is very low and the aerosol concentration (and hence the number of potential IN) is rather small in the upper troposphere, the most important freezing mechanism in synoptic cirrus is the homogeneous nucleation of water droplets or aerosol solution droplets. Compared to pure water, liquid aerosol droplets reduce the necessary saturation ratio and thereby accelerate the freezing process (DeMott et al., 1997; Chen et al., 2000; Koop et al., 2000; Hoose and Möhler, 2012).

A typical generation process of cirrus occurs at warm fronts when a warm air mass is moving against a colder air mass. Since warm air is less dense and hence lighter than cold air, the warm air mass is unable to displace the colder air mass and is forced upward. This lifting process leads to the formation of clouds, typically starting with cirrus and cirrostratus which are formed in the warm air situated high above the cold air well ahead of the warm front. As the front approaches, the clouds evolve into lower and more dense altostratus and finally nimbostratus which likely precipitate. Warm fronts are characterized by a rather slow movement since it is difficult for the warm air to move against the colder and more dense air. The lifting is rather slow (in the order of $\mathrm{cm\,s^{-1}}$) leading to a large coverage and a longer lifetime of the cloud (Krämer et al., 2016). Model studies suggest that cirrus formed under such low vertical velocity conditions are characterized by a small IWC and a small ice crystal number concentration (Heymsfield and Miloshevich, 1993; Krämer et al., 2016).

In case of a cold front, the cold air mass is able to quickly lift up the warmer and less dense air mass leading to larger updraught velocities and stronger convection. Cold fronts move much faster in comparison to warm fronts and can produce dramatic weather changes. The cloud evolution starts with cumulus that may grow into cumulonimbus. Cirrus do not necessarily form in connection with cold fronts but may remain as residua of the convective clouds after the front has passed and the lower portion of the cloud has dispersed.

Strong winds in the upper troposphere, the so-called jet streams, also influence the generation of cirrus clouds. A typical cirriform cloud type generated in the environment of a jet stream is *cirrus uncinus.* The Latin word *uncinus* means "hooked", so these cirrus appear as white, comma shaped structures terminating at the top in a hook (WMO, 2017). Heymsfield (1975a,b,c) studied this type of cloud in a series of papers and found that the formation and dynamics of *cirrus uncinus* are strongly influenced by vertical wind shear occurring in the vicinity of jet streams. As indicated in the schematic model in Fig. 1.4, one can distinguish

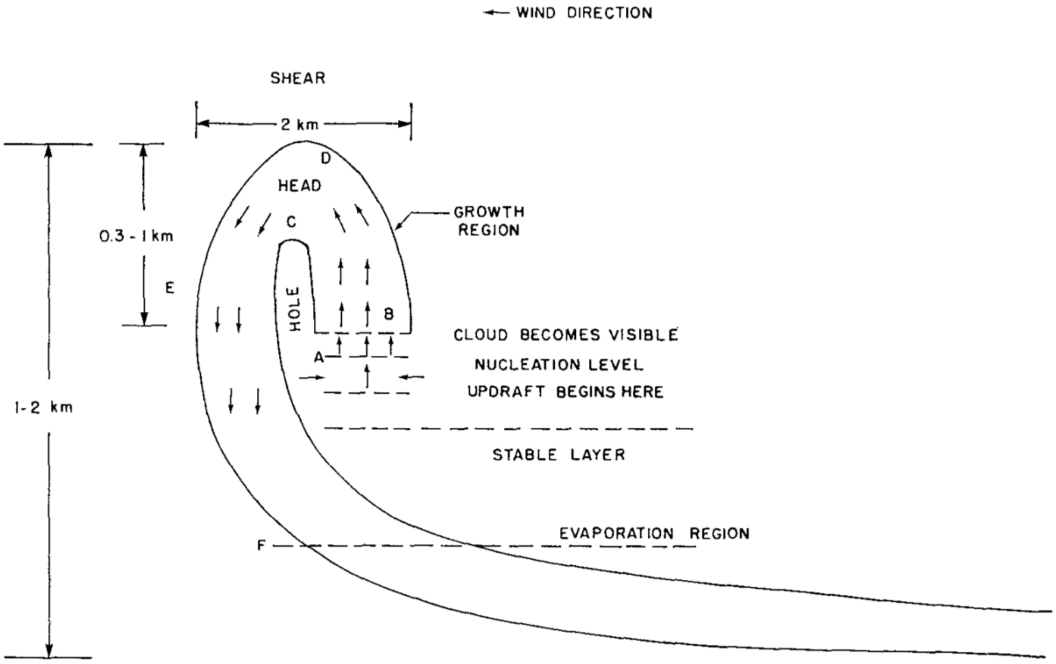

Figure 1.4: Conceptual model of the cirrus uncinus cloud after Heymsfield (1975b).

two parts of the cloud: the head and the trail. The head is situated in a region of strong wind shear and is divided into two parts which are clearly separated by a zone with a minimum crystal concentration ("hole"). The particles are generated near the base of the head in the updraught zone characterized by larger vertical velocities compared to the warm front cirrus (in the order of $\mathrm{m\,s^{-1}}$). The ice crystals continue growing until they fall out of the head region of the cloud on the downdraught side (Heymsfield, 1975a). In the trail, the crystal size decreases due to evaporation which may destabilize regions of the atmosphere below the original cloud generating layer leading to an additional cirrus development (Lynch et al., 2002).

Anvil Cirrus

Anvil cirrus originate from deep convective clouds. Thus, their formation process is characterized by large updraught speeds (in the order of $\mathrm{m\,s^{-1}}$) which means that the conditions for homogeneous freezing (large supersaturation and low temperatures) are attained readily. Hence, the homogeneous freezing of cloud droplets is an important nucleation mechanism of ice in convective clouds which will convert all remaining water to ice when the temperature falls below -38 °C (e.g. DeMott et al., 1997). However, before the homogeneous freezing conditions are fulfilled, heterogeneous nucleation may also play an important role since boundary layer aerosols are lifted together with the air mass and as a consequence the concentration of available IN is higher than in the upper troposphere where synoptic cirrus clouds are formed in situ. This means the properties of anvil cirrus are likely to be different from the properties of synoptic cirrus because the freezing mechanisms as well as the concentration and nature of available IN are different.

Orographic Cirrus

Terrain-induced orographic lifting is also characterized by strong updraughts of 0.5 to 10 m s^{-1} (DeMott et al., 1997) which leads to favourable conditions for homogeneous freezing (Heymsfield and Miloshevich, 1993). Since these conditions are achieved quickly due to the fast updraught, an outburst of homogeneous nucleated ice crystals appears which results in a large number of particles that remain rather small because the available water vapour is distributed equally on many particles (Krämer et al., 2016). As a consequence, the observed IWC of cirrus formed under these conditions is rather large. Furthermore, they are generally characterized by a short lifetime and small scale. However, mountain wave cirrus can be observed over longer periods because the cirrus is continuously formed in a standing wave (Heymsfield and Miloshevich, 1993; Krämer et al., 2016).

TTL Cirrus

Tropical tropopause layer (TTL) cirrus are a special case of cirrus clouds. The temperature in the TTL is very low and TTL cirrus form under uniquely cold conditions (about -70 °C to -90 °C) in high altitudes (15 km to 20 km) (Lynch et al., 2002). The TTL is characterized by a very slow large-scale ascent in the order of 0.01 m s^{-1} (Krämer et al., 2016). The majority of cirrus formed under these conditions is characterized by very low ice crystal number concentrations in combination with a high supersaturation with respect to ice (Krämer et al., 2009; Jensen et al., 2013). The moisture is supplied by the deep convection in the tropics.

Recent model simulations by Spichtinger and Krämer (2013) and Dinh et al. (2016) suggest that the small number concentrations are due to homogeneous freezing in very slow large-scale updraughts superposed by short high-frequency gravity waves caused by convection. Due to the shortness of the waves, the updraught is reversed quickly and the ice nucleation process is stopped when only a few ice crystals have been formed resulting in a low IWC. However, TTL cirrus are a current research item and have not been fully understood yet.

Contrail Cirrus

There is a broad consensus that the modern air traffic influences the formation of clouds in the upper troposphere. Boucher (1999) showed that the cirrus cloud coverage increased in the main flight corridors of the air-traffic between the years 1982 and 1991. Contrail cirrus are initiated by the emissions of aeroplanes and hence of anthropogenic origin. The jet engines introduce moisture and particles in the surrounding atmosphere which are likely sulphur-based haze particles that freeze homogeneously during the mixing process with the surrounding air (Lynch et al., 2002). This leads to a high concentration of small ice crystals for a short time period. Subsequently, the ice crystals may either sublimate quickly if the surrounding air is rather dry or develop into a cirrostratus cloud due to contrail-spreading processes under favourable ambient conditions. In the second case, the cloud layer will look more and more like a natural cirrus cloud and may finally be hard to distinguish from a natural cirrus. The microphysical properties of contrail cirrus probably differ from those of natural cirrus and are not well-known nowadays. They constitute a current research question.

1.3 Properties of Cirrus Clouds

In the previous section, the formation of different cirrus types has been described. The aim of this section is to introduce quantities that can be used to describe their characteristics. For this purpose, definitions of the microphysical, optical and radiative properties of cirrus clouds are provided which will be relevant in this thesis. Thus, it should not be understood as a complete description of all conceivable cloud properties and it should be noted that most of the definitions given in this section can be generalized for all cloud types. Furthermore, the differentiation into the three subgroups microphysical, optical and radiative properties was performed for structuring purposes rather than an actual classification since all of the properties described below are strongly related.

In a first step, we will focus on the microphysical properties which comprise the morphological characteristics of the ice crystals composing the cloud as well as their size distribution and the microphysical parameters integrated over the size distribution. Secondly, the optical properties describing the single scattering characteristics of the cloud particles are defined which will be of significant importance for the methodology proposed in Chapter 3 of this thesis. Finally, the radiative properties are introduced which describe the interactions of the cloud as a whole with atmospheric radiation, e.g. the absorption, scattering and reflection of radiation by the cloud. Hence, the radiative properties are the most important properties from a climatic point of view. However, they strongly depend on the microphysical and the single scattering properties.

1.3.1 Microphysical Properties

From the microphysical point of view, the particles inside a cloud are characterized by their shape and size. A very important parameter to describe the microphysics of a cloud is the *particle size distribution.* Further microphysical properties are integrated over this size distribution, e.g. the *particle number concentration*, the *ice water content* (or liquid water content in the case of a liquid cloud) and the *effective diameter* (or radius). Before these parameters will be defined, the different ice crystal shapes which can be observed in cirrus clouds are summarized.

The shapes and sizes of ice crystals occurring in the atmosphere are strongly variable. Due to the molecular structure of ice, the underlying form of the crystals is hexagonal. Frequently observed particle shapes include columns, plates, dendrites, bullet-rosettes and aggregates thereof.

Weickmann (1945, 1949) was the first to perform in situ measurements in cirrus clouds to investigate ice cloud particles. He reported relationships between temperature, relative humidity and ice crystal shape from data collected in different cirrus cloud types over Germany. The particle shapes he observed include plates, hollow and solid prisms as well as bullet-rosettes. He noticed that humidity and temperature are the governing factors that determine the crystal shape.

Similarly, Heymsfield and Platt (1984) concluded that the ambient temperature is the most determining factor for ice crystal habits. They reported crystal shapes in mid-latitude cirrus for the three temperature intervals larger than -40 °C, between -40 °C and -50 °C, and below -50 °C, and distinguished between cirrus clouds formed in fast updraughts (”convective”) and cirrus clouds formed in slow updraughts (”stable”). For temperatures above -40 °C they found predominantly spatial crystal shapes, such as bullet-rosettes, and for temperatures below -50 °C the predominant shapes were hollow or solid columns. Between -40 °C and -50 °C the reported crystal shapes depend on the nature of the cloud. ”Convective” cirrus were predominantly composed of spatial crystals, whereas in the ”stable” case hollow columns prevailed. Close to the cloud top, Heymsfield and Platt (1984) found predominantly hollow columns and hexagonal plates for all cloud types and temperatures.

Figure 1.5 borrowed from Heymsfield and Iaquinta (2000) shows an example of a balloon-borne ice crystal replicator measurement during the First International Satellite Cloud Climatology Project (ISCCP; Schiffer and Rossow (1983)) Regional Experiment (FIRE; Cox et al. (1987)) Cirrus-II field campaign in 1991 in Coffeyville, Kansas, (Mace et al., 1995). It illustrates and confirms the findings of Heymsfield and Platt (1984). The particles near the cloud base at the warmest temperatures are complex aggregates and spatial forms. With increasing altitude and decreasing temperature, the particle size decreases. In the upper portion of the cloud, the prevailing ice crystal shapes are simpler hexagonal columns and plates.

Figure 1.5 underlines not only the large variability of different shapes that may occur within a single cirrus cloud but also the large range of particle sizes. According to Dowling and Radke (1990), who reviewed a large number of existing studies up to the date of their paper, the crystal dimension ranges between 1 and 8000 μm. The *particle size distribution* (PSD), denoted by $n(D)$, is an important microphys-

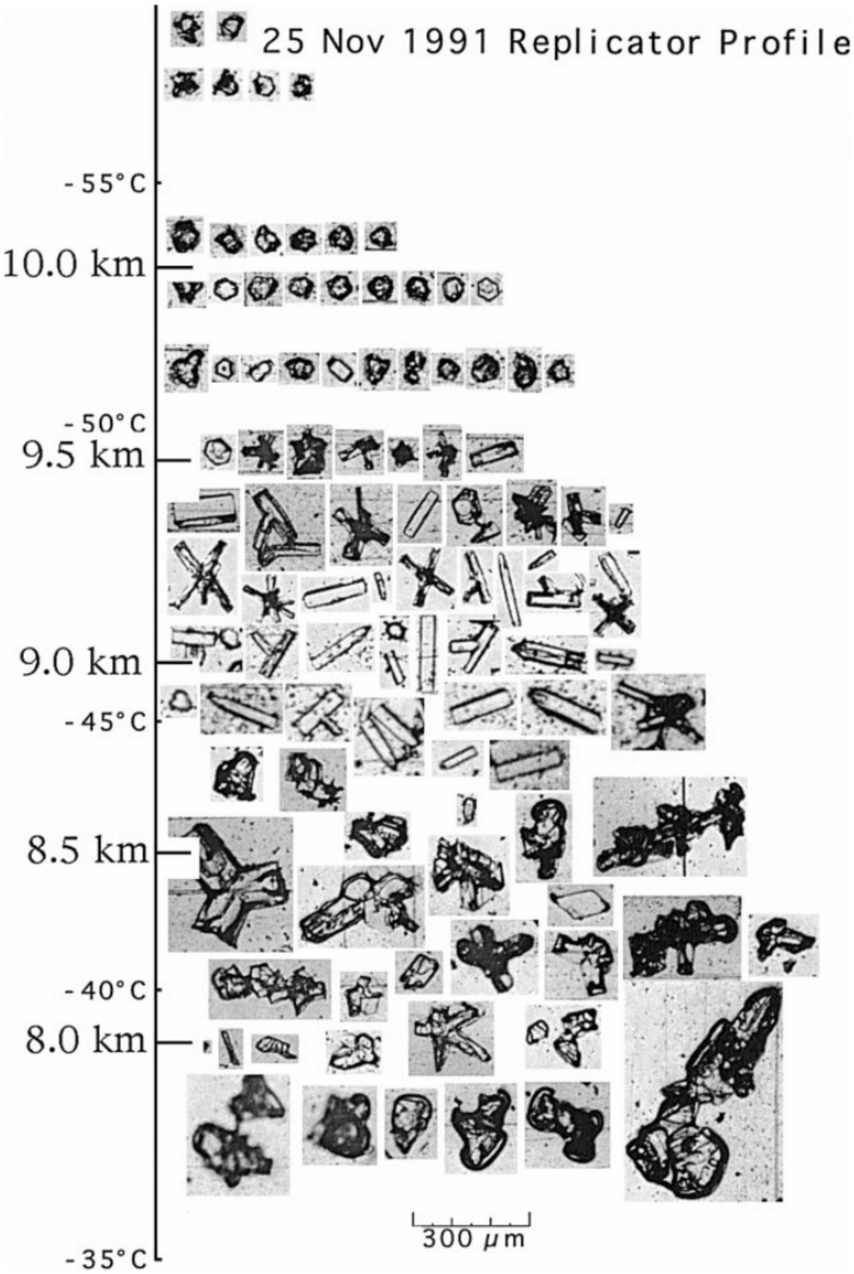

Figure 1.5: Example of a balloon-borne measurement of ice particle habits from an ice crystal replicator. The data was collected on November 25, 1991, during the FIRE Cirrus-II campaign near Coffeyville, Kansas (Heymsfield and Iaquinta, 2000).

ical parameter and gives the infinitesimal number of particles $\mathrm{d}N$ of a maximum dimension $\mathrm{d}D$ within a considered volume element. Thus, it can be defined by,

$$n(D) = \frac{\mathrm{d}N}{\mathrm{d}D}, \tag{1.1}$$

and the total number of particles (N_{tot}), or *particle number concentration*, is then given by,

$$N_{\mathrm{tot}} = \int_0^\infty n(D')\,\mathrm{d}D'. \tag{1.2}$$

As discussed above, the shapes of ice crystals are very complex and it is not straight-forward to quantify the size of a non-spherical particle. A widely used parameter to represent the size of an ice crystal is the *effective diameter*, although it should be noted that different definitions exist in the literature (McFarquhar and Heymsfield, 1998). The most common definition was suggested by Mitchell (2002) who used the ratio of the size distribution volume $V(D)$ to the projected area $A(D)$ of a crystal with maximum dimension D. According to this definition, the *effective diameter* is expressed by,

$$D_{\mathrm{eff}} = \frac{3}{2}\frac{\int_0^\infty V(D')\,n(D')\,\mathrm{d}D'}{\int_0^\infty A(D')\,n(D')\,\mathrm{d}D'}. \tag{1.3}$$

Another important parameter for the microphysical description of cirrus clouds is the *ice water content* (IWC) which is the quantity that is retrieved with the algorithm presented in Chapter 3 of this thesis. It is a direct measure of the mass of ice in a specified amount of dry air. Hence, its unit is given in $\mathrm{kg\,m^{-3}}$ (or $\mathrm{g\,m^{-3}}$). It is defined by,

$$\mathrm{IWC} = \rho_{\mathrm{ice}} \int_0^\infty V(D')\,n(D')\,\mathrm{d}D', \tag{1.4}$$

where ρ_{ice} is the bulk ice density of $0.92\,\mathrm{g\,m^{-3}}$ (Mitchell, 2002). Integrating the IWC over the whole cloud layer, leads to the definition of the *ice water path* (IWP),

$$\mathrm{IWP} = \int_{z_{\mathrm{base}}}^{z_{\mathrm{top}}} \mathrm{IWC}(z')\,\mathrm{d}z', \tag{1.5}$$

where z_{base} and z_{top} correspond to the cloud base and top altitudes, respectively. The IWP is an important parameter in this thesis since the passive thermal infrared radiances are sensitive to the integrated cloud properties.

Finally, it is noteworthy that the effective diameter and the IWC can be linked easily by combining Eqs. 1.3 and 1.4 which leads to,

$$D_{\mathrm{eff}} = \frac{3}{2}\frac{\mathrm{IWC}}{\rho_{\mathrm{ice}}\int_0^\infty A(D')\,n(D')\,\mathrm{d}D'}. \tag{1.6}$$

Furthermore, the effective diameter provides a link between the microphysical and the radiative properties because the projected area in the denominator is related to the optical extinction. The optical properties of cirrus clouds are defined in the next section.

1.3.2 Single Scattering Properties

The bulk single scattering properties of cirrus clouds are of significant importance in this thesis because they are crucial for the radiative transfer calculations used in our methodology described in Chapter 3. They are also required in global climate models to calculate the radiative impact of cirrus (Baran, 2009; Baran et al., 2014b). It is important to notice that all properties described in this section depend on the wavelength, although no index indicating this dependency is assigned to the different properties for reasons of clarity.

The existence of optical phenomena such as the 22° and 46° halos proves the presence of scattering inside ice clouds. Halos generally occur in cirrostratus and they appear as a ring of light around the sun (cf. Fig. 1.2c for an illustration). Their presence is due to the hexagonal structure of ice. The 22° halo is formed when the incoming sun rays are refracted between faces of hexagonal ice crystals that are inclined by 60° towards each other. In case of the 46° halo, the rays are refracted from a top face to a side face (or vice versa) of hexagonal crystals where the faces are inclined by 90°.

To describe the scattering of an incident unpolarized light beam by an ensemble of ice crystals suspended in the atmosphere, the *Stokes vector* $\vec{S}$ is a useful quantity which characterizes the energetic and polarization properties of an electromagnetic wave. It consists of four components which all carry the unit of an *irradiance* ($\mathrm{W\,m^{-2}}$, cf. Eq. 1.14 for definition), usually expressed by,

$$\vec{S} = (I, Q, U, V)^T, \tag{1.7}$$

where I represents the total irradiance, Q quantifies the irradiance of the parallel minus the perpendicular component of the linearly polarized electromagnetic wave (with respect to a reference plane), U is the portion of the irradiance polarized linearly with respect to a plane tilted by 45° with respect to the reference plane, and V represents the circularly or elliptically polarized irradiance.

In case of sunlight being scattered by atmospheric ice crystals, the Stokes vector of the incident light $(I_{\text{inc}}, Q_{\text{inc}}, U_{\text{inc}}, V_{\text{inc}})^T$ is related to the Stokes vector of the scattered light $(I_{\mathrm{sca}}, Q_{\mathrm{sca}}, U_{\mathrm{sca}}, V_{\mathrm{sca}})^T$ by the so-called *phase matrix* which is a 4 x 4 matrix defined for each scattering angle Θ by (van de Hulst, 1957),

$$\begin{pmatrix} I_{\mathrm{sca}} \\ Q_{\mathrm{sca}} \\ U_{\mathrm{sca}} \\ V_{\mathrm{sca}} \end{pmatrix} = \frac{C_{\mathrm{sca}}}{4\pi r^2} \begin{pmatrix} P_{11} & P_{12} & 0 & 0 \\ P_{21} & P_{22} & 0 & 0 \\ 0 & 0 & P_{33} & P_{34} \\ 0 & 0 & P_{43} & P_{44} \end{pmatrix} \begin{pmatrix} I_{\mathrm{inc}} \\ Q_{\mathrm{inc}} \\ U_{\mathrm{inc}} \\ V_{\mathrm{inc}} \end{pmatrix}, \tag{1.8}$$

where C_{sca} is the scattering cross section and r the distance between the scattering ice crystal and the observer. The phase matrix presented in Eq. 1.8 corresponds to the special case where the ice crystals in the cloud are randomly oriented. In this case, it only depends on the scattering angle Θ which is the angle between the incident and the refracted rays.

The only element of the phase matrix relevant for this thesis is P_{11}. For an unpolarized incident light beam (which is the case for sunlight), P_{11} is proportional to the scattered light and is called the *scattering phase function* (Baran, 2007; Baran and Labonnote, 2007). It is normalized by,

$$\frac{1}{2}\int_{-1}^{1} P_{11}(\Theta)\,\mathrm{d}(\cos\Theta) = 1, \tag{1.9}$$

and strongly depends on the shape and size of the ice crystals. Figure 1.6 shows examples of phase functions for different ice crystal shapes at a wavelength of $0.87\,\mu$m. For ice crystals with a hexagonal shape, the two peaks at $22\,^\circ$ and $46\,^\circ$ corresponding to the halos can clearly be identified. Furthermore, these crystal shapes lead to an enhanced scattering in backward direction for scattering angles between $175\,^\circ$ and $180\,^\circ$. However, atmospheric ice crystals are not always of the perfect idealized shapes presented in Fig. 1.6. They might be distorted, their surfaces might be roughened, and/or they might contain inclusions of air bubbles or aerosols (Baran, 2007). All these processes lead to the removal or reduction of the optical features of the phase function which means the halos at $22\,^\circ$ and $46\,^\circ$ as well as the backscattering peak (e.g. Macke et al., 1996; Yang and Liou, 1998; C.-Labonnote et al., 2001). The phase function, especially in the exact backscattering direction, is a crucial parameter in our methodology and for visible wavelengths its value varies significantly for the different ice crystal models shown in Fig. 1.6 (between about 0.08 and 4.0 for the phase functions at $0.87\,\mu$m illustrated in the figure). This backscattering peak of the phase function will be discussed in more detail in Chapter 3 where the microphysical model used in our algorithms will be described.

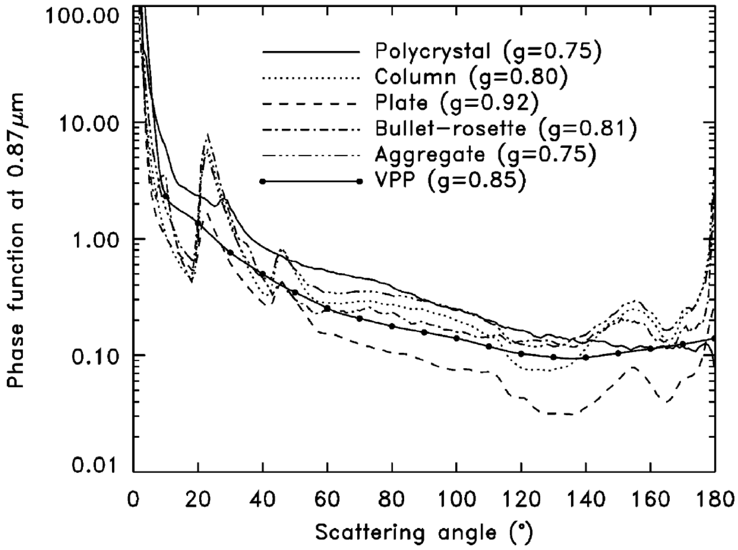

Figure 1.6: Example of scattering phase functions for different particle shapes at a wavelength of 0.87 μm. Ice crystal models: polycrystal (full line), hexagonal ice column (dotted line), hexagonal plate (dashed line), six-branched bullet-rosette (dot-dashed line) and hexagonal ice aggregate (double-dot dashed line). "VPP" stands for an experimentally determined phase function (full line with filled circles). The according asymmetry parameter g is reported in the legend (Baran, 2009).

The asymmetry parameter g reported in Fig. 1.6 is defined as the average cosine of the scattering angle (Baran, 2007),

$$g = \langle \cos\Theta \rangle = \frac{1}{2} \int_{-1}^{1} \cos\Theta \, P_{11}(\Theta) \, \mathrm{d}(\cos\Theta). \tag{1.10}$$

It describes the portions of the incident radiation which are scattered in forward and backward direction by one single value between -1 and 1. A value of -1 means that all incident light is scattered in the backward direction, and a value of 1 means that all incident light is scattered in the forward direction. If g is equal to zero, the incident light is scattered equally in the forward and backward hemispheres. Since the scattering phase function P_{11} strongly depends on the crystal shape and size, the asymmetry parameter also depends on these two properties. Values of g at a wavelength of 0.55 μm reported in the literature for different ice crystal models range between 0.74 for the polycrystal (Macke et al., 1996) and an interval of 0.77 to 0.86 for solid hexagonal columns (Takano and Liou, 1989). Measurements of g for atmospheric ice crystals that can be found in the literature suggest a value of around 0.74 ± 0.02 (Baran, 2007).

Further important single scattering properties are the *volume* (or *bulk*) *extinction* and *scattering coefficients*, σ_{ext} and σ_{sca}, respectively. They are defined as follows,

$$\begin{aligned}\sigma_{\text{ext}} &= \int Q_{\text{ext}}(\vec{q})\,\langle S(\vec{q})\rangle\, n(\vec{q})\,\mathrm{d}\vec{q},\\ \sigma_{\text{sca}} &= \int Q_{\text{sca}}(\vec{q})\,\langle S(\vec{q})\rangle\, n(\vec{q})\,\mathrm{d}\vec{q},\end{aligned} \tag{1.11}$$

where $Q_{\text{ext}}(\vec{q})$ and $Q_{\text{sca}}(\vec{q})$ are the extinction and scattering efficiency factors, respectively, defined as the ratio of the extinction (scattering) cross section to the projected area of the ice crystal. $\langle S(\vec{q})\rangle$ represents the orientation-averaged projected area and $n(\vec{q})$ the PSD. The vector $\vec{q}$ indicates the different particle shapes and sizes in the PSD and all parameters in Eqs. 1.11 are expressed as functions of $\vec{q}$. To obtain the bulk coefficients, Eqs. 1.11 are integrated over the q domain.

Finally, the *single scattering albedo*, ϖ_0, is given by,

$$\varpi_0 = \frac{\sigma_{\text{sca}}}{\sigma_{\text{ext}}}, \tag{1.12}$$

which takes values between zero and unity. A value of zero means that the extinction is solely due to absorption, a value of unity means that the extinction is solely due to scattering.

1.3.3 Radiative Properties

The radiative properties of cirrus clouds which are important for this thesis are on the one hand the *emissivity* in the thermal infrared at the wavelengths of the radiometer, and on the other hand the *optical thickness* at the visible lidar wavelength. Before defining these two quantities, it might be useful to start with the definitions of some relevant quantities describing atmospheric radiation.

The fundamental radiant quantity is the *radiant energy* E_{rad}, expressed in units of Joules, which can be measured based on first principles. From the radiant energy the other radiative variables are derived subsequently. The *radiant energy flux* Φ (or *radiant power*), in units of Watts, is defined as the variation of the radiant energy, $\mathrm{d}E_{\text{rad}}$, in a given time interval, $\mathrm{d}t$,

$$\Phi = \frac{\mathrm{d}E_{\text{rad}}}{\mathrm{d}t}. \tag{1.13}$$

Considering the radiant energy flux received or emitted by a surface, leads to the definition of the *radiant energy flux density*, which may also be called *irradiance*, I, in units of $\mathrm{W\,m^{-2}}$. I is a measure of the total radiant energy in a given time interval per differential area element, d^2A,

$$I = \frac{\mathrm{d}^3 E_{\mathrm{rad}}}{\mathrm{d}t\,\mathrm{d}^2A} = \frac{\mathrm{d}^2\Phi}{\mathrm{d}^2A}. \tag{1.14}$$

The radiant energy in a given time interval per differential area element and per solid angle, $\mathrm{d}^2\Omega$, defines the so-called *radiance* L in units of $\mathrm{W\,m^{-2}\,sr^{-1}}$,

$$L = \frac{\mathrm{d}^5 E_{\mathrm{rad}}}{\mathrm{d}t\,\mathrm{d}^2A\,\mathrm{d}^2\Omega} = \frac{\mathrm{d}^4\Phi}{\mathrm{d}^2A\,\mathrm{d}^2\Omega}. \tag{1.15}$$

For the rest of this thesis, the radiance defined after Eq. 1.15 will be used to represent atmospheric radiation since it is the quantity obtained from the thermal infrared radiometer measurements.

In general, any object of a temperature T emits radiation at any wavelength λ. The basic law that describes this radiation is Planck's law,

$$B_\lambda(T) = \frac{2hc^2}{\lambda^5} \cdot \frac{1}{\exp(\frac{hc}{\lambda kT}) - 1}, \tag{1.16}$$

where h is Planck's constant ($6.63 \cdot 10^{-34}$ J s), k is Boltzmann's constant ($1.38 \cdot 10^{-23}$ $\mathrm{J\,K^{-1}}$) and c is the speed of electromagnetic radiation in vacuum ($2.998 \cdot 10^8$ $\mathrm{m\,s^{-1}}$). $B_\lambda(T)$ in Eq. 1.16 represents the spectral radiance in units of $\mathrm{W\,m^{-2}\,\mu m^{-1}\,sr^{-1}}$ (if the wavelength is given in μm) that a perfect emitter, a so-called blackbody, would emit according to its temperature. Such perfect emitters do not exist in reality and real objects deviate from this ideal behaviour. The *emissivity* ϵ_λ describes the degree of deviation of the radiance emitted by the real object from the radiance emitted by a blackbody at a given temperature and wavelength. Hence, this monochromatic emissivity can be defined as the ratio of the spectral radiance that is actually emitted by a real object to the spectral radiance a blackbody would emit at temperature T,

$$\epsilon_\lambda = \frac{L_\lambda(T)}{B_\lambda(T)}. \tag{1.17}$$

On its way through the atmosphere, radiation is modified by several different processes. One commonly observed phenomenon is the attenuation of radiation due to scattering and absorption processes when passing through an aerosol or cloud layer. The Bouguer-Lambert-Beer law describes the extinction of the spectral radiance L_λ along a path of length s through an atmospheric layer, e.g. a cloud, without taking multiple interactions such as emission and multiple scattering processes into account. The variation of the spectral radiance when passing through the layer may be expressed by,

$$\mathrm{d}L_\lambda = -\sigma_{\mathrm{ext},\lambda}(s) \cdot L_\lambda \, \mathrm{d}s, \tag{1.18}$$

where $\sigma_{\mathrm{ext},\lambda}(s)$ is the volume extinction coefficient in units of m^{-1}. Equation 1.18 provides the differential form of the Bouguer-Lambert-Beer law. Integration of this equation shows an exponential decrease of the initial spectral radiance $L_{\lambda,0}$ at $s = 0$ after the path ds,

$$L_\lambda(s) = L_{\lambda,0} \cdot \exp\left(-\int_0^s \sigma_{\mathrm{ext},\lambda}(s') \, \mathrm{d}s'\right). \tag{1.19}$$

In the case of attenuation due to a cloud layer, the boundaries of the integral would be the cloud base and top altitudes (z_{base} and z_{top}, respectively). The *extinction optical thickness*, $\tau_{\mathrm{ext},\lambda}$, of the cloud layer is then defined as,

$$\tau_{\mathrm{ext},\lambda} = \int_{z_{\mathrm{base}}}^{z_{\mathrm{top}}} \sigma_{\mathrm{ext},\lambda}(z) \, \mathrm{d}z. \tag{1.20}$$

Thus, the extinction optical thickness is a dimensionless measure of transparency of an atmospheric layer, e.g. a cirrus cloud. It describes the total attenuation due to scattering and absorption. However, it is possible to define a *scattering optical thickness*, $\tau_{\mathrm{sca},\lambda}$, and an *absorption optical thickness*, $\tau_{\mathrm{abs},\lambda}$, in the same manner. In the first case, only the attenuation due to scattering processes is taken into account and $\sigma_{\mathrm{ext},\lambda}$ in Eqs. 1.18 to 1.20 is replaced by the volume scattering coefficient $\sigma_{\mathrm{sca},\lambda}$. Similarly, in the second case only attenuation due to absorption is regarded and the volume absorption coefficient $\sigma_{\mathrm{abs},\lambda}$ is used. Hence, the volume coefficients are related via,

$$\sigma_{\mathrm{ext},\lambda} = \sigma_{\mathrm{sca},\lambda} + \sigma_{\mathrm{abs},\lambda}. \tag{1.21}$$

To get an idea about which ranges of extinction optical thickness in the visible wavelength region are relevant for cirrus clouds, the work of Sassen and Cho (1992) can be used as a reference. Sassen and Cho (1992) classified cirrus clouds based on the optical thickness obtained from lidar measurements of the FIRE Extended Time Observations (ETO) cirrus research program at the University of Utah Facility for Atmospheric Remote Sensing (FARS), and associated observations to the different optical thickness intervals. Their results are summarized in Table 1.2. The minimum optical thickness that can be detected by the human eye is approximately 0.03. Cirrus with an optical thickness less than 0.03 are classified as subvisual. Even though they are invisible to the human eye, they can be detected with a lidar and

Category of cirrus	Optical thickness interval	Observations
subvisual	< 0.03	invisible
thin	0.03 - 0.3	translucent, appear bluish
opaque	0.3 - 3.0	appear white
	> 3.0	complete attenuation lidar

Table 1.2: Classification of cirrus clouds based on the optical thickness after Sassen and Cho (1992).

it has been shown that especially subvisual cirrus in the TTL have an important influence on the radiative budget of the Earth (e.g. McFarquhar et al., 2000; Davis et al., 2010). Semi-transparent cirrus with an optical thickness between 0.03 and 0.3 are characterized by their ability to let light pass through and they appear in bluish colours. In contrast, cirrus with an optical thickness between 0.3 and 3.0 are opaque and appear white. When the optical thickness exceeds 3.0, the lidar signal is completely attenuated. Such a large optical thickness is rare for cirrus and corresponds in general to the range where cirrostratus develops into altostratus.

1.4 Impact of Cirrus Clouds on the Climate

In the previous section, the properties of cirrus clouds have been described from a microphysical point of view and important optical and radiative properties have been defined. To estimate the impact of cirrus on the radiative budget of the Earth, the global distribution of these properties has to be investigated. The first paragraph of this section aims to provide an overview of the characteristics of cirrus clouds on a global scale before the state-of-the-art concerning the radiative impact of cirrus clouds is discussed.

1.4.1 Climatology

Cirrus clouds occur all around the globe and in all seasons. Recent estimates suggest a global cirrus occurrence frequency of about 40 % with a higher frequency of about 60 % in the tropics (Stubenrauch et al., 2017). Their global character has been studied from various types of observations including in situ measurements as well as ground-based and satellite remote sensing with passive and active sensors at wavelengths covering a large portion of the electromagnetic spectrum. To get a global picture of the characteristics of cirrus, all available sources of information should be combined. In particular, when regarding ground-based or airborne measurements, it is important to be aware that observations at a specific locality and time do not account for regional variabilities (Sassen and Campbell, 2001). To obtain global coverage, satellite data is required. Ever since the importance of cirrus clouds for the global climate system has been recognized starting in the 1970s (e.g. Cox, 1971; Liou, 1974, 1986), several studies following an approach of combining different sources of information to obtain a cirrus climatology have been published. In the following, a brief summary of the results is presented in order to get an overview of the global distribution of the cirrus properties that will be studied in this thesis.

A first review of early studies dating from the above-mentioned epoch was provided by Dowling and Radke (1990). They developed a set of typical characteristics of cirrus clouds including macro- and microphysical properties. The investigated variables are the cloud altitude, geometrical thickness, particle number concentration, IWC and crystal dimension. The typical values and observed ranges for these parameters are summarized in Table 1.3.

Property	Typical value	Observed range
Geometrical thickness (in km)	1.5	0.1 - 8
Cloud centre altitude (in km)	9	4 - 20
Crystal number concentration (in L^{-1})	30	10^{-4} - 10^{4}
IWC (in $g\,m^{-3}$)	0.025	10^{-4} - 1.2
Crystal dimension (in μm)	250	1 - 8000

Table 1.3: Typical values and observed ranges of cirrus cloud properties, adapted from Dowling and Radke (1990).

The series of papers by Sassen and Campbell (2001); Sassen and Benson (2001); Sassen and Comstock (2001) provides a mid-latitude cirrus climatology from a long-term data record (10 years) from the FARS measurement site at the University of Utah which is equipped with a wide range of different active and passive remote sensing instruments (Sassen and Campbell, 2001). The cloud altitude and geometrical thickness averaged over 10 years reported by Sassen and Campbell (2001) compare well to the results of Dowling and Radke (1990). The annual averages of the cloud base and top altitudes were quantified to 8.79 km and 11.2 km, respectively, and the annual average of the geometrical thickness to 1.81 km. Additionally, Sassen and Campbell (2001) reported the annual averages of the temperatures at the cloud base and top (-34.4 °C and -53.9 °C, respectively) as well as pressure, wind speed and wind direction. Furthermore, they presented seasonal averages of all investigated parameters and explained seasonal variations by analysing the synoptic conditions throughout the year. Sassen and Comstock (2001) added radiative properties obtained from the LIRAD method introduced by Platt (1973, 1979) to this climatology, although their study only comprises seven years of data and excludes all clouds of an optical thickness less than 0.05 due to restrictions arising from the infrared radiometer measurements. The LIRAD method allows to obtain, amongst other parameters, the optical thickness at the visible lidar wavelength as well as the infrared emissivity. The mean value for the visible optical thickness over their entire cirrus sample is 0.75 ± 0.91 and the retrieved values range from about 0.003 to 3.0. About 30 % of the cirrus clouds were classified as thin (semi-transparent) having an optical thickness less than 0.3. The mean of the infrared emissivity is 0.30 ± 0.22 and the emissivities range from 0 to 0.85.

The series of ground-based studies by Sassen and Campbell (2001); Sassen and Benson (2001); Sassen and Comstock (2001) provides an extensive set of reference

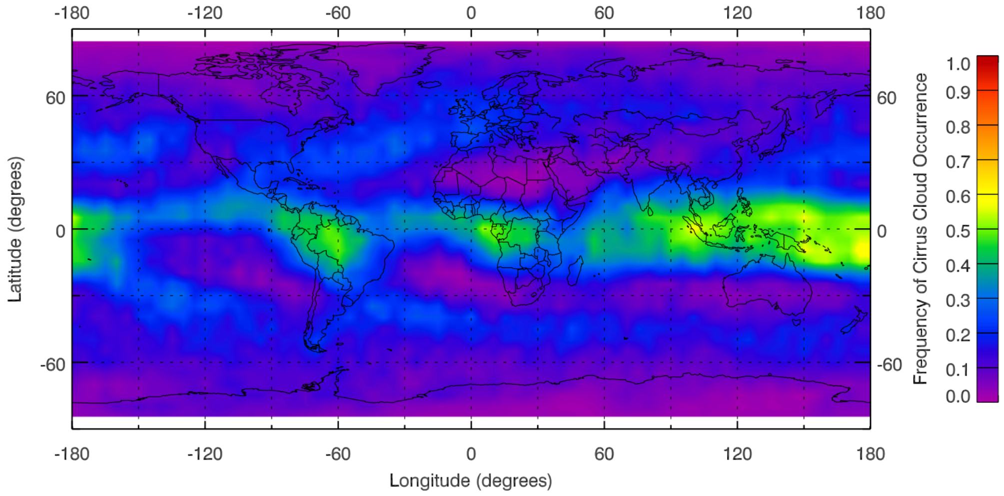

Figure 1.7: Global distribution of occurrence frequency of cirrus clouds identified from CloudSat/CALIPSO, averaged over one year (Sassen et al., 2008). They defined cirrus clouds by having a visible optical thickness smaller than 3 - 4 and a cloud top temperature less than -40 °C.

properties for mid-latitude cirrus. However, it is restricted to a certain locality and might be biased by the local meteorological and geographical characteristics of the measurement site. Recent advances in satellite remote sensing, in particular the CPR aboard CloudSat (Stephens et al., 2008) and the CALIOP lidar aboard CALIPSO (Winker et al., 2003, 2009, 2010), have given access to high quality measurements of the global distribution of cirrus clouds. Sassen et al. (2008) analysed the first year of data collected from June 2006 to June 2007. Figure 1.7 shows the global distribution of the yearly averaged frequency of cirrus cloud occurrence and Fig. 1.8 shows the latitudinal distribution of cirrus cloud heights for the same one-year period. The maximum occurrence of cirrus clouds is found in the tropics (about ± 15 ° latitude) at high altitudes. These observations can be explained by the presence of anvil cirrus originating from the deep convection in the tropics. The cirrus cloud occurrence frequency is particularly high over the west-central Pacific Ocean warm pool, Indonesia, and the continental equatorial western Africa and South America. The northern and southern mid-latitude storm tracks are also associated with a significant cirrus cloud coverage, although the amount is much smaller than in the tropics and the cloud heights are lower. Minima of cirrus cloud coverage are found in the polar regions as well as in the sub-tropics around ± 30 ° latitude where the air is generally descending on a large scale due to the Hadley circulation.

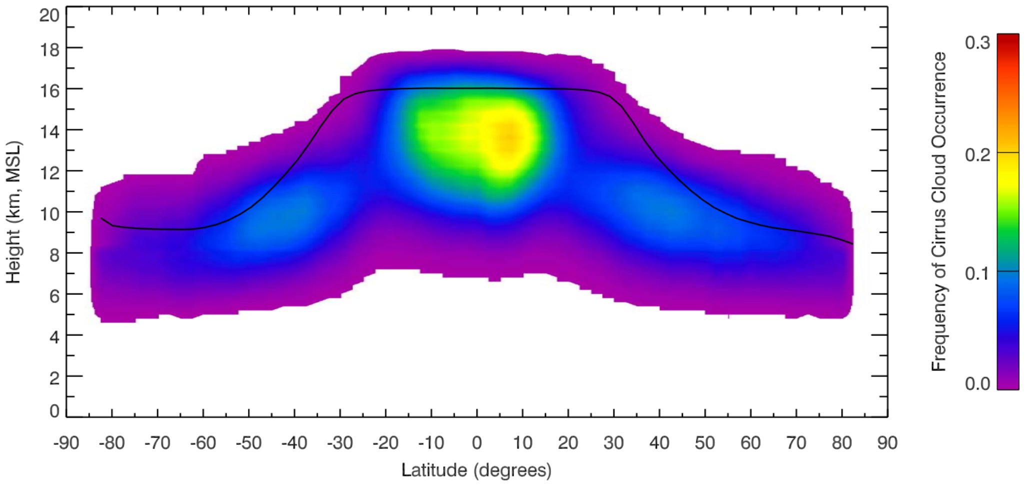

Figure 1.8: Latitudinal distribution of cirrus cloud heights from CloudSat/CALIPSO, averaged over one year. The black line represents the mean tropopause heights averaged over the same one-year period (Sassen et al., 2008).

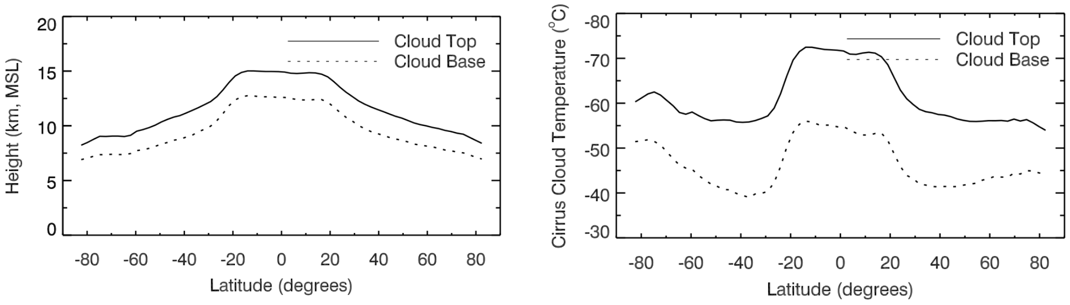

(a) Cirrus base and top heights **(b)** Cirrus base and top temperatures

Figure 1.9: Latitudinal dependence of the average cirrus base and top heights as well as temperatures (Sassen et al., 2008).

Figure 1.9 shows the latitudinal dependence of the one-year average of cirrus base and top altitudes as well as the cloud base and top temperatures. As indicated in Fig. 1.8, the mean base and top altitudes are much higher in the tropics than in the mid-latitudes. Consequently, the mean temperatures for tropical cirrus are significantly lower leading to the conclusion that the microphysical properties of tropical and mid-latitudinal cirrus are probably very different because they strongly depend on the temperature. In the mid-latitudes at about 40 °N (approximate geographical latitude of the FARS measurement site (Sassen and Campbell, 2001)), the mean altitudes of the cirrus base and top in Fig. 1.9 are approximately 9 km and 11 km, respectively, which is comparable with the altitudes observed by Sassen and Campbell (2001). The zonal average temperature at the base and top, however, seems to be colder (less than -40 °C at the cloud base and less than -55 °C at the cloud top) compared to the values observed at the FARS measurement site by Sassen and Campbell (2001).

The temperature of the cirrus cloud is a crucial parameter when estimating the radiative impact of the cloud. In terms of radiative properties, the visible cloud optical thickness and the emissivity are the fundamental properties to describe the interactions of the cloud with atmospheric radiation. The aim of the following paragraph is to provide an overview of our knowledge about the important but complex impact of cirrus clouds on the radiation budget of our planet.

1.4.2 Radiative Impact

As mentioned above, the radiative impact of clouds is governed on the one hand by macrophysical properties such as coverage, lifetime, altitude and temperature, and on the other hand by microphysical properties that determine the optical and radiative characteristics of the cloud.

Figure 1.10 illustrates the global radiation budget and shows the two effects related to clouds: their *albedo effect* in the solar wavelength domain (yellow) and their *greenhouse effect* in the thermal infrared (pink). The albedo effect describes the process when the incident solar radiation at the cloud top is reflected back to space leading to a cooling of the underlying atmosphere and surface since they receive less solar energy. On the contrary, the greenhouse effect leads to a warming because the thermal infrared radiation emitted by the Earth's surface is absorbed by the cloud and subsequently the cloud re-emits thermal infrared radiation according to its own colder temperature, partly back to the surface and partly out to space. Thus, less

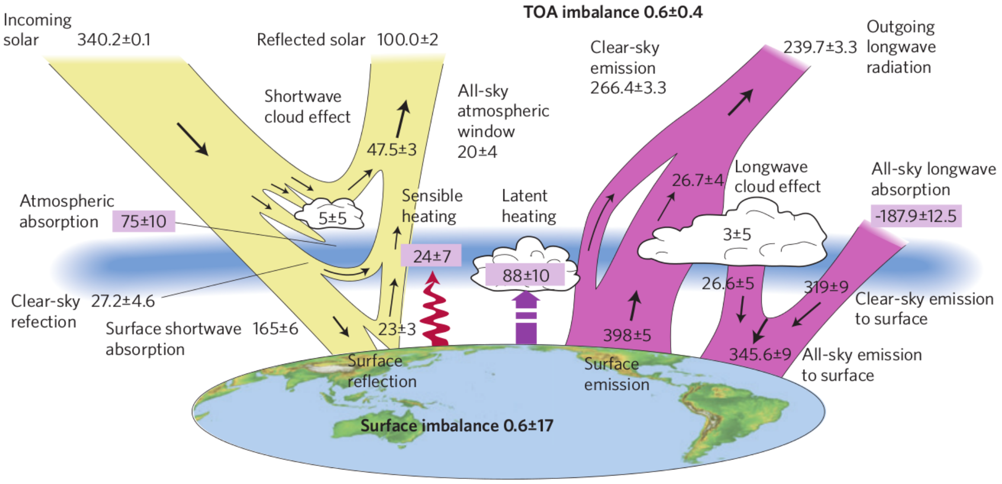

Figure 1.10: Global annual mean energy budget of the Earth for the approximate period 2000 - 2010. Solar fluxes are indicated in yellow, infrared fluxes in pink (in $\mathrm{W\,m^{-2}}$) (Stephens et al., 2012).

energy is leaving the Earth-atmosphere system when clouds are present. The larger the temperature difference between the surface and the cloud, the more energy is intercepted due to the greenhouse effect.

The albedo effect strongly depends on the visible optical thickness of the cloud and the greenhouse effect on the infrared emissivity as well as on the altitude and temperature of the cloud (Stephens and Webster, 1981). These properties vary considerably for the different cloud types existing in the atmosphere. Generally, low clouds are optically thick and hence they reflect a large amount of the incoming solar radiation and transmit only a small portion. The temperature difference with the Earth's surface is rather small leading to a small greenhouse effect. Thus, low clouds have an overall cooling effect on the planet. On the contrary, high cirrus clouds are generally optically thin and therefore they transmit a larger portion of the incoming solar radiation to the underlying atmosphere while only a small part is reflected back to space. Because of their high altitude, there is a large temperature difference between the Earth's surface and the cloud which leads to a significant greenhouse effect that nevertheless depends on their emissivity as well. Consequently, high and optically thin cirrus clouds are considered to have a moderate warming effect. Globally, the cooling effect of the low clouds outweighs the warming effect of high clouds, so altogether clouds have a cooling effect on the Earth-atmosphere system (Wielicki et al., 1995).

However, these considerations are highly generalized and the impact of cirrus clouds is much more complex. It has been studied since the early 1970s but the global net radiative effect of cirrus is still not answered definitely nowadays. The study of Cox (1971) was the first to estimate that tropical cirrus may have a tendency of warming the Earth's surface due to a strong greenhouse effect because they are located in high altitudes where it is very cold while the underlying atmosphere is warm. Hence, the temperature difference between the cloud and the Earth's surface is large which leads to a large greenhouse effect. In contrast, mid-latitude cirrus are more likely to produce a weaker greenhouse effect due to their lower altitudes and hence warmer temperatures in combination with a colder atmosphere. Thus, the albedo effect might be the dominant effect of cirrus in mid-latitudes. However, theses findings also suggest that the impact of cirrus in the mid-latitudes varies depending on the season.

The results of Cox (1971) are based solely on observations. Liou (1986) provided an extensive review of the composition, structure and radiative properties of cirrus and performed numerical experiments revealing the various influences of this cloud type. The results underlined the importance of cirrus for the global climate system and lead to further measurement campaigns and model studies investigating cirrus clouds. One recent study was presented by Hong et al. (2016) who integrated up-to-date ice cloud retrievals from the CALIPSO/CloudSat missions in their model simulations. They estimated a positive global net radiative effect of ice clouds of 5.1 ± 3.8 $\mathrm{W\,m^{-2}}$. However, they also showed that the net radiative effect depends on the region as illustrated in Fig. 1.11. Their results confirm the early observations of Cox (1971) because they found a strong positive net radiative effect due to high and very cold cirrus clouds in the tropics leading to a large greenhouse effect. On the contrary, in the mid-latitudes, especially over ocean, the greenhouse effect is smaller due to a smaller temperature difference between the cloud and the Earth's surface. In this case, the solar albedo effect prevails and a cooling due to ice clouds is simulated, in particular for the southern hemisphere.

However, even though several studies have tried to estimate the net radiative effect of cirrus it is still not well quantified nowadays. This is due to the large variability of ice crystal shapes and sizes observed in the atmosphere which makes it difficult to properly characterize the single scattering properties of cirrus clouds which are required in global climate models to calculate their radiative impact (Baran et al., 2014b). Hence, the net radiative effect depends not only on the macrophysical prop-

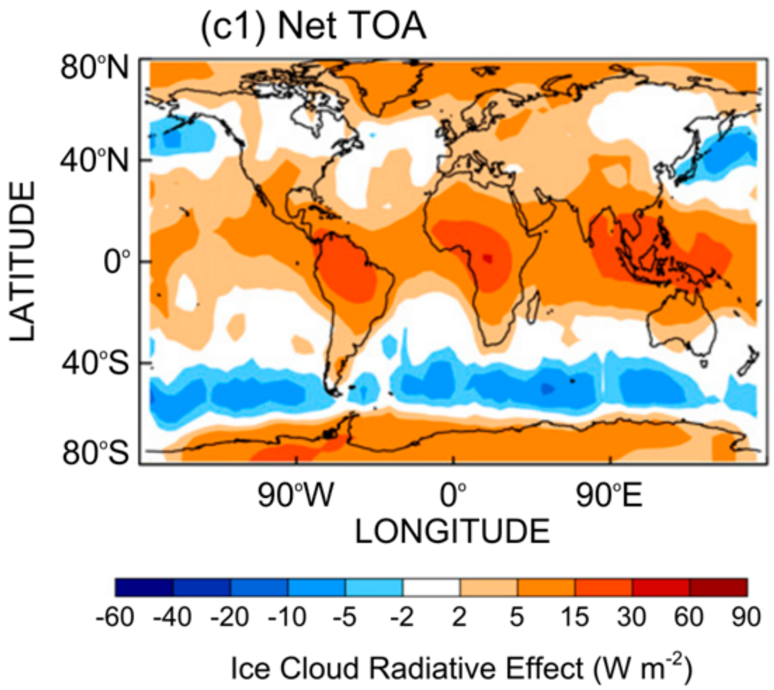

Figure 1.11: Global distribution of the net ice cloud radiative effect at top-of-atmosphere (TOA) (Hong et al., 2016).

erties but also on the microphysical characteristics of the ice crystals. Already 20 years ago, Zhang et al. (1999) showed that the cloud radiative forcing of cirrus clouds is extremely sensitive to the particle shape and size distribution. They investigated the solar, infrared and net radiative effects of cirrus clouds for different ice crystal models including hexagonal columns, polycrystals and ice spheres. Furthermore, they assumed two different shapes of the PSD, namely single- and bi-modal. Figure 1.12 shows some of their results indicating the importance of ice crystal shape and size for the radiative impact. Furthermore, a recent study of Järvinen et al. (2018) investigated the influence of particle heterogeneities, such as deformations and surface roughness, on the optical properties of ice crystals and analysed the consequences for the radiative effect of ice clouds. They showed that an increasing particle complexity leads to a more important short-wave cooling effect compared to pristine ice crystals. Thus, an exact knowledge of the microphysical properties of cirrus is required to estimate their effect on the global climate.

Another open question is related to anthropogenic influences on cirrus cloud radiative forcing. Zhang et al. (1999) suggested that contrail cirrus with a large number of small ice particles produce a negative cloud radiative forcing and therefore

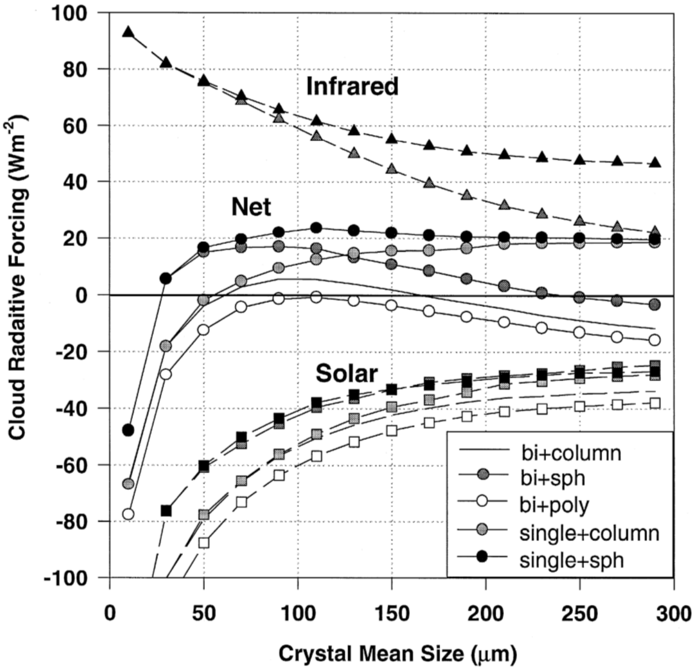

Figure 1.12: Cirrus net, infrared and solar radiative forcing depending on the crystal mean size, the crystal shape and pattern of size spectrum. Calculations were performed for an IWC of 0.01 $\mathrm{g\,m^{-3}}$ and a cloud thickness of 2 km (Zhang et al., 1999).

have a cooling effect on the atmosphere. This contradicts Boucher (1999) who estimated an additional positive forcing due to contrail cirrus. Furthermore, the aerosol indirect effect on ice clouds is still very uncertain. According to DeMott et al. (2010), an increased number of IN in the upper troposphere is likely to reduce the number of ice crystals. This seems to be irrational at first glance, but can be explained by the fact that heterogeneous ice nucleation processes do not require the same high supersaturation and low temperature as homogeneous ice nucleation. Thus, in the presence of an increased number of IN, the ice formation starts earlier which favours the sublimation of the remaining water vapour on the heterogeneously formed ice crystals and suppresses homogeneous ice nucleation since the required large supersaturation can no longer be realized. As a consequence, errors in the representation of IN in climate models will lead to different predicted microphysical properties and hence a different cloud radiative forcing. Nowadays, clouds and particularly the interactions between aerosols and clouds, are still considered to contribute the largest uncertainty in global climate change estimates (Boucher et al., 2013).

To summarize, the general impact of high and optically thin cirrus clouds is a warming of the atmosphere but there are still many open questions and the global net radiative effect of cirrus is still not completely understood nowadays.

CHAPTER 2

Instrumentation and Data

This chapter is dedicated to the description of the instrumentation and the data used in this work to study cirrus cloud properties. In a first step, the measurement platform in Lille is introduced and its climatological characteristics are presented.

Secondly, the thermal infrared radiometer is described and the measurement principle and calibration aspects are explained before a short description of the data collected with this instrument at our measurement site is given.

The third section of this chapter deals with the lidar measurements. A technical description of the micropulse lidar is provided which is followed by the explanation of the measurement principle and the lidar equation. Afterwards, the basic information provided by the lidar measurements, namely the cloud detection and the derivation of the cloud optical thickness via the transmission method, are presented because these information will be used in all algorithms described in Chapter 3 of this thesis.

Finally, the ancillary data which is also common in all steps of our methodology is introduced. This ancillary data comprises the European Centre for Medium-Range Weather Forecasts (ECMWF) reanalysis data of meteorological parameters as well as the Optical Properties of Aerosols and Clouds (OPAC) data base which provides the optical properties of different aerosol types.

2.1 Measurement Site

The data used in this work is originating from the measurement platform on the roof top of the laboratory building of the Laboratoire d'Optique Atmosphérique (LOA) which is located on the campus of the University of Lille in Villeneuve d'Ascq, a town situated in the Lille metropolitan area. As indicated in Fig. 2.1, it is located in the North of France in close proximity to the border to Belgium.

The climatological features of our measurement location are presented in Figs. 2.2 and 2.3. Figure 2.2 shows the climate graph for Villeneuve d'Ascq. The average temperature is 10.1 °C and the temperature amplitude over the year is relatively small. The annual precipitation amounts to 679 mm and is spread almost equally over all months. Figure 2.3 shows the wind direction distribution (in %) averaged over the whole year for the weather station at the airport Lille-Lesquin which is situated in about 5 km direct distance from the university campus. The prevailing wind direction is west to south-west which is typical for a mid-latitude site at the west coast of a continent due to the global circulation pattern. The air masses transported by these winds are relatively warm and humid since they are originating over the ocean. This results in a temperate oceanic climate with cool summers and cool winters. Thus, the occurrence frequency of clouds is high and precipitation is spread throughout the whole year. The climate in Villeneuve d'Ascq is classified after the Köppen-Geiger climate classification as Cfb, where C stands for a temperate climate, f indicates significant precipitation in all seasons and b means that the average temperature of the warmest month is below 22 °C. As a conclusion, the meteorological conditions in Villeneuve d'Ascq are not perfectly adapted to study cirrus clouds from ground-based measurements because the sky is often covered with low clouds and precipitation occurs frequently. However, the prevailing cirrus generating processes for our measurement site are synoptic perturbations (cf. Sect. 1.2.2). Additionally, contrail induced cirrus occur frequently due to the above-mentioned proximity to the airport.

The measurement platform of the LOA disposes of a wide range of different instruments. Figure 2.4 shows a photo of the site. The instrumentation comprises a meteorological station that records temperature, pressure, wind speed and direction, humidity and precipitation. Several fluxmeters are installed to measure the direct and diffuse solar radiation fluxes from the half-space (pyranometer), the direct beam solar irradiance (pyrheliometer), the terrestrial radiation flux in the thermal infrared

Figure 2.1: Localization of the University of Lille in Villeneuve d'Ascq, France. Source: `https://www.google.de/maps/place/Lille+1+University/@49.5030512,-0.8983429,1206205m/data=!3m1!1e3!4m5!3m4!1s0x47c2d64d7432cc3b:0x975b789ee1f01e43!8m2!3d50.609049!4d3.138063?hl=en`.

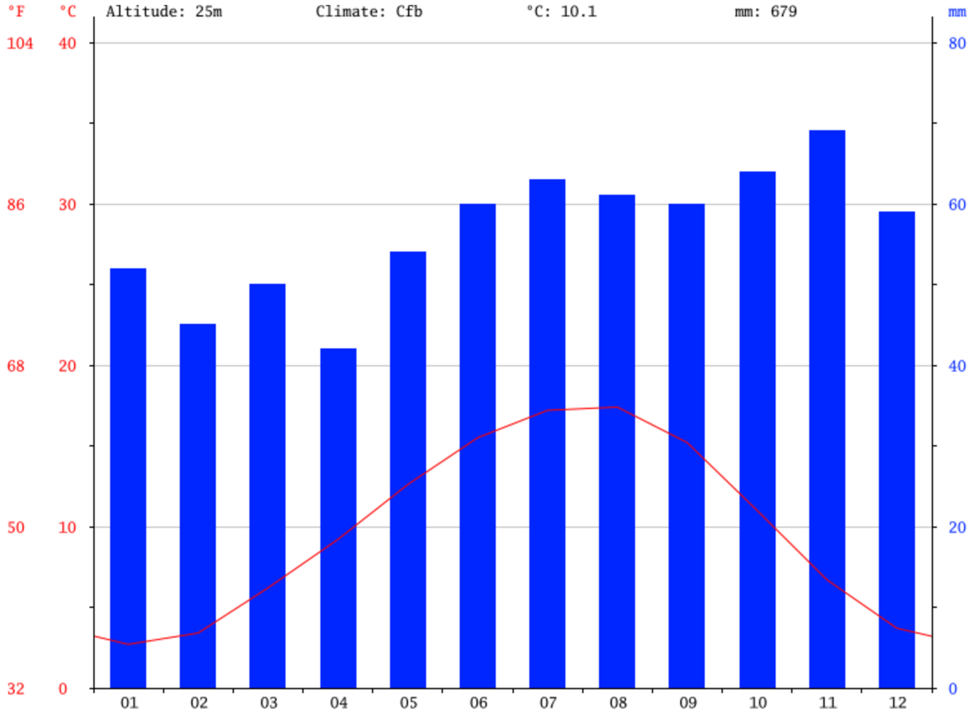

Figure 2.2: Climate graph of temperature (left axis) and precipitation (right axis) for Villeneuve d'Ascq. Source: `https://fr.climate-data.org/location/8078/`.

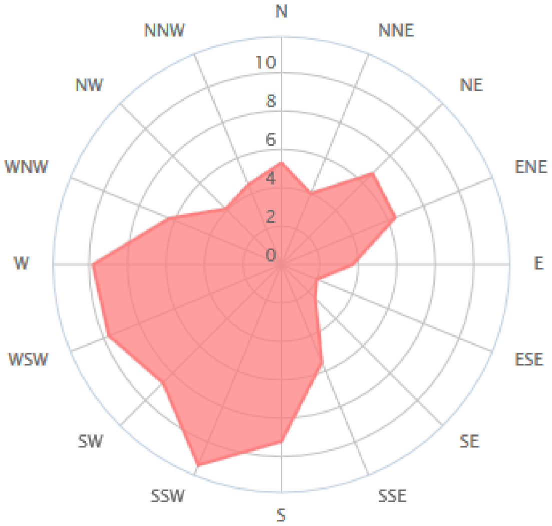

Figure 2.3: Wind distribution for the weather station at Lille airport. Source: `https://www.windfinder.com/windstatistics/lille`.

Figure 2.4: The measurement site of the LOA in Villeneuve d'Ascq. Source: `http://www-loa.univ-lille1.fr/observations/sno.html`.

(pyrgeometer), the intensity of the spectral solar ultraviolet irradiation (UV spectroradiometer) and the solar ultraviolet irradiance (UV pyranometer). In addition, the platform contains a sky imager and instruments to measure particle concentrations and size distributions (nephelometer, aethalometer, granulometer, SMPS spectrometer).

In this work, we will focus on lidar and thermal infrared radiometer measurements. The platform contains two lidar systems: a multi-wavelength Raman lidar called LILAS developed recently at the LOA, and a much simpler micropulse lidar. The latter is used here because the aim of this thesis is to develop a method applicable to different measurement sites and the majority of ground-based lidars which are operated nowadays are simpler systems (Campbell et al., 2015). The second instrument of importance in this work is the thermal infrared radiometer. Both instruments are described in detail in the following Sects. 2.2 and 2.3, starting with the thermal infrared radiometer.

2.2 The Thermal Infrared Radiometer CLIMAT

The *Conveyable Low-Noise Infrared Radiometer for Measurements of Atmosphere and Ground Surface Targets*, or shortly CLIMAT (Sicard et al., 1999; Legrand et al., 2000; Brogniez et al., 2003), was developed at the LOA in the 1990s in cooperation with the company CIMEL Electronique and several research institutes (the Institut National de Recherche Agronomique, Avignon (INRA), the Centre de Recherches Géophysiques, Garchy (CRG/CNRS) and the Groupement Scientifique de Télédétection Spatiale, Strasbourg (ENSPS/GSTS)). Financial support was provided by the French national space agency (Centre National d'Etudes Spatiales, CNES). In the following, a description of the instrument, the measurement principle and the provided data is given.

2.2.1 Technical Description

The CLIMAT instrument was developed to measure brightness temperatures (or equivalent radiances) in the thermal infrared wavelength region from 8 to 14 μm. There are two different types of this instrument: one was designed for ground-based measurements (type CE-312T), and the other one for airborne measurements (CLIMAT-AV, type CE-332). Figure 2.5a illustrates the ground-based version consisting of the optical head (left-hand side) and the control unit (right-hand side). The optical head contains the optical elements as well as the detector, and the control unit contains the electronics and the memory of the instrument. While the control unit is common for both instrument types, the optical head is of slightly different design. As illustrated in Fig. 2.5b, the airborne version CE-332 consists of three independent cavities, each containing their own optics. On the contrary, the ground-based version CE-312T contains one single cavity and is equipped with a filter wheel that places up to six interference filters one after another in front of the only optics. Thus, the measurements with the ground-based version of the instrument are performed successively, while the airborne version measures simultaneously for the different channels.

However, the main features of the optical head are the same for both instrument types. By way of example, Fig. 2.6 shows a simplified schematic of the optical head of the instrument version CLIMAT-AV CE-332. The main optics consists of two germanium lenses: the objective (”Lentille frontale Ge”) which is a standard

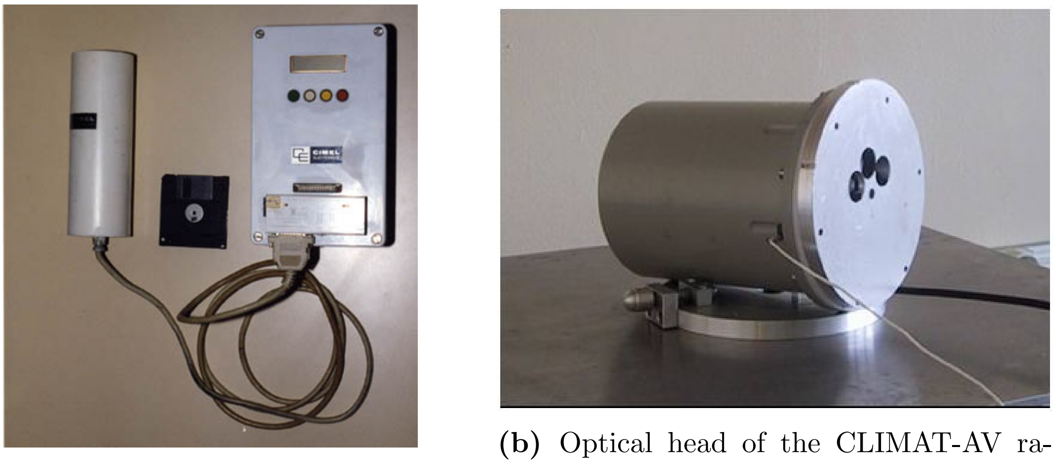

(a) CLIMAT radiometer type CE-312T.

(b) Optical head of the CLIMAT-AV radiometer type CE-332.

Figure 2.5: Illustration of the two types of the CLIMAT instrument.

convex-plane lens, and the condenser (”Condenseur Ge”) which is a ”best-shaped” meniscus designed to minimize the geometrical aberrations (Legrand et al., 2000). The condenser is situated in the focal plane of the objective. Table 2.1 summarizes the characteristics of the lenses used in both instrument types.

The optical head is constructed respecting the so-called Köhler design. That means the detector (”Détecteur”) is located in the conjugate plane of the objective with respect to the condenser. This design has several advantages. Firstly, since the incident radiation from a remote target is uniformly distributed on the objective, the detector situated in the conjugate plane is also uniformly illuminated. This avoids hot spots and prevents biases arising from a non-homogeneous illumination of the detector's surface. Secondly, the field of view (FOV) is geometrically well-defined and corresponds to the theoretical FOV defined by the ratio of the condenser's diameter to its distance to the objective. That means all the rays coming from the target and reaching the objective from inside the theoretical FOV will reach the detector. At the same time, no ray coming from outside this FOV is able to reach the detector. Finally, this design allows to easily modify the FOV of the instrument by replacing the objective with a lens of a different focal length which assures the instrument's flexibility for a large range of applications.

The detector of the instrument is a thermopile of model 1M manufactured by Dexter (Dexter Research Center, Inc., Dexter, Michigan). Table 2.2 adapted from Legrand et al. (2000) summarizes its characteristics. A thermopile converts thermal energy in electrical energy and is composed of several thermocouples connected in

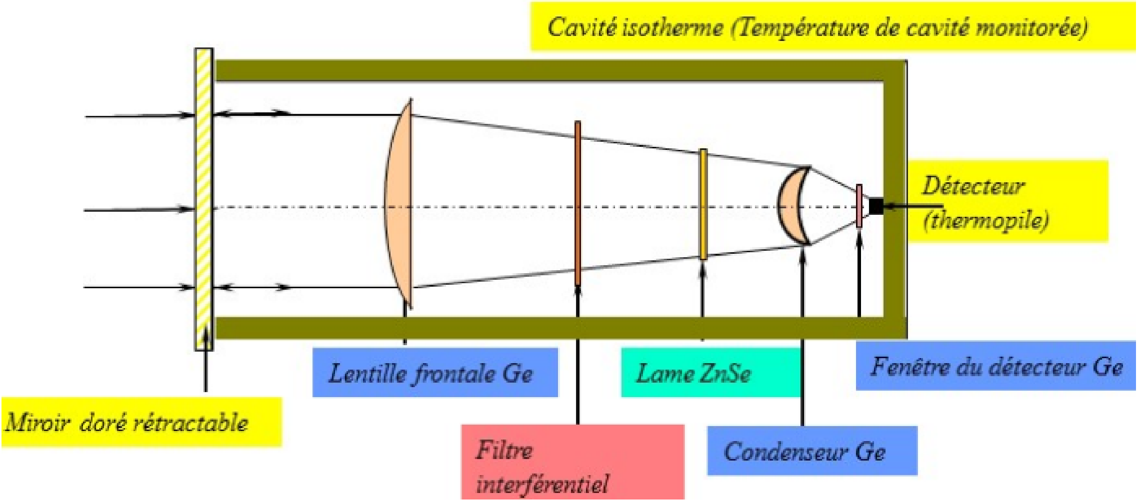

Figure 2.6: Simplified schematic of the optical head of the CLIMAT-AV radiometer (type CE-332). The temperature sensor to monitor the cavity temperature is located next to the detector (courtesy of G. Brogniez).

Lens	Focal length	Effective diameter
Objective CE-332	50.80 mm	11.80 mm
Objective CE-312T	25.40 mm	5.60 mm
Condenser (both types)	3.23 mm	4.35 mm

Table 2.1: Characteristics of the lenses used in the optical heads of the two CLIMAT radiometer types.

Property	
Active area	$0.6\,\mathrm{x}\,0.6\,\mathrm{mm}^2$
Number of junctions	40
Resistor	$60\,\mathrm{k\Omega}$
Voltage noise	$31.3\,\mathrm{nV\,Hz}^{-1/2}$
Responsivity	$120\,\mathrm{V\,W}^{-1}$
Noise equivalent power (NEP)	$0.26\ \mathrm{nW\,Hz}^{-1/2}$
Time constant	12 ms
Field of view	80 °

Table 2.2: Characteristics of the thermopile used as detector in the CLIMAT instrument (model 1M Dexter, values are given for a temperature of 296 K), adapted from Legrand et al. (2000).

series. Each thermocouple consists of two different electrical conductors which form electrical junctions at differing temperatures. Due to the thermoelectric effect, the temperature difference between the heated and the cold junction produces a voltage which varies proportionally to this temperature difference. The output voltage of a single thermocouple is very small. Thus, in order to increase the signal, a thermopile connects multiple thermocouples in series because in this configuration the thermoelectric voltages are added. For the thermopile integrated in the CLIMAT instrument, the temperature of the cold junction is determined by the ambient temperature of the cavity and the hot junction is heated by the incident radiation. From the output voltage the radiance of the measured target can be deduced. The measurement principle will be described in detail in the Sect. 2.2.2.

Another important element in the optical head is the gold-plated mirror ("Miroir doré rétractable" in Fig. 2.6) which can be placed in front of the objective to compare the radiation originating from inside the cavity to the radiation coming from the target. According to the manufacturer, the reflection coefficient of the mirror reaches up to 99.74 % (Legrand et al., 2000). Further elements are the zinc selenide filter ("Lame en ZnSe") which assures that radiation at wavelengths larger than 15 μm is hindered to reach the detector, and the detector window ("Fenêtre du détecteur Ge") which is transparent in the thermal infrared.

While the airborne CLIMAT-AV version consists of three independent cavities containing each one interference filter ("Filtre interférentiel"), the ground-based version integrates a filter wheel that can hold up to six interference filters as mentioned

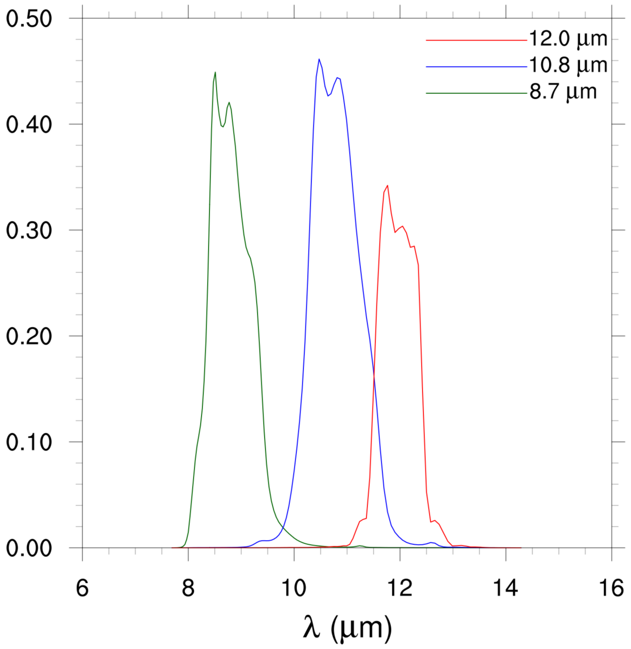

Figure 2.7: Spectral transmittance of the three channels of the airborne CLIMAT-AV instrument installed on the measurement platform of the LOA.

above. Another important difference between both instrument types is the reduced FOV of 3.5 ° for the airborne version compared to 10 ° for the ground-based version. Although this work is dealing with ground-based measurements, the CLIMAT instrument installed on the measurement platform of the LOA in Lille is of type CLIMAT-AV CE-332 (airborne version).

The spectral characteristics of this instrument have been chosen in agreement with the properties of the atmospheric window region from 8 to 14 μm. The channels are centred at 8.7 μm, 10.8 μm and 12.0 μm coinciding with the channels of the IIR aboard CALIPSO (Winker et al., 2003). Figure 2.7 shows the spectral transmittance functions of the three channels of the CLIMAT-AV instrument used in this thesis. To characterize the total spectral response of each channel, the spectral responses of each individual optical element contained in the instrument's optical head were measured one by one with a spectrometer in the laboratory. The product of all single spectral responses then gives the total spectral response of the filter. It should be noted that these measurements imply an experimental error on the final filter functions which is difficult to quantify. In Fig. 2.7, the channel centred at 8.7 μm is represented by the green colour, the channel centred at 10.8 μm in blue and the channel centred at 12.0 μm in red. All channels have a full width at half maximum

(FWHM) of about 1 μm. For the rest of this thesis we will call them C09, C11 and C12, respectively.

2.2.2 Measurement Principle and Calibration

The CLIMAT radiometer measures radiances or equivalent brightness temperatures. However, the monochromatic radiance given by (cf. Eq. 1.17),

$$L_\lambda(T) = \epsilon_\lambda \cdot B_\lambda(T), \tag{2.1}$$

cannot be obtained directly from measurements. As discussed above, every channel of the instrument is characterized by a function of transmittance shown in Fig. 2.7. These filter functions $f_i(\lambda)$ for each channel i are defined over the spectral interval $\Delta\lambda_i$ which corresponds to the above-mentioned bandwidth of about 1 μm for each filter, around its central wavelength λ_i. The radiance measured by channel i is then defined as the product of the spectral radiance and the filter function of the channel integrated over its bandwidth,

$$L_i^{\text{int}} = \int_{\Delta\lambda_i} L_\lambda(T) \cdot f_i(\lambda) \,\mathrm{d}\lambda. \tag{2.2}$$

This radiance can be expressed as an equivalent brightness temperature $T_{b,i}$ which is defined as the temperature of the blackbody that would emit a radiance equal to L_i^{int},

$$L_i^{\text{int}} = B_i^{\text{int}}(T_{b,i}), \tag{2.3}$$

with,

$$B_i^{\text{int}}(T_{b,i}) = \int_{\Delta\lambda_i} B_\lambda(T_{b,i}) \cdot f_i(\lambda) \,\mathrm{d}\lambda. \tag{2.4}$$

For the remainder of this thesis, we will consider for each channel the radiance normalized by its filter function,

$$L_i = \frac{L_i^{\text{int}}}{\int_{\Delta\lambda_i} f_i(\lambda) \,\mathrm{d}\lambda}, \tag{2.5}$$

and its unit will be expressed in $\mathrm{W\,m^{-2}\,sr^{-1}\,\mu m^{-1}}$, which will be used as unit for the Planck function as well.

The CLIMAT instrument works based on a differential principle. That means it measures successively the signal coming from the target of brightness temperature $T_{b,\text{tar}}$ and the signal originating from its own cavity containing the detector and the mirror at a temperature T_{cav}. The target measurement is composed of the radiation originating from the target plus some background radiation emitted by the different elements of the cavity. Thus, the cavity measurement is required to identify this background signal. It is realized with the help of the gold-plated mirror described in the previous section which can be placed in front of the detector. The real signal of the target is then obtained by simply calculating the difference between the two successive measurements for each channel,

$$\Delta C_i = C_{i,\text{tar}} - C_{i,\text{cav}}, \tag{2.6}$$

where $C_{i,\text{tar}}$ and $C_{i,\text{cav}}$ represent the digital counts for the target and cavity measurements of channel i, respectively. This difference of the digital counts is proportional to the difference of the radiances, ΔL_i, originating from the target and the cavity,

$$\Delta C_i = S_i \cdot \Delta L_i, \tag{2.7}$$

where S_i is the sensitivity of the considered channel obtained during calibration.

The instrument has to be calibrated regularly to take into account possible changes of the sensitivities due to ageing of the instrument or environmental influences (cf. Table 2.4). The calibration is performed in the laboratory with the help of a blackbody serving as source of radiation. The blackbody is heated or cooled to different temperatures T_{bb} and for each temperature the difference of the digital counts measured for the blackbody and the cavity with the help of the mirror, $\Delta C_i = C_{i,\text{bb}} - C_{i,\text{cav}}$, is plotted against the difference of the according radiances of the blackbody and the cavity, $\Delta L_i = L_i(T_{\text{bb}}) - L_i(T_{\text{cav}})$, calculated with Eq. 2.5. The temperatures T_{bb} of the blackbody and T_{cav} of the cavity are measured with a platinum probe of high precision (absolute error 0.05 °C). The ambient temperature needs to be constant during the calibration to avoid possible variations of the sensitivity due to temperature changes. To find the desired radiometric sensitivity for each channel, a linear regression is performed between ΔC_i and ΔL_i where the slope of the regression line is the desired sensitivity S_i. Figure 2.8 shows an example of calibration curves for the three channels of the CLIMAT-AV instrument installed on our measurement platform. This calibration was performed at the LOA in April 2018 for an ambient temperature of 21 °C and the blackbody temperature varied between -45 °C and 50 °C.

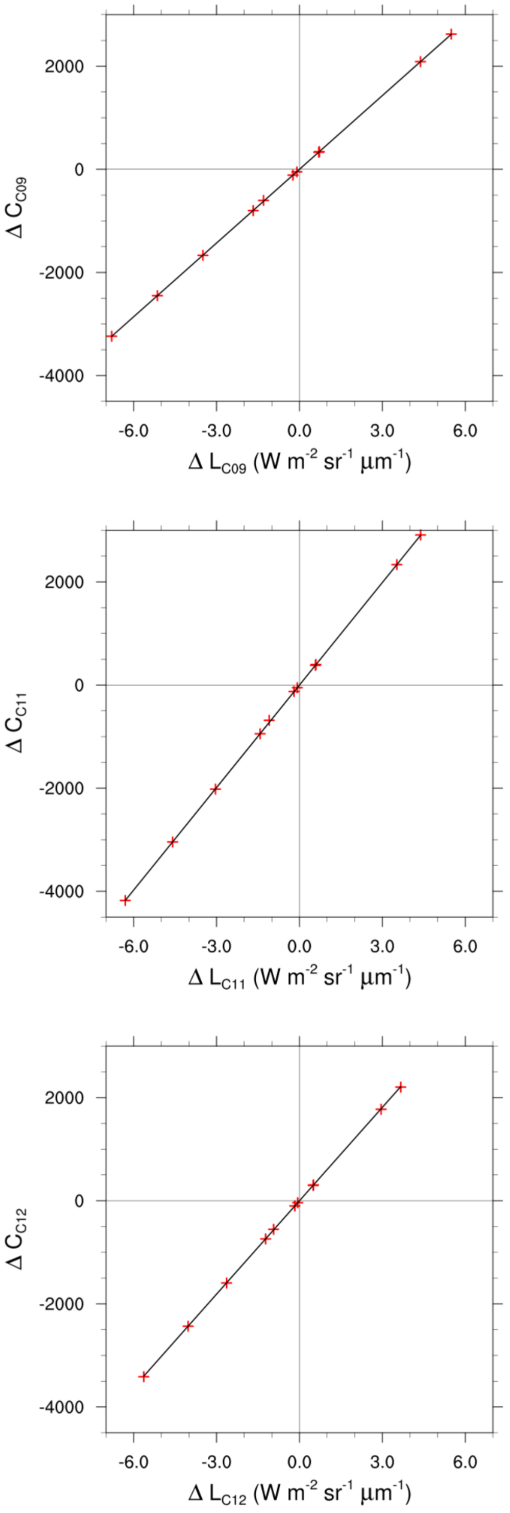

Figure 2.8: Example of calibration curves for the CLIMAT-AV instrument installed on the LOA measurement platform. The calibration measurements were performed in the laboratory of the LOA by B. Damiri in April 2018 for an ambient temperature of 21 °C. The obtained sensitivities for all calibrations used in this work are summarized in Table 2.4.

When sensing an atmospheric target, its radiance $L_i(T_{b,\mathrm{tar}})$ is obtained from the sensitivity and the difference of the measured digital counts between the target and the cavity measurements following Eq. 2.7,

$$C_{i,\mathrm{tar}} - C_{i,\mathrm{cav}} = S_i \cdot (L_i(T_{b,\mathrm{tar}}) - L_i(T_{\mathrm{cav}})). \tag{2.8}$$

Solving Eq. 2.8 for $L_i(T_{b,\mathrm{tar}})$ leads to the expression,

$$L_i(T_{b,\mathrm{tar}}) = \frac{C_{i,\mathrm{tar}} - C_{i,\mathrm{cav}}}{S_i} + L_i(T_{\mathrm{cav}}), \tag{2.9}$$

which is used to transform the measured digital counts into normalized radiances. The temperature of the cavity is recorded during the measurement and the internal radiance of the cavity $L_i(T_{\mathrm{cav}})$ which is required in Eq. 2.9 can thus be obtained from Eq. 2.5.

However, Eq. 2.9 is true when the temperature of the cavity during the measurement is close to its temperature during the calibration. Unfortunately, the sensitivities of the channels are not constant. They vary with the cavity temperature because the responsivity of the thermopile used as detector depends on its temperature. Consequently, when regarding field measurements performed at a temperature T'_{cav} of the cavity, it is necessary to correct the sensitivities. According to Legrand et al. (2000), the corrected sensitivity S'_i can be expressed as an exponential function of the temperature difference between the actual temperature of the cavity during the measurement, T'_{cav}, and the temperature of the cavity during calibration, T_{cav},

$$S'_i = S_i \cdot \exp(\alpha_i(T'_{\mathrm{cav}} - T_{\mathrm{cav}})), \tag{2.10}$$

where α_i is the coefficient for the temperature correction. The manufacturer provides a value of -0.0015 K^{-1} for this coefficient. However, this value is a correction factor for the temperature dependence of the detector alone. To characterize the temperature dependence of the sensitivity of the whole instrument, calibrations have to be performed at different cavity temperatures. Furthermore, for the CLIMAT-AV instrument installed at the LOA in Lille this coefficient has to be specified for each channel separately because the three channels use different cavities.

An experiment to characterize the temperature dependence of the CLIMAT-AV instrument at our measurement site has been conducted in April/May 2018. During this experimental phase, the sensitivities of the three channels have been derived for five different cavity temperatures around 6, 14, 21, 29 and 40 °C. The resulting sensitivities are shown in Fig. 2.9. The error bars on the sensitivities

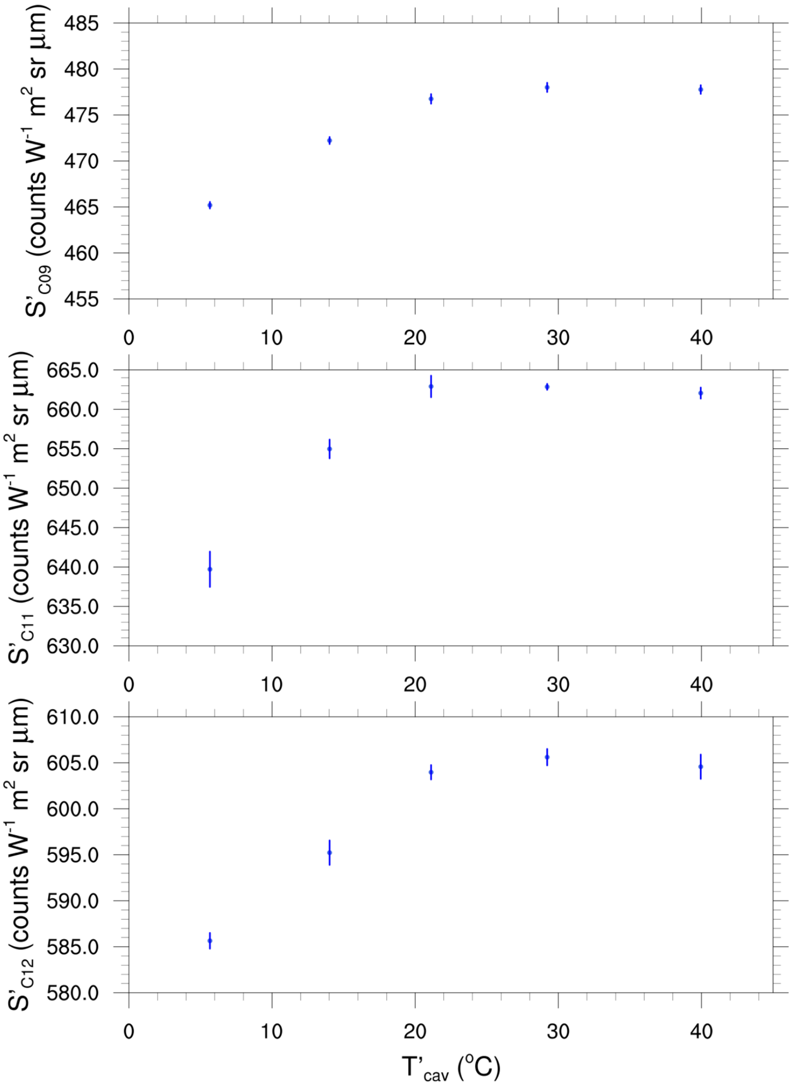

Figure 2.9: Temperature dependence of the sensitivities of the three channels of the CLIMAT-AV instrument installed on the measurement platform of the LOA. The measurements were performed in the laboratory of the LOA by B. Damiri in April/May 2018.

are calculated based on the linear regression between ΔC_i and ΔL_i explained above which is performed for each of the sensitivities in Fig. 2.9 based on multiple different blackbody temperatures during the calibration (cf. Fig. 2.8 for an example). For temperatures between 6 and 21 °C, the sensitivities of all channels increase with increasing temperature. For temperatures larger than 21 °C, the sensitivities seem to be more or less constant (cf. Table 2.3). Consequently, we distinguish two different temperature ranges for the characterization of the temperature dependence of the instrument's sensitivities: $T'_{\mathrm{cav}} < 21\,^{\circ}\mathrm{C}$ and $T'_{\mathrm{cav}} > 21\,^{\circ}\mathrm{C}$.

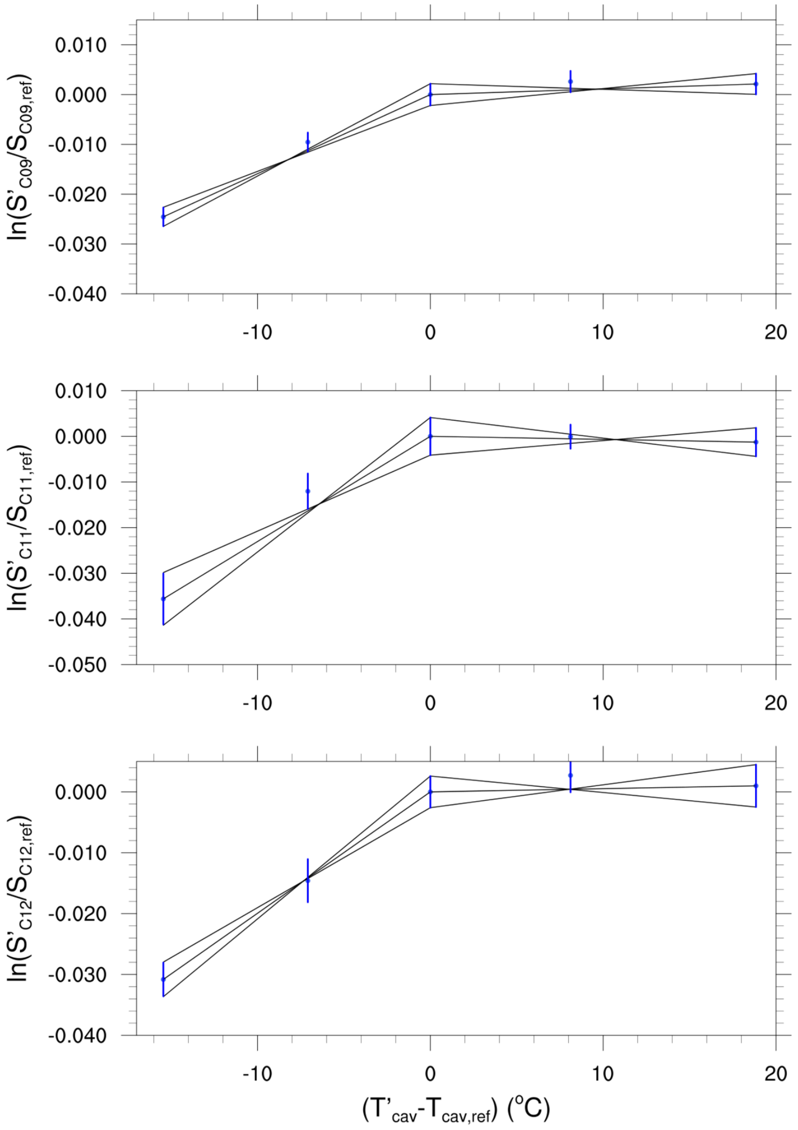

Figure 2.10: Temperature correction of the sensitivities of the three channels of the CLIMAT-AV instrument installed on the measurement platform of the LOA. The measurement at $T_{\text{cav,ref}} = 21\,^{\circ}\text{C}$ has been used as reference measurement. The measurements were performed in the laboratory of the LOA by B. Damiri in April/May 2018.

The temperature correction is performed based on Eq. 2.10, which means that one temperature/sensitivity pair has to be chosen as a reference because the equation,

$$\ln\left(\frac{S'_i}{S_{i,\mathrm{ref}}}\right) = \alpha_i \cdot \left(T'_{\mathrm{cav}} - T_{\mathrm{cav,ref}}\right), \tag{2.11}$$

yields a straight line with slope α_i. We chose the cavity temperature $T_{\mathrm{cav,ref}} = 21\,^{\circ}\mathrm{C}$ and its according sensitivities for each channel as reference because the calibration of the instrument is usually performed at room temperature. The temperature dependence is not derived during every calibration of the instrument and is assumed to be constant over its lifetime. Figure 2.10 shows the plotted straight lines of $\ln\left(S'_i/S_{i,\mathrm{ref}}\right)$ against the temperature difference $\left(T'_{\mathrm{cav}} - T_{\mathrm{cav,ref}}\right)$ for the three channels. Due to the small number of available points, the slope α_i is calculated for the first temperature interval ($T'_{\mathrm{cav}} < 21\,^{\circ}\mathrm{C}$) between the first and the third point ($T'_{\mathrm{cav}} = 6\,^{\circ}\mathrm{C}$ and $T'_{\mathrm{cav}} = 21\,^{\circ}\mathrm{C}$), and for the second temperature interval ($T'_{\mathrm{cav}} > 21\,^{\circ}\mathrm{C}$) between the third and the fifth point ($T'_{\mathrm{cav}} = 21\,^{\circ}\mathrm{C}$ and $T'_{\mathrm{cav}} = 40\,^{\circ}\mathrm{C}$). The intermediate points at $T'_{\mathrm{cav}} = 14\,^{\circ}\mathrm{C}$ and $T'_{\mathrm{cav}} = 29\,^{\circ}\mathrm{C}$, respectively, are shown to be situated on these straight lines considering their error bars. To obtain an error associated with α_i, the maximum and minimum slope between the two respective points are calculated by passing one straight line from the lower end of the first point's error bar to the upper end of the second point's error bar ($\alpha_{i,\mathrm{max}}$) as well as one straight line from the upper end of the first point's error bar to the lower end of the second point's error bar ($\alpha_{i,\mathrm{min}}$). The error associated with α_i is then defined as,

$$\Delta\alpha_i = \frac{\left|\alpha_{i,\mathrm{max}} - \alpha_{i,\mathrm{min}}\right|}{2}. \tag{2.12}$$

Table 2.3 summarizes the values of the temperature correction coefficient α_i including its error derived as explained above for the three channels of the CLIMAT-AV instrument installed at the LOA.

Including the temperature correction into Eq. 2.9, finally leads to the expression,

$$L_i(T_{b,\mathrm{tar}}) = \frac{C_{i,\mathrm{tar}} - C_{i,\mathrm{cav}}}{S_i \cdot \exp\left(\alpha_i \left(T'_{\mathrm{cav}} - T_{\mathrm{cav}}\right)\right)} + L_i(T'_{\mathrm{cav}}), \tag{2.13}$$

for the transformation of the measured digital counts to normalized radiances. For the measurement error $\Delta L_i(T_{b,\mathrm{tar}})$, the error on S_i originating from the linear regression and the error on α_i described above are taken into account. Hence, $\Delta L_i(T_{b,\mathrm{tar}})$ can be calculated via,

$$\Delta L_i(T_{b,\mathrm{tar}}) = \left|\frac{\partial L_i}{\partial S_i}\right| \Delta S_i + \left|\frac{\partial L_i}{\partial \alpha_i}\right| \Delta\alpha_i, \tag{2.14}$$

	$T'_{\mathrm{cav}} < 21\,°\mathrm{C}$	$T'_{\mathrm{cav}} > 21\,°\mathrm{C}$
α_{C09} (K^{-1})	0.001589 ± 0.000266	0.000113 ± 0.000227
α_{C11} (K^{-1})	0.002305 ± 0.000640	-0.000067 ± 0.000385
α_{C12} (K^{-1})	0.001994 ± 0.000352	0.000053 ± 0.000322

Table 2.3: Temperature correction coefficients α_i for the two temperature ranges $T'_{\mathrm{cav}} < 21\,°\mathrm{C}$ and $T'_{\mathrm{cav}} > 21\,°\mathrm{C}$ for the three channels of the CLIMAT-AV instrument installed on the LOA measurement platform.

Date	T_{cav}	S_{C09}	S_{C11}	S_{C12}
Sep 2014	22 °C	487.75 ± 2.21	669.73 ± 1.34	614.55 ± 2.50
Nov 2016	24 °C	474.84 ± 0.39	648.18 ± 0.82	602.04 ± 1.53
Apr 2018	21 °C	476.75 ± 0.52	662.90 ± 1.37	603.97 ± 0.78

Table 2.4: Sensitivities (expressed in units of counts $\mathrm{W}^{-1}\,\mathrm{m}^{2}\,\mathrm{sr}\,\mu\mathrm{m}$) of the three channels of the CLIMAT-AV instrument installed on the LOA measurement platform for the three calibrations used in this work.

where the calculation of the derivatives $\frac{\partial L_i}{\partial S_i}$ and $\frac{\partial L_i}{\partial \alpha_i}$ is straightforward from Eq.2.13.

As indicated above, another error on the measured radiances is arising from the measurements of the spectral response functions of the instrument's channels. However, this error is difficult to quantify. The algorithm developed in this thesis did not converge for channel C09 while for channels C11 and C12 convergence was obtained. This convergence issue of channel C09 is probably connected with a bad characterization of the spectral filter function of this channel. It will be discussed in more detail in Chapter 3 of this thesis and finally resulted in the exclusion of this channel.

2.2.3 Description of the Data Provided by CLIMAT

As mentioned above, the CLIMAT instrument installed on the measurement platform of the LOA in Lille is of type aircraft (CE-332). That means the measurements are performed simultaneously for the three channels. Measurements are available for the time period of November 2014 to June 2018, so the data used in this work has been treated depending on the time period with three different calibrations performed in September 2014, November 2016 and April 2018. The respective sensitivities are presented in Table 2.4.

However, the instrument is operated only selectively on days when the meteorological conditions are favourable, meaning days when precipitation can be excluded because the instrument cannot be exposed to rain. As discussed in Sect. 2.1, precipitation in Lille is spread throughout the whole year and occurs frequently. Hence, the number of days during the above-mentioned period where measurements were possible is limited and especially night time measurements are rare. In total, the instrument was working on 171 days for a variable duration ranging between one and 24 hours. 33 days of data are available where cirrus clouds were measured simultaneously with the thermal infrared radiometer and the lidar (cf. Table 2.6).

The instrument in Lille is installed on a motorized device which allows to measure the radiances from different viewing angles ranging between 0° and 45°. A computer software controls the desired parameters for operation, meaning the acquisition time, the frequency of the mirror measurements and the measurement angles. Before May 13, 2016, the instrument measured for different viewing angles (indicated by "multi-angle" in Table 2.6). Since then, only the vertical viewing direction has been measured which is the only direction considered in this work. As a consequence, before May 13, 2016, exploitable measurements are less frequent because the instrument was changing the viewing direction regularly.

The frequency of mirror measurements varies over the nearly four years of data. In the beginning of the period, the internal radiance was measured hourly or half-hourly, later every 10 or 15 minutes because experience showed that temperature variations of the cavity and hence the internal radiance are important. However, the temporal variations of the mirror measurements are taken into account in the so-called mirror correction. That means a linear interpolation between two successive mirror measurements is performed and the linearly interpolated value is used as mirror reference when applying Eq. 2.13.

The acquisition time defines the time of measuring for each angle. When only the vertical direction is considered, the instrument measures the sky almost continuously and the only interruptions occur during the mirror measurements. Independent of the acquisition time, the raw data is recorded approximately every 0.16 seconds, hence 6 - 7 times per second. The treatment of the data follows two steps: firstly, the measured digital counts are transformed into normalized radiances after Eq. 2.13 on this fine time resolution. Secondly, the normalized radiances are synchronized with the lidar measurements by averaging over one minute intervals corresponding exactly to the average interval of the lidar data. This data and the lidar instrument are described in detail in the following section.

2.3 The Micropulse Lidar

Lidar stands for *Light Detection and Ranging* and describes an active remote sensing technique. Nowadays, there exist highly developed lidar systems, e.g. Raman lidars (Ansmann et al., 1990, 1992), high spectral resolution lidars (HSRL) (Grund and Eloranta, 1990; Turner and Eloranta, 2008), or differential absorption lidars (DIAL) (Godin et al., 1989).

Raman lidars dispose of several channels to measure elastic and inelastic backscattering at the same time. Elastic backscattering means that emission and reception of the signal take place at the same wavelength, whereas inelastic backscattering is characterized by a change of frequency between the emitted and received signal due to the excitation of different vibrational or rotational levels of the molecules. These measurements can be used for example to derive profiles of the water vapour mixing ratio or temperature. However, the main advantage is that the extinction coefficient can be obtained directly from the measurements of the channels with inelastic backscattering without making assumptions about the backscatter-to-extinction ratio.

HSRL lidars are also capable of measuring particle extinction directly with the help of two channels: one that measures the backscattering originating from the entire atmosphere (molecular plus particle), and one that measures only the molecular contribution by removing with an absorption filter the central portion of the signal which is associated with aerosol or cloud particles. From these two simultaneous measurements the particle extinction can be derived from the change in the slope of the molecular signal relative to a clear sky atmosphere.

DIAL lidars are used to measure the atmospheric concentration of gases such as water vapour or ozone. They use measurements at two different wavelengths, one situated in an absorption line of the considered gas and the other at a non-absorbing wavelength. If the two wavelengths are close to each other, the scattering by molecules can be considered to be equal and in this case the difference of the signal between the two wavelengths is only due to absorption.

Other lidars, for example the spaceborne lidar CALIOP (Winker et al., 2003, 2009, 2010), include depolarization measurements from which the cloud phase can be determined since ice crystals tend to depolarize the incident visible radiation whereas for water droplets no such depolarization is observed (Sassen, 1991).

However, these advanced systems are expensive and not every ground-based measurement platform is equipped with such a lidar. The lidar used in this thesis is a relatively simple micropulse lidar developed by the company CIMEL Electronique. In this section, the instrument is introduced.

2.3.1 Technical Description

The *Cloud and Aerosol Micro Lidar* (CAML-CE370) is a lidar with elastic backscattering which operates at a single wavelength and does not include depolarization channels. However, the advantage of this instrument is that it works automatically and continuously. It consists of two parts: the control unit containing the laser and the acquisition units, and the optical head containing the telescope. Both parts are connected via an optical fibre of a length of 10 m. This setup allows the optical head to be situated outdoors while the control unit is situated indoors which can thus easily be isolated against temperature and humidity influences.

The main characteristics of the instrument are summarized in Table 2.5. The laser integrated in the instrument is a double Neodymium-YAG (Nd:YAG II) laser that emits laser pulses at a wavelength of 532 nm. The pulse duration is approximately 100 ns and the pulse energy around 10 - 20 μJ. The high repetition rate of 4.7 kHz assures a power of 100 - 150 mW. The laser pulse is propagated from the laser to the instruments telescope via the optical fibre. When leaving the telescope, the laser beam has a diameter of about 200 mm which corresponds to the diameter of the telescope. At this point all eye security regulations are fulfilled, hence the instrument can be operated everywhere without security constraints.

Atmospheric particles scatter the radiation emitted by the laser in all directions. A portion of the radiation is backscattered in the opposite direction and returns to the telescope on the same way where it came from. This backscattered radiation is focused by the lens back into the optical fibre. In the control unit, which is schematically represented in Fig. 2.11, it is led from a beam splitter consisting of a half-reflecting mirror with an inclination of 45 ° ("Séparateur de faisceau") through an optical filter centred at 532 nm of a width of 0.2 nm ("Filtre 532 nm"). This filter reduces the noise from the atmospheric background by only allowing the desired wavelength to pass through. The conversion of the received radiation into an electrical signal is realized by a photon counter (an avalanche photodiode (APD), "Compteur de photons") where the numerical counts are averaged over 4096 shots ("Moyenne (4096)") by a field programmable gate array (FPGA) to increase the

Property	
Laser type	frequency doubled Nd:YAG
Wavelength	532 nm
Pulse duration	100 ns
Pulse energy	10 - 20 μJ
Repetition rate	4.7 kHz
Telescope diameter	200 mm
Beam divergence	55 μrad
Range resolution	15 m
Temporal resolution	1 min

Table 2.5: Main characteristics of the CAML-CE370 lidar system.

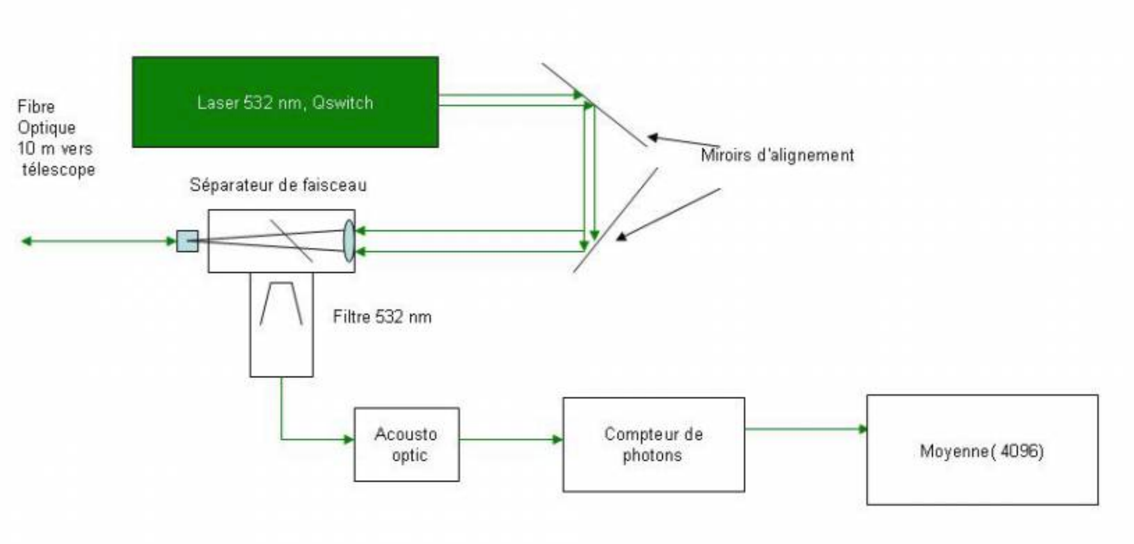

Figure 2.11: Schematic of the control unit of the CAML-CE370 lidar (courtesy of T. Podvin).

signal to noise ratio. The detection is divided up into 2048 gates of each 100 ns which allows to obtain a profile of numerical counts ranging from 0 to 30 km with a vertical resolution of 15 m. However, for altitudes above 15 km the lidar signal becomes very noisy, so the maximum altitude considered in this work is set to 15 km.

Furthermore, the *After Pulse* phenomenon has to be taken into account which is due to the fact that the emitted laser pulse and the received backscattered radiation share the same optical fibre. During the emission of the laser pulse, some fractions of it are reflected inside the optical fibre and reach the circuit of detection. To reduce this parasite signal an acousto-optic modulator (AOM, "Acousto optic" in Fig. 2.11) which is synchronized with the pulse emission is integrated into the instrument and deflects 99.9 % of the signal. Nevertheless, the remaining portion still saturates the detector for a short time interval and the gates corresponding to this period are not exploitable. The first usable altitude in the profile is approximately 300 m.

In December 2011, the optical head of the micropulse lidar at the LOA measurement site has been integrated in a thermal enclosure system to avoid the problems of possible condensation and of a temperature dependence of the characteristics of the optical system. This feature of the instrument is provided optionally by the manufacturer but highly recommended for continuous outdoor operation.

2.3.2 Measurement Principle and Lidar Equation

As indicated above, the basic principle of lidar measurements is the emission of a short laser pulse into the atmosphere and the reception of the intensity that is backscattered by the atmospheric particles. The time difference Δt between the emission and the reception of the pulse yields information about the distance Δr between the atmospheric particles and the instrument, $\Delta r = (c \cdot \Delta t)/2$, where c is the speed of light.

The lidar equation describes the backscattered power received by the lidar telescope $P(r)$ as function of the range r which is related to the initially emitted power P_0 and the optical properties of the molecules and particles in the atmosphere. It may be expressed by,

$$P(r) = K \frac{P_0}{r^2} O(r) \left(\beta_{\mathrm{mol}}(r) + \beta(r)\right) \exp\left[-2 \int_0^r \left(\sigma_{\mathrm{mol}}(r') + \eta\sigma(r')\right) \mathrm{d}r' \right], \qquad (2.15)$$

where K is an instrument constant depending on the optical elements of the telescope and the electronic detection system. $O(r)$ is the so-called overlap function that describes the portion of the backscattered power which is focused into the optical fibre for altitudes below the altitude of total overlap. For the micropulse lidar, the altitude of total overlap is 2000 m which means that $O(r)$ is equal to unity for altitudes above 2000 m. Hence, this function is important for the study of aerosols in the layers close to the ground but for the altitude of cirrus clouds its value becomes unity. The division by r^2 on the right-hand side of the lidar equation (cf. Eq. 2.15) describes the effect of the solid angle: the higher the particles are located in the atmosphere, the smaller the solid angle allowing them to backscatter into the FOV of the telescope (Mortier, 2013). Thus, the multiplication $P(r)r^2$ is also referred to as range-corrected signal.

The terms $\beta(r)$ and $\sigma(r)$ in Eq. 2.15 represent the bulk backscatter (in units of $\mathrm{m}^{-1}\,\mathrm{sr}^{-1}$) and extinction (in m^{-1}) coefficients, respectively, of atmospheric particles, meaning aerosol or cloud particles. $\beta_{\mathrm{mol}}(r)$ and $\sigma_{\mathrm{mol}}(r)$ stand for the respective molecular backscatter and extinction coefficients which can be obtained from the empiric expressions of Flamant (2008),

$$\begin{aligned} \sigma_{\mathrm{mol}} &= 1.17\left[\frac{\lambda}{0.55\,\mu\mathrm{m}}\right]^{-4.09}\left[\frac{p}{1013\,\mathrm{hPa}}\frac{288\,\mathrm{K}}{T}\right]10^{-5} \quad \left[\mathrm{m}^{-1}\right], \\ \beta_{\mathrm{mol}} &= \frac{3}{8\pi}\sigma_{\mathrm{mol}} \quad \left[\mathrm{m}^{-1}\,\mathrm{sr}^{-1}\right], \end{aligned} \tag{2.16}$$

where λ is the wavelength of the lidar in μm, $3/(8\pi)\,\mathrm{sr}^{-1}$ is the constant molecular backscatter-to-extinction ratio (Fernald, 1984), p is the atmospheric pressure in hPa and T is the temperature in K. The required profiles of atmospheric pressure and temperature are obtained from ECMWF reanalysis which will be introduced in Sect. 2.4.

The exponential term in the lidar equation Eq. 2.15 describes the two-way transmission,

$$T^2(r) = \exp\left[-2\int_0^r \left(\sigma_{\mathrm{mol}}(r') + \eta\sigma(r')\right)\mathrm{d}r'\right], \tag{2.17}$$

where η is the multiple scattering factor introduced by Platt (1973, 1979). Although multiple scattering is more important for space-borne lidars due to a large FOV in combination with a large distance between the instrument and the target, these effects should not be neglected for ground-based measurements. However, for the geometry of the micropulse lidar (FOV of 55 μrad) used in our study and assuming a cirrus cloud of 1 km thickness in 10 km altitude, the particle size would have to be of an order of magnitude of 1 mm and hence very large to cause a recognizable diffraction effect. Hence, in our case of optically thin cirrus clouds, the single scattering hypothesis can be justified. That means the radiation emitted by the laser is considered to be scattered only once at a range r and returns directly back to the telescope. In this case, the distance between the scattering particle and the instrument can be calculated with the above-mentioned equation $\Delta r = (c \cdot \Delta t)/2$, where a linear relationship between the travel time and the distance of the scattering particle from the telescope is assumed. However, the interactions between the radiation emitted by the laser and the atmospheric particles may be more complex. In an optically thicker medium, the laser pulse may be scattered several times in forward direction before it is scattered backwards and on its way back to the telescope it may also be exposed to multiple scattering processes. In this case, the linear relationship between the time and the distance is no longer valid because the return of the pulse is delayed due to the multiple scattering processes which means that the altitude of the backscattering particle is overestimated. As a consequence, the multiple scattering factor should be taken into account in the lidar equation. The value of η depends on the microphysical properties of the scattering medium, the characteristics of the instrument (FOV, divergence of the laser beam) and the distance of the scattering particles to the instrument. For cirrus clouds, it typically varies between 0.5 and 1 (Platt, 1973).

2.3.3 Data and Information Provided by the Lidar

The first micropulse lidar of type CAML-CE370 was installed on the LOA measurement platform in December 2006. It was changed to a new lidar system of the same type in April 2015. Hence, one advantage of the lidar measurements is the long record of available data which is enabled by the automatic operation mode.

Until December 5, 2016, the lidar was measuring with a zenith angle of $\Theta = 0\,^{\circ}$, thus looking directly vertical. Between December 5, 2016, and March 27, 2017, the viewing angle was changed to an inclination of $\Theta = 42.5\,^{\circ}$ which leads to a vertical resolution of $15\,\mathrm{m} \cdot \cos(\Theta)$ instead of 15 m. Furthermore, during this period the telescope was not properly fixed and covered a growing portion of the lens. Hence, the viewing angle changed further and the quality of the lidar data during this period cannot be assured. Thus, no data from this period has been treated in this work. On March 27, 2017, the angle has been changed back to $\Theta = 0\,^{\circ}$ before finally

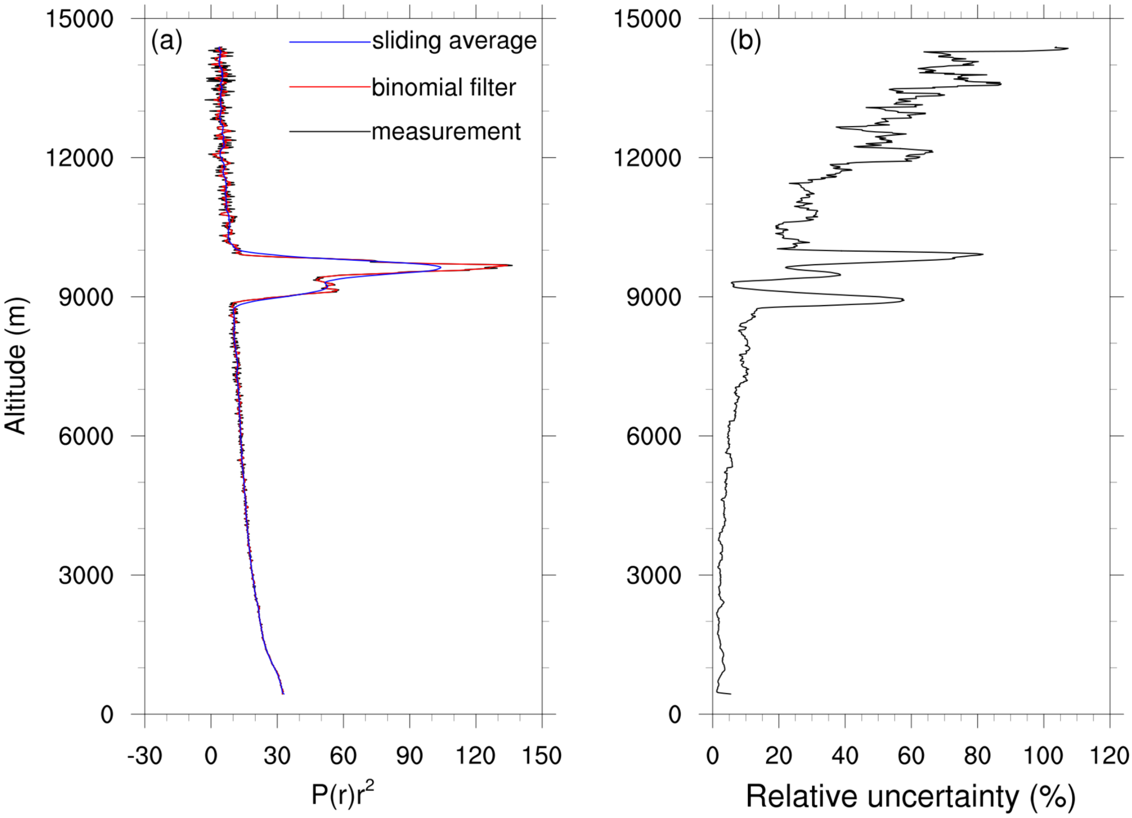

Figure 2.12: Lidar measurement and error for the lidar profile measured on November 30, 2016, at 18.18 UTC. (a) The lidar measurement is represented in black, application of a vertical binomial filter to this signal in red, and a vertical sliding average in blue. (b) Relative uncertainty in $P(r)r^2$ (in %).

an inclination of $\Theta = 3\,^\circ$ with respect to the zenith has been installed on March 31, 2017 (cf. Table 2.6).

As mentioned in Sect. 2.2.3, the measured lidar profiles are averaged over one minute. In order to further reduce the noise in the high altitudes of cirrus clouds, which is necessary to perform retrievals of their properties, a sliding average over time is calculated averaging each profile with the two preceding and the two following profiles, hence an average over five minutes. It should be noted that the same kind of averaging is performed for the radiometer data to be consistent when using the synergy of both instruments.

However, even after the averaging over time the noise in the micropulse lidar profiles is still quite large in cirrus cloud altitudes (cf. black line in Fig. 2.12 a for an example), and hence a vertical binomial filter is applied to the measured profiles (represented by the red line in Fig. 2.12 a). This averaging technique is advantageous compared to a vertical sliding average (blue line in Fig. 2.12 a), since the main characteristics, such as the strength of the peak, are kept with this type of filter. However, the error on the lidar measurements is calculated with the help of the sliding average. Since the measurement noise increases with increasing height, the error on the lidar measurement should be expressed as a function of altitude. It is calculated as standard deviation around the mean over a vertically sliding window of 20 gates. An example is shown in Fig. 2.12 b for the lidar profile measured on November 30, 2016, at 18.18 UTC.

The lidar measurements provide an information about the cloud altitude. Furthermore, the attenuation due to the cloud layer and hence its visible optical thickness can be derived from the shift of the signal below and above the cloud. These basic information obtained from the lidar measurements are used in all steps of the methodology to study cirrus clouds presented in Chapter 3 of this thesis and will be described in the following. However, it should be noted that the calibration of the lidar signal is described in Sect. 3.4.2 in the context of our retrieval algorithm.

Cloud Detection

The first step in the study of cirrus clouds is their detection. According to Platt et al. (1994), the cloud base altitude is defined as the altitude above which solid hydrometeors exist and can be detected. These hydrometeors can be water droplets, ice crystals or rain. The definition and detection of the cloud top altitude is somewhat more complicated since the lidar signal might be completely attenuated in the cloud layer. In this case, the retrieved cloud top altitude is only an "apparent" cloud top altitude where total attenuation is reached. When regarding thin cirrus clouds, the lidar signal often penetrates the cloud completely. This complete penetration can be identified by the presence of Rayleigh scattering above the cloud top altitude. Platt et al. (1994) describe three methods to retrieve cloud base and top altitudes, two of which were tested in this work and will be briefly described and compared here.

The first method is the approach of Pal et al. (1992) which uses the fact that the intensity of the backscattered lidar signal decreases exponentially with altitude in a cloud free atmosphere as described by the lidar equation (cf. Eq. 2.15). If a cloud is present, the backscattered signal increases significantly at the cloud base because of enhanced backscattering due to the larger cloud particles. As a consequence, the altitude of the cloud base can be located in the level where the lidar signal changes

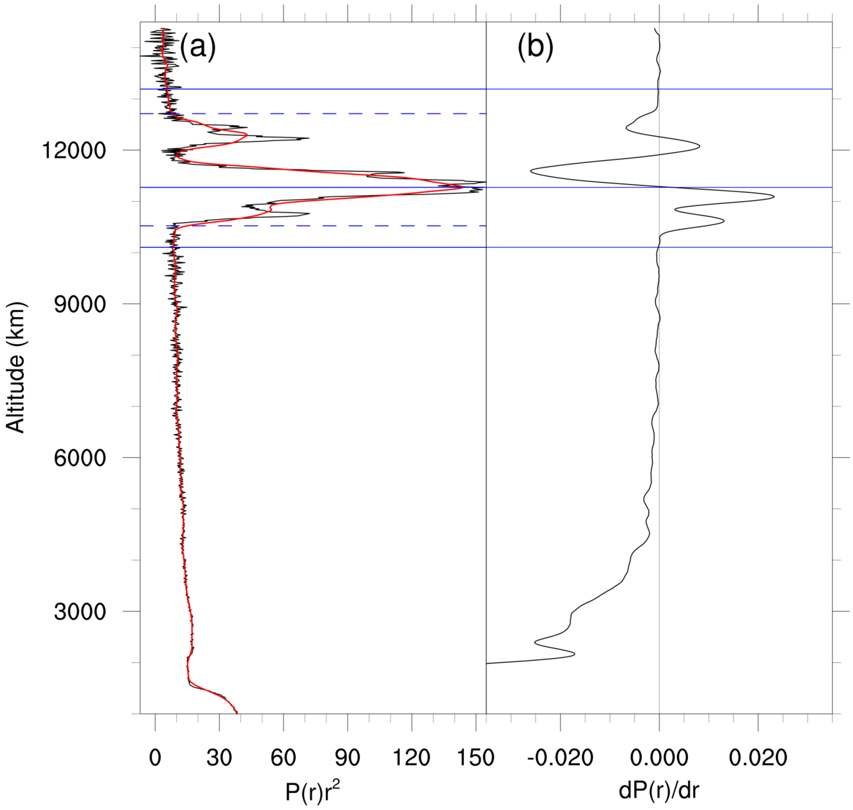

Figure 2.13: Illustration of the cloud detection method of Pal et al. (1992) for the cloudy profile measured on April 18, 2018, at 18 UTC. (a) Range-corrected lidar signal $P(r)r^2$ (black) and sliding average over 20 gates (red). (b) Slope $\mathrm{d}P(r)/\mathrm{d}r$ in arbitrary units showing the zero crossings. The solid horizontal blue lines represent the altitudes of the defined cloud base, peak and top altitudes from the method of Pal et al. (1992) (10.1 km, 11.3 km and 13.2 km, respectively). The dashed horizontal blue lines indicate the cloud base and top altitudes from the second cloud detection method of Platt et al. (1994) for comparison purposes (10.5 km and 12.7 km, respectively).

the slope. This is realized by calculating the first derivative, $\mathrm{d}P(r)r^2/\mathrm{d}r$, of the signal and searching for the altitude where the slope changes sign from negative to positive. This zero crossing takes place at the boundary between the clearer air below the cloud and the region containing cloud particles.

Figure 2.13 presents an example of this approach for a profile containing a cirrus cloud measured on April 18, 2018, at 18 UTC. The black line in Fig. 2.13 a shows the range-corrected lidar signal, $P(r)r^2$, and the red line shows a vertical sliding average because the first derivative of the signal, $\mathrm{d}P(r)r^2/\mathrm{d}r$, shown in Fig. 2.13 b is calculated over a vertically sliding window (Pal et al., 1992). The number of gates for this sliding average has to be adjusted depending on the lidar system. At the lowest solid horizontal blue line in Fig. 2.13 indicating the cloud base altitude, $\mathrm{d}P(r)r^2/\mathrm{d}r$ changes sign from negative to positive which means there is a local minimum in the signal. At the cloud peak, defined as the altitude where the backscattered signal in the cloud is strongest (middle solid blue line), a zero crossing from positive to negative can be found which means there is a local maximum in the signal. In theory, these zero crossings directly give the altitude of the cloud base and the cloud peak. In practice, however, multiple zero crossings may arise from noise in the lidar return, from inhomogeneities inside the cloud or from aerosols that may be present in the atmosphere. Thus, two threshold tests proposed by Mortier (2013) are implemented to reject the unimportant zero crossings. The first threshold test compares the difference between the signal at the peak and base altitudes to the measurement noise. For this purpose, the function $N(r_{\mathrm{base},i})$ is defined which describes the variation of noise with altitude. To calculate $N(r_{\mathrm{base},i})$, a second degree polynomial fit of the standard deviation of the signal at each base (plus the eight gates below that base) is performed. The threshold test is then defined by,

$$P(r_{\mathrm{peak},i})\, r^2_{\mathrm{peak},i} - P(r_{\mathrm{base,i}})\, r^2_{\mathrm{base},i} \geq T_1 \cdot N(r_{\mathrm{base},i}), \tag{2.18}$$

where $P(r_{\mathrm{peak},i})r^2_{\mathrm{peak},i}$ and $P(r_{\mathrm{base},i})r^2_{\mathrm{base},i}$ are the range-corrected signals at the peak and base altitudes, respectively, and T_1 is a threshold of rejection which depends on the lidar system and the desired sensitivity. For the micropulse lidar installed on the LOA measurement platform, Mortier (2013) found that a value of $T_1 = 10$ is most suitable.

As mentioned above, the detection of the cloud top is more complicated and uncertain when realized with a ground-based lidar (e.g. Pal et al., 1992; Platt et al., 1994). If the lidar pulse penetrates the cloud completely, the transition of the cloud signal to the clear air signal above the cloud can be found with a similar method as described for the cloud base and peak by searching the altitude where the sign of $\mathrm{d}P(r)r^2/\mathrm{d}r$ changes from negative to positive, meaning there is a local minimum in the lidar signal. However, in many cases the signal is completely attenuated before the cloud top is reached making a precise retrieval of the cloud top impossible because the signal decreases into the background noise and does not contain the necessary information. Nevertheless, following Platt et al. (1994) an "apparent" cloud top altitude can still be derived which is defined as the altitude where the backscattered signal, $P(r_{\mathrm{top}})\, r^2_{\mathrm{top}}$, decreases below the level of the signal at the cloud base altitude, $P(r_{\mathrm{base}})\, r^2_{\mathrm{base}}$, and thus drops down to the same background intensity as below the cloud. This "apparent" cloud top height underestimates the real cloud top height.

In the case of multiple layers, the condition,

$$P(r_{\mathrm{base},i+1})r^2_{\mathrm{base},i+1} \leq P(r_{\mathrm{base},i})r^2_{\mathrm{base},i}, \tag{2.19}$$

has to be fulfilled. Otherwise, the layers i+1 and i are considered to be one cloud layer. The presence of several peaks in the backscattered signal within a single cloud is not uncommon and can be explained by vertical inhomogeneity of the cloud.

Finally, to assure that the detected potential cloud base, peak and top altitudes correspond to a cloud layer and not to an aerosol layer that would have a much smaller peak, the following second threshold test is applied,

$$\frac{P(r_{\mathrm{peak},i})\, r^2_{\mathrm{peak},i}}{P(r_{\mathrm{top},i})\, r^2_{\mathrm{top},i}} \geq T_2. \tag{2.20}$$

Mortier (2013) set $T_2 = 4$, but applying this value in our algorithm leads to the rejection of a quite important number of cirrus clouds. Hence, we decided to chose the value of T_2 depending on the altitude of the cloud. For clouds below 7.5 km, $T_2 = 4$ is used in order to not mistake aerosol layers in low levels as clouds. For high clouds above 7.5 km, the value $T_2 = 2$ is used to keep optically thin cirrus layers, accepting the risk that this sometimes leads to incorrect retrievals because maximum/minimum pairs resulting from instrument noise are not rejected.

As discussed above, this method uses a sliding average. Applying this type of average leads to an upward or downward shift of the zero crossings. To take that into account, the algorithm searches for the minimum or maximum of the range-corrected signal in the environment of each calculated zero crossing and accepts these positions for the cloud base, peak and top altitudes as proposed by Pal et al. (1992). However, the results of this detection algorithm still show for a lot of profiles a downward shift for the cloud base altitude compared to the altitude where one would visually define the cloud base from looking at the measured signal. This is also the case for the example shown in Fig. 2.13 where the cloud base is found in an altitude of 10.1 km, although from looking at the measured signal the cloud base altitude seems to be located around 10.5 km. Similarly, the cloud top altitude seems to be too high. Hence, a second method described by Platt et al. (1994) was tested.

This second approach is somewhat simpler and straight-forward. The cloud base altitude is defined as that altitude, where the signal increases above the molecular background level and this increase is larger than n times the standard deviation of the background fluctuations (Platt et al., 1994). Secondly, it is required that the signal continues to increase for m following altitude gates. This second condition assures that sudden maxima in the signal due to noise are not misinterpreted as clouds.

The procedure to find the cloud base and top altitudes with this approach is the following: Starting from an altitude of 300 m (to avoid the blind zone of the lidar below 300 m due to the After Pulse phenomenon), potential base altitudes are searched where the signal (in this case expressed as $\ln(P(r)r^2)$) increases over five consecutive altitude gates (hence, $m = 5$). When an altitude is found that fulfils this condition, the molecular signal below this potential base altitude is calculated by performing a linear regression over the 100 altitude gates (1500 m) just below the potential base. In addition, the mean and the standard deviation of the signal for this altitude interval are calculated since the standard deviation is required for the second test which is a threshold test. The potential cloud base is accepted if the observed increase of the signal, compared to the molecular fit, is larger than four times the standard deviation (hence, $n = 4$). After a cloud base was defined, the according cloud top is searched. This is done in a similar way by searching for the altitude where the signal increases over five consecutive gates, but by starting from the far range of the measured lidar profile (15 km) and proceeding downwards. Furthermore, the signal in the altitude of the potential cloud top has to be smaller than the signal at the cloud base. In case multiple potential cloud tops are found, the threshold test comparing the increase of the signal to the molecular background is performed firstly for the potential cloud top altitude closest to the cloud base. If this test is not true for the lowest potential cloud top, higher cloud tops are tested. It should be noted that for the cloud top a value of $n = 2$ is chosen because the standard deviation above the cloud is much larger than below the cloud. In case no cloud top could be detected with these criteria, the altitude where the signal drops below the molecular background fit of the base is defined as cloud top altitude. In case a cloud top has been detected, the procedure is restarted from the gate above the defined cloud top altitude to search for a possible second cloud layer.

For the profile shown in Fig. 2.13, the derived cloud base and top altitudes from the second method are 10.5 km and 12.7 km, respectively (cf. dashed horizontal blue lines in Fig. 2.13). These altitudes seem to correspond better to the values one would expect from looking at the measured signal (cf. Fig. 2.15 as well). Furthermore, Fig.

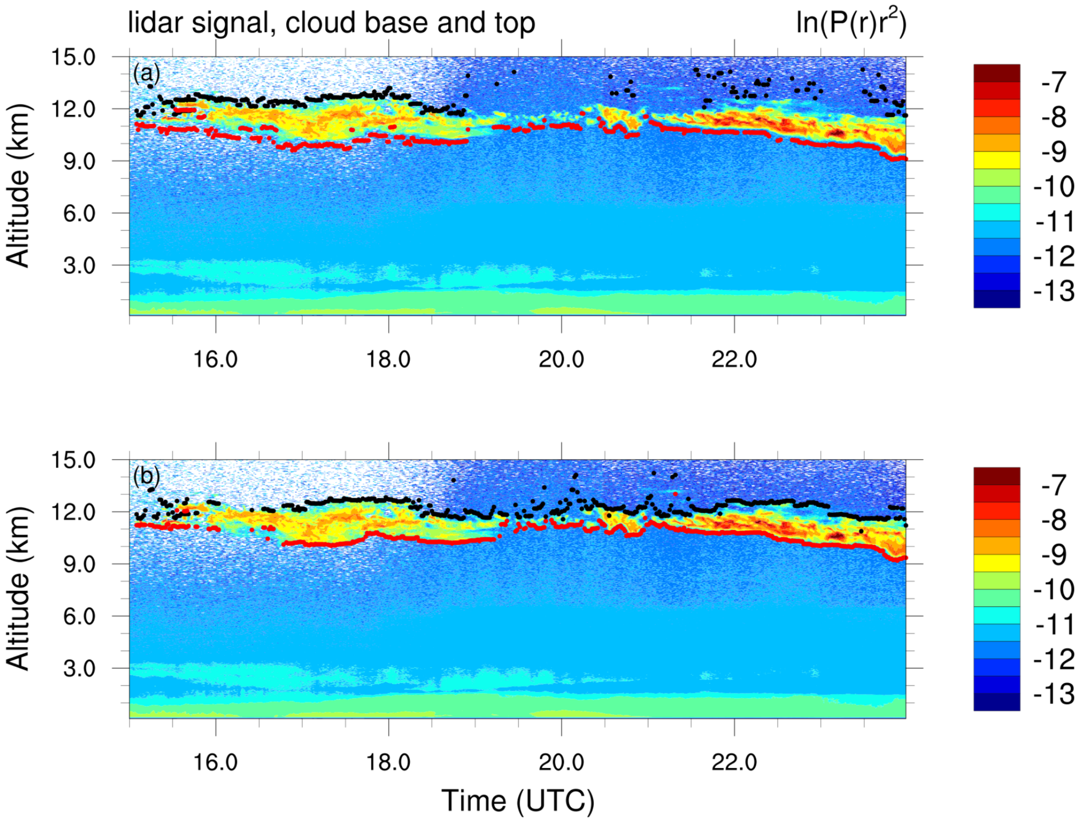

Figure 2.14: Comparison of the two different cloud detection methods for April 18, 2018, 15-24 UTC. Logarithm of the range-corrected lidar signal, $\ln(P(r)r^2)$, overlaid by the results of the cloud detection algorithms, (a) from the method of Pal et al. (1992), and (b) from the method of Platt et al. (1994). Red points mark the cloud bases and black points the cloud tops.

2.14 compares the results of the two cloud detection algorithms where the method of Pal et al. (1992) is shown in Fig. 2.14 a and the method of Platt et al. (1994) in Fig. 2.14 b. It is obvious that especially the cloud top detection works better with the latter method. In addition, the cloud base altitudes from the second method seem to be closer to the increase of the lidar signal than the cloud base altitudes from the method of Pal et al. (1992). Consequently, the second cloud detection method was chosen in our methodology presented in Chapter 3. However, the first method is also implemented in our algorithms for comparison purposes and seems to be advantageous in case of multiple cloud layers. It should be noted that independent of the cloud detection method, a temperature is assigned to the retrieved cloud base and top altitudes. This is done by comparing the retrieved altitudes to atmospheric temperature profiles obtained from ECMWF reanalysis which will be described in Sect. 2.4.1.

Cloud Optical Thickness

Another fundamental parameter which can be derived directly from the lidar measurements is the extinction optical thickness of the cloud, τ_{cld}, defined in Eq. 1.20. It depends on the wavelength, so the optical thickness obtained from the lidar measurements corresponds to the visible optical thickness at the lidar wavelength of 532 nm. For the remainder of this thesis, all discussions including the optical thickness of cirrus are referring to the optical thickness at this wavelength.

The method used here to retrieve the optical thickness is the transmission method introduced by Young (1995) that has been applied by several different authors (e.g. Elouragini and Flamant, 1996; Chen et al., 2002; Giannakaki et al., 2007). In this method, the optical thickness is derived from the shift of the signal below and above the cloud due to the extinction of the cloud. Following Chen et al. (2002), the transmission can be expressed by,

$$T = \left(\frac{P_{\text{top}}}{P_{\text{base}}} \right)^{1/2}, \tag{2.21}$$

where P_{top} and P_{base} are molecular fits of the range-corrected lidar signal at the cloud top and the cloud base, respectively. Furthermore, the transmission is related to the optical thickness via,

$$T^2 = \exp\left[-2\eta\, \tau_{\text{cld}}\right], \tag{2.22}$$

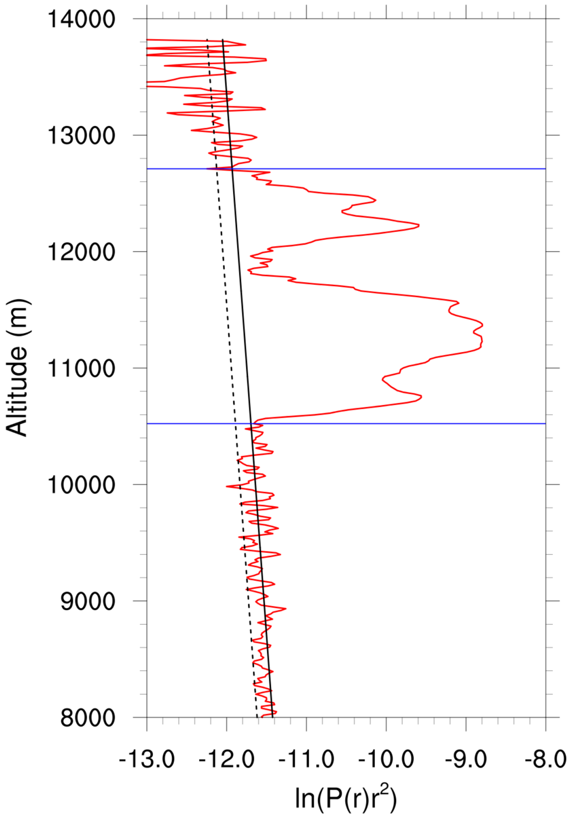

Figure 2.15: Illustration of the transmission method of Young (1995) for the profile measured on April 18, 2018, at 18 UTC. Red line: Logarithm of the range-corrected lidar signal, solid black line: molecular fit (using ECMWF reanalysis data) at the cloud base, dashed black line: molecular fit at the cloud top, blue horizontal lines: cloud base and top altitudes retrieved with the method of Platt et al. (1994).

as defined in Eq. 2.17. Hence, the optical thickness of the cloud is given by,

$$\tau_{\text{cld}} = \frac{\ln(P_{\text{top}}) - \ln(P_{\text{base}})}{-2\eta}. \tag{2.23}$$

An example of application of this method is presented in Fig. 2.15 for the same lidar profile shown in Fig. 2.13 measured on April 18, 2018, at 18 UTC. As in the cloud detection algorithm described previously, the molecular signal at the cloud base is calculated from a linear regression of the lidar signal over 100 gates (1500 m) below the defined cloud base altitude (represented by the solid black line in Fig. 2.15). Similarly, the molecular signal at cloud top is obtained (dashed black line). From the shift of these two lines, a transmission of 0.78 and an effective visible optical thickness of $\tau^{\star}_{\text{cld}} = \eta\,\tau_{\text{cld}} = 0.247 \pm 0.150$ have been derived for this profile. To obtain the real optical thickness τ_{cld}, further information about the multiple scattering factor η is required. The error on $\tau^{\star}_{\mathrm{cld}}$ arises from the measurement noise, especially above the cloud, and is calculated based on the linear regressions for the molecular signal.

It should be noted that when regarding lidar measurements, another interesting quantity is the integrated attenuated backscatter, γ', which links the measured signal to the optical thickness. Platt (1973) showed that the integration of the attenuated backscatter coefficient between the cloud base and top leads to the expression,

$$\gamma' = (k/2\eta)\big\{1 - \exp\left[-2\eta\,\tau_{\mathrm{cld}}\right]\big\}, \tag{2.24}$$

where k is the backscatter-to-extinction ratio. The exponential term in Eq. 2.24 can be replaced by the two-way transmission (cf. Eq. 2.22) (Platt et al., 1999),

$$\gamma' = (k/2\eta)\big\{1 - T^2\big\}. \tag{2.25}$$

In case of a fully attenuating cloud, the transmission is zero and Eq. 2.25 simplifies to,

$$\gamma' = (k/2\eta). \tag{2.26}$$

Hence, the backscatter-to-extinction ratio can be calculated via $k{=}2\eta\gamma'$ if the multiple scattering factor η is estimated previously. In case of semi-transparent clouds, the two-way transmission can be obtained from the shift of the lidar signal below and above the cloud as described above. Another method to retrieve the effective lidar ratio is the classical Klett-Fernald inversion (Klett, 1981, 1985; Fernald, 1984). However, since we are using a very different approach in our methodology where the retrieval of the backscatter-to-extinction ratio is based on a microphysical ice cloud model, the two methods mentioned above to retrieve this parameter have not been applied in this work.

Date	Time period	Θ_{CLIMAT}	Θ_{lidar}	Remarks algorithm
09/04/2015	13-19 UTC	multi-angle	0 °	no convergence
10/04/2015	10-16 UTC	multi-angle	0 °	good retrievals
14/04/2015	16-21 UTC	multi-angle	0 °	no convergence
16/04/2015	2-6 UTC	multi-angle	0 °	no convergence
19/04/2015	8-23 UTC	multi-angle	0 °	good retrievals
24/04/2015	10-15 UTC	multi-angle	0 °	no convergence
26/01/2016	13-17 UTC	multi-angle	0 °	no convergence
28/01/2016	9-17 UTC	multi-angle	0 °	very thin cirrus, large errors
24/02/2016	9-13 UTC	multi-angle	0 °	good retrievals
12/03/2016	2-16 UTC	multi-angle	0 °	no convergence
14/03/2016	14-24 UTC	multi-angle	0 °	very thin cirrus, large errors
15/03/2016	0-16 UTC	multi-angle	0 °	no convergence
02/05/2016	8-13 UTC	multi-angle	0 °	no convergence
26/07/2016	7-9 UTC	only vertical	0 °	good retrievals
19/09/2016	7-12 UTC	only vertical	0 °	good retrievals
27/09/2016	10-16 UTC	only vertical	0 °	good retrievals
28/09/2016	10-16 UTC	only vertical	0 °	no convergence
03/10/2016	8-9 UTC	only vertical	0 °	no convergence
30/11/2016	3-24 UTC	only vertical	0 °	good retrievals
01/12/2016	0-12 UTC	only vertical	0 °	no convergence
05/12/2016	9-16 UTC	only vertical	0 °	no convergence
30/03/2017	8-16 UTC	only vertical	0 °	good retrievals
10/05/2017	11-16 UTC	only vertical	3 °	no convergence
16/05/2017	7-8 UTC	only vertical	3 °	no convergence
17/05/2017	9-15 UTC	only vertical	3 °	good retrievals
22/05/2017	8-16 UTC	only vertical	3 °	good retrievals
23/05/2017	7-11 UTC	only vertical	3 °	no convergence
29/05/2017	8-10 UTC	only vertical	3 °	very thin cirrus, large errors
05/07/2017	7-13 UTC	only vertical	3 °	no convergence
07/07/2017	8-9 UTC	only vertical	3 °	no convergence
28/08/2017	7-16 UTC	only vertical	3 °	no convergence
18/04/2018	14-24 UTC	only vertical	3 °	good retrievals
19/04/2018	0-17 UTC	only vertical	3 °	good retrievals

Table 2.6: Days when cirrus clouds were measured simultaneously with the lidar and the CLIMAT instrument at the LOA measurement site. Θ_{CLIMAT} and Θ_{lidar} are the viewing angles of CLIMAT and the lidar, respectively. The last column indicates the quality of the retrievals with our algorithm. No convergence can either be due to a bad characterization of the atmospheric profile not allowing the thermal infrared measurements to converge, or to noisy lidar measurements. Horizontal lines indicate dates when the calibration of CLIMAT changed (cf. Table 2.4).

2.4 Ancillary Data

In our methodology presented in Chapter 3, additional information about meteorological parameters describing the state of the atmosphere and the surface is required. As mentioned above, the temperature at the cloud base and the cloud top is retrieved after the cloud detection is performed. Furthermore, the molecular backscattering and extinction coefficients which are needed in the lidar equation are calculated based on profiles of atmospheric pressure and temperature (cf. Eq. 2.16). For the radiative transfer calculations at the thermal infrared wavelengths, the surface temperature as well as atmospheric profiles of temperature, water vapour and ozone are required. This meteorological parameters are obtained from ECMWF reanalysis described below. Furthermore, the single scattering properties of atmospheric particles have to be assumed. In case of cirrus clouds, the model that links the microphysics of the cloud to its single scattering properties is of central importance in our methodology and will be described in detail in Sect. 3.1. The aerosol properties, however, are obtained from the OPAC database which will be briefly introduced in the second part of this section.

2.4.1 ECMWF Reanalysis

The European Centre for Medium-Range Weather Forecasts (ECMWF) data used in this thesis is the operational analysis product produced with the current ECMWF forecast model by assimilating in real time the latest observations. This product is available either on 25 pressure levels or on 137 model levels with a vertical hybrid sigma-pressure coordinate which means that the vertical levels are following the surface orography in the lower levels and are smoothly transformed into pure pressure levels with increasing altitude. The horizontal resolution is a $0.1^\circ \times 0.1^\circ$ latitude/longitude grid and the model runs are realized for the four time steps 0, 6, 12 and 18 UTC.

In this thesis, the vertical resolution of 137 model levels has been chosen. To obtain the meteorological parameters representative for our measurement site, the data for the four surrounding model grid-points has been selected and averaged by taking into account the distance of each grid-point to the measurement site. All four time steps are treated in this way and when analysing the data with our methodology described in Chapter 3, the time step closest to the measurement time is selected which may lead to discontinuities in the time series of the retrieved parameters due to changing the atmospheric profile. As mentioned above, the meteorological parameters used in this thesis obtained from the ECMWF operational analysis dataset include the surface temperature as well as profiles of pressure, temperature, specific humidity and ozone.

2.4.2 OPAC Database

The Optical Properties of Aerosols and Clouds (OPAC) database (Hess et al., 1998b) provides the single scattering properties of liquid and ice clouds of varying characteristics as well as the single scattering properties of ten different aerosol types. It includes the extinction, scattering, and absorption coefficients, the single scattering albedo, the asymmetry parameter as well as the phase function, and allows the calculation of these properties for aerosols at 61 wavelengths between 0.25 and $40\,\mu$m.

The two aerosol types from this database used in this thesis are a *water-insoluble* (INSO) aerosol and a *water-soluble* aerosol (WASO) (Hess et al., 1998b). The INSO aerosol type mainly consists of soil particles and some organic material, the WASO aerosol type of water soluble sulphates, nitrates, and also organic substances. The latter is suitable to describe anthropogenic aerosol (Hess et al., 1998b) and is thus representative for our measurement site which is located in an urban/industrial area. Table 2.7 summarizes the single scattering properties of these two aerosol types at the visible lidar wavelength. These values show that at 532 nm, the INSO aerosol is far more absorbent than the WASO aerosol. The single scattering properties in the thermal infrared of the two aerosol types are summarized in Table 2.8.

Altogether it can be concluded that the characteristics of these two aerosols are very different. It should be noted that the INSO aerosol type is rather unrealistic for our measurement site. However, the idea behind using this aerosol model is to test the impact on our retrievals when very different aerosol types are chosen. The influence of the choice of the aerosol model on our retrievals will be discussed in detail in Chapters 3 and 4.

Single scattering property	WASO	INSO
Extinction efficiency factor (Q_{ext})	0.928	2.264
Single scattering albedo (ϖ_0)	0.986	0.727
Asymmetry parameter (g)	0.706	0.829
Lidar ratio (in sr)	66	37

Table 2.7: Single scattering properties of the WASO and INSO aerosol types at the lidar wavelength of 532 nm.

	8.7 μm			10.8 μm			12.0 μm		
	Q_{ext}	ϖ_0	g	Q_{ext}	ϖ_0	g	Q_{ext}	ϖ_0	g
WASO	0.026	0.045	0.073	0.014	0.014	0.042	0.027	0.004	0.033
INSO	1.421	0.586	0.773	1.658	0.617	0.680	1.408	0.645	0.685

Table 2.8: Single scattering properties of the WASO and INSO aerosol types at the thermal infrared radiometer wavelengths.

CHAPTER 3

Methodology for the Study of Cirrus Cloud Properties

In this chapter, the methodology to study high level cirrus clouds developed during this thesis is presented for a case study observed on November 30, 2016. The methodology consists of three main steps: firstly, a method to retrieve integrated cirrus properties based on the thermal infrared (TIR) radiometer measurements has been developed. In a second step, the lidar measurements have been used to obtain information about the vertical distribution of the cloud properties and an algorithm to retrieve IWC profiles has been established. These IWC profiles strongly depend on the backscatter-to-extinction ratio which has to be assumed when regarding simple micropulse lidar measurements alone. Hence, in a third step the TIR radiometer and lidar measurements are combined because the TIR radiometer measurements can be used to constrain the backscatter-to-extinction ratio as will be shown in the course of this chapter.

There are two concepts which are common in all three steps of our methodology: the microphysical model for ice clouds and the inversion method which is based on optimal estimation theory. Hence, these two concepts will be described previously to the different retrieval algorithms. The microphysical model is presented in the first section of this chapter, and optimal estimation theory is introduced in the second section.

Subsequently, the third section deals with the integrated properties of ice clouds which can be obtained from TIR radiometer measurements alone. More specifically, an algorithm based on optimal estimation to retrieve the IWP of the cloud is presented. The method, however, uses the cloud base and top altitudes as well as the according temperature retrievals obtained from the lidar measurements as described in Sect. 2.3.3 to define the time periods when cirrus clouds are present. It should be remarked that in all our algorithms cirrus clouds are defined by having a temperature of less than -25 °C at the cloud base which is situated in an altitude higher than 6 km. This temperature criterion has been used in previous studies (e.g. Goldfarb et al., 2001; Hoareau et al., 2013), although it should be noted that supercooled liquid droplets may still exist at this temperature as discussed in Sect. 1.2.1.

The fourth section of this chapter introduces the algorithm to retrieve from the lidar measurements the above-mentioned IWC profiles in cirrus clouds together with a profile of aerosol extinction for the layers below the cloud. The challenge when regarding simple micropulse lidar measurements alone is to find ways to constrain the so-called backscatter-to-extinction ratio because the lidar equation (cf. Eq. 2.15) contains two unknown parameters, namely backscattering and extinction. This ambiguity between backscattering and extinction will be discussed in detail in Sect. 3.4.3 before two strategies to constrain the backscatter-to-extinction ratio are presented in Sect. 3.5. In a first step, the visible optical thickness obtained from the transmission method described in Sect. 2.3.3 is used to constrain the backscatter-to-extinction ratio. However, in this approach the optical thickness is obtained from the same instrument. Although the transmission method is independent of the optimal estimation algorithm, it still remains a retrieval product that might depend on the instrument's characteristics. Furthermore, in this method the exact knowledge of the cloud base and top altitudes is required. As discussed in Sect. 2.3.3, especially the cloud top detection is challenging from ground-based lidar measurements. Instead of relying on such a retrieval product, we show in a second step that the TIR radiometer measurements can be used as well to constrain the backscatter-to-extinction ratio since they are sensitive to the integrated cloud properties, in particular the IWP. Therefore, the TIR radiometer measurements are integrated in the optimal estimation framework of the lidar only algorithm to retrieve the backscatter-to-extinction ratio together with the IWC profile of cirrus. This synergy algorithm is described in Sect. 3.6 before finally a brief summary of the methodology presented in this chapter is provided in the last section.

3.1 The Microphysical Model for Cirrus

As discussed in Sect. 1.3.1, the variation of ice crystal shapes and sizes which can be observed in atmospheric cirrus clouds is very large (cf. Fig. 1.5). Typical crystal shapes comprise hexagonal ice columns or plates, single bullets, bullet-rosettes with varying numbers of branches, and aggregates thereof (e.g. Heymsfield and Platt, 1984; Heymsfield and Iaquinta, 2000; Baran, 2007). Generally, the complexity of the ice particles increases with increasing size. Korolev et al. (2000) showed that the majority of cirrus ice crystals larger than 125 μm is of irregular shape and that pristine habits such as columns and plates are rare. Similarly, Heymsfield and Miloshevich (2003) found bullet-rosettes and aggregates of bullet-rosettes to be the dominant shape for particles larger than 100 μm. These complex aggregates may be further randomized by inhomogeneities of their surface, possible inclusions of air bubbles or aerosols, or by crystal distortions (Baran, 2007).

Due to this large variability, the modelling of the single scattering properties of cirrus cloud particles is challenging. In order to model their scattering and absorption properties, idealized geometric shapes have to be assumed. The modelling of hexagonal columns, hexagonal plates and bullet-rosettes is straight-forward because these shapes are symmetric and their three-dimensional geometry is well-defined. To represent more complex structures, however, several concepts have been developed.

One of these concepts is the polycrystal described by Macke et al. (1996). The underlying structure of the polycrystal is a tetrahedron, hence a three-dimensional shape consisting of four triangular surfaces. A part of each of these triangles is replaced by a smaller tetrahedron. The obtained structure is the so-called first-generation triadic Koch fractal. Repeating this procedure at the new smaller triangles leads to the second-generation. The polycrystal is a disordered version of this second-generation triadic Koch fractal which means that the smaller tetrahedrons are randomly displaced. It attempts to represent in a single model the strong variability of atmospheric ice crystals.

Another idealized shape to represent ice crystals is the hexagonal ice aggregate presented by Yang and Liou (1998). It consists of eight arbitrarily attached hexagonal elements whose surfaces can be roughened in order to introduce further randomization. Based on the hexagonal ice aggregate, Baran and Labonnote (2006) developed the chain-like aggregate which is a variant of the former where two of the original hexagonal elements have been elongated and re-transformed into a chain. Hence, this model represents the properties of more spatial and chain-like ice crystals. A strategy to further increase the randomization of the crystals is the Inhomogeneous Hexagonal Monocrystal (IHM) introduced by C.-Labonnote et al. (2001). The IHM incorporates inclusions of air bubbles or aerosols, but keeps the simple structure of a hexagonal column.

It should be noted that the shape of ice crystals smaller than $100\,\mu$m is quite uncertain due to instrument limitations (Baran, 2007). Since they can appear quasi-spherical or spheroidal, McFarquhar et al. (1999) suggested to regard them as spheres and use Lorentz-Mie theory to model their scattering properties. However, Yang et al. (2003) showed that this approximation is inappropriate and proposed to use the droxtal instead to better represent the more complex structure of small ice crystals compared to spheres.

However, the geometric shapes explained above represent single ice crystal models. As illustrated in Fig. 1.5, real ice clouds consist of an ensemble of particles of different shapes. Hence, it is more appropriate to construct an ensemble of different ice crystal habits instead of assuming one single geometrical form over the whole size spectrum. Such an approach has been proposed by Baum et al. (2005) who showed that single crystal habit models could not accurately reproduce the IWC measured during field campaigns whereas a mixture of particle shapes improved the comparison with the observations. Their ensemble of particles includes droxtals, hexagonal plates, solid columns, hollow columns, hexagonal ice aggregates and bullet-rosettes.

In this thesis, the ensemble model of Baran and Labonnote (2007) is used which attempts to reproduce the observed behaviour that the complexity of the ice crystals tends to increase with increasing size. In order to represent the change of the ice crystal habits as a function of the particle size, an ensemble model consisting of six members is used. They are illustrated in Fig. 3.1. The smallest ice crystals are represented by the first two members, which are simple hexagonal ice columns (Fig. 3.1 a) and bullet-rosettes (Fig. 3.1 b). Bullet-rosettes have been introduced in the model because they are a commonly observed shape of ice crystals in mid-latitude cirrus (e.g. Heymsfield and Platt, 1984; Baran, 2007). The further members represent larger and more complex ice crystals by arbitrarily attaching up to ten hexagonal elements to create chain-like aggregates.

The bulk single scattering properties, which have been defined in Sect. 1.3.2, are calculated for the ensemble model by integrating over the particle size distribution (PSD) parametrized after Field et al. (2005, 2007). This parametrization is based

(a) Hexagonal column (b) Six-branched bullet-rosette

(c) Three-branched (d) Five-branched

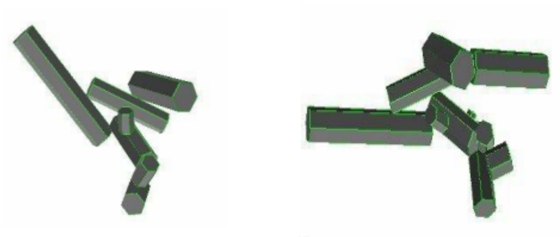

(e) Eight-branched (f) Ten-branched

Figure 3.1: The ensemble model of Baran and Labonnote (2007). (a) Hexagonal ice column representing the smallest member, (b) Six-branched bullet-rosette, (c) Three-branched ice crystal, (d) Five-branched ice crystal, (e) Eight-branched ice crystal, and (f) Ten-branched ice crystal representing the largest member.

on a large number of in situ measured PSD functions in the mid-latitudes and the tropics. It is independent of assumptions about the ice crystal shape and does not include measurements of ice crystal sizes less than 100 μm since the shattering of large ice crystals on the inlets and tips of particle probes produces small ice artefacts that may bias the measurements of the PSD (Strapp et al., 2001; Field et al., 2003; Lawson, 2011). Hence, for particles smaller than 100 μm an exponential PSD function is assumed. Field et al. (2005, 2007) showed that the PSD functions of ice crystals can be represented by a single underlying PSD from which the required PSD can be generated with the help of two moments. The second moment is proportional to the IWC (when the particle mass is proportional to the size squared) and is linked to any other moment via polynomial fits to the in-cloud temperature. Consequently, the only parameters required to obtain the PSD are the IWC and the in-cloud temperature.

Baran et al. (2011, 2014a,b) constructed a large database combining the ensemble model and the Field et al. (2005, 2007) parametrization. They used this parametrization to generate the PSD functions for a total number of 20622 in situ measurements of IWC and in-cloud temperature from different aircraft-based field campaigns located in the tropics and in the mid-latitudes. Subsequently, for each of these PSD functions the single scattering properties were calculated for 145 wavelengths between 0.2 and 120 μm.

Vidot et al. (2015) tested this ice optical property database and developed a new ice cloud parametrization that predicts the bulk absorption and scattering coefficients as well as the asymmetry parameter as a function of the in-cloud temperature and IWC. In this parametrization, no a priori information about the particle shape and the effective diameter of the ice crystals is required. The equations to calculate the parameters mentioned above are expressed as follows,

$$\begin{aligned}\log_{10}\left[\sigma_{\mathrm{abs},\lambda}(T,\mathrm{IWC})\right] &= A_{a,\lambda} + B_{a,\lambda}T + C_{a,\lambda}\log_{10}(\mathrm{IWC}) + D_{a,\lambda}T^2\\ &\quad + E_{a,\lambda}(\log_{10}(\mathrm{IWC}))^2 + F_{a,\lambda}T\log_{10}(\mathrm{IWC}),\\ \log_{10}\left[\sigma_{\mathrm{sca},\lambda}(T,\mathrm{IWC})\right] &= A_{s,\lambda} + B_{s,\lambda}T + C_{s,\lambda}\log_{10}(\mathrm{IWC}) + D_{s,\lambda}T^2\\ &\quad + E_{s,\lambda}(\log_{10}(\mathrm{IWC}))^2 + F_{s,\lambda}T\log_{10}(\mathrm{IWC}),\\ g_\lambda(T,\mathrm{IWC}) &= A_{g,\lambda} + B_{g,\lambda}T + C_{g,\lambda}\log_{10}(\mathrm{IWC}),\end{aligned} \tag{3.1}$$

where the set of parametrization coefficients for the absorption coefficient ($A_{a,\lambda}$ to $F_{a,\lambda}$), the scattering coefficient ($A_{s,\lambda}$ to $F_{s,\lambda}$) and the asymmetry parameter ($A_{g,\lambda}$ to $C_{g,\lambda}$) is obtained by using a non-linear least squares fitting procedure over the ensemble model optical property database described in Baran et al. (2014a).

The single scattering properties required in the algorithms developed during this thesis are the extinction coefficient, the single scattering albedo and the scattering phase function. As defined in Eq. 1.21, the extinction coefficient can be obtained from the sum of the scattering and absorption coefficients, and the single scattering albedo is the ratio of the scattering coefficient to the extinction coefficient (cf. Eq. 1.12). The scattering phase function is generated from the asymmetry parameter using the analytical phase function of Baran et al. (2001) which is a linear piecewise parametrization of the Henyey-Greenstein phase function (Henyey and Greenstein, 1941) depending only on the asymmetry parameter.

As mentioned above, atmospheric ice crystals are often distorted, roughened or contain inclusions of air bubbles or aerosols. These processes remove or reduce the optical features of the phase function such as the halos at 22 ° and 46 ° or the backscattering peak (e.g. Macke et al., 1996; Yang and Liou, 1998; C.-Labonnote et al., 2001). Thus, the analytical phase function is kept smooth and featureless. Figure 3.2 shows an example of the analytical phase function. Baran et al. (2001) demonstrated that it satisfyingly reproduces short-wave multi-angle satellite and

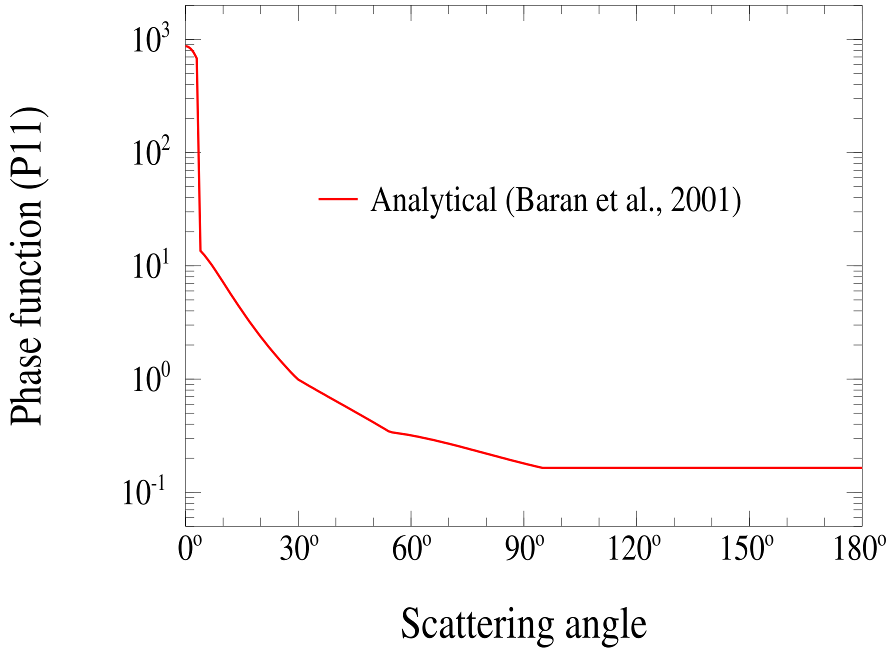

Figure 3.2: Example of the analytical phase function of Baran et al. (2001) (courtesy of L. C.-Labonnote).

aircraft observations and Baran and Francis (2004) showed a good agreement with high-resolution infrared observations between 3 and 18 μm. Furthermore, it has been shown to be in good agreement with the backscattering features observed from POLarization and Directionality of the Earth's Reflectances (POLDER,Deschamps et al. (1994)) measurements (Baran and Labonnote, 2007). The phase function, especially in the exact backscattering direction, is a crucial parameter in our methodology and will be discussed in more detail in Sect. 3.4.3.

To summarize, the ice cloud parametrization of Vidot et al. (2015) based on the ensemble model of Baran and Labonnote (2007) and Baran et al. (2014a) provides the link between the physical properties we seek to retrieve with our algorithms (IWC and hence the IWP), and the single scattering properties required for the forward modelling in the optimal estimation method which will be introduced theoretically in the next section. For the remainder of this thesis, the microphysical model described above will be referred to as BV2015 model (or parametrization).

3.2 Inversion Method: Optimal Estimation

Nowadays, methods based on optimal estimation theory (Rodgers, 1976, 1990, 2000) are a common approach for the inversion of remote sensing data. The work of Delanoë and Hogan (2008, 2010) or Sourdeval et al. (2015, 2016) could be cited here as examples for the retrieval of cloud properties from satellite data using such an approach. The GARRLiC (Lopatin et al., 2013) and LIRIC (Chaikovsky et al., 2016) algorithms are examples for the retrieval of aerosol properties. One advantage of the optimal estimation method is that it directly provides an estimation of the uncertainties together with the retrieved quantities. Furthermore, it allows to easily combine measurements of different instruments in a common retrieval framework as has been shown by all authors cited above. Hence, it is a well-adapted tool to retrieve physical properties of atmospheric parameters from instrument synergies.

This thesis aims to establish such a synergy of lidar and TIR radiometer measurements to retrieve properties of cirrus clouds. Thus, the inversion method we chose for the algorithms presented in the following sections is based on optimal estimation. In this section, we will introduce the theory of this approach before the application of this theoretical framework to each of the different measurement types alone, and finally the synergy of these measurements is presented in Sects. 3.3 to 3.6.

The general relation between the measurement vector $\vec{y}$ and the state vector $\vec{x}$ can be expressed by,

$$\vec{y} = \mathbf{F}(\vec{x}) + \vec{\epsilon}, \tag{3.2}$$

where $\vec{\epsilon}$ represents the uncertainties arising from the measurements and the forward model $\mathbf{F}$. The forward model is a physical model that describes the link between the state vector and the measurement vector. This connection has to be inverted in order to retrieve the elements of the state vector. During this inversion process, the information provided by the measurement vector is used.

Optimal estimation is based on a Bayesian approach to probability (Rodgers, 2000). The act of measurement can be understood as a mapping of the state vector into the measurement space where the forward model performs the mapping. The error $\vec{\epsilon}$ is only known statistically, hence a point in the state space maps into a region in the measurement space determined by the probability density function (pdf) of $\vec{\epsilon}$. The idea of the Bayesian approach is to start from some prior expectation about a quantity and then update the knowledge about this quantity in the light of new information. The incomplete knowledge about the state before the measurement can be quantified as a pdf over the state space ($P(\vec{x})$). Since the measurements are connected to experimental error, they cannot be considered to be perfect which means that they also have to be described by a pdf over the measurement space ($P(\vec{y})$). The Bayes' theorem describes the mapping of the measurement pdf into the state space and its link to prior knowledge. It is given by,

$$P(\vec{x}|\vec{y}) = \frac{P(\vec{y}|\vec{x})\,P(\vec{x})}{P(\vec{y})}, \tag{3.3}$$

where $P(\vec{y}|\vec{x})$ is the conditional pdf of $\vec{y}$ given $\vec{x}$. That means $P(\vec{y}|\vec{x})\,\mathrm{d}\vec{y}$ is the probability that $\vec{y}$ lies in the multidimensional volume $(\vec{y}, \vec{y} + \mathrm{d}\vec{y})$ for a given vector $\vec{x}$. $P(\vec{x}|\vec{y})$ describes the posterior pdf of the state vector when a measurement is given and provides the desired information to update the prior knowledge of the state because the new information contained in the measurement reduces the volume of possible posterior states in comparison to the prior volume of possible states. To summarize, the optimal estimation method seeks to reduce at maximum the number of possible states that are prior contained in the state space by using the information provided by the measurement. The size of the final volume of possible states gives an estimation about the uncertainty of the state vector.

One of the major hypotheses in optimal estimation theory is that the pdfs are considered to follow a Gaussian distribution (Rodgers, 2000). The pdf of the ensemble of possible states in the state space can be expressed by,

$$P(\vec{x}) = \frac{1}{(2\pi)^{n/2}|\mathbf{S}_a|^{1/2}} \exp\left\{-\frac{1}{2}(\,\vec{x} - \vec{x}_a\,)^T \mathbf{S}_a^{-1}(\,\vec{x} - \vec{x}_a\,)\right\}, \tag{3.4}$$

where $\vec{x}_a$ is the prior knowledge of the state vector (a priori) and $\mathbf{S}_a$ describes the variance-covariance matrix which represents the uncertainties of $\vec{x}_a$. The parameter n stands for the number of dimensions of the state space and corresponds to the number of parameters to be inverted. The pdf $P(\vec{y}|\vec{x})$ can be written in the same manner,

$$P(\vec{y}|\vec{x}) = \frac{1}{(2\pi)^{m/2}|\mathbf{S}_\epsilon|^{1/2}} \exp\left\{-\frac{1}{2}\left[\mathbf{F}(\vec{x}) - \vec{y}\right]^T \mathbf{S}_\epsilon^{-1}\left[\mathbf{F}(\vec{x}) - \vec{y}\right]\right\}, \tag{3.5}$$

where $\mathbf{S}_\epsilon$ is the variance-covariance matrix representing the errors of the measurement vector $\vec{y}$ and the forward model $\mathbf{F}$, and m is the number of dimensions of the measurement space. Finally, the pdf of the retrieved state vector $\hat{\vec{x}}$ for a given measurement vector $\vec{y}$ reads,

$$P(\vec{x}|\vec{y}) = \frac{1}{(2\pi)^{n/2}|\mathbf{S}_{\hat{x}}|^{1/2}} \exp\left\{-\frac{1}{2}(\,\vec{x} - \hat{\vec{x}}\,)^T \mathbf{S}_{\hat{x}}^{-1}(\,\vec{x} - \hat{\vec{x}}\,)\right\}, \tag{3.6}$$

where $\mathbf{S}_{\hat{x}}$ represents the variance-covariance matrix of the retrieved state vector.

The best estimation of the state vector corresponds to the state vector that maximizes the posterior pdf given in Eq. 3.3. It can be obtained by searching the minimum of the so-called cost function (Rodgers, 2000),

$$\Phi = [\,\vec{y} - \mathbf{F}(\vec{x})\,]^T \mathbf{S}_\epsilon^{-1} [\,\vec{y} - \mathbf{F}(\vec{x})\,] + [\,\vec{x} - \vec{x}_a\,]^T \mathbf{S}_a^{-1} [\,\vec{x} - \vec{x}_a\,]. \tag{3.7}$$

This cost function contains two contributions: the first term on the right-hand side of Eq. 3.7 represents the contribution arising from the forward model and the measurement, and the second term represents the contribution arising from the a priori. In our case, the retrieval should be independent of the a priori because there are no a priori information available about the cloud properties that will be retrieved with our algorithms. Thus, the second contribution of the cost function should be close to zero which can be easily obtained by assigning a sufficiently large error to the assumed a priori.

In order to find the best estimate of the state vector $\hat{\vec{x}}$ which minimizes the cost function Φ, the approach of Levenberg-Marquardt (Levenberg, 1944; Marquardt, 1963) is applied which is described in detail by Rodgers (2000). This iterative method is based on the Newton-Gauss method to which the parameter γ is added that regulates the size of each iteration step. The step size varies depending on the variation of the cost function. If Φ increases after the iteration step, γ is also increased and a new step which is smaller than the previous one is calculated. This process is repeated until Φ is reduced. On the contrary, if Φ decreases, γ is also decreased and the new state vector is accepted as the retrieval. The equation for this iteration is given by,

$$\vec{x}_{i+1} = \vec{x}_i + [(1+\gamma)\mathbf{S}_a^{-1} + \mathbf{K}_i^T \mathbf{S}_\epsilon^{-1} \mathbf{K}_i]^{-1} \{\mathbf{K}_i^T \mathbf{S}_\epsilon^{-1} [\vec{y} - \mathbf{F}(\vec{x}_i)] - \mathbf{S}_a^{-1} [\vec{x}_i - \vec{x}_a]\}, \tag{3.8}$$

where $\mathbf{K}$ is the Jacobian containing the sensitivities of each of the parameters of the state vector to each individual measurement. Sometimes, $\mathbf{K}$ is referred to as *Weighting Matrix* or *Kernel* because it acts as a matrix of weights in Eq. 3.8.

To test for convergence, the following test is applied,

$$[\,\vec{y} - \mathbf{F}(\hat{\vec{x}})\,]^T \mathbf{S}_\epsilon^{-1} [\,\vec{y} - \mathbf{F}(\hat{\vec{x}})\,] \ll m, \tag{3.9}$$

where m is the number of elements in the measurement vector. When this convergence test is true and convergence has been reached, the variance-covariance matrix of the retrieved state vector is given by,

$$\mathbf{S}_{\hat{x}} = (\mathbf{S}_a^{-1} + \mathbf{K}^T \mathbf{S}_\epsilon^{-1} \mathbf{K})^{-1}, \tag{3.10}$$

where $\mathbf{K}$ and $\mathbf{S}_\epsilon$ correspond to the last iteration step.

As explained above, the variance-covariance matrix $\mathbf{S}_\epsilon$ contains the error contributions of the measurement and the forward model. Hence, it can be decomposed as follows,

$$\mathbf{S}_\epsilon = \mathbf{S}_m + \mathbf{S}_f, \tag{3.11}$$

where $\mathbf{S}_m$ represents the variance-covariance matrix of the measurement, and $\mathbf{S}_f$ the variance-covariance matrix of the forward model. It should be noted that the exact calculation of the latter is given by,

$$\mathbf{S}_f = \mathbf{K}_b\,\mathbf{S}_b\,\mathbf{K}_b^T, \tag{3.12}$$

where $\mathbf{S}_b$ contains the variances for the elements of vector $\vec{b}$ which consists of the non-retrieved parameters used in the forward model. The matrix $\mathbf{K}_b$ represents the sensitivity of the forward model to each of these non-retrieved parameters. In the algorithms presented in the following sections, all variance-covariance matrices are assumed to be diagonal. This is often the case in operational algorithms since the calculation time for the matrix $\mathbf{K}_b$ can be quite long. It is justified in a first approximation because the only difference between assuming a diagonal variance-covariance matrix for $\mathbf{S}_f$ and performing an exact calculation after Eq. 3.12 is that the final error on the retrieved quantities changes slightly.

To summarize, the optimal estimation method provides a robust mathematical framework for the simultaneous inversion of remote sensing data from different sensors. Furthermore, it allows to precisely characterize the errors on the retrieved quantities (cf. Eq. 3.10) if the uncertainties connected with the forward model and the measurements are well-known. Hence, it is very important to characterize the measurement error as well as the errors on all non-retrieved parameters of the forward model as precisely as possible.

3.3 Retrieval of Ice Water Path from the Thermal Infrared Radiometer Measurements

This section focuses on the information about cirrus clouds that can be obtained from the passive TIR radiometer measurements. These measurements are sensitive to the optical and integrated properties of the cloud, for example the IWP.

During the past decades, measurements in the TIR wavelength region have been performed from space (e.g. MODIS aboard Terra and Aqua (King et al., 1992, 2003), HIRS aboard the NOAA polar satellites (Wylie et al., 1994), AIRS aboard Aqua (Chahine et al., 2006), IASI aboard Metop-A and Metop-B (Clerbaux et al., 2009), or the IIR aboard CALIPSO (Winker et al., 2003)), from aircraft (e.g. during the Field Radiation Experiment on Natural Cirrus and High-level clouds (FRENCH/DIRAC 2001) (Brogniez et al., 2004), or during the Cirrus Cloud Experiment (CIRCLE-2) and Biscay '08 campaigns (Sourdeval et al., 2012, 2013)), as well as from the ground (e.g. Platt, 1973; Sassen and Comstock, 2001; Blanchard et al., 2017).

A well-established method using radiances in the TIR wavelength region measured from satellites is the split window technique (Inoue, 1985, 1987; Wu, 1987; Parol et al., 1991). This method allows to retrieve the cloud top temperature and the effective emissivity of semi-transparent cirrus clouds from two channels centred around $11\,\mu$m and $12\,\mu$m, respectively. The above-cited authors showed that the brightness temperature difference (BTD) between these two channels depends on the cloud optical thickness as well as on the cloud microphysical properties, and that the BTD is always more important for thin cirrus clouds than for thick clouds or under clear sky conditions. In this context, Dubuisson et al. (2008) showed with the help of radiative transfer calculations performed for different ice crystal models that it is possible to retrieve microphysical properties of cirrus clouds from passive TIR radiometer measurements alone.

However, a common approach when retrieving cloud properties from TIR measurements while simultaneous lidar measurements are available is to use the information about the cloud altitude (and hence implicit the cloud temperature) provided by the lidar to improve the retrievals from the passive TIR measurements (e.g. Chiriaco et al., 2004; Garnier et al., 2012, 2013, 2015; Blanchard et al., 2017).

The algorithm presented in this section follows such an approach which means it integrates the information from the micropulse lidar to identify the time periods when cirrus clouds are present, and to obtain the cloud altitude as well as the cloud temperature information as described in Sect. 2.3.3. Nevertheless, it will be referred to as TIR only algorithm hereinafter to distinguish it from the synergy algorithm presented in Sect. 3.6.

As discussed in Sect. 3.2, all algorithms developed during this thesis are based on optimal estimation theory since this technique allows to easily combine different types of measurements in a common retrieval framework. The aim of this thesis is to develop a synergy between lidar and TIR measurements, meaning a simultaneous inversion of both kinds of observations to improve the retrievals of cirrus cloud properties in the sense that they are coherent with two independent sets of measurements.

The TIR only algorithm is the first step in the development process of this synergy. It was inspired by the multilayer algorithm of Sourdeval et al. (2015, 2016) which is also based on optimal estimation theory. The multilayer algorithm (Sourdeval et al., 2015, 2016) uses the three IIR channels centred at 8.65, 10.6 and 12.0 μm together with two MODIS (Aqua) channels, one in the visible (0.85 μm) and one in the near infrared (2.13 μm), to retrieve simultaneously the IWP of one ice cloud layer as well as the optical thickness and droplet effective radius of up to two liquid water cloud layers. The two MODIS channels are used to obtain information about the liquid cloud layers. In our case, we are focusing on cirrus clouds and for the retrieval of the IWP, measurements in the TIR wavelength region are sufficient. Hence, our TIR only algorithm retrieves the IWP from the measurements of the three channels of the TIR radiometer CLIMAT-AV introduced in Sect. 2.2.

3.3.1 Description of the Thermal Infrared Only Algorithm

In the following, the application of the optimal estimation framework described theoretically in Sect. 3.2 will be presented for the TIR only algorithm.

State Vector and Measurement Vector

As mentioned above, the TIR only algorithm seeks to retrieve the IWP of cirrus clouds. The IWP is a vertically integrated property (cf. Eq. 1.5) and as discussed in Sect. 1.3.1, the TIR radiometer measurements are sensitive to the integrated properties of the cloud. Figure 3.3 shows simulations of the bottom of atmosphere (BOA) radiances for the three TIR radiometer channels as a function of the IWP.

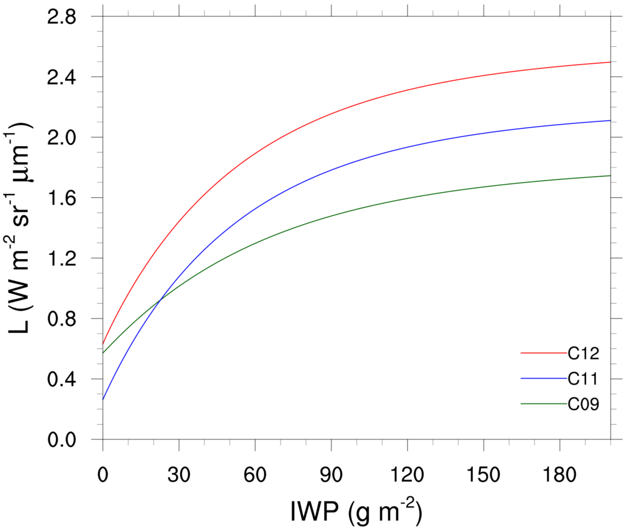

Figure 3.3: BOA radiances for the three TIR radiometer channels (C09 green, C11 blue and C12 red) simulated with LIDORT as function of IWP (assuming a constant IWC profile). The cirrus cloud is assumed to be situated between 9 and 10.5 km altitude and the atmospheric profiles of temperature, water vapour and ozone required in the simulations correspond to the ECMWF reanalysis profiles for November 30, 2016, 12 UTC.

These simulations have been performed with the radiative transfer model described in the next section. The atmospheric profiles considered in the simulations correspond to the reanalysis data of November 30, 2016, at 12 UTC and the BV2015 parametrization is used to obtain the optical properties of the cloud as described below. The cirrus cloud is assumed to be situated between 9 and 10.5 km altitude which represents approximately the altitude of the cirrus cloud measured during the second half of the case study which will be discussed in detail in the course of this chapter (cf. Fig. 3.4). Figure 3.3 shows that the TIR radiances of all channels increase with increasing IWP. This increase is rather strong for IWPs smaller than $60\,\mathrm{g\,m^{-2}}$ and shows a saturation effect for large IWPs. The increase of the radiances is stronger for channels C11 and C12 than for C09, indicating a larger sensitivity to the IWP of the former compared to the latter which could be expected from the TIR absorption. Furthermore, it follows from Fig. 3.3 that a set of three defined TIR radiances corresponds to a certain IWP which proofs that the IWP can be retrieved from these radiances.

As a consequence, the state vector $\vec{x}$ of the TIR only algorithm is defined by,

$$\vec{x} = (\mathrm{IWP}), \tag{3.13}$$

and the measurement vector $\vec{y}$ contains the measured radiances of the three TIR radiometer channels,

$$\vec{y} = (L_{\mathrm{C09}},\, L_{\mathrm{C11}},\, L_{\mathrm{C12}})^T\,. \tag{3.14}$$

Forward Model

The forward model **F** in the TIR only algorithm is given by the Linearized Discrete Ordinate Radiative Transfer model (LIDORT) (Spurr et al., 2001). The required inputs to simulate the TIR radiances with this model comprise atmospheric profiles of temperature, water vapour and ozone, surface parameters such as the surface emissivity and temperature, as well as optical properties of atmospheric particles, in our case the ice crystals in the cirrus cloud.

The vertical resolution of the radiative transfer calculations can be defined according to individual needs. Since the profiles of atmospheric temperature, water vapour and ozone are obtained from the ECMWF reanalysis described in Sect. 2.4.1, we use the 137 model levels of the reanalysis profiles as basis for the vertical grid. Inside the cloud, a finer vertical grid corresponding to the lidar resolution of 15 m is used. The cloud base and top altitudes are obtained from the cloud detection described in Sect. 2.3.3. The atmospheric profiles are then linearly interpolated between the model levels below the cloud base and above the cloud top altitude to obtain the atmospheric parameters on the 15 m vertical resolution corresponding to the lidar. Consequently, the number of layers and the vertical resolution of the radiative transfer calculations is variable and depends on the cloud base and top altitudes as well as on the vertical resolution of the ECMWF reanalysis profile.

The interpolation to the fine vertical lidar resolution inside the cirrus cloud has been integrated to prepare for the synergy algorithm described in Sect. 3.6. Due to the additional information from the lidar measurements, the radiative transfer calculations in the synergy algorithm can be performed taking into account the vertical profile of IWC as will be discussed in detail in Sect. 3.6. However, this information is not available from the TIR radiometer measurements alone. Hence, in the TIR only algorithm, the cloud is assumed to be homogeneous and the amount of ice is distributed equally over all layers inside the cloud. This means, the IWC is assumed to be constant with altitude which can be justified for ice clouds with a small IWP as has been demonstrated by Feofilov et al. (2015). The temperature on the other hand might vary since it is interpolated to the finer vertical grid between to reanalysis profile levels. The optical properties of the bulk ice are then calculated on this fine vertical grid layer by layer as functions of IWC and temperature with the BV2015 parametrization described in Sect. 3.1. The required single scattering properties for each layer are the extinction coefficient, the single scattering albedo and the phase function coefficient of the development in the Legendre polynomial.

Jacobian

The Jacobian **K** contains the variations of each of the components of the forward model resulting from variations of each of the components of the state vector,

$$\mathbf{K} = \begin{pmatrix} \frac{\partial L_{\mathrm{C09}}}{\partial(\mathrm{IWP})} \\ \frac{\partial L_{\mathrm{C11}}}{\partial(\mathrm{IWP})} \\ \frac{\partial L_{\mathrm{C12}}}{\partial(\mathrm{IWP})} \end{pmatrix}. \tag{3.15}$$

The advantage of LIDORT is that it provides not only radiances but also weighting functions for atmospheric or surface parameters from one single simulation. Hence, the derivatives with respect to IWP can be obtained directly from the radiative transfer calculations without the need to calculate finite differences. Therefore, the use of LIDORT results in a reasonable computation time of the algorithm although a fine vertical resolution is used.

In order to calculate the linearized output, the model not only requires the atmospheric parameter itself but also its linearization. In case of the sensitivities of the forward model with respect to IWP, the profile linearization with respect to the IWC is performed since the IWC is the parameter from which the optical properties are obtained for each layer with the BV2015 parametrization. The Jacobian with respect to IWP is linked to the Jacobians with respect to IWC via,

$$\frac{\partial L_i}{\partial(\mathrm{IWP})} = \frac{1}{\Delta R} \sum_{n=1}^{N_{\mathrm{ice}}} \frac{\partial L_i}{\partial(\mathrm{IWC}_n)}, \tag{3.16}$$

where N_{ice} is the number of ice layers and ΔR the vertical resolution of 15 m of the lidar which corresponds to the thickness of each layer of the fine vertical grid inside the cirrus cloud.

As mentioned above, the required optical properties to calculate the radiative transfer in the ice cloud layers are the extinction coefficient, the single scattering albedo and the phase function coefficient of the development in the Legendre polynomial. Hence, to calculate the profile of the Jacobian with respect to IWC, $\frac{\partial L_i}{\partial(\mathrm{IWC}_n)}$, the derivatives of the extinction coefficient, the single scattering albedo and the phase function coefficient of the development in the Legendre polynomial with respect to the IWC are required as inputs in LIDORT. A detailed explanation about how to calculate profiles of Jacobians is provided in the LIDORT User's Guide (Spurr, 2012).

Variance-Covariance Matrices

As discussed in Sect. 3.2, all variance-covariance matrices are assumed to be diagonal. The variance-covariance matrix of the a priori can be expressed as follows,

$$\mathbf{S}_a = (\sigma^2_{\mathrm{IWP}_a}), \tag{3.17}$$

where $\sigma^2_{\mathrm{IWP}_a}$ represents the variance of the IWP used as a priori (IWP$_a$). This a priori is used as a first guess from which the iteration is started. It is set to a value of $30\,\mathrm{g\,m^{-2}}$ corresponding to a realistic value for a mid-latitude cirrus. However, the error on the a priori has been chosen sufficiently large in order to obtain a retrieval that is independent of it, and has been quantified to 500 %.

The error variance-covariance matrix, $\mathbf{S}_\epsilon$, is composed of the variance-covariance matrix of the measurement, $\mathbf{S}_m$, and the variance-covariance matrix of the forward model $\mathbf{S}_f$ (cf. Eq. 3.12). $\mathbf{S}_m$ contains the errors on the measured radiances from the TIR radiometer in its three channels,

$$\mathbf{S}_m = \begin{pmatrix} \sigma^2_{L_{\mathrm{C09}}} & 0 & 0 \\ 0 & \sigma^2_{L_{\mathrm{C11}}} & 0 \\ 0 & 0 & \sigma^2_{L_{\mathrm{C12}}} \end{pmatrix}. \tag{3.18}$$

The measurement errors have been discussed in Sect. 2.2.2 and are obtained from Eq. 2.14 where $\sigma_{L_i} = \Delta L_i$.

The variance-covariance matrix of the forward model, $\mathbf{S}_f$, contains contributions for all parameters that are not inverted. We consider the following non-retrieved parameters (and the errors attributed to them): surface emissivity (2 %), surface temperature (1 K) and the profiles of atmospheric temperature (1 K for each layer), water vapour (10 % for each layer) and ozone (2 % for each layer). The standard deviations are calculated via,

$$\sigma_{b_j} = \frac{\partial \mathrm{F}}{\partial b_j} \cdot b_j \cdot \frac{p_{b_j}(\%)}{100}, \tag{3.19}$$

where b_j represents the considered non-retrieved parameter, $p_{b_j}(\%)$ its error in percent and $\frac{\partial \mathrm{F}}{\partial b_j}$ the sensitivity of the forward model to this parameter. Similarly to the

Jacobian with respect to IWC explained above, the latter can be calculated directly in LIDORT for all desired parameters (cf. LIDORT User's Guide (Spurr, 2012)). Finally, $\mathbf{S}_f$ is given by,

$$\mathbf{S}_f = \begin{pmatrix} \sum \sigma^2_{b_j,L_{\mathrm{C09}}} & 0 & 0 \\ 0 & \sum \sigma^2_{b_j,L_{\mathrm{C11}}} & 0 \\ 0 & 0 & \sum \sigma^2_{b_j,L_{\mathrm{C12}}} \end{pmatrix}. \tag{3.20}$$

3.3.2 Case Study Results of the Thermal Infrared Only Algorithm

As mentioned above, a case study has been selected to illustrate our methodology and all results shown in this chapter correspond to this case study. The cirrus cloud which will be analysed was observed on November 30, 2016, between 15 and 19 UTC. This day has been chosen because the TIR radiometer was calibrated in the beginning of November, 2016, and hence the TIR radiometer measurements are expected to be of good quality. Furthermore, the amount of water vapour in the atmosphere was small during this day which facilitates the retrieval of cloud properties since ground-based TIR radiometer measurements suffer from a high sensitivity to water vapour. This has been shown by Dubuisson et al. (2008) who found that the sensitivity of ground-based measurements in the TIR wavelength region to cloud properties is weaker for a moist atmosphere than for a dry atmosphere. On the contrary, the atmospheric temperature on November 30, 2016, was low and varied little around 0 °C during the day, resulting in a variation of the cavity temperature of the instrument during the measurement between 2.9 °C and 10.6 °C which is considerably colder than the cavity temperature during the calibration (24 °C for the calibration of November 2016, cf. Table 2.4). Thus, the temperature correction of the sensitivity of the TIR radiometer discussed in Sect. 2.2.2 has a very important influence on the processing of the measurements. For the temperature range of the cavity observed during this case study, the relative difference between the non-corrected and corrected radiances ranges between 20 % and 25 % for channels C12 and C09, and between 50 % and 55 % for channel C11. This large impact on channel C11 is due to the small radiances measured with this channel. Since the temperature correction is rather uncertain as discussed in Sect. 2.2.2, it results in a large measurement error, especially for channel C11. The measurement error for channel C11 ranges between 7 % and 10 %, depending on the difference between the actual cavity temperature during the measurement and the cavity temperature during calibration. For channels C09 and C12, the measurement error is smaller and takes values of 3 % to 4 %, and 4 % to 5 %, respectively.

Figure 3.4 shows the lidar and TIR radiometer measurements during the above-mentioned period. The lidar signal and the cloud detection are presented in Fig. 3.4 a. Obviously, the macrophysical properties of the observed cloud varied during the considered period. In the beginning, the cloud is geometrically thick with a cloud base altitude between 7 and 8 km. Between approximately 16.6 and 17.2 UTC, there appear to be two cloud layers. The cloud base of the lower layer is still situated in 7 to 8 km altitude but the geometrical thickness is much smaller. The lidar signal, however, is strong compared to the second half of the observed period between 17.2 and 18.5 UTC where a higher and optically thinner cirrus was present. The radiometer measurements shown in Figs. 3.4 b to 3.4 d are coherent with these observations since all three channels show a quite strong increase in the measured radiances at the beginning of the cloud phase where the lower and hence warmer cirrus was present. It is interesting to note that the increase of the radiances due to the cloud is stronger for channels C11 and C12 than for channel C09 which confirms the conclusion from the simulations shown in Fig. 3.3 that channel C09 is less sensitive to the IWP than channels C11 and C12. In the second half of the period, the signal in all three channels is considerably weaker due to the higher and optically thinner cloud. However, it should be noted that a second small increase in the measured radiances can be observed around 18.2 UTC which corresponds to a strong increase of the lidar signal at the same time. This illustrates the high sensitivity of our TIR radiometer to cloud properties.

Before the TIR only algorithm can be applied, it is necessary to verify if the TIR radiances measured under clear sky conditions are reproduced by the forward model. As mentioned in Sect. 2.4.1, the ECMWF reanalysis profile closest in time to the measurements is chosen to represent the atmospheric profile. Hence, for the case study introduced above, the reanalysis profile of 18 UTC was selected in a first step since the time period between 15 and 19 UTC is regarded. Figures 3.4 b to 3.4 d show not only the TIR radiometer measurements but also the according clear sky simulations performed with LIDORT for the three channels. The dashed line represents the simulation performed with the atmospheric temperature and gas profiles from the 18 UTC reanalysis. Between 15.5 and 15.8 UTC as well as after 18.8 UTC no clouds were present (cf. Fig. 3.4 a). Hence, the clear sky simulation should correspond to the measurements in these time intervals. It is obvious from Fig. 3.4 that this is not the case. The clear sky radiances simulated with the 18 UTC profile overestimate the measured radiances of all three TIR radiometer channels, particularly strong in case of channels C11 and C12. As a consequence, retrievals of the TIR only algorithm for the considered case study with the reanalysis profile of 18 UTC would lead to an underestimation of the IWP because the contribution of the cloud to the measured radiances would be underestimated.

Consequently, we tested if the clear sky simulations performed with the reanalysis profile of 12 UTC better represent the measured radiances. The results are shown as solid lines in Figs. 3.4 b to 3.4 d. In particular, the radiances measured under clear sky conditions with channel C11 are much better reproduced by the simulations with the reanalysis profile of 12 UTC. For channel C12, the simulations are also situated in the error range of the measurements. On the other hand, the simulations with the 12 UTC reanalysis profile underestimate the measured radiances of channel C09.

The quite different clear sky simulations for the two reanalysis profiles are mainly due to the different water vapour profiles. Figure 3.5 shows the profiles of temperature (Fig. 3.5 a) and specific humidity (Fig. 3.5 b) for 12 UTC (blue line) and 18 UTC (red line) from the reanalysis. The temperature profiles for the two time steps are quite similar, although the temperature in the lowest layer of the 18 UTC profile is 2 K colder than at 12 UTC (275 K compared to 277 K). However, this temperature difference alone does not explain the large differences in the simulated radiances. As expected from Dubuisson et al. (2008), a more important influence is arising from the water vapour profile. The specific humidity shown in Fig. 3.5 b shows a large variation between the two profiles in almost all altitudes up to 9 km. The total amount of water vapour in the atmospheric column is $0.976\,\mathrm{g\,cm^{-2}}$ at 18 UTC compared to $0.622\,\mathrm{g\,cm^{-2}}$ at 12 UTC. This strongly increased amount of water vapour is the main reason for the larger simulated radiances at 18 UTC. However, the measurements from the TIR radiometer do not reflect such a strong water vapour increase. This leads to the conclusion that the reanalysis profiles do not represent local water vapour variations exactly enough to precisely simulate the measured TIR radiances since the spatial and temporal resolutions of the reanalysis data are too coarse. Hence, the error on the water vapour profile in the optimal estimation method is the largest error amongst all errors on the non-retrieved parameters.

Nevertheless, we performed a retrieval for our case study with the reanalysis profile of 12 UTC and by only taking into account channels C11 and C12 because

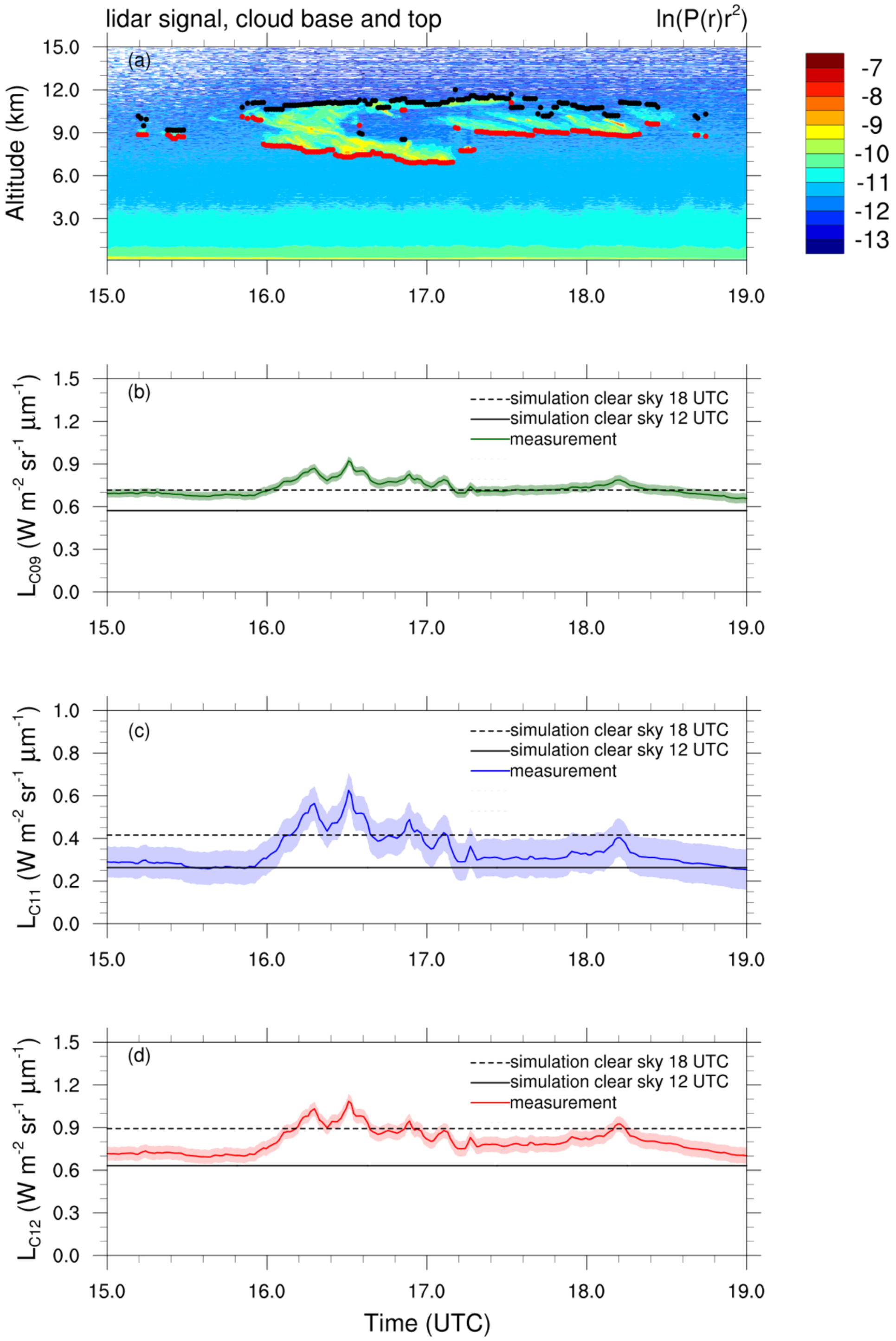

Figure 3.4: TIR radiometer measurements and clear sky simulations with the ECMWF reanalysis profiles of 12 UTC (solid lines) and 18 UTC (dashed lines) for November 30, 2016, 15 to 19 UTC. (a) Logarithm of the range-corrected lidar signal overlaid by the cloud detection, (b) radiance of channel C09, (c) radiance of channel C11, and (d) radiance of channel C12. The shaded zones in plots (b) to (d) represent the measurement error.

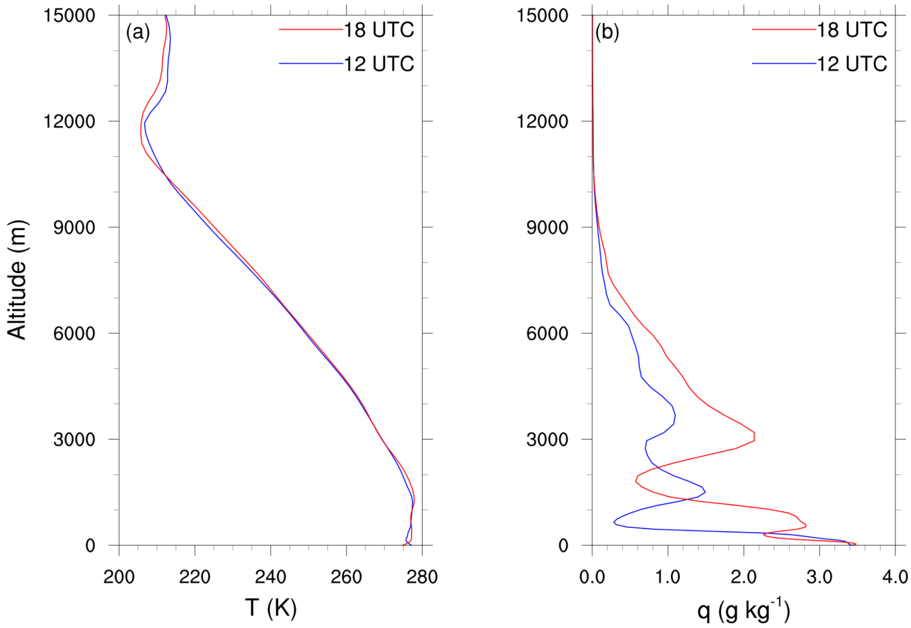

Figure 3.5: ECMWF reanalysis profiles of (a) temperature and (b) specific humidity at 12 UTC (blue) and 18 UTC (red) for November 30, 2016.

the measured clear sky radiances of these two channels are reproduced satisfyingly with the 12 UTC profile since the simulations are comprised within the error bars of the measurement. In fact, the use of two channels is sufficient to retrieve the IWP from the TIR radiometer measurements. Furthermore, before applying the TIR only algorithm, we always verify if the clear sky measurements are represented by the forward model. For all days analysed with this method (cf. Table 2.6), this convergence problem of channel C09 has been observed. As mentioned in Sect. 2.2.2, we believe that this is due to a bad characterization of the spectral filter function of this channel and consequently this channel is at present excluded from our retrievals.

The results for the case study considering channels C11 and C12 are shown in Fig. 3.6 where Fig. 3.6 a recalls the measured lidar signal overlaid by the cloud detection. Figure 3.6 b shows the retrieved IWP which is larger in the first half of the cloudy period between 16 and 17.2 UTC where the lidar signal is stronger as discussed above. The convergence of the algorithm is shown to be sufficient since the cost function (normalized by the size of the measurement vector) has been reduced successfully ($\Phi_{\mathrm{normalized}} \ll 1$, cf. Fig. 3.6 c) and the forward model after the last iteration step corresponds to the measurements of both channels considering the error ranges (Fig. 3.6 d).

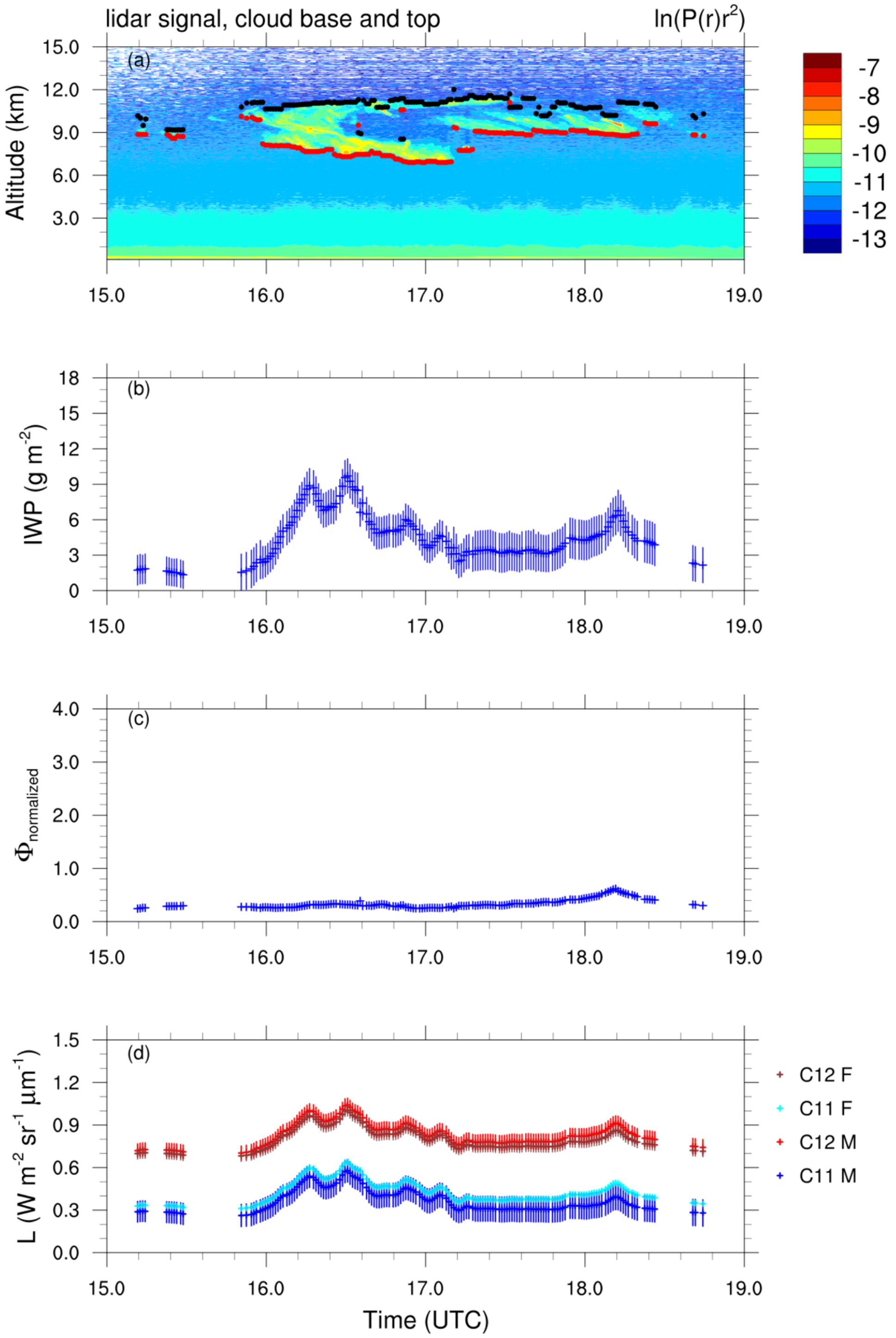

Figure 3.6: Retrieval results from the TIR only algorithm for November 30, 2016, 15 to 19 UTC. (a) Logarithm of the range-corrected lidar signal overlaid by the cloud detection, (b) retrieved IWP, (c) cost function normalized by the size of the measurement vector after the last iteration step, and (d) TIR radiometer measurements (C11 M and C12 M) and forward model after the last iteration step (C11 F and C12 F).

However, the TIR only algorithm uses the lidar measurements only to get an information about the cloud base and top altitudes as well as to define the time when cirrus clouds were present. Consequently, the cloud has to be assumed homogeneous with a constant IWC profile. This assumption is commonly applied in retrieval methods that use passive measurements. The profiles of backscattering by atmospheric particles obtained from the active lidar measurements, however, yield more information that can be used to obtain an idea about the vertical distribution of for example the IWC inside the cirrus cloud. The algorithm presented in the next section exploits this information.

3.4 Retrieval of Ice Water Content Profiles from the Lidar Measurements

The TIR only algorithm demonstrates the capability of passive TIR radiometer measurements to constrain integrated cirrus properties. It was developed to retrieve the IWP as a first step of our methodology. The cloud has been assumed to be homogeneous which means that the amount of ice was distributed equally over the whole cloud. As discussed in Sect. 1.3.1 (cf. Fig. 1.5), this assumption is not representative for real ice clouds. Lidar measurements provide vertical profiles of particle backscattering and the algorithm presented in this section, as a second step of our methodology, benefits from this vertical information resulting in the possibility to retrieve profiles of IWC.

Nowadays, active lidar measurements are performed from satellite (CALIPSO) and from the ground. Many studies exist in the literature which exploit these measurements to obtain information about cirrus cloud occurrence frequencies and their properties (examples are Berthier et al. (2008); Sassen et al. (2008); Campbell et al. (2015) for spaceborne studies, Ansmann et al. (1993); Keckhut et al. (2006); Giannakaki et al. (2007); Seifert et al. (2007); Liu et al. (2015) for ground-based studies, Pandit et al. (2015); Córdoba-Jabonero et al. (2017) for a combination of both, and many more could be cited here). These studies exploit different more or less developed lidar systems. Classical techniques to obtain the cloud optical thickness and the lidar ratio are the solutions to the lidar equation proposed by Klett (1981, 1985) (backward integration) and Fernald (1984) (forward integration), which have been applied by several authors (e.g. Sassen and Comstock, 2001; Giannakaki et al., 2007; Seifert et al., 2007).

As discussed above, our algorithm follows a different approach which is based on optimal estimation in order to facilitate afterwards the integration of the TIR radiometer measurements in a common retrieval framework. It closely follows the method described by Stephens et al. (2001), who developed an algorithm to retrieve extinction profiles of aerosols and clouds from spaceborne lidar measurements from the Lidar In-space Technology Experiment (LITE, Winker et al. (1996)). However, we are focusing on the application of this formalism to ground-based data from the micropulse lidar introduced in Sect. 2.3. In contrast to Stephens et al. (2001), the main purpose of our algorithm is to retrieve profiles of IWC in cirrus clouds. Nevertheless, we also retrieve a particle extinction for every layer of the profile that does not contain a cloud, although it should be noted that these retrievals are characterized by a large uncertainty due to strong assumptions for the backscatter-to-extinction ratio of aerosols. In the following sections, this lidar only algorithm will be described before the results for the case study of November 30, 2016, and the influence of the microphysical ice cloud model presented in Sect. 3.1 on the retrievals will be discussed.

3.4.1 Description of the Lidar Only Algorithm

Following the same strategy as for the TIR only algorithm described in Sect. 3.3.1, we will define in a first step the elements that are required in the optimal estimation method.

State Vector and Measurement Vector

The state vector $\vec{x}$ contains the desired quantities to be retrieved. In case of the lidar only algorithm, these are a profile of extinction (denoted by σ) outside the cirrus cloud and a profile of IWC inside the cloud,

$$\vec{x} = [\sigma(r_1), \sigma(r_2), \ldots, \sigma(r_{\text{j\_base-1}}), \text{IWC}(r_{\text{j\_base}}), \ldots, \text{IWC}(r_{\text{j\_top}}), \sigma(r_{\text{j\_top+1}}), \ldots, \sigma(r_{\text{N}})]^T, \tag{3.21}$$

where the subscripts j_base and j_top denote the range index of the base cloud layer and the top cloud layer, respectively. The measurement vector $\vec{y}$ consists of the measured lidar profile expressed as the logarithm of the calibrated range-corrected signal,

$$\vec{y} = [\ln(C \cdot P(r_1) r_1^2), \ln(C \cdot P(r_2) r_2^2), \ldots, \ln(C \cdot P(r_{\text{N}}) r_{\text{N}}^2)]^T, \tag{3.22}$$

where C reunites all factors related to the calibration into a single constant (cf. Eq. 3.23).

Figure 3.7 illustrates the measurement vector and the state vector. The measured signal is represented schematically by the red line and the equidistant black lines indicate the range resolution of the lidar system. As mentioned in Sect. 2.3.1, the measurements provide an information about the backscattering particles every 15 m and the same constant vertical resolution is used for the state vector.

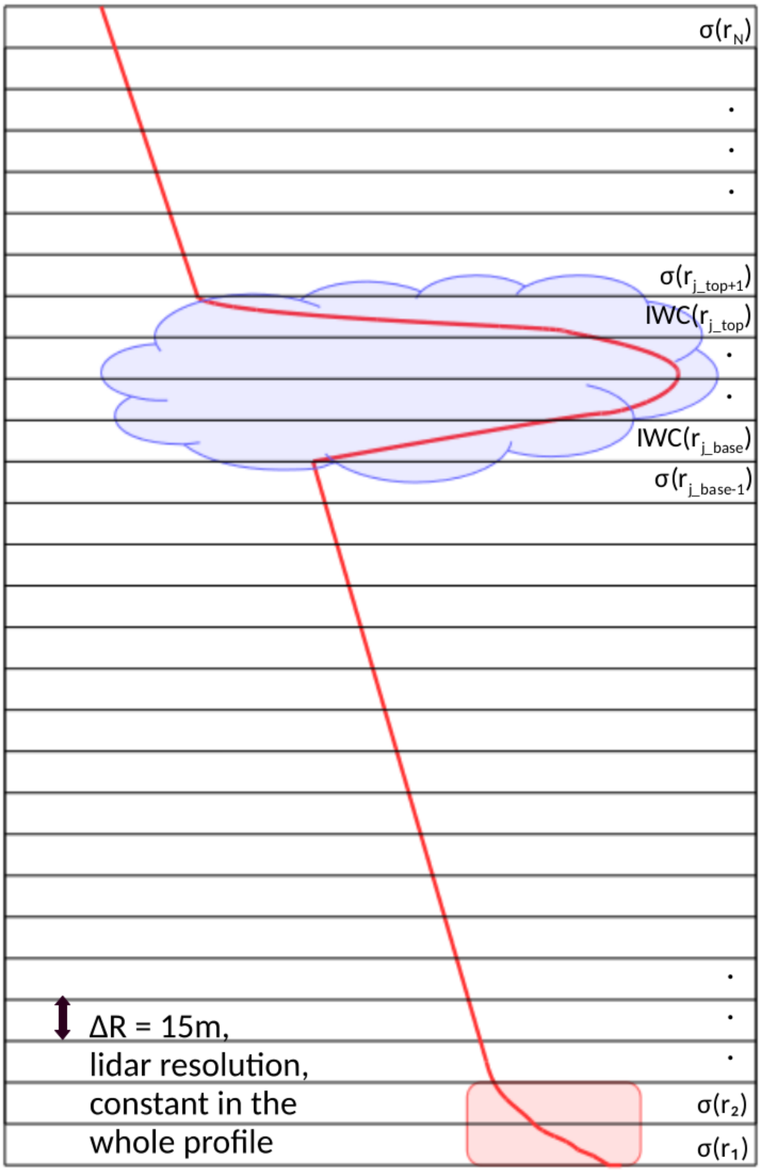

Figure 3.7: Illustration of the state vector $\vec{x}$ and the measurement vector $\vec{y}$ of the lidar only algorithm. The red line represents the lidar signal (measurement vector) and the horizontal black lines illustrate the measurement levels.

Forward Model

For the lidar retrieval problem, the forward model can be expressed by the lidar equation which has been presented in Sect. 2.3.2 and is recalled here in slightly different notation,

$$C \cdot P(r)\, r^2 = (\beta_{\mathrm{mol}}(r) + \beta(r)) \exp\left[-2 \int_0^r (\sigma_{\mathrm{mol}}(r') + \eta\sigma(r'))\, \mathrm{d}r'\right], \tag{3.23}$$

where C is the calibration constant mentioned above depending on the instrument's characteristics as well as the atmospheric conditions.

Expressing Eq. 3.23 logarithmically and in discretized form, leads to our forward model $\mathbf{F}$,

$$\mathrm{F}(x_j, b_j) = \ln(\beta_{\mathrm{mol}}(r_j) + k(r_j)\, \sigma(r_j)) - 2 \sum_{l=1}^{j} \left[\bar{\sigma}_{\mathrm{mol},l} + \eta\bar{\sigma}_l\right] \Delta R, \tag{3.24}$$

defined at each range r_j where $j = 2, ..., N$. The overline indicates layer mean values, e. g. $\bar{\sigma}_l = 0.5\,(\sigma_l + \sigma_{l-1})$, and ΔR represents the above-mentioned range resolution of 15 m of the lidar system. Vector $\vec{b}$ represents the non-retrieved parameters and is defined below (cf. Eqs. 3.31). Inside the cloud, the state vector $\vec{x}$ defined in Eq. 3.21 contains the IWC. Hence, the extinction $\sigma(r_j)$ required in Eq. 3.24 is calculated as a function of IWC, $\sigma(\mathrm{IWC}(r_j))$, for all r_j inside the cloud with the BV2015 parametrization for cirrus described in Sect. 3.1.

When regarding measurements from a simple micropulse lidar, assumptions are required for the so-called backscatter-to-extinction ratio because the lidar equation (cf. Eq. 3.23) contains two unknowns: backscattering and extinction. The intrinsic ambiguity between these two effects arises from the combination of scattering and absorption processes in the atmosphere. As has been carried out in Eq. 3.24, the backscattering coefficient of aerosol or cloud particles represented by $\beta(r)$ in Eq. 3.23 can be replaced by,

$$\beta(r) = k(r) \cdot \sigma(r), \tag{3.25}$$

where $k(r)$ represents the range-dependent backscatter-to-extinction ratio. Unfortunately, this parameter is highly variable and depends strongly on the type, size and shape of the atmospheric particles.

In this thesis, we are focusing on the retrieval of cirrus cloud properties. Thus, the backscatter-to-extinction coefficient for aerosols is assumed to be constant. Since our measurement site is located in an urban/industrial area, a lidar ratio of 66 sr has been used for aerosols in all retrievals for the case study shown in this chapter. This value corresponds to the WASO aerosol type from the OPAC database (Hess et al., 1998b) introduced in Sect. 2.4.2. However, this aerosol model does not necessarily represent the aerosols which were present during the measurement. Hence, we assigned a large error to this parameter in our optimal estimation algorithm. The influence of the aerosol model will be further discussed in Chapter 4 of this thesis.

The backscatter-to-extinction ratio for cirrus clouds is calculated using the definition of Mishchenko et al. (1997),

$$k = \varpi_0 \cdot p_{11}(\pi), \tag{3.26}$$

where ϖ_0 is the single scattering albedo of the bulk ice and $p_{11}(\pi)$ the normalized phase function in the exact backscattering direction. These two parameters are obtained for each cirrus cloud layer as functions of IWC and in-cloud temperature from the BV2015 parametrization. The phase function in the exact backscattering direction is a crucial parameter in our methodology and will be discussed in more detail in Sect. 3.4.3.

The multiple scattering factor, which is represented by η in Eq. 3.23, is set to unity for aerosol layers and in a first approximation to 0.75 for cirrus clouds. This value has been chosen based on the PhD thesis of Nohra (2016) who evaluated the multiple scattering factor of cirrus clouds by comparing the optical thickness retrieved from the micropulse lidar to the optical thickness retrieved from the spaceborne CALIOP lidar and adjusting η to find a coherent retrieval. The multiple scattering factor used for the CALIOP version 3 retrievals is $\eta = 0.6$ (Garnier et al., 2015). As discussed in Sect. 2.3.2, the multiple scattering effect for ground-based lidars is less important because they have a much smaller FOV in combination with a shorter distance to the cloud. Nevertheless, it should not be neglected because large ice crystals may considerably increase the forward scattering of the laser beam (Donovan and van Lammeren, 2001). All retrieval results for our case study shown in this chapter are performed for $\eta = 0.75$. However, similarly as for the backscatter-to-extinction ratio of aerosols, our knowledge of this parameter is rather poor. Thus, we assign a large error (25%) to it in the optimal estimation algorithm. A further discussion and sensitivity study of this parameter will be presented in Chapter 4 of this thesis.

Jacobian

The Jacobian contains the sensitivities of the forward model to each element of the state vector (Eq. 3.21),

$$\mathbf{K} = \begin{pmatrix}
\frac{\partial \mathrm{F}_1}{\partial \sigma_1} & \cdots & \frac{\partial \mathrm{F}_1}{\partial \sigma_{\mathrm{j\_base\text{-}1}}} & \frac{\partial \mathrm{F}_1}{\partial \mathrm{IWC}_{\mathrm{j\_base}}} & \cdots & \frac{\partial \mathrm{F}_1}{\partial \mathrm{IWC}_{\mathrm{j\_top}}} & \frac{\partial \mathrm{F}_1}{\partial \sigma_{\mathrm{j\_top+1}}} & \cdots & \frac{\partial \mathrm{F}_1}{\partial \sigma_{\mathrm{N}}} \\
\frac{\partial \mathrm{F}_2}{\partial \sigma_1} & \cdots & \frac{\partial \mathrm{F}_2}{\partial \sigma_{\mathrm{j\_base\text{-}1}}} & \frac{\partial \mathrm{F}_2}{\partial \mathrm{IWC}_{\mathrm{j\_base}}} & \cdots & \frac{\partial \mathrm{F}_2}{\partial \mathrm{IWC}_{\mathrm{j\_top}}} & \frac{\partial \mathrm{F}_2}{\partial \sigma_{\mathrm{j\_top+1}}} & \cdots & \frac{\partial \mathrm{F}_2}{\partial \sigma_{\mathrm{N}}} \\
\vdots & \cdots & \vdots & \vdots & \cdots & \vdots & \vdots & \cdots & \vdots \\
\frac{\partial \mathrm{F}_{\mathrm{j\_base\text{-}1}}}{\partial \sigma_1} & \cdots & \frac{\partial \mathrm{F}_{\mathrm{j\_base\text{-}1}}}{\partial \sigma_{\mathrm{j\_base\text{-}1}}} & \frac{\partial \mathrm{F}_{\mathrm{j\_base\text{-}1}}}{\partial \mathrm{IWC}_{\mathrm{j\_base}}} & \cdots & \frac{\partial \mathrm{F}_{\mathrm{j\_base\text{-}1}}}{\partial \mathrm{IWC}_{\mathrm{j\_top}}} & \frac{\partial \mathrm{F}_{\mathrm{j\_base\text{-}1}}}{\partial \sigma_{\mathrm{j\_top+1}}} & \cdots & \frac{\partial \mathrm{F}_{\mathrm{j\_base\text{-}1}}}{\partial \sigma_{\mathrm{N}}} \\
\frac{\partial \mathrm{F}_{\mathrm{j\_base}}}{\partial \sigma_1} & \cdots & \frac{\partial \mathrm{F}_{\mathrm{j\_base}}}{\partial \sigma_{\mathrm{j\_base\text{-}1}}} & \frac{\partial \mathrm{F}_{\mathrm{j\_base}}}{\partial \mathrm{IWC}_{\mathrm{j\_base}}} & \cdots & \frac{\partial \mathrm{F}_{\mathrm{j\_base}}}{\partial \mathrm{IWC}_{\mathrm{j\_top}}} & \frac{\partial \mathrm{F}_{\mathrm{j\_base}}}{\partial \sigma_{\mathrm{j\_top+1}}} & \cdots & \frac{\partial \mathrm{F}_{\mathrm{j\_base}}}{\partial \sigma_{\mathrm{N}}} \\
\vdots & \cdots & \vdots & \vdots & \cdots & \vdots & \vdots & \cdots & \vdots \\
\frac{\partial \mathrm{F}_{\mathrm{j\_top}}}{\partial \sigma_1} & \cdots & \frac{\partial \mathrm{F}_{\mathrm{j\_top}}}{\partial \sigma_{\mathrm{j\_base\text{-}1}}} & \frac{\partial \mathrm{F}_{\mathrm{j\_top}}}{\partial \mathrm{IWC}_{\mathrm{j\_base}}} & \cdots & \frac{\partial \mathrm{F}_{\mathrm{j\_top}}}{\partial \mathrm{IWC}_{\mathrm{j\_top}}} & \frac{\partial \mathrm{F}_{\mathrm{j\_top}}}{\partial \sigma_{\mathrm{j\_top+1}}} & \cdots & \frac{\partial \mathrm{F}_{\mathrm{j\_top}}}{\partial \sigma_{\mathrm{N}}} \\
\frac{\partial \mathrm{F}_{\mathrm{j\_top+1}}}{\partial \sigma_1} & \cdots & \frac{\partial \mathrm{F}_{\mathrm{j\_top+1}}}{\partial \sigma_{\mathrm{j\_base\text{-}1}}} & \frac{\partial \mathrm{F}_{\mathrm{j\_top+1}}}{\partial \mathrm{IWC}_{\mathrm{j\_base}}} & \cdots & \frac{\partial \mathrm{F}_{\mathrm{j\_top+1}}}{\partial \mathrm{IWC}_{\mathrm{j\_top}}} & \frac{\partial \mathrm{F}_{\mathrm{j\_top+1}}}{\partial \sigma_{\mathrm{j\_top+1}}} & \cdots & \frac{\partial \mathrm{F}_{\mathrm{j\_top+1}}}{\partial \sigma_{\mathrm{N}}} \\
\vdots & \cdots & \vdots & \vdots & \cdots & \vdots & \vdots & \cdots & \vdots \\
\frac{\partial \mathrm{F}_{\mathrm{N}}}{\partial \sigma_1} & \cdots & \frac{\partial \mathrm{F}_{\mathrm{N}}}{\partial \sigma_{\mathrm{j\_base\text{-}1}}} & \frac{\partial \mathrm{F}_{\mathrm{N}}}{\partial \mathrm{IWC}_{\mathrm{j\_base}}} & \cdots & \frac{\partial \mathrm{F}_{\mathrm{N}}}{\partial \mathrm{IWC}_{\mathrm{j\_top}}} & \frac{\partial \mathrm{F}_{\mathrm{N}}}{\partial \sigma_{\mathrm{j\_top+1}}} & \cdots & \frac{\partial \mathrm{F}_{\mathrm{N}}}{\partial \sigma_{\mathrm{N}}}
\end{pmatrix}, \tag{3.27}$$

where the terms $\mathrm{F}(x_j, b_j)$, $\sigma(r_j)$ and $\mathrm{IWC}(r_j)$ have been shortened to F_j, σ_j and IWC_j, respectively, to increase the readability. This short notation will be used for all variables which are a function of range for the remainder of this thesis.

In the case of ice cloud layers, the partial derivatives are expressed by,

$$K_{ij} = \frac{\partial \mathrm{F}_i}{\partial \mathrm{IWC}_j} = \frac{\partial \mathrm{F}_i}{\partial \sigma_j} \frac{\partial \sigma_j}{\partial \mathrm{IWC}_j}, \tag{3.28}$$

since the extinction is given as a function of IWC in the BV2015 parametrization. The partial derivatives with respect to IWC, $\frac{\partial \sigma_j}{\partial \mathrm{IWC}_j}$, are obtained directly by differentiating this parametrization (cf. Eqs. 3.1).

The partial derivatives with respect to extinction follow from the differentiation of Eq. 3.24 and are given by (Stephens et al., 2001),

$$K_{ij} = \begin{cases} 0 & \text{for } i < j \\ -2\eta\Delta R & \text{for } i > j \\ \frac{k_i}{\beta_{\mathrm{mol},i} + k_i\sigma_i} - 2\eta\Delta R & \text{for } i = j \end{cases} . \tag{3.29}$$

Variance-Covariance Matrices

Following Stephens et al. (2001) and as in case of the TIR only algorithm discussed above, all variance-covariance matrices are assumed to be diagonal. Hence, the variance-covariance matrix of the a priori can be represented by,

$$S_{a,ii} = \sigma^2_{a,i}, \tag{3.30}$$

where $\sigma^2_{a,i}$ are the variances of each of the elements of the a priori state vector. We chose sufficiently large values for these variances in order to reduce the contribution of the a priori information relative to the information contained in the measurement vector.

As mentioned above, vector $\vec{b}$ in Eq. 3.24 represents the non-retrieved parameters which are each a function of altitude,

$$\begin{aligned} b_1 &= \{\,\beta_{\mathrm{mol},j}\,; j = 1, \ldots, N\}, \\ b_2 &= \{\,k_j\,; j = 1, \ldots, N\}, \\ b_3 &= \{\,\eta_j\,; j = 1, \ldots, N\}. \end{aligned} \tag{3.31}$$

σ_{mol} does not need to be considered as a non-retrieved parameter because it can be obtained from β_{mol} by multiplication with the constant molecular backscatter-to-extinction ratio (cf. Eq. 2.16). The variance-covariance matrix of the forward model and the measurement is then defined by,

$$S_{\epsilon,ii} = \sigma^2_{y,i} + \sigma^2_{b1,i} + \sigma^2_{b2,i} + \sigma^2_{b3,i}, \tag{3.32}$$

where $\sigma_{y,i}$ represents the measurement error. The errors on the non-retrieved parameters are represented by $\sigma_{b1,i}$, $\sigma_{b2,i}$ and $\sigma_{b3,i}$, and can be calculated via,

$$\begin{aligned} \sigma_{b1,i} &= \frac{p_\beta(\%) \cdot \beta_{\mathrm{mol},i}}{\beta_{\mathrm{mol},i} + k_i\,\sigma_i}, \\ \sigma_{b2,i} &= \frac{p_k(\%) \cdot k_i\,\sigma_i}{\beta_{\mathrm{mol},i} + k_i\,\sigma_i}, \\ \sigma_{b3,i} &= p_\eta(\%) \cdot (-2\,\eta\,\sigma_i\,\Delta R), \end{aligned} \tag{3.33}$$

where $p_\beta(\%)$, $p_k(\%)$ and $p_\eta(\%)$ represent the percentage errors assumed for the molecular backscattering profile, the backscatter-to-extinction ratio and the multiple scattering factor, respectively.

As discussed above, the error on the multiple scattering factor for ice clouds is chosen to be large and is set to $p_\eta(\%)$=25%. Similarly, the backscatter-to-extinction ratio for aerosols is poorly known and has been quantified to $p_{k,\mathrm{aer}}(\%)$=25%. The same error has also been attributed to the backscatter-to-extinction ratio for ice clouds since the knowledge of the phase function in the exact backscattering direction used in Eq. 3.26 is also rather poor ($p_{k,\mathrm{ice}}(\%)$=25%). The phase function in backscattering direction will be discussed in detail below since it is an important parameter in our methodology. The error attributed to the molecular backscattering profile obtained from the empiric equation of Flamant (2008) (cf. Eq. 2.16) and by using the atmospheric temperature and pressure profiles from ECMWF reanalysis, is set to $p_\beta(\%)$=2%. As discussed in Sect. 2.3.3, the error on the lidar measurements depends on the altitude because the measurement noise increases with increasing altitude. As illustrated in Fig. 2.12, it is calculated as standard deviation around the mean over a vertically sliding window of 20 gates.

3.4.2 Case Study Results of the Lidar Only Algorithm

This section focuses on the application of the lidar only algorithm described above. In a first step, the calibration of the lidar signal is explained before the retrievals for the case study of November 30, 2016, are shown.

Calibration of the Lidar Signal

Before the algorithm can be applied to a measured lidar profile, the measurement needs to be calibrated since it depends not only on instrument characteristics but also on the atmospheric temperature and pressure profiles. Our calibration method follows the approach of Stephens et al. (2001). They propose to select a reference zone where the signal is assumed to be purely molecular and match this portion of the profile to the theoretical molecular signal. The lidar equation for the molecular signal reads (cf. Eqs. 2.15 and 3.23),

$$\mathrm{C}' \cdot P(r) r^2 = \beta_{\mathrm{mol}}(r) \cdot \exp\left[-2 \int_0^r \sigma_{\mathrm{mol}}(r')\,\mathrm{d}r'\right]. \tag{3.34}$$

Thus, the calibration constant C′ can be obtained by plotting the molecular signal against the measured signal and fitting a straight line to it. C′ is then given by the slope of this straight line. Figure 3.8 shows an example of such a calibration. To find the molecular reference zone we proceed as follows: in a first step, the zone between 4000 m altitude until 500 m below the detected cloud base altitude is chosen as reference zone because it is likely that there are no or very few particles in this

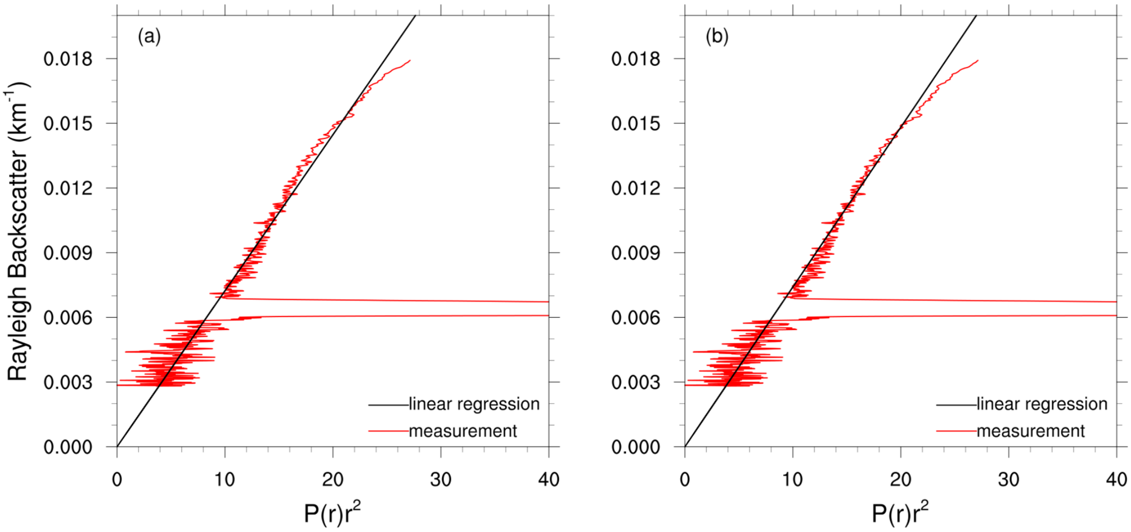

Figure 3.8: Example of the calibration of the lidar signal for the profile measured on November 30, 2016, at 18.18 UTC. (a) Starting reference zone from 4000 m to 500 m below the cloud base. (b) Adjusted reference zone from 5325 m to 5625 m.

zone since the aerosols are usually located in the boundary layer. As illustrated in Fig. 3.8 a, a linear regression of the theoretical molecular signal against the measured signal is performed for this starting reference zone. If there are altitudes where the difference between the regression line and the molecular signal is negative, the molecular signal has been overestimated. Hence, we search for the largest negative deviation from the regression line which corresponds to the minimum of the lidar signal. The according altitude plus ten gates below and ten gates above this altitude (hence a zone of 300 m in total) is then considered to be zone where the particle concentration is minimal and the signal purely molecular. As illustrated in Fig. 3.8 b, the linear regression is repeated for this zone and the slope of this line represents the calibration constant C'. It should be noted here that an automatic search for the minimum of the signal is challenging and that this procedure may still slightly overestimate the value of C' for some individual profiles.

However, this approach works well for satellite data when the first layers seen by the lidar are purely molecular layers. When this method is applied to ground-based data, the calibration factor is biased because of the extinction by aerosols in the boundary layer. The lidar equation between the beginning of the molecular reference zone at range r_0 and another range r also situated in this reference zone is given by,

$$\begin{aligned} \mathrm{C} \cdot P(r)r^2 &= \beta_{\mathrm{mol}}(r) \cdot \exp\left[-2\int_0^{r_0} (\sigma_{\mathrm{mol}}(r') + \sigma(r'))\,\mathrm{d}r'\right] \cdot \exp\left[-2\int_{r_0}^{r} \sigma_{\mathrm{mol}}(r')\,\mathrm{d}r'\right] \\ &= \beta_{\mathrm{mol}}(r) \cdot \exp\left[-2\int_0^{r} \sigma_{\mathrm{mol}}(r')\,\mathrm{d}r'\right] \cdot \exp\left[-2\int_0^{r_0} \sigma(r')\,\mathrm{d}r'\right] \\ &= \beta_{\mathrm{mol}}(r) \cdot T^2_{\mathrm{mol}}(r) \cdot T^2_{\sigma}(r_0), \end{aligned} \tag{3.35}$$

where $T^2_{\mathrm{mol}}(r)$ represents the molecular transmission of the layers between the ground and the current range r, and $T^2_{\sigma}(r_0)$ represents the particle transmission between the ground and the bottom altitude of the reference zone r_0. It should be noted that the multiple scattering factor has been omitted in Eq. 3.35 because it is set to unity for aerosols. Since we assume that there are no particles present in the reference zone, $T^2_{\sigma}(r_0)$ is constant in this zone. By comparing Eqs. 3.35 and 3.34, it follows,

$$\mathrm{C} = \mathrm{C'} \cdot T^2_{\sigma}(r_0). \tag{3.36}$$

However, the lidar signal used in the retrieval algorithm is calibrated with C' because the aerosol extinction in the boundary layer changes during the iteration. Hence, the aerosol transmission below the reference zone has to be taken into account in the lidar equation,

$$\mathrm{C}' \cdot P(r)r^2 = \frac{1}{T^2_{\sigma}(r_0)} \cdot (\beta_{\mathrm{mol}}(r) + \beta(r)) \cdot T^2_{\mathrm{mol}}(r) \cdot T^2_{\sigma}(r), \tag{3.37}$$

which means a summand equal to $\ln\left(\frac{1}{T^2_{\sigma}(r_0)}\right)$ has to be added to the forward model given by Eq. 3.24.

Retrieval Results

To start the iteration, a first guess is required and as in the TIR only algorithm, we chose the a priori to be the first guess. Following Stephens et al. (2001), the a priori for the layers close to the ground where aerosols are present is calculated from a one step solution of the lidar equation in order to reach faster convergence of the algorithm,

$$\sigma_{a,i} = \left\{\exp\left[y_i + 2\sum_{l=1}^{i-1}(\sigma_{\mathrm{mol},l} + \sigma_{a,l})\Delta R\right] - \beta_{\mathrm{mol},i}\right\}/k_i, \tag{3.38}$$

where the multiple scattering factor is omitted because it is equal to unity for aerosols. For the layers above the boundary layer the molecular extinction is used as a priori, and for ice cloud layers we start the iteration from a small IWC of $0.001\,\mathrm{g\,m^{-3}}$.

Figure 3.9 presents an example of a measured lidar profile (represented by the red lines in Figs. 3.9 a and b) which contains a cirrus cloud in altitudes between 8865 and 10200 m (indicated by the horizontal blue lines). The profile was measured on November 30, 2016, at 18.18 UTC. The black lines show the calculated forward model, in Fig. 3.9 a for the a priori and in Fig. 3.9 b when convergence is reached. The forward model of the a priori is already close to the measurement for the layers close to the ground because the a priori for these layers has been pre-calculated based on the lidar equation (cf. Eq. 3.38). For the higher layers where no or very few particles are present, the measured signal is also close to the a priori forward model since the molecular extinction has been chosen as a priori for these layers. Inside the cloud, the increase of the a priori forward model corresponds to the small IWC assumed to be constant over the cloud from which the iteration is started. After the last iteration step, the forward model and the measured lidar signal overlay each other almost perfectly indicating that the retrieval was successful and that the cost function has been reduced by reducing the difference between the measurement and the forward model. The relative difference between the measurement and the forward model after the last iteration step shown in Fig. 3.9 c is smaller than 1 % over the whole profile confirming the good convergence.

Figure 3.10 shows the corresponding retrieved IWC (Fig. 3.10 a) and extinction (Fig. 3.10 b) profiles. As explained in Sect. 3.4.1, the IWC is retrieved for cirrus cloud layers and the particle extinction for the rest of the profile. Thus, the extinction profile inside the cloud shown in Fig. 3.10 b is not retrieved directly but recalculated from the IWC using the BV2015 parametrization. The layers close to the ground show an enhanced extinction due to aerosols, even though it remains rather small since only few aerosols seemed to be present during this day. In the middle portion of the profile, the particle extinction is very close to zero indicating that there were almost no particles present in this zone. Due to the ice crystals inside the cirrus cloud, the extinction is increased importantly for the layers corresponding to the cloud.

The retrieval results for the case study of November 30, 2016, 15 to 19 UTC, are presented in Fig. 3.11. The vertical black lines in all plots of this panel indicate the profiles measured at 16.33 UTC and 18.18 UTC which will be discussed in detail in the course of this chapter. Figure 3.11 a recalls the measured lidar signal

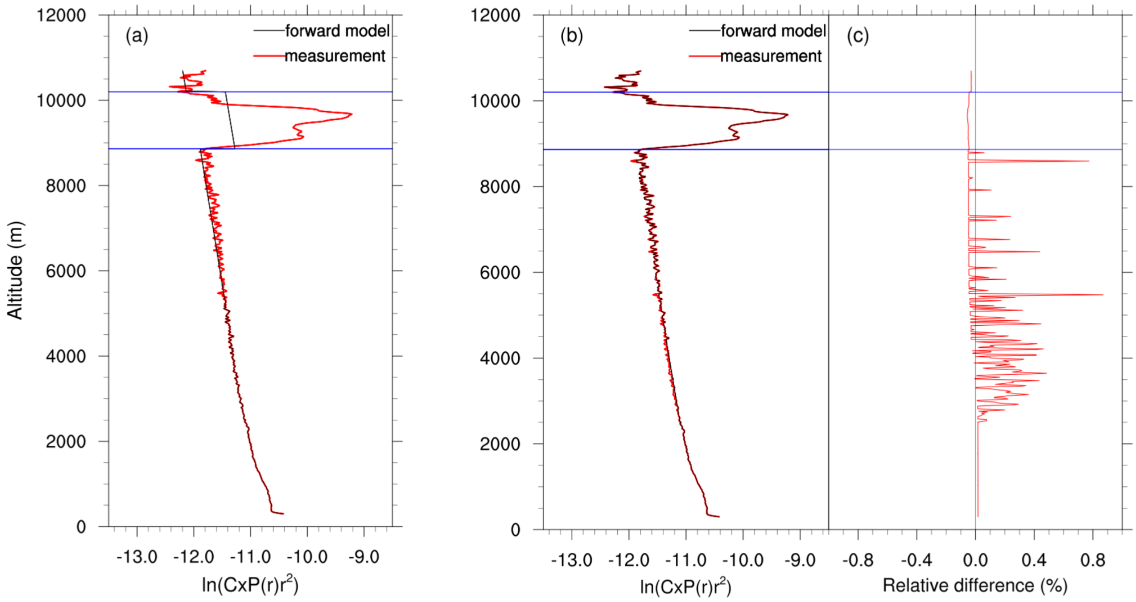

Figure 3.9: Forward model of the lidar only algorithm of the (a) a priori and (b) after the last iteration step (black lines) for the profile measured on November 30, 2016 at 18.18 UTC (the red lines represent the measurement, the horizontal blue lines indicate the defined cloud base and top altitudes (8865 m and 10200 m, respectively)). (c) Relative difference between the measurement and the forward model after the last iteration step.

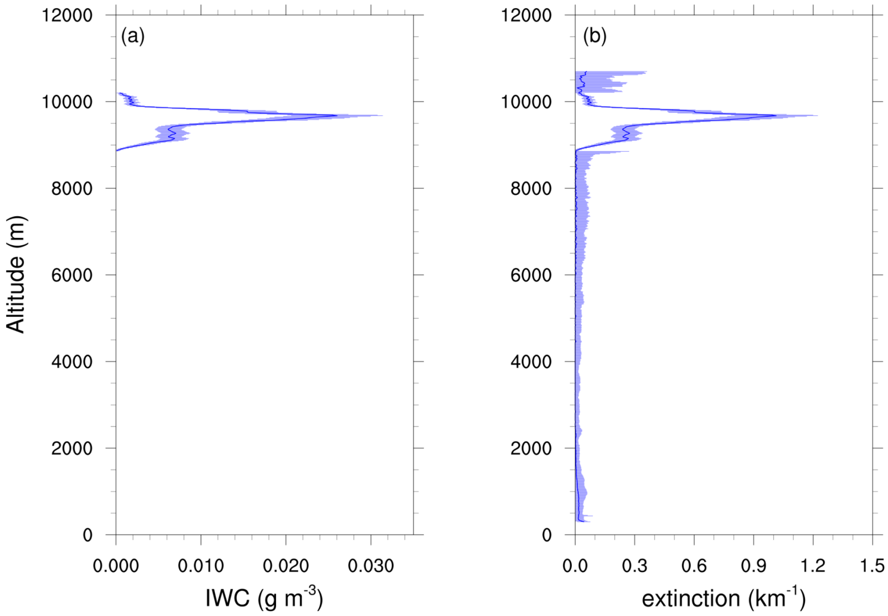

Figure 3.10: (a) Retrieved IWC and (b) extinction profiles from the lidar only algorithm for the profile measured on November 30, 2016 at 18.18 UTC (cf. Fig. 3.9). Shaded areas represent the error on the retrieved parameters. The cloud optical thickness obtained from the retrieved extinction profile is 0.402 ± 0.096 compared to 0.267 ± 0.126 from the transmission method (assuming $\eta = 0.75$).

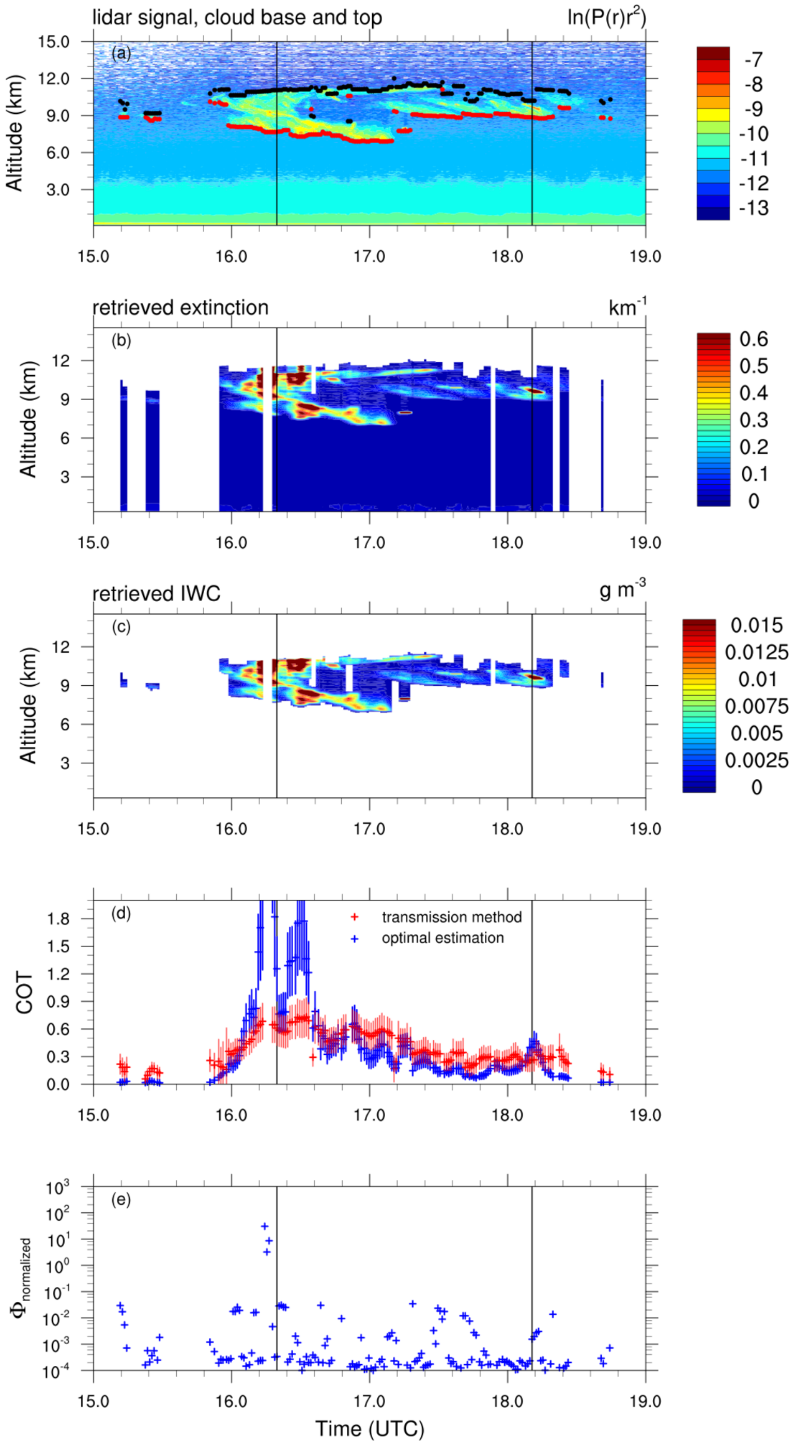

Figure 3.11: Retrieval results from the lidar only algorithm for November 30, 2016, 15 to 19 UTC. (a) Logarithm of the range-corrected lidar signal overlaid by the cloud detection, (b) retrieved extinction profiles, (c) retrieved IWC profiles, (d) cloud optical thickness from the lidar only algorithm (blue) and the transmission method introduced in Sect. 2.3.3 (red), and (e) cost function after the last iteration step normalized by the measurement vector. The vertical black lines represent the two example profiles measured at 16.33 and 18.18 UTC.

overlaid by the cloud detection described in Sect. 2.3.3. The retrieved extinction profiles are shown in Fig. 3.11 b which are recalculated in the cirrus cloud from the retrieved IWC (shown in 3.11 c) with the BV2015 parametrization. All retrievals are performed up to a maximum altitude corresponding to the retrieved cloud top altitude plus 500 m. However, since the detection of the cloud top is rather uncertain and since the noise of the lidar measurements increases with altitude as has been discussed in Sect. 2.3.3, the retrievals of extinction for the layers above the cloud are associated with large errors (cf. Fig. 3.10 b). Figure 3.11 d shows the cloud optical thickness (COT) at the visible lidar wavelength calculated from the extinction profiles derived from the retrievals of our algorithm (blue) in comparison to the COT obtained from the transmission method of Young (1995) explained in Sect. 2.3.3 (red). Between approximately 16.6 and 18.2 UTC, the COT from both methods compares quite well. However, the cirrus cloud observed during this period is optically and geometrically thin. In the beginning of the cloudy period where the cloud was geometrically and optically thicker, the COT obtained from our optimal estimation algorithm is considerably larger than the COT retrieved from the transmission method. Furthermore, the lidar only algorithm did not converge for some profiles during this phase. The cost function (normalized by the size of the measurement vector) after the retrieval is presented in Fig. 3.11 e. For some profiles around 16.25 UTC, the value of the normalized cost function after the iteration remains large ($\Phi_{\text{normalized}} \gg 1$) and consequently, the corresponding retrieval results are not considered in Figs. 3.11 b to 3.11 d. However, for the majority of profiles a good convergence is obtained ($\Phi_{\text{normalized}} \ll 1$).

Figure 3.12 presents a comparison of the retrieved IWP from the lidar only algorithm and the TIR only algorithm. The IWP obtained from the former is significantly larger than the IWP obtained from the latter for the optically and geometrically thicker cloud in the beginning of the considered period. For the optically thin cloud between 17.2 and 18.3 UTC, the retrieved IWP from both algorithm compares quite well. However, the incoherences between the retrievals obtained from both algorithms are connected with an insufficient knowledge about the backscatter-to-extinction ratio as will be discussed in the following.

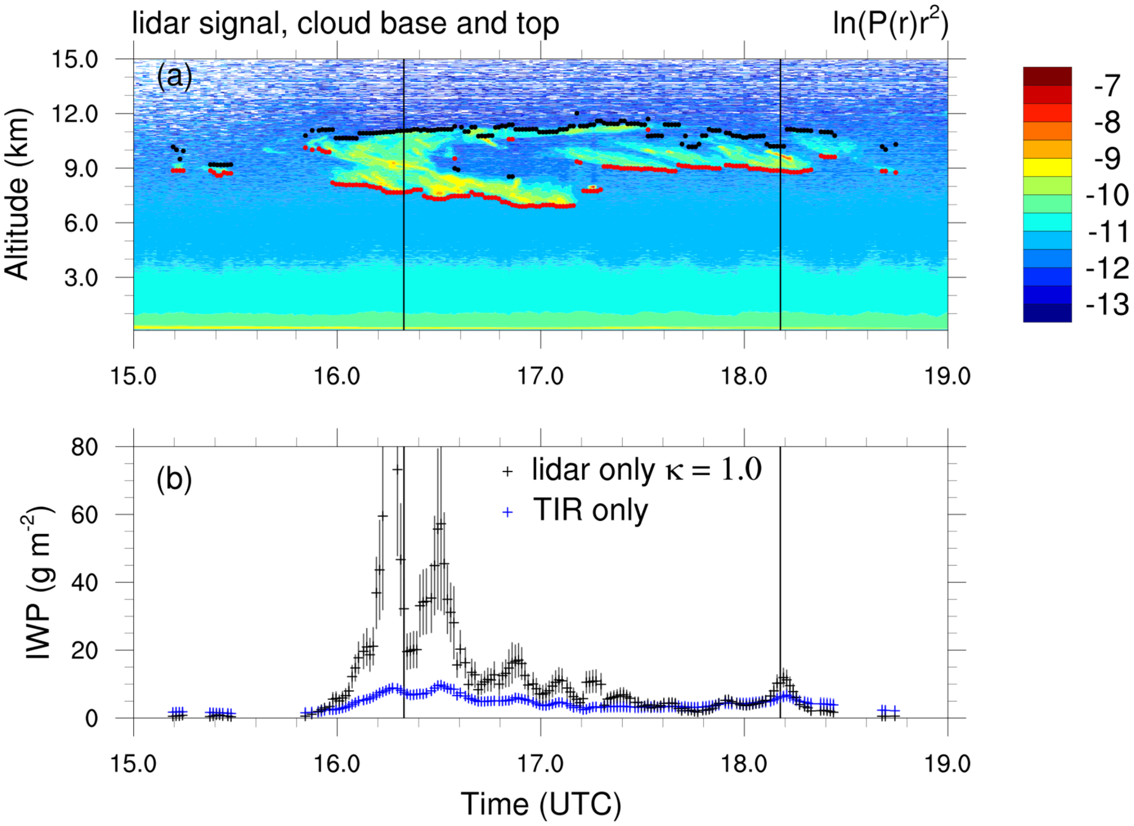

Figure 3.12: Comparison of the retrieval results from the TIR only algorithm and the lidar only algorithm for November 30, 2016, 15 to 19 UTC. (a) Logarithm of the range-corrected lidar signal overlaid by the cloud detection, and (b) retrieved IWP where the blue colour represents the TIR only algorithm and the black colour the lidar only algorithm. The vertical black lines represent the two example profiles measured at 16.33 and 18.18 UTC.

3.4.3 Influence of the Backscatter-to-Extinction Ratio in the Lidar Only Algorithm

As explained in Sect. 3.4.1, the backscatter-to-extinction ratio for cirrus clouds is calculated as the product of the single scattering albedo, ϖ_0, and the normalized phase function in the exact backscattering direction, $p_{11}(\pi)$, following the definition of Mishchenko et al. (1997) (cf. Eq. 3.26). Consequently, the retrievals from the lidar only algorithm strongly depend on these two parameters. The single scattering albedo and the phase function are obtained from the BV2015 parametrization. The former is considered to be represented sufficiently exact in this model, the latter on the other hand is much more uncertain, especially in the exact backscattering direction.

Figure 3.13 shows examples of phase functions for ice crystals calculated from the BV2015 parametrization and the ensemble model of Baran and Labonnote (2007) introduced in Sect. 3.1, assuming a thin cirrus cloud with a small IWC. The features of the phase function strongly depend on the characteristics of the considered ice crystals as discussed in Sect. 1.3.2 (cf. Fig. 1.6). Figure 3.13 draws special attention to particle heterogeneity arising from a roughened surface of the crystal and/or from spherical inclusions (Hess et al., 1998a; C.-Labonnote et al., 2001; Baran and Labonnote, 2006; Baran, 2007). In our case, particularly the representation of the exact backscattering direction (zoom in Fig. 3.13) is important since it is used in the definition of the backscatter-to-extinction ratio. The existence of a backscattering peak strongly depends on the heterogeneity of the considered particles. The black line represents the phase function obtained from the ensemble model for a bulk ice of particles with a smooth surface and without any other heterogeneities. In this case, the phase function shows a strong increase in backscattering direction. This backscattering peak disappears when the particles of the same bulk ice are considered to dispose of heterogeneities such as surface roughness or spherical inclusions, as illustrated by the blue and green lines in Fig. 3.13 which represent phase functions computed from the same model and bulk ice but by considering moderately and severely heterogeneous particles, respectively.

However, as discussed in Sect. 1.3.1, real cirrus clouds formed under atmospheric conditions are composed of a mixture of ice crystals comprising very different characteristics, including different shapes, sizes and degrees of heterogeneity. Their phase functions in the exact backscattering direction have not yet been characterized accu-

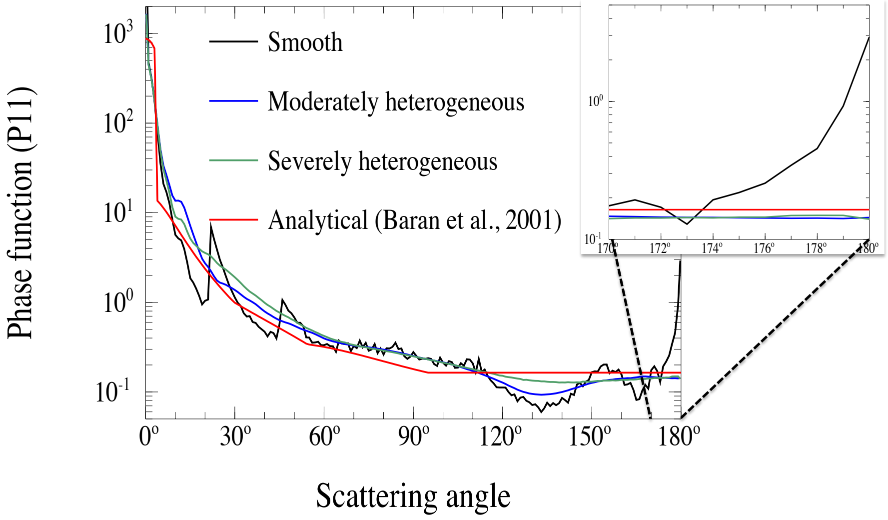

Figure 3.13: Examples of phase functions for different degrees of particle heterogeneity. Black line: phase function for bulk ice crystals with a smooth surface, blue line: introduction of some heterogeneity, green line: maximum degree of heterogeneity (particle roughness, air bubbles). The red line represents the phase function obtained from the parametrization of Baran et al. (2001) (courtesy of L. C.-Labonnote).

rately enough. Furthermore, it is not possible to perform exact calculations of phase functions in operational retrieval algorithms because they are numerically expensive. Hence, assumptions on the phase function have to be introduced.

As described in Sect. 3.1, we obtain the asymmetry parameter from the BV2015 parametrization and from this asymmetry parameter the analytical phase function of Baran et al. (2001) is generated which is used in our algorithm to represent the phase function of the bulk ice crystals in the observed cirrus clouds. This parametrization is represented by the red line in Fig. 3.13. As discussed in Sect. 3.1, it is kept smooth and featureless in order to represent particles that are roughened, distorted or contain inclusions of air bubbles or aerosols. Hence, the analytical phase function does not include a backscattering peak and assumes a constant value for scattering angles larger than 95 °. However, Zhou and Yang (2015) as well as Ding et al. (2016) showed recently that this assumption is not sufficient to realistically represent the phase functions of atmospheric ice crystals. They found that a narrow backscattering peak also exists for ice particles with rough surfaces, even in case of a high degree of heterogeneity. According to these authors, the backscattering of ice crystals is generally underestimated. Zhou and Yang (2015) showed that the value of the phase function of real bulk ice crystals at 180 ° should be 1.5 to 2.0 times larger than the value of the phase function at 175°. This is obviously not the case for the analytical phase function integrated in our algorithm.

Therefore, we tested the influence of their findings on our algorithm since they have a direct impact on the backscatter-to-extinction ratio and hence on our retrievals. The results of this test are shown in Fig. 3.14 for two example profiles measured on November 30, 2016, at 16.33 UTC (Fig. 3.14 a) and 18.18 UTC (Fig. 3.14 b, cf. also Fig. 3.10). Figure 3.14 shows the retrieved IWC profiles for different backscatter-to-extinction ratios, $k' = \kappa \cdot k$, where k is the original backscatter-to-extinction ratio calculated from Eq. 3.26. The blue line represents the original retrieval where $\kappa = 1.0$, the red and green line represent retrievals with modified backscatter-to-extinction ratios by factors of $\kappa = 1.5$ and $\kappa = 2.0$, respectively. Increasing the backscatter-to-extinction ratio evidently leads to a reduced IWC. However, the effect of modifying the backscatter-to-extinction ratio is rather strong and the decrease of the IWC important. Integration of the IWC over the whole cloud layer results for the profile measured at 18.18 UTC in an IWP of $10.32 \pm 2.47\,\mathrm{g\,m^{-2}}$ for the original retrieval ($\kappa = 1.0$) compared to $5.98 \pm 1.43\,\mathrm{g\,m^{-2}}$

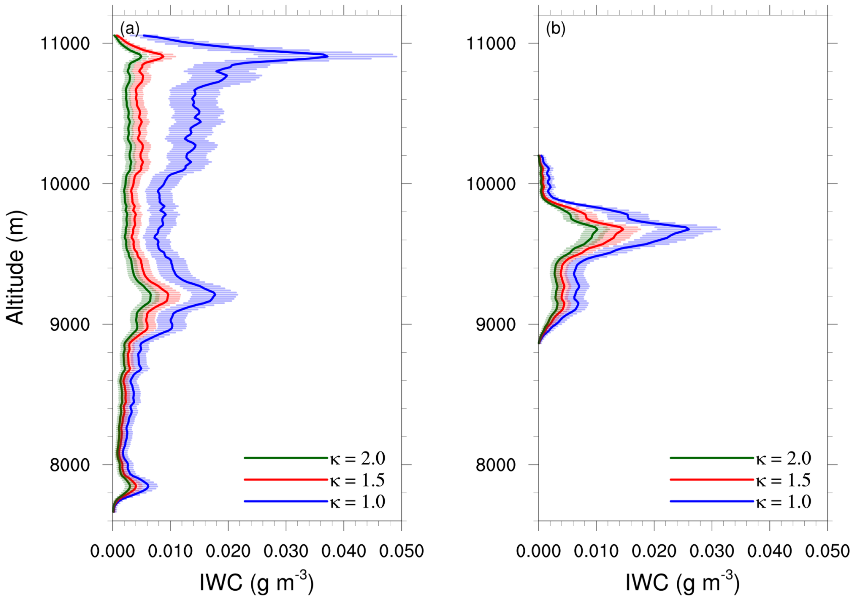

Figure 3.14: Dependence of the retrieved IWC on the backscatter-to-extinction ratio for the lidar profiles measured on November 30, 2016 at (a) 16.33 UTC and (b) 18.18 UTC. Shaded zones represent the error on the retrieval and the different colours stand for different factors κ (blue: $\kappa = 1.0$, red: $\kappa = 1.5$ and green: $\kappa = 2.0$).

and $4.22 \pm 1.01\,\mathrm{g\,m^{-2}}$ for the retrievals with modified backscatter-to-extinction ratios by factors of $\kappa = 1.5$ and $\kappa = 2.0$, respectively.

The cloudy profile measured at 16.33 UTC corresponds to a geometrically thick cloud (cf. Fig. 3.11 a). For this profile, the use of the backscatter-to-extinction ratio calculated directly from Eq. 3.26 results in a strong increase of IWC towards the cloud top which seems to be rather unrealistic. For the retrievals with the modified backscatter-to-extinction ratios, this peak at the cloud top is reduced importantly resulting in a more realistic shape of the IWC profile. The IWP is reduced by a factor of 4 between the retrieval considering $\kappa = 1.0$ ($\mathrm{IWP} = 32.21 \pm 8.93\,\mathrm{g\,m^{-2}}$) and $\kappa = 2.0$ ($\mathrm{IWP} = 8.58 \pm 2.25\,\mathrm{g\,m^{-2}}$).

These results show the importance of a good characterization of the backscatter-to-extinction ratio which has a strong influence on the retrieved IWC and constitutes the major source of uncertainty in our algorithm. As discussed in Sect. 2.3, the extinction coefficient can be obtained directly from highly developed lidar systems, such as Raman or HSRL lidars. On the contrary, for a simple micropulse lidar such as the lidar used in this thesis, the challenge is to find ways to constrain the backscatter-to-extinction ratio. In the next section, we will propose two strategies to address this challenge.

3.5 Strategies to Constrain the Backscatter-to-Extinction Ratio

The first strategy presented in this section to constrain the backscatter-to-extinction ratio follows the approach of Stephens et al. (2001) who included the visible optical thickness as an additional measurement in the optimal estimation framework to retrieve both the backscatter-to-extinction ratio and the extinction profile simultaneously. Stephens et al. (2001) obtained the optical thickness from the transmission method. However, this means that the backscatter-to-extinction ratio is constrained by a retrieval product which may itself be subject to a large uncertainty, especially due to the challenging cloud top retrieval in our case of ground-based lidar measurements. Furthermore, it strongly depends on the multiple scattering factor as will be discussed below. Instead of relying on such a retrieval product, we will show in a second step that the TIR radiometer measurements also constrain the backscatter-to-extinction ratio of cirrus clouds (Platt, 1973, 1979) since they are sensitive to the IWP as discussed in Sect. 3.3.

3.5.1 Use of the Visible Optical Thickness

In the approach proposed by Stephens et al. (2001), the visible optical thickness of the cloud obtained from the transmission method is used as an additional measurement. Hence, the measurement vector is expanded by this optical thickness τ_{cld},

$$\vec{y} = [\ln(C \cdot P(r_1) r_1^2), \ln(C \cdot P(r_2) r_2^2), \ldots, \ln(C \cdot P(r_{\mathrm{N}}) r_{\mathrm{N}}^2), \tau_{\mathrm{cld}}]^T. \tag{3.39}$$

This allows to retrieve the backscatter-to-extinction ratio together with the extinction profile since the total extinction of the cloud is constrained. Stephens et al. (2001) integrated the backscatter-to-extinction ratio k directly in the state vector. Our lidar only algorithm, however, retrieves the IWC for cirrus cloud layers and the IWC is linked to the extinction and to the backscatter-to-extinction ratio via the BV2015 microphysical model. The backscatter-to-extinction ratio is calculated via Eq. 3.26. Thus, we expand the state vector by the correction factor κ which has been introduced in the previous section since the single scattering albedo and the phase function in backscattering direction are obtained from the BV2015 parametrization.

Consequently, the state vector is expressed by (using the short notation introduced in the context of Eq. 3.27),

$$\vec{x} = [\sigma_1, \sigma_2, \ldots, \sigma_{\text{j\_base-1}}, \text{IWC}_{\text{j\_base}}, \ldots, \text{IWC}_{\text{j\_top}}, \sigma_{\text{j\_top+1}}, \ldots, \sigma_{\text{N}}, \kappa]^T, \tag{3.40}$$

where $k' = k \cdot \kappa = \varpi_0 \cdot p_{11}(\pi) \cdot \kappa$ represents the new backscatter-to-extinction ratio. It should be noted that ϖ_0 and $p_{11}(\pi)$ are calculated for each layer with the BV2015 parametrization depending on the according IWC and temperature. The correction factor κ, however, is assumed to be constant over the whole cloud.

In this variation of the lidar only algorithm, both measurement vector and state vector are composed of N+1 elements. The forward model for the additional measurement τ_{cld} is simply calculated via,

$$\text{F}_{\text{N+1}} = \sum_{j_{\text{cld}}=1}^{\text{N}_{\text{cld}}} \sigma_{j_{\text{cld}}} \, \Delta R, \tag{3.41}$$

where the subscript j_{cld} indicates cloudy layers, N_{cld} is the total number of cloudy layers, and the extinction for each of these layers is calculated from the according IWC with the BV2015 parametrization ($\sigma_{j_{\text{cld}}} = \sigma(\text{IWC}_{j_{\text{cld}}})$).

Since the state vector and the measurement vector are each expanded by one element, the Jacobian given by Eq. 3.27 has to be expanded by one row and one column. The additional column contains the derivations of the forward model with respect to the new state vector element κ. For cirrus layers, they are calculated analytically by differentiating Eq. 3.24 with respect to κ,

$$K_{i,\text{N+1}} = \frac{\partial \text{F}_i}{\partial \kappa} = \frac{\varpi_0 \cdot p_{11}(\pi) \cdot \sigma_i}{\beta_{\text{mol},i} + \varpi_0 \cdot p_{11}(\pi) \cdot \kappa \cdot \sigma_i}, \tag{3.42}$$

and for all other layers they are set to zero. The new row of the Jacobian contains the derivation of the forward model for τ_{cld} with respect to all state vector elements, hence for layers corresponding to the cloud,

$$K_{\text{N+1},j} = \frac{\partial \text{F}_{\text{N+1}}}{\partial (\text{IWC}_j)} = \frac{\partial \text{F}_{\text{N+1}}}{\partial \sigma_j} \, \frac{\partial \sigma_j}{\partial \text{IWC}_j} = \Delta R \, \frac{\partial \sigma_j}{\partial \text{IWC}_j}, \tag{3.43}$$

and all other elements of the last row, including $K_{\text{N+1,N+1}}$, are set to zero.

Consequently, the variance-covariance matrices are also expanded to (N+1) x (N+1) matrices. Since they are assumed to be diagonal, the new diagonal element of the a priori variance-covariance matrix is defined by,

$$S_{a,\text{N+1,N+1}} = \sigma^2_{a,\kappa}, \tag{3.44}$$

where the error on the a priori for the correction factor κ is chosen sufficiently large for the same reason as discussed above for the other elements of the a priori state vector. Based on the publications of Zhou and Yang (2015) and Ding et al. (2016), the a priori for κ is set to 1.7.

The new diagonal element of the error variance-covariance matrix is defined by,

$$S_{\epsilon,\mathrm{N+1,N+1}} = \sigma^2_{y,\tau_{\mathrm{cld}}}, \tag{3.45}$$

containing only a "measurement" error on τ_{cld} which is in fact the error on the cloud optical thickness obtained from the transmission method arising from the linear regression of the signals below and above the cloud explained in Sect. 2.3.3. It should be noted that no error is assigned to the forward model of τ_{cld}, since it is a simple integration of the extinction over the cloud layer. All other elements of S_ϵ are defined in the same way as in the original lidar only algorithm, with one exception: the error on the backscatter-to-extinction ratio for ice clouds was initially set to $p_{k,\mathrm{ice}}(\%)$=25% due to a poor knowledge of the phase function in the exact backscattering direction. This variation of the lidar only algorithm retrieves a correction factor for the backscatter-to-extinction ratio which should be interpreted as a correction factor for the phase function in the exact backscattering direction since we assume that the single scattering albedo is represented sufficiently exact by the BV2015 microphysical model. Hence, the large error on the backscatter-to-extinction ratio for ice cloud layers is replaced by an error of $p_{\varpi_0}(\%)$=1% for the single scattering albedo.

Figure 3.15 shows the retrieval results obtained with this variation of the lidar only algorithm for the case study of November 30, 2016, 15 to 19 UTC. Figure 3.15 e indicates that overall the method works well since the optical thickness calculated from the retrieved extinction profiles (blue) corresponds to the optical thickness obtained from the transmission method (red). In particular, the convergence for the optically and geometrically thicker cloud in the beginning of the period is better compared to the original lidar only algorithm. On the other hand, for the optically very thin cloud in the second half of the period, the lidar only algorithm that is constrained by the optical thickness did not converge. This might simply be due to the fact that the cloud is optically too thin to perform reasonable retrievals with this method. The retrieved extinction and IWC (Figs. 3.15 b and c, respectively) are reduced compared to the original lidar only algorithm which is due to the optical thickness constraint. Figure 3.15 d shows the retrieved correction factor κ (in blue, with axis on the right-hand side) and the corresponding lidar ratio in sr (red, axis

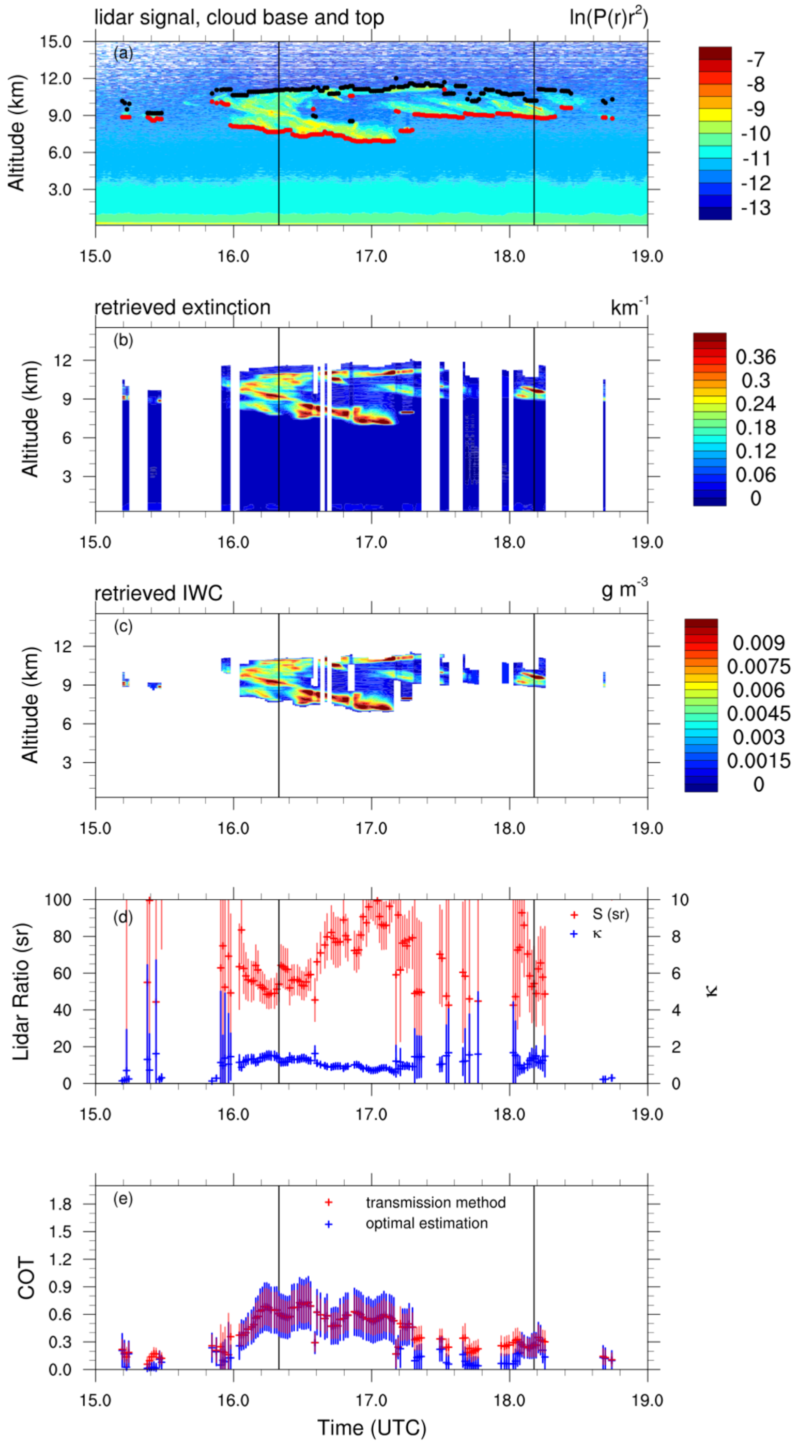

Figure 3.15: Retrieval results from the variation of the lidar only algorithm constrained by the COT for $\eta = 0.75$ and aerosol properties corresponding to the WASO aerosol type for November 30, 2016, 15 to 19 UTC. (a) Logarithm of the range-corrected lidar signal overlaid by the cloud detection, (b) retrieved extinction profiles, (c) retrieved IWC profiles, (d) lidar ratio (sr) on the left axis (red) and retrieved factor κ on the right axis (blue), and (e) cloud optical thickness from the lidar only algorithm (blue) and the transmission method introduced in Sect. 2.3.3 (red). The vertical black lines represent the two example profiles measured at 16.33 and 18.18 UTC.

on the left-hand side) which is defined as $S{=}1/k'$ and might be easier to interpret. All in all, the correction factor κ ranges between values of approximately 0.7 and 2. Thus, for some profiles the results correspond quite well to the findings of Zhou and Yang (2015) and Ding et al. (2016), although especially around 17 UTC the retrieved correction factors are smaller than 1 for a larger number of profiles. Furthermore, the corresponding lidar ratios largely overestimate the values for cirrus clouds reported in the literature. The average value of the retrieved lidar ratio for the period between 16 and 17.2 UTC is $70.7 \pm 17.6\,\mathrm{sr}$. When only considering the period between 16 and 16.6 UTC where the largest vertical extension of the cloud was observed, the average of the retrieved lidar ratio is considerably lower with $57.0 \pm 7.1\,\mathrm{sr}$. However, the lidar ratios for cirrus clouds reported in the literature range between 20 and 40 sr (e.g. Chen et al., 2002; Giannakaki et al., 2007; Seifert et al., 2007; Josset et al., 2012; Garnier et al., 2015).

It is important to notice that the assumed multiple scattering factor strongly influences these retrievals. As discussed in Sect. 2.3.3, the optical thickness of the cloud obtained from the transmission method is an effective optical thickness $\tau^{\star}_{\mathrm{cld}}$ with $\tau^{\star}_{\mathrm{cld}} = \eta\,\tau_{\mathrm{cld}}$. All retrievals shown previously were performed assuming a multiple scattering factor of $\eta = 0.75$ as mentioned above. Thus, the effective optical thickness obtained from the transmission method was divided by 0.75 before the retrievals were performed. Figure 3.16 shows the same results as in Fig. 3.15, but for a multiple scattering factor of $\eta = 1$. The retrieved correction factors κ shown in Fig. 3.15 d are larger and hence the lidar ratios smaller as in the case of $\eta = 0.75$. For the period between 16 and 16.6 UTC, the average value of the lidar ratios retrieved with a multiple scattering factor of $\eta = 1$ is $43.6 \pm 7.5\,\mathrm{sr}$, and for the whole period between 16 and 17.2 UTC an average lidar ratio of $54.3 \pm 14.3\,\mathrm{sr}$ is found. These values are closer to the literature.

However, these results show that a precise characterization of the optical thickness of the cloud is crucial for the application of this method since small changes in the optical thickness result in very different retrievals of the lidar ratio. The optical thickness obtained from the transmission method strongly depends on the defined cloud base and top altitudes and particularly the retrieval of the cloud top is difficult from a ground-based lidar (cf. Sect. 2.3.3). A little change in the cloud boundaries leads to a different retrieved optical thickness and thus a different retrieval of the lidar ratio. Furthermore, the multiple scattering factor plays an important role and it is necessary to better characterize this parameter before applying this method.

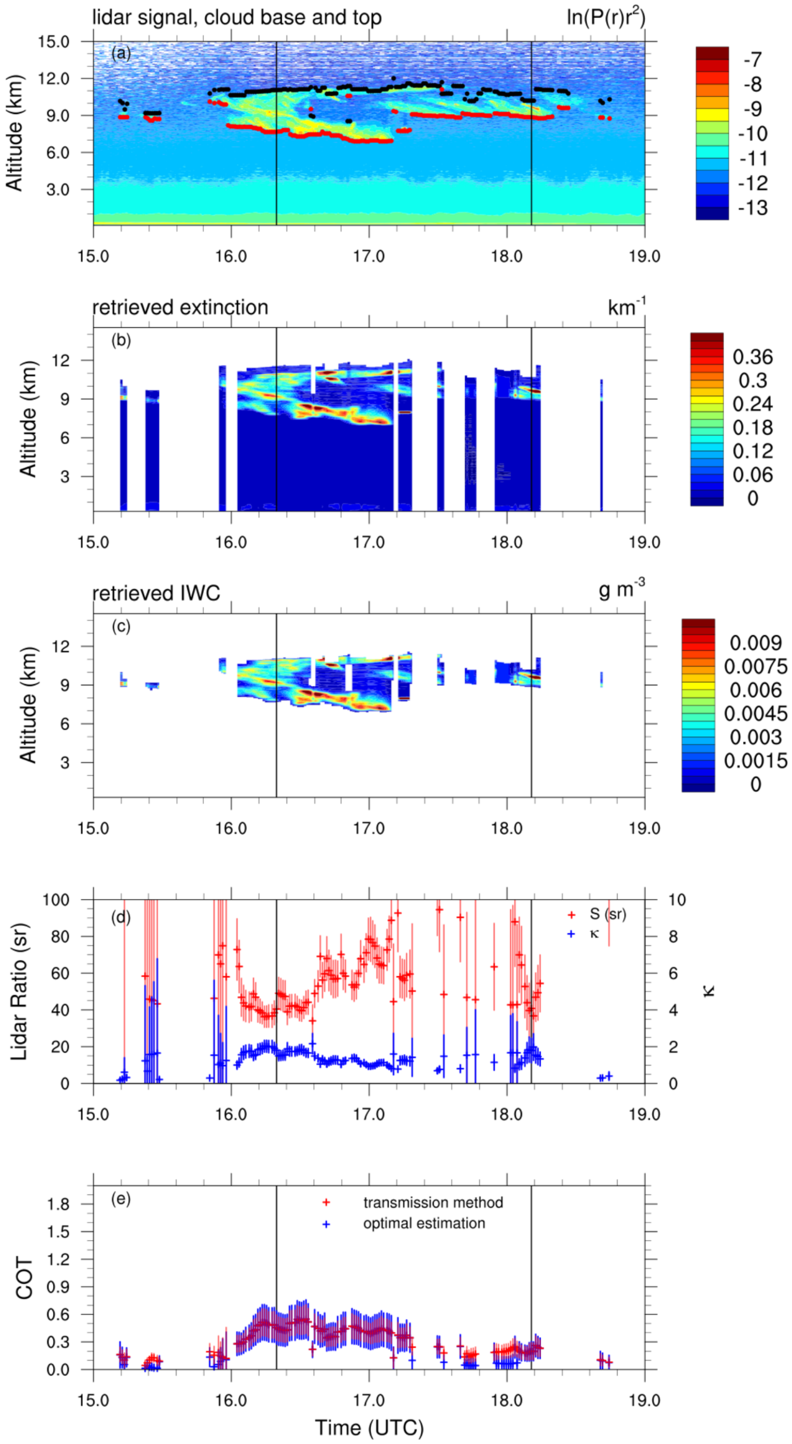

Figure 3.16: Same as Fig. 3.15, but the retrievals were performed with $\eta = 1.0$.

As a consequence, instead of constraining the backscatter-to-extinction ratio with a retrieval product that is subject to rather large uncertainties, we propose to use the TIR measurements to constrain the backscatter-to-extinction ratio since they are independent of the lidar measurements.

3.5.2 Use of Thermal Infrared Radiances

As discussed in Sect. 3.3, the TIR radiances are sensitive to the IWP. This means, they can be used to constrain the amount of ice in the cloud and hence the backscatter-to-extinction ratio. Similarly as in the previous section, we will consider the correction factor κ for the backscatter-to-extinction ratio here which can be interpreted as a correction factor for the phase function in the exact backscattering direction as discussed above.

To show the potential of the TIR radiances to constrain this correction factor, retrievals with the original lidar only algorithm have been performed for different factors κ ranging between 1.0 and 3.0. Subsequently, the retrieved IWC profiles have been used to simulate the according TIR radiances. As shown in Fig. 3.4, only the measurements of channels C11 and C12 under clear sky conditions could be reproduced by the clear sky simulations with the radiative transfer model LIDORT. The atmospheric profile which has to be selected to obtain a good agreement between the clear sky measurements and simulations is the ECMWF reanalysis profile of 12 UTC. Hence, in the analysis described in the following, only channels C11 and C12 are considered and the profile of 12 UTC has been used in the radiative transfer calculations.

Figure 3.17 a shows the dependence of the simulated TIR radiances on the correction factor κ for the lidar profile measured on November 30, 2016, at 18.18 UTC. Channel C11 is illustrated in blue and channel C12 in red. The solid lines represent the simulations with LIDORT and the dashed lines the TIR measurement at 18.18 UTC. The shaded zones around the dashed lines indicate the measurement error. In Fig. 3.17 b, the corresponding COT calculated from the retrieved extinction profile is shown by the blue crosses and the black line represents the COT obtained from the transmission method with its according error illustrated in grey. With increasing correction factor κ, the COT decreases as well as the simulated radiances. Furthermore, for a correction factor between $\kappa = 1.1$ and $\kappa = 1.5$ the simulated radiances for channel C12 coincide with the measurement of this channel considering the error range of the measurement. For channel C11, this is the case for $\kappa \geq 1.4$. Hence, it

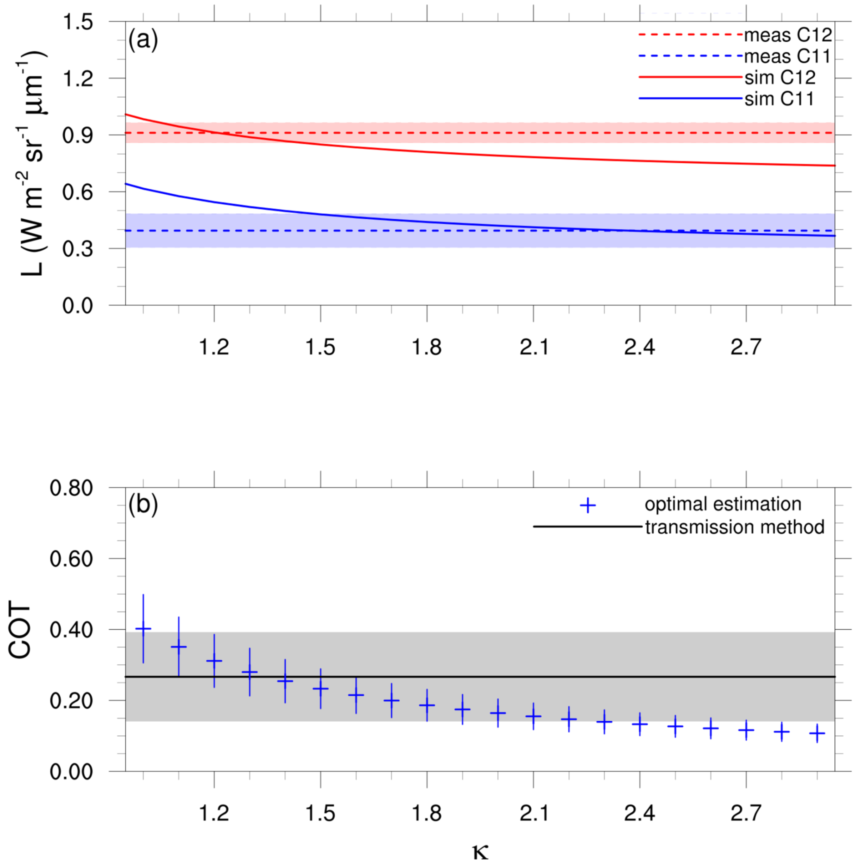

Figure 3.17: (a) Dependence of the simulated TIR radiances on the correction factor κ for the backscatter-to-extinction ratio ranging between 1.0 and 3.0 for the lidar profile measured on November 30, 2016, at 18.18 UTC. The TIR radiometer measurements of channels C11 (blue) and C12 (red) are represented by the dashed lines, shaded zones indicate the measurement error. (b) Corresponding visible COT. The black line represents the COT derived from the transmission method and the shaded grey zone its error range.

can be concluded that for this profile the correction factor κ should range between 1.4 and 1.5 to obtain a retrieval of an IWC profile which allows both the forward model of the lidar as well as the TIR forward model to converge towards the according measurements. In addition, the COT from the transmission method agrees well with the COT computed from the retrieved extinction profile for this range of correction factors. It should be noted that a multiple scattering factor of $\eta = 0.75$ has been applied in these retrievals which results in a coherent retrieval between the visible optical thickness and the TIR radiometer measurements for this profile. These results allow the conclusion that the TIR radiometer measurements provide a constraint for the backscatter-to-extinction ratio by constraining the amount of ice in the cirrus cloud and thereby help to obtain an information about the phase function in the exact backscattering direction. Since the use of the analytical phase function of Baran et al. (2001) does not lead to a coherent retrieval between the lidar and the TIR radiometer measurements, it can be concluded that this phase function may not be exact enough to represent the phase function of real atmospheric ice crystals in the exact backscattering direction.

The same analysis has been performed for the lidar profile measured at 16.33 UTC on November 30, 2016, where the observed cirrus cloud was geometrically and optically thicker. The result is presented in Fig. 3.18. For the retrieval performed with $\kappa = 1$, which means that the backscatter-to-extinction ratio has been obtained directly from the microphysical model via Eq. 3.26 and that no correction factor has been applied to the phase function in the exact backscattering direction, the COT calculated from the retrieved extinction profile is much larger than the COT obtained from the transmission method. At the same time, the simulated TIR radiances with the corresponding retrieved IWC profile largely overestimate the measured radiances. Furthermore, Fig. 3.14 showed an increase of IWC at the cloud top for this case which seems to be rather unrealistic. These results suggest that for the profile measured at 16.33 UTC a non-corrected backscatter-to-extinction ratio does not lead to a realistic retrieval. It can be argued from Fig. 3.18 a that a correction factor κ which allows the TIR forward model to converge towards the TIR measurements should range between 2.0 and 2.3. However, the retrieved COT corresponding to this range of κ is slightly smaller than the COT from the transmission method.

These results show that the ensemble of measurements should be used to find a retrieval that corresponds best to all available information. It has been confirmed

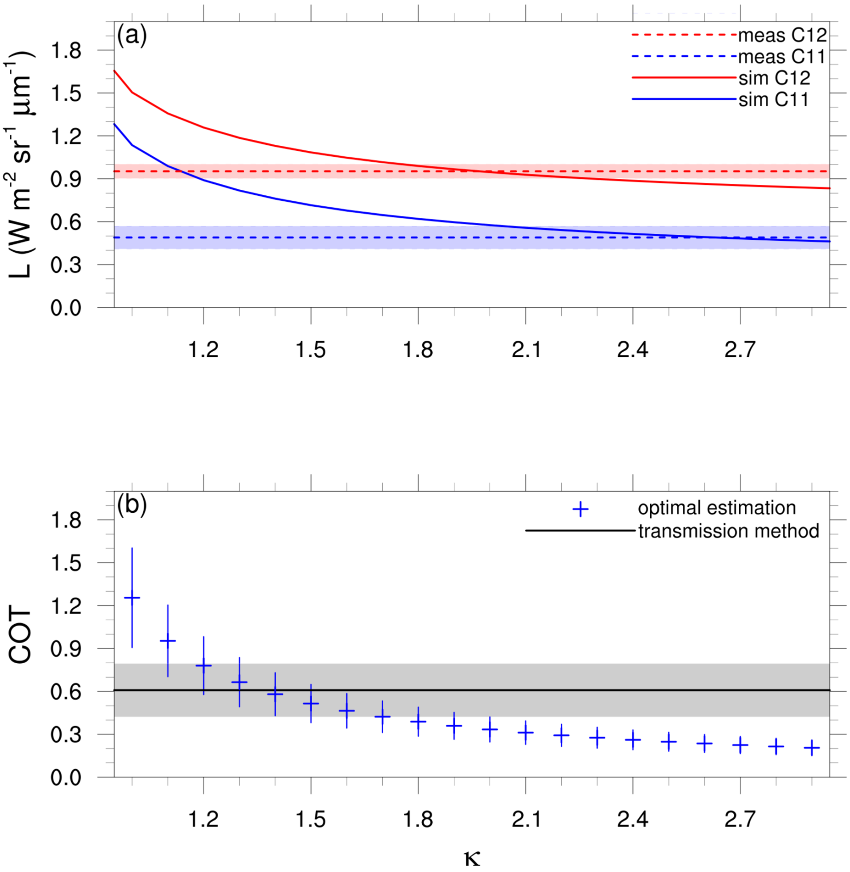

Figure 3.18: Same as Fig. 3.17 for the lidar profile measured on November 30, 2016, at 16.33 UTC.

that the TIR radiances provide an additional constraint for the amount of ice inside the cloud which strongly depends on the backscatter-to-extinction ratio. Under the assumption that the single scattering albedo is known sufficiently exact (cf. Eq. 3.26), the results shown here lead to the conclusion that the phase function in the exact backscattering direction can be constrained with the help of the TIR measurements.

This second approach to constrain the backscatter-to-extinction ratio resulted in the synergy algorithm combining the active lidar and the passive TIR radiometer measurements in a common retrieval framework to retrieve in addition to the IWC/extinction profiles the correction factor κ for the phase function of the ice crystals in the exact backscattering direction. This synergy algorithm will be presented in the following section.

3.6 Synergy Algorithm Combining Lidar and Thermal Infrared Radiometer Measurements

Synergistic approaches combining lidar and TIR radiometer measurements have been used since the 1970s. The most famous method is the LIRAD method introduced by Platt (1973, 1979). It allows to retrieve the visible cloud optical thickness and the infrared emissivity. The lidar backscatter coefficient of the cloud ($\beta(r)$) is related to the bulk absorption coefficient in the TIR ($\sigma_{\mathrm{abs,TIR}}(r)$) via the parameter ζ, where $\sigma_{\mathrm{abs,TIR}}(r) = \zeta\beta(r)$ (Sassen and Comstock, 2001). An initial guess is chosen for ζ and the theoretical TIR radiances are calculated from $\sigma_{\mathrm{abs,TIR}}(r)$ and compared to the TIR measurements. ζ is varied until the theoretical and measured radiances converge. The TIR emissivity can then be derived from the final TIR absorption coefficient and ζ contains an information about the backscatter-to-extinction ratio. This method and variations of it have been applied by several authors (e.g. Platt and Dilley, 1981; Platt et al., 1987; Comstock and Sassen, 2001; Sassen and Comstock, 2001; Platt et al., 2002; Blanchard et al., 2017).

For spaceborne data, synergistic approaches combining lidar and TIR measurements have been developed in connection with the CALIPSO mission. The studies of Chiriaco et al. (2004) and Garnier et al. (2012, 2013, 2015) show the potential of integrating the information from the active CALIOP measurements in the retrieval algorithm for the passive IIR instrument. Recently, Saito et al. (2017) proposed a method to combine these measurements in a variational algorithm based on optimal estimation to simultaneously retrieve the IWP, the particle effective radius and the surface temperature, as well as two morphological parameters of the ice crystals, namely the fraction of plates and the surface roughness of ice aggregates. Their measurement vector is composed of the layer-integrated total attenuated backscatter and the depolarization ratio at 532 nm obtained from CALIOP, as well as the brightness temperatures at 8.65, 10.6 and 12.0 μm measured by the IIR.

Our synergy algorithm, which constitutes the final step of our methodology, is based on the optimal estimation framework introduced in the previous sections. It uses the whole measured lidar profile to obtain an information about the vertical distribution of IWC in cirrus clouds, and incorporates the TIR radiometer measurements to constrain the backscatter-to-extinction ratio as discussed in Sect. 3.5.2.

3.6.1 Description of the Synergy Algorithm

The synergy algorithm finally combines the lidar only and the TIR only algorithms to retrieve a profile of IWC in cirrus clouds together with the correction factor κ for the phase function in the exact backscattering direction. The common optimal estimation framework for these two sets of measurements will be described in the following.

State Vector and Measurement Vector

As discussed in detail in Sect. 3.5, our aim is to constrain the backscatter-to-extinction ratio. Since the definition of this parameter allows to obtain it directly from the BV2015 microphysical model, the objective is to improve this microphysical model, especially the representation of the phase function in the exact backscattering direction. Therefore, the correction factor κ for the backscatter-to-extinction ratio has been introduced in the previous section which can be interpreted as a correction factor for the phase function in the exact backscattering direction. Following the approach presented in Sect. 3.5.1, the new backscatter-to-extinction ratio may be expressed by,

$$k' = \varpi_0 \cdot p'_{11}(\pi) = \varpi_0 \cdot p_{11}(\pi) \cdot \kappa, \tag{3.46}$$

where $p'_{11}(\pi)$ represents the corrected phase function in the exact backscattering direction. As in case of the variation of the lidar only algorithm which is constrained by the visible optical thickness (cf. Sect. 3.5.1), the correction factor κ is added to the previous state vector of the original lidar only algorithm (cf. Eqs. 3.21 and 3.40),

$$\vec{x} = [\sigma_1, \sigma_2, \ldots, \sigma_{\text{j\_base-1}}, \text{IWC}_{\text{j\_base}}, \ldots, \text{IWC}_{\text{j\_top}}, \sigma_{\text{j\_top+1}}, \ldots, \sigma_{\text{N}}, \kappa]^T. \tag{3.47}$$

The measurement vector $\vec{y}$, initially containing the logarithm of the calibrated range-corrected lidar signal (plus the visible optical thickness in case of the variation of the lidar only algorithm presented in Sect. 3.5.1), is expanded by the radiances measured by the TIR radiometer,

$$\vec{y} = [\ln(C \cdot P(r_1) r_1^2), \ln(C \cdot P(r_2) r_2^2), \ldots, \ln(C \cdot P(r_{\text{N}}) r_{\text{N}}^2), L_{\text{C09}}, L_{\text{C11}}, L_{\text{C12}}]^T. \tag{3.48}$$

However, as in case of the TIR only algorithm, only the measurements of the radiometer channels reproduced by the forward model under clear sky conditions are considered in the application of the synergy algorithm, that means channels C11 and C12 for the case study of November 30, 2016.

Forward Model

The forward model for the lidar is the same as in case of the lidar only algorithm and is given by the lidar equation in form of Eq. 3.24. The only modification is that the backscatter-to-extinction ratio for ice cloud layers is now calculated from Eq. 3.46. For the TIR radiances, the radiative transfer model LIDORT is used as forward model which has been introduced in Sect. 3.3 since it is also used as forward model in the TIR only algorithm. However, in the TIR only algorithm, the cloud was assumed to be homogeneous. This assumption is no longer necessary in the synergy algorithm because the lidar measurements provide an information about the vertical distribution of the IWC which is given in the state vector on the vertical lidar resolution. Hence, these profiles can be considered in the TIR forward model which is an improvement of our method compared to most operational retrieval algorithms existing nowadays.

Furthermore, the synergy with the lidar measurements allows to integrate atmospheric aerosols in the radiative transfer calculations. The profile of the particle extinction coefficient outside cirrus cloud layers given by the state vector allows to calculate the visible optical thickness of aerosols which is linked via Mie theory to the optical thickness at the TIR wavelengths. This information is then used in the TIR forward model to more realistically simulate the atmospheric TIR radiances. However, we have to assume an aerosol model and the two aerosol models that are currently integrated in our algorithm are the WASO and INSO aerosol types from the OPAC database described in Sect. 2.4.2.

As in case of the TIR only algorithm, the single scattering properties of the cirrus cloud required in the radiative transfer calculations are obtained from the BV2015 parametrization as functions of IWC and temperature for each layer. The vertical grid inside the cloud corresponds to the lidar resolution, outside the cloud the reanalysis model levels are used since the atmospheric profiles required in the radiative transfer calculations are obtained from ECMWF reanalysis.

Jacobian

The Jacobian of the synergy algorithm contains in addition to the Jacobian of the lidar only algorithm one new column for the sensitivity of the forward model to the new state vector element κ, and three new rows for the sensitivity of the TIR forward model to each state vector parameter,

$$\mathbf{K} = \begin{pmatrix}
\frac{\partial \mathrm{F}_1}{\partial \sigma_1} & \cdots & \frac{\partial \mathrm{F}_1}{\partial \sigma_{\text{j_base-1}}} & \frac{\partial \mathrm{F}_1}{\partial \mathrm{IWC}_{\text{j_base}}} & \cdots & \frac{\partial \mathrm{F}_1}{\partial \mathrm{IWC}_{\text{j_top}}} & \frac{\partial \mathrm{F}_1}{\partial \sigma_{\text{j_top+1}}} & \cdots & \frac{\partial \mathrm{F}_1}{\partial \sigma_{\mathrm{N}}} & \frac{\partial \mathrm{F}_1}{\partial \kappa} \\
\frac{\partial \mathrm{F}_2}{\partial \sigma_1} & \cdots & \frac{\partial \mathrm{F}_2}{\partial \sigma_{\text{j_base-1}}} & \frac{\partial \mathrm{F}_2}{\partial \mathrm{IWC}_{\text{j_base}}} & \cdots & \frac{\partial \mathrm{F}_2}{\partial \mathrm{IWC}_{\text{j_top}}} & \frac{\partial \mathrm{F}_2}{\partial \sigma_{\text{j_top+1}}} & \cdots & \frac{\partial \mathrm{F}_2}{\partial \sigma_{\mathrm{N}}} & \frac{\partial \mathrm{F}_2}{\partial \kappa} \\
\vdots & \cdots & \vdots & \vdots & \cdots & \vdots & \vdots & \cdots & \vdots & \vdots \\
\frac{\partial \mathrm{F}_{\text{j_base-1}}}{\partial \sigma_1} & \cdots & \frac{\partial \mathrm{F}_{\text{j_base-1}}}{\partial \sigma_{\text{j_base-1}}} & \frac{\partial \mathrm{F}_{\text{j_base-1}}}{\partial \mathrm{IWC}_{\text{j_base}}} & \cdots & \frac{\partial \mathrm{F}_{\text{j_base-1}}}{\partial \mathrm{IWC}_{j\text{_top}}} & \frac{\partial \mathrm{F}_{\text{j_base-1}}}{\partial \sigma_{\text{j_top+1}}} & \cdots & \frac{\partial \mathrm{F}_{\text{j_base-1}}}{\partial \sigma_{\mathrm{N}}} & \frac{\partial \mathrm{F}_{\text{j_base-1}}}{\partial \kappa} \\
\frac{\partial \mathrm{F}_{\text{j_base}}}{\partial \sigma_1} & \cdots & \frac{\partial \mathrm{F}_{\text{j_base}}}{\partial \sigma_{\text{j_base-1}}} & \frac{\partial \mathrm{F}_{\text{j_base}}}{\partial \mathrm{IWC}_{\text{j_base}}} & \cdots & \frac{\partial \mathrm{F}_{\text{j_base}}}{\partial \mathrm{IWC}_{\text{j_top}}} & \frac{\partial \mathrm{F}_{\text{j_base}}}{\partial \sigma_{\text{j_top+1}}} & \cdots & \frac{\partial \mathrm{F}_{\text{j_base}}}{\partial \sigma_{\mathrm{N}}} & \frac{\partial \mathrm{F}_{\text{j_base}}}{\partial \kappa} \\
\vdots & \cdots & \vdots & \vdots & \cdots & \vdots & \vdots & \cdots & \vdots & \vdots \\
\frac{\partial \mathrm{F}_{\text{j_top}}}{\partial \sigma_1} & \cdots & \frac{\partial \mathrm{F}_{\text{j_top}}}{\partial \sigma_{\text{j_base-1}}} & \frac{\partial \mathrm{F}_{\text{j_top}}}{\partial \mathrm{IWC}_{\text{j_base}}} & \cdots & \frac{\partial \mathrm{F}_{\text{j_top}}}{\partial \mathrm{IWC}_{\text{j_top}}} & \frac{\partial \mathrm{F}_{\text{j_top}}}{\partial \sigma_{\text{j_top+1}}} & \cdots & \frac{\partial \mathrm{F}_{\text{j_top}}}{\partial \sigma_{\mathrm{N}}} & \frac{\partial \mathrm{F}_{\text{j_top}}}{\partial \kappa} \\
\frac{\partial \mathrm{F}_{\text{j_top+1}}}{\partial \sigma_1} & \cdots & \frac{\partial \mathrm{F}_{\text{j_top+1}}}{\partial \sigma_{\text{j_base-1}}} & \frac{\partial \mathrm{F}_{\text{j_top+1}}}{\partial \mathrm{IWC}_{\text{j_base}}} & \cdots & \frac{\partial \mathrm{F}_{\text{j_top+1}}}{\partial \mathrm{IWC}_{\text{j_top}}} & \frac{\partial \mathrm{F}_{\text{j_top+1}}}{\partial \sigma_{\text{j_top+1}}} & \cdots & \frac{\partial \mathrm{F}_{\text{j_top+1}}}{\partial \sigma_{\mathrm{N}}} & \frac{\partial \mathrm{F}_{\text{j_top+1}}}{\partial \kappa} \\
\vdots & \cdots & \vdots & \vdots & \cdots & \vdots & \vdots & \cdots & \vdots & \vdots \\
\frac{\partial \mathrm{F}_{\mathrm{N}}}{\partial \sigma_1} & \cdots & \frac{\partial \mathrm{F}_{\mathrm{N}}}{\partial \sigma_{\text{j_base-1}}} & \frac{\partial \mathrm{F}_{\mathrm{N}}}{\partial \mathrm{IWC}_{\text{j_base}}} & \cdots & \frac{\partial \mathrm{F}_{\mathrm{N}}}{\partial \mathrm{IWC}_{\text{j_top}}} & \frac{\partial \mathrm{F}_{\mathrm{N}}}{\partial \sigma_{\text{j_top+1}}} & \cdots & \frac{\partial \mathrm{F}_{\mathrm{N}}}{\partial \sigma_{\mathrm{N}}} & \frac{\partial \mathrm{F}_{\mathrm{N}}}{\partial \kappa} \\
\frac{\partial \mathrm{F}_{\mathrm{C09}}}{\partial \sigma_1} & \cdots & \frac{\partial \mathrm{F}_{\mathrm{C09}}}{\partial \sigma_{\text{j_base-1}}} & \frac{\partial \mathrm{F}_{\mathrm{C09}}}{\partial \mathrm{IWC}_{\text{j_base}}} & \cdots & \frac{\partial \mathrm{F}_{\mathrm{C09}}}{\partial \mathrm{IWC}_{\text{j_top}}} & \frac{\partial \mathrm{F}_{\mathrm{C09}}}{\partial \sigma_{\text{j_top+1}}} & \cdots & \frac{\partial \mathrm{F}_{\mathrm{C09}}}{\partial \sigma_{\mathrm{N}}} & \frac{\partial \mathrm{F}_{\mathrm{C09}}}{\partial \kappa} \\
\frac{\partial \mathrm{F}_{\mathrm{C11}}}{\partial \sigma_1} & \cdots & \frac{\partial \mathrm{F}_{\mathrm{C11}}}{\partial \sigma_{\text{j_base-1}}} & \frac{\partial \mathrm{F}_{\mathrm{C11}}}{\partial \mathrm{IWC}_{\text{j_base}}} & \cdots & \frac{\partial \mathrm{F}_{\mathrm{C11}}}{\partial \mathrm{IWC}_{\text{j_top}}} & \frac{\partial \mathrm{F}_{\mathrm{C11}}}{\partial \sigma_{\text{j_top+1}}} & \cdots & \frac{\partial \mathrm{F}_{\mathrm{C11}}}{\partial \sigma_{\mathrm{N}}} & \frac{\partial \mathrm{F}_{\mathrm{C11}}}{\partial \kappa} \\
\frac{\partial \mathrm{F}_{\mathrm{C12}}}{\partial \sigma_1} & \cdots & \frac{\partial \mathrm{F}_{\mathrm{C12}}}{\partial \sigma_{\text{j_base-1}}} & \frac{\partial \mathrm{F}_{\mathrm{C12}}}{\partial \mathrm{IWC}_{\text{j_base}}} & \cdots & \frac{\partial \mathrm{F}_{\mathrm{C12}}}{\partial \mathrm{IWC}_{\text{j_top}}} & \frac{\partial \mathrm{F}_{\mathrm{C12}}}{\partial \sigma_{\text{j_top+1}}} & \cdots & \frac{\partial \mathrm{F}_{\mathrm{C12}}}{\partial \sigma_{\mathrm{N}}} & \frac{\partial \mathrm{F}_{\mathrm{C12}}}{\partial \kappa}
\end{pmatrix}. \tag{3.49}$$

The sensitivities of the TIR radiances to the extinction profile outside the cloud are set to zero because they are assumed to be small. The last three elements of the Jacobian presented in Eq. 3.49 are also set to zero because the correction factor κ does not have a direct influence on the TIR radiances. As described in Sect. 3.3 for the TIR only algorithm, the sensitivities of the TIR radiances to the IWC profile inside the cloud are calculated directly in LIDORT. This numerical efficiency of the radiative transfer model is the second reason allowing the use of the fine vertical lidar resolution in the state vector (next to the availability of the vertical information thanks to the lidar measurements).

Finally, the partial derivatives of the lidar forward model with respect to κ are set to zero outside the cloud and calculated analytically as derivation of the forward model (Eq. 3.24) for the ice cloud layers as in case of the variation of the lidar only algorithm constrained by the optical thickness (cf. Eq. 3.42),

$$\frac{\partial \mathrm{F}_i}{\partial \kappa} = \frac{\varpi_0 \cdot p_{11}(\pi) \cdot \sigma_i}{\beta_{\mathrm{mol},i} + \varpi_0 \cdot p_{11}(\pi) \cdot \kappa \cdot \sigma_i}, \tag{3.50}$$

where the layer extinction σ_i is calculated from the IWC with the BV2015 parametrization.

Variance-Covariance Matrices

As for the algorithms described above, the variance-covariance matrices of the synergy algorithm are also considered to be diagonal. Concerning the lidar, they are defined in the same way as in case of the original lidar only algorithm described in Sect. 3.4.1. The only difference is that the error on the backscatter-to-extinction ratio for ice cloud layers is replaced by the error of $p_{\varpi_0}(\%)$=1 % for the single scattering albedo, since the correction factor κ for the phase function in the exact backscattering direction is retrieved with the synergy algorithm. This error has already been introduced and discussed in Sect. 3.5.1. For the variance-covariance matrix of the TIR forward model, the same non-retrieved parameters (and according errors) are considered as in case of the TIR only algorithm (cf. Sect. 3.3.1), which are the surface emissivity (2 %), surface temperature (1 K) and the profiles of atmospheric temperature (1 K for each layer), water vapour (10 % for each layer) and ozone (2 % for each layer). As described in Sect. 3.3.1, the variances are calculated via

$$\sigma_{\mathrm{b}_j} = \frac{\partial \mathrm{F}}{\partial \mathrm{b}_j} \cdot \mathrm{b}_j \cdot \frac{\mathrm{p}_{\mathrm{b}_j}(\%)}{100}, \tag{3.51}$$

where b_j represents the considered non-retrieved parameter, $\mathrm{p}_{\mathrm{b}_j}(\%)$ its error in percent and $\frac{\partial \mathrm{F}}{\partial \mathrm{b}_j}$ the sensitivity of the forward model to this parameter, where the latter can be calculated directly in LIDORT for all desired parameters. The measurement error on the TIR radiances ($\sigma_{y,i_{\mathrm{TIR}}}$) has been discussed in detail in Sect. 2.2.2 and is introduced in the synergy algorithm in the same way as described for the TIR only algorithm described in Sect. 3.3.1. The diagonal elements of the variance-covariance matrix representing the errors of the TIR measurements and forward model are then defined by,

$$S_{\epsilon,ii_{\mathrm{TIR}}} = \sigma^2_{y,i_{\mathrm{TIR}}} + \sum_j \sigma^2_{\mathrm{b}_j,i_{\mathrm{TIR}}}. \tag{3.52}$$

3.6.2 Case Study Results of the Synergy Algorithm

This section presents the application of the synergy algorithm to the case study of November 30, 2016. The retrievals shown here have been performed for a multiple scattering factor $\eta = 0.75$. The influence of the multiple scattering factor will be discussed in more detail in Chapter 4. In a first step, we will show that the convergence of the synergy algorithm is at least as good as the convergence of both lidar only algorithms presented above. Secondly, the results for the time period between 15 and 19 UTC of November 30, 2016, are presented.

Similarly as in case of the TIR only algorithm, it is necessary to verify if the measured radiances under clear sky conditions are reproduced by the clear sky simulation of the TIR forward model before the synergy algorithm can be applied. For our case study, it already has been discussed in Sect. 3.3 that the ECMWF reanalysis profile of 12 UTC represents the atmospheric conditions allowing to converge between the clear sky measurements and the forward model for channels C11 and C12. In contrast, channel C09 could not be reproduced by the forward model and has been excluded. The same conclusion has to be drawn for the synergy algorithm, although it should be noted that the information about the aerosols in the lowest layer of the atmosphere obtained from the lidar measurements are integrated in the TIR forward model of the synergy algorithm as mentioned above. This means that the clear sky simulation was performed taking into account the aerosol absorption in the lowest layers of the atmosphere. The results for the two aerosol models are presented in Fig. 3.19. Since the aerosol extinction on November 30, 2016, was rather small, the simulations shown in this figure are very similar to the clear sky simulations without aerosols shown in Fig. 3.4. The INSO aerosol type is more absorbent than the WASO aerosol type which leads to slightly larger radiances resulting from the simulations with the INSO aerosol type, especially in channel C11. The clear sky simulations including aerosols reproduce for both aerosol types the measurements of channels C11 and C12 where no clouds are present. However, since the WASO aerosol type is supposed to represent urban/industrial aerosols, it has been used in the retrievals shown for the lidar only algorithm in this chapter and will also be used for the retrievals presented here. The influence of the aerosol model on the retrievals is further discussed in Chapter 4 of this thesis.

Figure 3.20 shows the same example as given in Fig. 3.9 but in this case obtained from the synergy algorithm. To recall, the lidar measurement is represented by the red lines and the blue horizontal lines indicate the cloud base and top altitudes of the cirrus defined in 8865 m and 10200 m altitude, respectively. The black lines show the calculated lidar forward model, in Fig. 3.20 a for the a priori and in Fig. 3.20 b after the last iteration step. As in the case of the lidar only algorithm, the a priori for the lowest layers is calculated with Eq. 3.38 and for ice cloud layers the iteration is started from a small IWC of $0.001\,\mathrm{g\,m^{-3}}$. After the last iteration step, the agreement between the lidar forward model and the measured profile is

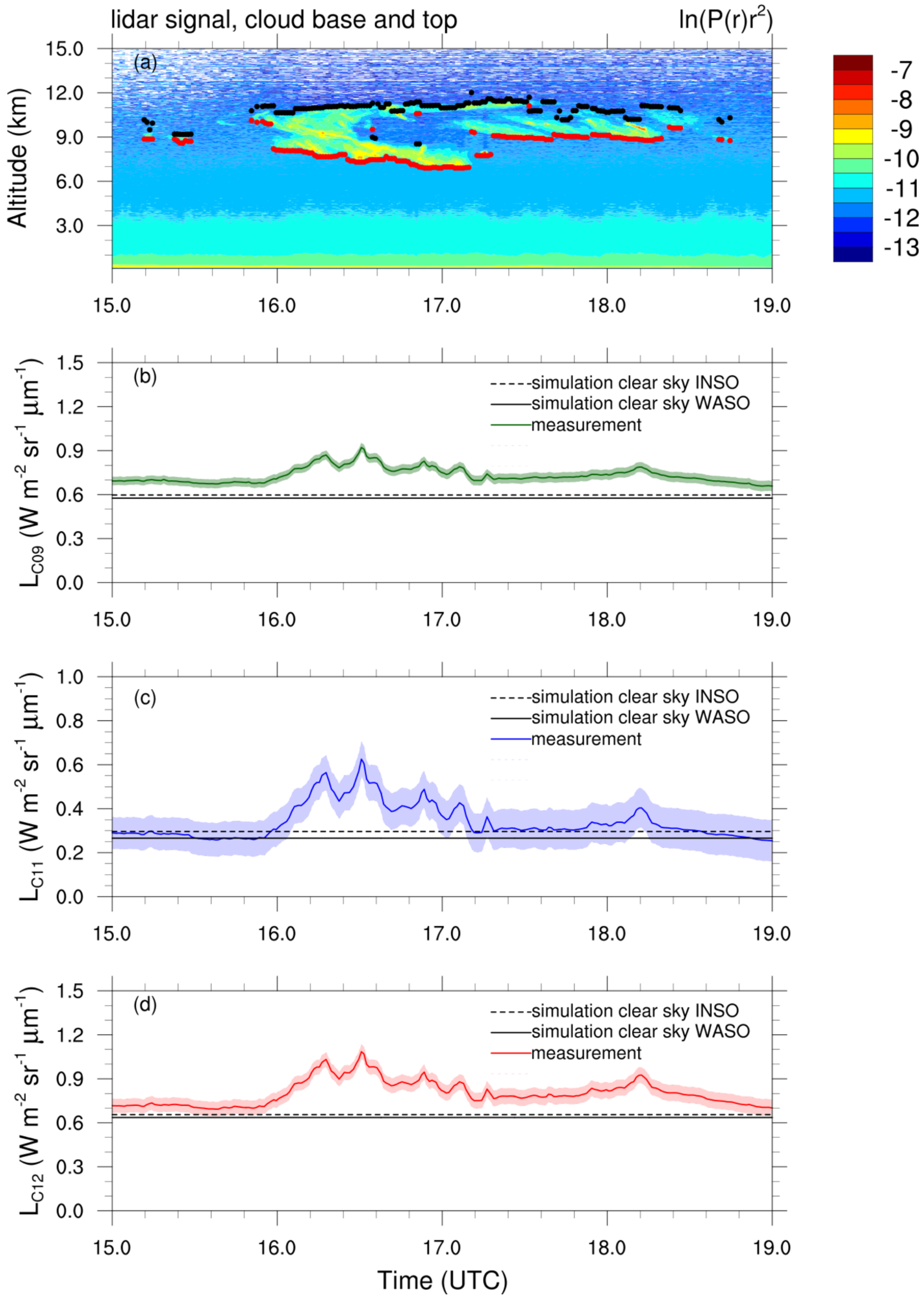

Figure 3.19: TIR radiometer measurements and clear sky simulations with the ECMWF reanalysis profiles of 12 UTC including aerosols for the aerosol models WASO (solid lines) and INSO (dashed lines) for November 30, 2016, 15 to 19 UTC. (a) Logarithm of the range-corrected lidar signal overlaid by the cloud detection, (b) radiance of channel C09, (c) radiance of channel C11, and (d) radiance of channel C12. The shaded zones in plots (b)-(d) represent the measurement error.

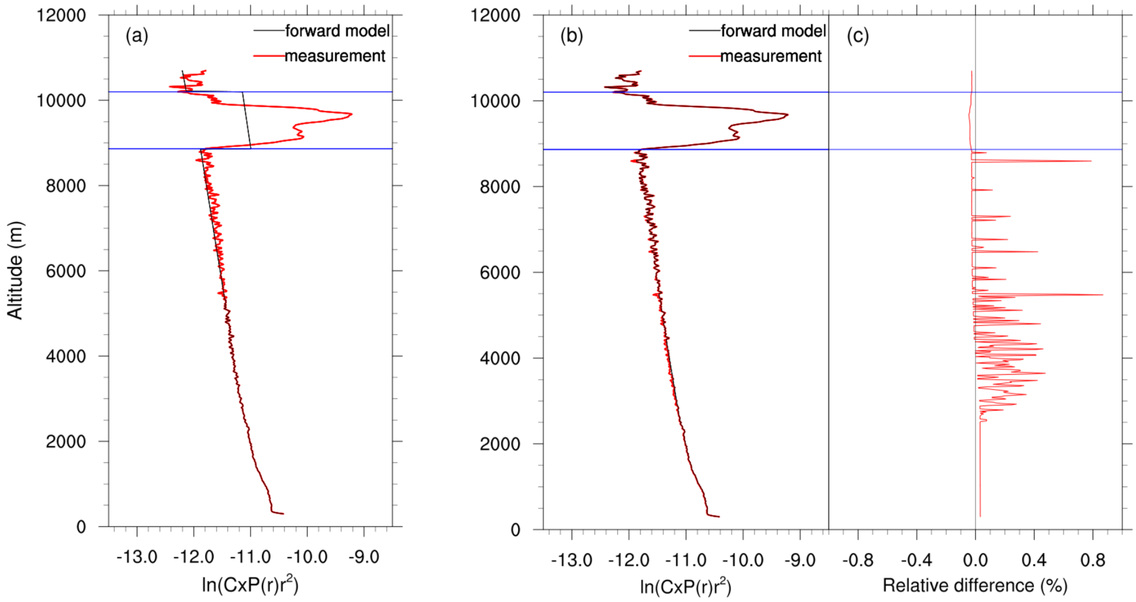

Figure 3.20: Lidar forward model of the synergy algorithm of the (a) a priori and (b) after the last iteration step (black lines) for the profile measured on November 30, 2016 at 18.18 UTC (the red lines represent the measurement, the horizontal blue lines indicate the defined cloud base and top altitudes (8865 m and 10200 m, respectively)). (c) Relative difference between the measurement and the forward model after the last iteration step.

very good and the relative difference between them is less than 1 % for all layers (cf. Fig. 3.20 c). Hence, concerning the lidar, the good convergence observed for the lidar only algorithm is confirmed in the synergy algorithm. Table 3.1 summarizes the TIR radiometer measurements and the forward model including their errors according to this profile. Since the values of the TIR forward model after the last iteration step are situated within the error range of the measurements, it can be concluded that the algorithm converged in the TIR as well.

The retrieved value for the correction factor κ is 1.48 ± 0.33 and confirms thus the value of 1.4 to 1.5 projected based on Fig. 3.17. Furthermore, it corresponds to the

Channel	C11	C12
TIR forward model a priori	0.3173	0.6889
TIR forward model after convergence	0.4853 ± 0.0209	0.8548 ± 0.0393
Measurement	0.3885 ± 0.0897	0.9054 ± 0.0534

Table 3.1: TIR forward model and measured normalized radiances for November 30, 2016, 18.18 UTC. All radiances are expressed in W m^{-2} sr^{-1} μm^{-1}.

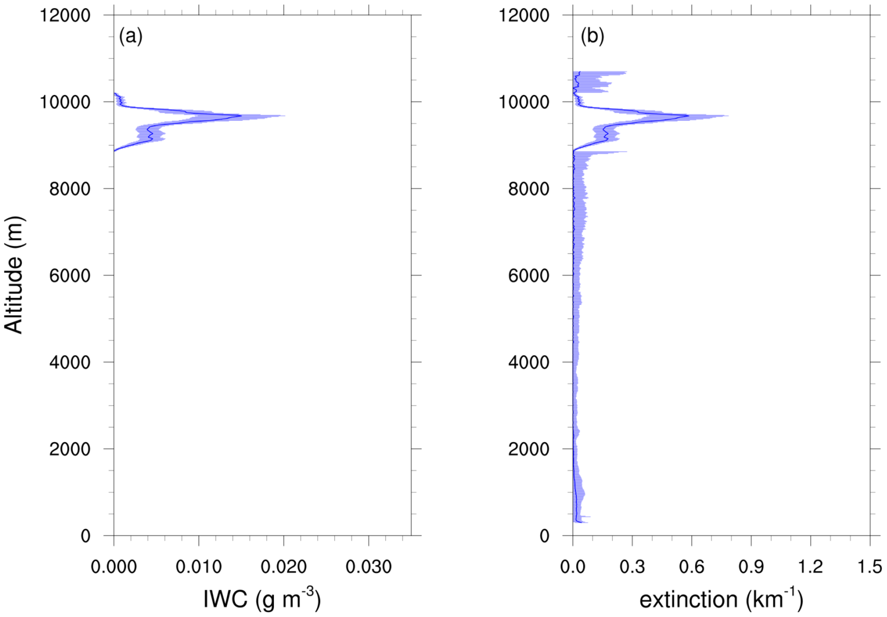

Figure 3.21: (a) Retrieved IWC and (b) extinction profiles from the synergy algorithm for the lidar profile measured on November 30, 2016 at 18.18 UTC (cf. Fig. 3.20). Shaded areas represent the error on the retrieved parameters. The COT obtained from the retrieved extinction profile is 0.239 ± 0.085 compared to 0.267 ± 0.126 from the transmission method (assuming $\eta = 0.75$).

range of 1.5 to 2.0 reported by Zhou and Yang (2015). The corresponding retrieved IWC and extinction profiles are shown in Fig. 3.21. In comparison to the result of the lidar only algorithm (cf. Fig. 3.10), it is obvious that the retrieved IWC and extinction are much smaller for the synergy algorithm because the backscatter-to-extinction ratio in the ice cloud is larger. The resulting IWP is with $6.13 \pm 2.19\,\mathrm{g\,m^{-2}}$ considerably smaller than the initial IWP of $10.32 \pm 2.47\,\mathrm{g\,m^{-2}}$ from the original lidar only algorithm.

Applying the synergy algorithm to the profile measured at 16.33 UTC results in a correction factor κ of 2.15 ± 0.33. Similarly as for the profile at 18.18 UTC, this value for the correction factor was predicted based on Fig. 3.18 in Sect. 3.5.2, since it corresponds to the range where the simulated TIR radiances converge to the measurements in Fig. 3.18. The according radiometer measurements and the TIR forward model after the last iteration step are presented in Table 3.2. Similarly to the profile at 18.18 UTC, the values of the TIR forward model after the iteration process are comprised within the error range of the measurements. Thus, it can be concluded that the algorithm found a solution allowing the lidar and TIR forward model to converge towards the corresponding measurements. For the retrieved

Channel	C11	C12
TIR forward model a priori	0.4012	0.7730
TIR forward model after convergence	0.5508 ± 0.0214	0.9220 ± 0.0395
Measurement	0.4925 ± 0.0793	0.9567 ± 0.0492

Table 3.2: TIR forward model and measured normalized radiances for November 30, 2016, 16.33 UTC. All radiances are expressed in $\mathrm{W\,m^{-2}\,sr^{-1}\,\mu m^{-1}}$.

correction factor, the large IWC peak at the cloud top which was observed from the original lidar only algorithm for $\kappa = 1.0$ (cf. Fig. 3.14), is reduced considerably resulting in a more realistic shape of the IWC profile. The IWP obtained from the synergy algorithm is $7.79 \pm 2.54\,\mathrm{g\,m^{-2}}$ compared to $32.21 \pm 8.93\,\mathrm{g\,m^{-2}}$ from the original lidar only algorithm. Hence, the retrieval with the synergy algorithm shows a very important decrease of IWP. However, the COT of 0.304 ± 0.099 obtained from the synergy algorithm is significantly smaller than the COT of 0.608 ± 0.186 obtained from the transmission method (for $\eta = 0.75$).

Finally, the temporal evolution of the retrieval results from the synergy algorithm for the time period from 15 to 19 UTC on November 30, 2016, is presented in Fig. 3.22. Figure 3.22 a recalls the measured lidar signal and the cloud detection, Fig. 3.22 b shows the retrieved IWC profiles and Fig. 3.22 c the retrieved correction factor κ for the phase function in the exact backscattering direction (blue) and the according lidar ratio in sr (red). A comparison of the COTs obtained from the synergy algorithm (blue) and the transmission method (red) is shown in Fig. 3.22 d. Finally, Fig. 3.22 e presents the TIR measurements and the forward model after the last iteration step together with the corresponding errors for channels C11 (blue) and C12 (red). This plot indicates that the majority of retrievals converges well in the TIR. Furthermore, all retrieval results in the other plots of this panel are only presented if the normalized cost function is considerably smaller than unity. Hence, the large number of results shown in this figure also indicates the generally good convergence of the synergy algorithm. The few retrievals that did not converge correspond to optically very thin clouds, for example around 18.4 UTC.

The retrieved lidar ratios from the synergy algorithm agree better with the literature as the lidar ratios from the variation of the lidar only algorithm constrained by the visible cloud optical thickness. For the geometrically and optically thicker cloud between 16 and 17.2 UTC where a considerable increase in the measured TIR radiances can be observed (cf. Fig. 3.19), the average value of the retrieved lidar

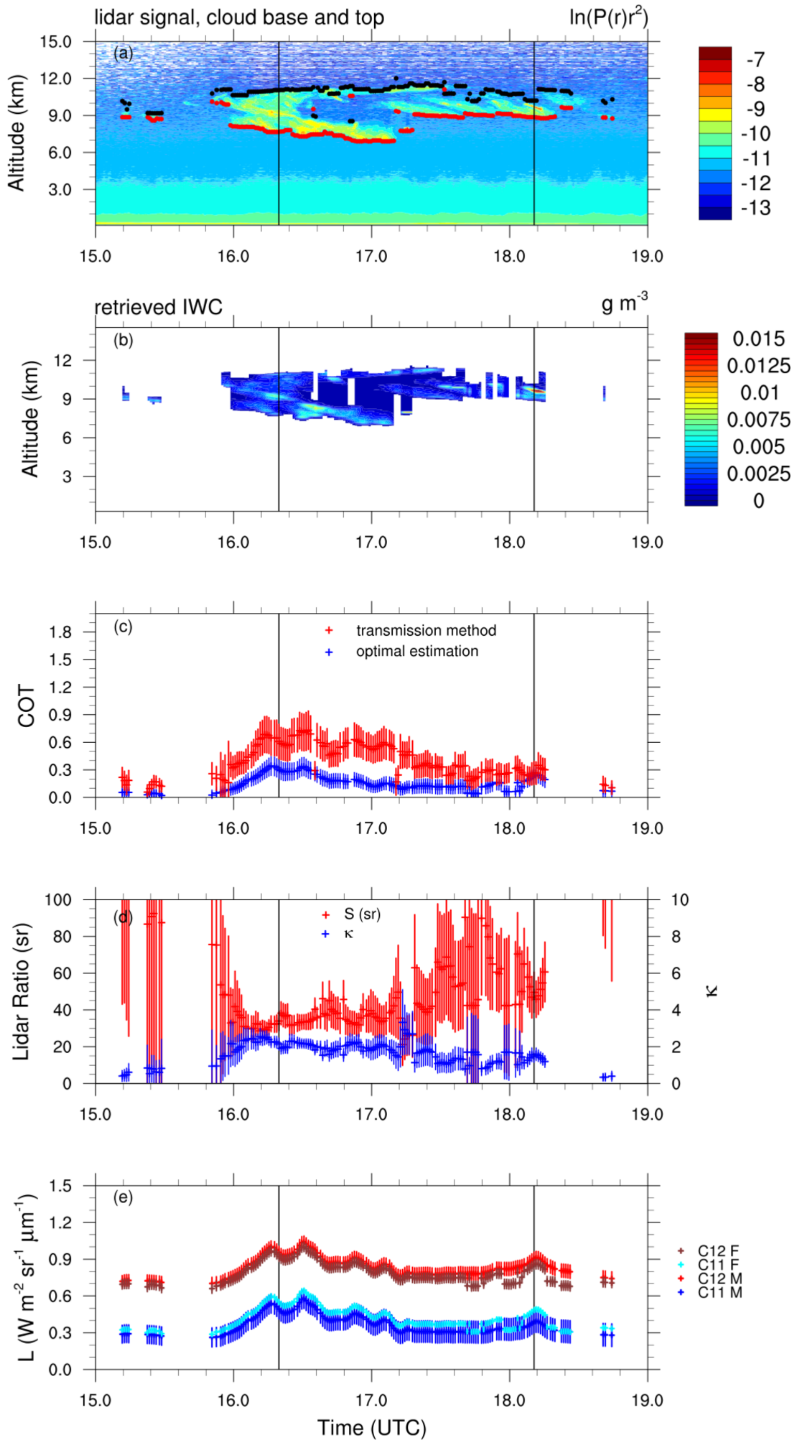

Figure 3.22: Retrieval results from the synergy algorithm for November 30, 2016, 15 to 19 UTC. (a) Logarithm of the range-corrected lidar signal overlaid by the cloud detection, (b) retrieved IWC profiles, (c) cloud optical thickness from the synergy algorithm (blue) and the transmission method introduced in Sect. 2.3.3 (red), (d) lidar ratio (sr) on the left axis (red) and retrieved factor κ on the right axis (blue), and (e) TIR radiometer measurements (C11 M and C12 M) and forward model after the last iteration step (C11 F and C12 F). The vertical black lines represent the two example profiles measured at 16.33 and 18.18 UTC.

ratio is $35.6 \pm 4.4\,\mathrm{sr}$ which agrees with the above-mentioned lidar ratios for cirrus clouds of 20 to 40 sr reported in the literature (e.g. Chen et al., 2002; Giannakaki et al., 2007; Seifert et al., 2007; Josset et al., 2012; Garnier et al., 2015). Between 17.2 and 18.3 UTC the retrieved lidar ratios are considerably larger (on average $52.6 \pm 15.3\,\mathrm{sr}$). However, the cloud observed during this period is optically very thin and the signal in the TIR radiances very small, so it is not surprising that our algorithm reaches its limit here. Furthermore, the values for the retrieved lidar ratios depend on the assumed multiple scattering factor which was set to $\eta = 0.75$ in the retrievals shown here. The comparison of the optical thickness obtained from the transmission method and the synergy algorithm presented in Fig. 3.22 d does not show a good agreement between both methods. The optical thickness from the synergy algorithm is systematically smaller than the optical thickness from the transmission method when the retrievals are performed with $\eta = 0.75$. A further discussion of the influence of the multiple scattering factor as well as the influence of the water vapour profile and the aerosol model on the retrieved parameters will be provided in Chapter 4.

3.7 Summary of the Methodology

Before proceeding to the discussion of the retrieval results, this section aims to summarize the methodology developed during this thesis. For this purpose, Fig. 3.23 shows a comparison of the retrieved IWP from the different algorithms presented in the course of this chapter.

In a first step, the algorithm to retrieve the IWP from the passive TIR radiometer measurements alone has been developed which uses, however, the information about the cloud altitude from the active lidar measurements. This algorithm assumes a constant IWC throughout the whole cloud layer which can be justified for ice clouds with a small IWP as has been shown by Feofilov et al. (2015). Furthermore, aerosols are not included in the radiative transfer calculations. The retrieved IWP from this algorithm is represented by the blue colour in Fig. 3.23.

Secondly, the information about the vertical distribution of the particles inside the cloud obtained from the lidar measurements has been investigated and an algorithm to retrieve IWC profiles from these measurements has been developed. The retrieval results from this algorithm strongly depend on the assumed backscatter-to-extinction ratio which is calculated from the BV2015 parametrization. The phase function in the exact backscattering direction, which defines the backscatter-to-extinction ratio, is poorly represented in this microphysical model and the IWP retrieved from the lidar only algorithm using this phase function directly (cf. Eq. 3.26) results generally in a larger IWP compared to the IWP obtained from the TIR only algorithm (black colour in Fig. 3.23). Hence, we presented two strategies to constrain the backscatter-to-extinction ratio: in a first step, the COT obtained from the transmission method of Young (1995) has been used for this purpose, and in a second step, we showed that the TIR radiometer measurements can also be used to constrain the backscatter-to-extinction ratio. These measurements have been integrated in the optimal estimation framework of the lidar only algorithm which constitutes the final synergy algorithm.

In both strategies, a correction factor for the backscatter-to-extinction ratio which can be interpreted as a correction factor for the phase function in the exact backscattering direction (cf. Eq. 3.46) is retrieved together with the IWC profile. In Fig. 3.23, the resulting IWP from the lidar only algorithm constrained by the COT from the transmission method is represented by the red colour. In the beginning of the period where the geometrically thick cloud has been observed, it is much

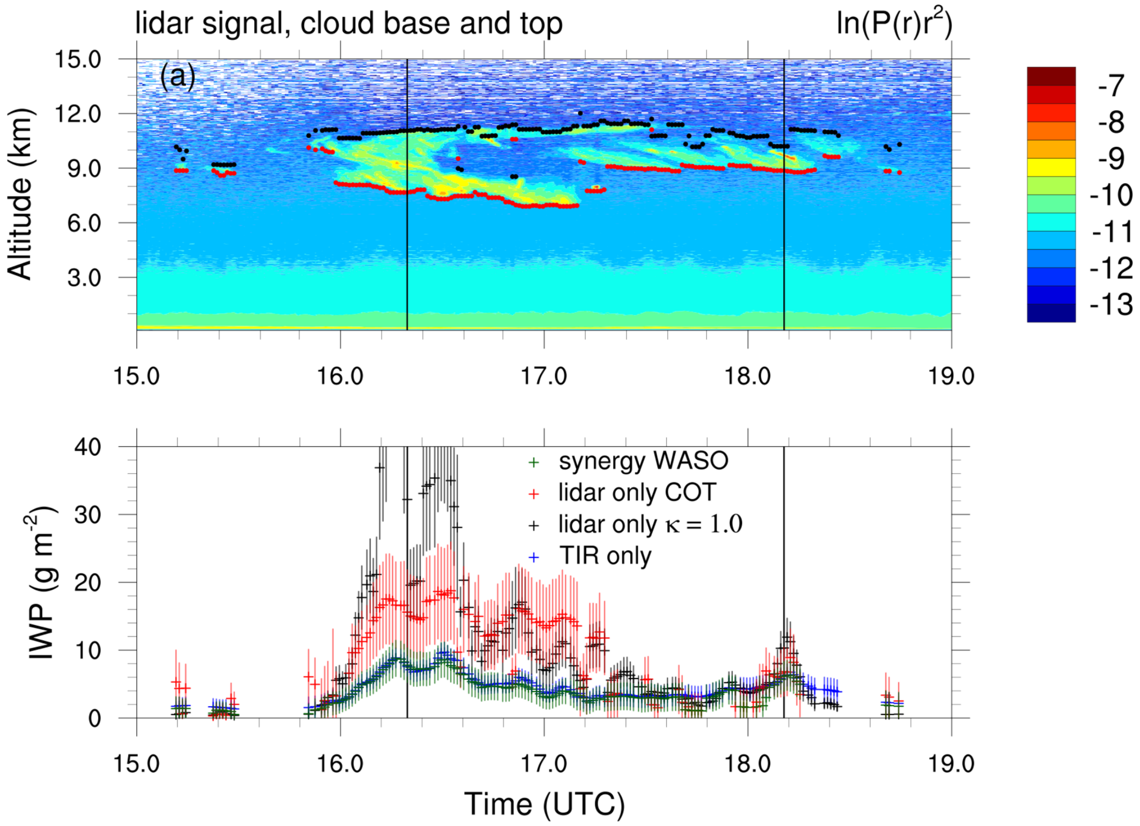

Figure 3.23: Comparison of the retrieval results from the different algorithms for November 30, 2016, 15 to 19 UTC. (a) Logarithm of the range-corrected lidar signal overlaid by the cloud detection, and (b) retrieved IWP from the different algorithms (blue: TIR only algorithm, black: original lidar only algorithm with the backscatter-to-extinction ratio calculated directly from the BV2015 parametrization (Eq. 3.26), red: lidar only algorithm constrained by the COT from the transmission method of Young (1995), and green: synergy algorithm assuming the WASO aerosol type (cf. Fig. 3.22)). The vertical black lines represent the two example profiles measured at 16.33 and 18.18 UTC.

smaller than the IWP obtained from the original lidar only algorithm. Nevertheless, it is still larger than the IWP from the TIR only algorithm. The IWP obtained from the synergy algorithm combining the TIR radiometer and lidar measurements (cf. Fig. 3.22) is represented by the green colour in Fig. 3.23. It is close to the IWP obtained from the TIR only algorithm since the IWP in the synergy algorithm is constrained by the TIR radiometer measurements. It should be noted that one improvement of the synergy algorithm compared to the TIR only algorithm is the integration of the information about the vertical distribution of the IWC inside the cloud in the TIR forward model. This information is accessible thanks to the active lidar measurements. Additionally, these measurements allow to consider aerosols in the layers below the cloud in the TIR forward model. However, as mentioned above the retrievals of the synergy algorithm depend on several non-retrieved parameters which will be discussed in the following chapter.

CHAPTER 4

Discussion

The retrieval results obtained from the algorithms presented in the previous chapter depend on several non-retrieved parameters. The aim of this chapter is to discuss the influence of these different quantities on the retrieved microphysics of cirrus clouds. The most important parameters are the multiple scattering factor, the water vapour profile and the assumed aerosol properties.

The first section of this chapter provides a discussion of the sensitivity of the retrieved quantities from the synergy algorithm to the parameters named above for the case study of November 30, 2016, introduced in Chapter 3. In a first step, the influence of the multiple scattering factor will be described. The multiple scattering factor has already been shown to have a large influence on the retrieval results from the variation of the lidar only algorithm which is constrained by the COT (cf. Figs. 3.15 and 3.16). Secondly, the impact of the atmospheric water vapour profile will be investigated before in a third step the influence of the two aerosol models described in Sect. 2.4.2 is tested.

However, the aerosol optical thickness as well as the amount of water vapour were rather small during November 30, 2016. Hence, the second part of this chapter will introduce a second case study dealing with April 18, 2018, where a longer period of a cirrus cloud in a constant altitude and of quite constant geometrical thickness has been observed. We will present and compare the retrievals of all algorithms introduced in Chapter 3 and discuss the difficulties in retrieving cirrus cloud properties during this case study due to different factors, in particular due to a rather high aerosol optical thickness and a more important amount of water vapour in the atmosphere.

The last section of this chapter summarizes the results from the sensitivity studies and the second case study. It should be noted that due to the poor amount of available retrievals (only 15 days with successful retrievals which are spread irregularly throughout the year, cf. Table 2.6), no statistical analysis of the retrieved cloud properties has been integrated in this manuscript.

4.1 Sensitivity Studies for the Case Study of November 30, 2016

This section aims to discuss, in this order, the influence of the multiple scattering factor, the atmospheric water vapour profile and the aerosol model on the retrieval results from our synergy algorithm by analysing the case study of November 30, 2016, with regard to these parameters. All retrievals shown in this section have been performed by only taking the TIR radiometer channels C11 and C12 into account. Channel C09 has been excluded for the reasons discussed in the previous chapter.

4.1.1 Influence of the Multiple Scattering Factor

It has been shown in Sect. 3.5.1 that the multiple scattering factor has an important influence on the retrieval results obtained from the variation of the lidar only algorithm which is constrained by the COT. To recall, due to multiple scattering by atmospheric particles, more radiation is returned to the lidar telescope than would be in case of one single scattering process per particle. Hence, the experimentally measured optical thickness is reduced compared to the real COT (Platt, 1979). The COT obtained from the transmission method of Young (1995) introduced in Sect. 2.3.3 is thus an effective optical thickness, $\tau^{\star}_{\text{cld}}$, linked to the real COT via $\tau^{\star}_{\text{cld}} = \eta\, \tau_{\text{cld}}$. As discussed in Sect. 2.3.1, the value of η depends on the microphysical properties of the cloud, the distance between the cloud and the instrument as well as the characteristics of the instrument, in particular the FOV and the divergence of the laser beam. According to Platt (1973), it typically varies between 0.5 and 1. Sassen and Comstock (2001) suggested a value of 0.9 for sub-visual cirrus, 0.8 for semi-transparent cirrus and 0.6 to 0.7 for opaque cirrus.

In the variation of the lidar only algorithm which is constrained by the COT, the effective COT derived from the transmission method is divided by the assumed multiple scattering factor to be consistent with the optimal estimation method since this assumed multiple scattering factor is also taken into account in the lidar forward model (cf. Eq. 3.24). Thus, the retrieval results of this algorithm strongly depend on the assumed multiple scattering factor which has been set to $\eta = 0.75$ in a first approximation as discussed in Sect. 3.4.1. However, in the synergy algorithm the COT is constrained by the TIR radiometer measurements. In the following, we will

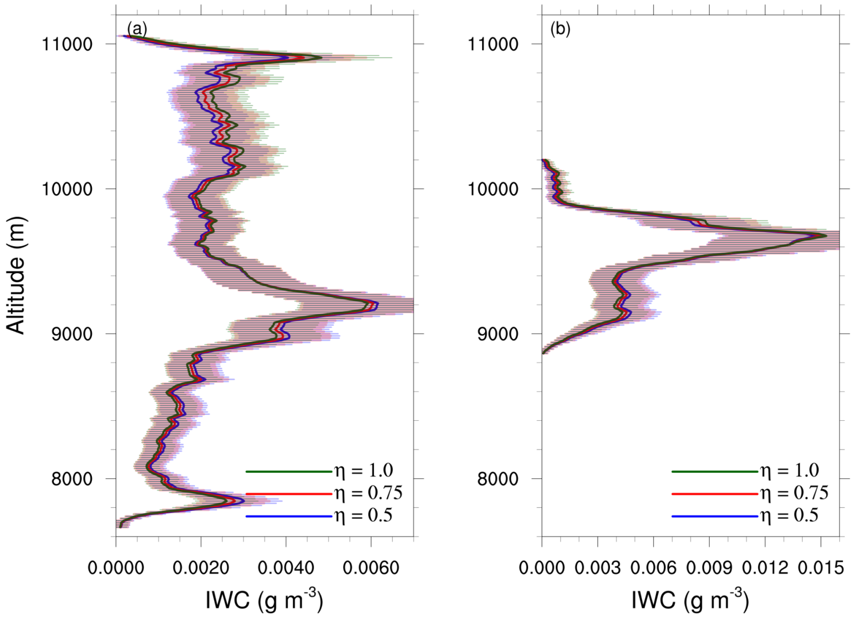

Figure 4.1: Dependence of the IWC retrieved from the synergy algorithm on the multiple scattering factor for the lidar profiles measured on November 30, 2016, at (a) 16.33 UTC and (b) 18.18 UTC. Shaded zones represent the error on the retrieval and the different colours stand for different multiple scattering factors (blue: $\eta = 0.5$, red: $\eta = 0.75$ and green: $\eta = 1.0$).

investigate the influence of a varying multiple scattering factor between $\eta = 0.5$ and $\eta = 1.0$ on the retrieved quantities from the synergy algorithm.

Figure 4.1 presents the retrieved IWC profiles from the synergy algorithm for multiple scattering factors of $\eta = 0.5$ (blue), $\eta = 0.75$ (red), and $\eta = 1.0$ (green) for the two example profiles measured on November 30, 2016, at 16.33 UTC (Fig. 4.1 a) and 18.18 UTC (Fig. 4.1 b) which have been introduced in Sects. 3.4.3 and 3.5.2. Both profiles show in the lower portion of the cloud a decrease of the IWC with increasing multiple scattering factor, whereas in the upper portion the IWC is enhanced for a larger multiple scattering factor. The assumption of single scattering ($\eta = 1.0$) leads to a decrease of the second term on the right-hand side of the lidar forward model (cf. Eq. 3.24). This decrease has to be compensated by the first term to match the measurement. Consequently, the correction factor κ increases because the total amount of ice inside the cloud is constrained by the TIR radiances which means the extinction cannot change significantly. However, since the correction factor κ is assumed to be constant over the whole cloud, the adjustment of κ results in an average value corresponding to an altitude approximately in the middle of the cloud where the retrieved extinction is equal for all assumed multiple scattering factors.

η	IWP ($\mathrm{g\,m^{-2}}$)	COT	κ
0.5	6.11 ± 2.19	0.238 ± 0.085	1.39 ± 0.33
0.75	6.13 ± 2.19	0.239 ± 0.085	1.48 ± 0.33
1.0	6.15 ± 2.19	0.240 ± 0.086	1.57 ± 0.33

Table 4.1: Dependence of the retrieved quantities from the synergy algorithm on the multiple scattering factor η for November 30, 2016, 18.18 UTC.

η	IWP ($\mathrm{g\,m^{-2}}$)	COT	κ
0.5	7.72 ± 2.53	0.301 ± 0.099	1.99 ± 0.33
0.75	7.79 ± 2.54	0.304 ± 0.099	2.15 ± 0.33
1.0	7.87 ± 2.56	0.306 ± 0.100	2.31 ± 0.34

Table 4.2: Dependence of the retrieved quantities from the synergy algorithm on the multiple scattering factor η for November 30, 2016, 16.33 UTC.

This correction factor κ is too large for the lower layers of the cloud which leads to a reduction of the extinction and hence the IWC for a multiple scattering factor of $\eta = 1.0$ compared to $\eta = 0.75$ and $\eta = 0.5$. At the same time, it is too small for the upper layers of the cloud leading to an increase of extinction and IWC for $\eta = 1.0$ compared to smaller multiple scattering factors. Tables 4.1 and 4.2 summarize the retrieved IWP, COT and correction factor κ for the two profiles measured at 18.18 UTC and 16.33 UTC, respectively. For both profiles it is obvious that the IWP and the COT are almost constant for the three multiple scattering factors tested here since they are constrained by the TIR radiances. On the other hand, the retrieval of the correction factor κ slightly increases with increasing multiple scattering factor to compensate the second term on the right-hand side of Eq. 3.24 which decreases with increasing multiple scattering factor while all other quantities remain almost constant.

Figure 4.2 underlines these findings by comparing the retrieval results obtained from the synergy algorithm for the three different multiple scattering factors. The retrievals were performed considering the atmospheric profile from the ECMWF reanalysis of 12 UTC and the WASO aerosol model. The retrieved IWP and COT shown in Figs. 4.2 b and 4.2 c, respectively, are almost equal for the three different multiple scattering factors over the whole time period between 15 and 19 UTC on November 30, 2016. On the other hand, the retrieved correction factor κ for the phase function in backscattering direction (Fig. 4.2 d) is increasing with increasing

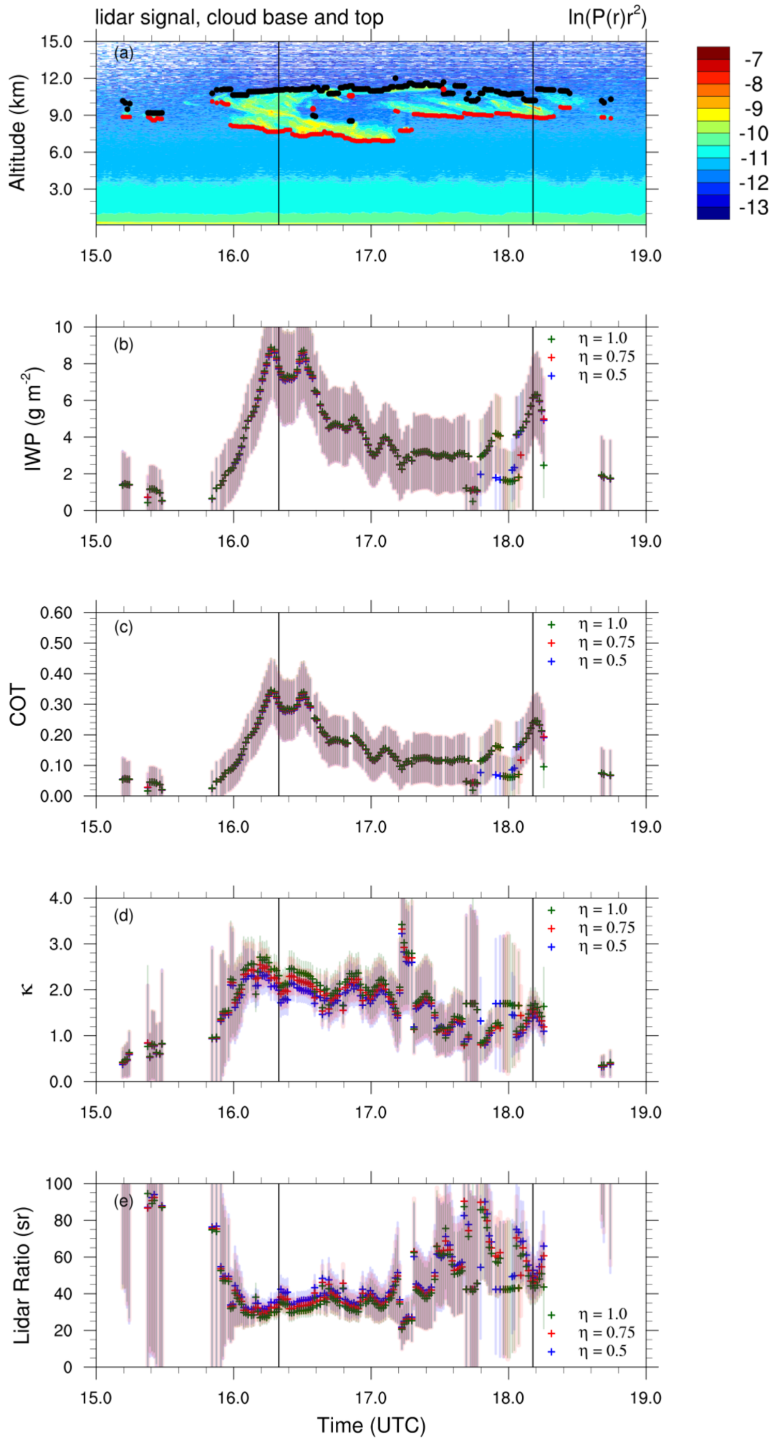

Figure 4.2: Retrieval results from the synergy algorithm for different multiple scattering factors considering the atmospheric profile from ECMWF reanalysis of 12 UTC and the WASO aerosol model for November 30, 2016, 15 to 19 UTC. (a) Logarithm of the range-corrected lidar signal overlaid by the cloud detection, (b) retrieved IWP, (c) retrieved COT, (d) retrieved correction factor κ, and (e) retrieved lidar ratio (sr). Blue: $\eta = 0.5$, red: $\eta = 0.75$ and green: $\eta = 1.0$.

Time period	$\eta = 0.5$	$\eta = 0.75$	$\eta = 1.0$
16.0 - 16.6 UTC	36.1 ± 3.7 sr	33.5 ± 3.3 sr	31.6 ± 3.4 sr
16.0 - 17.2 UTC	37.8 ± 4.4 sr	35.6 ± 4.4 sr	33.7 ± 4.4 sr
17.2 - 18.3 UTC	53.8 ± 15.0 sr	52.6 ± 15.3 sr	51.2 ± 15.1 sr
Total	44.8 ± 13.1 sr	43.2 ± 13.6 sr	41.7 ± 13.8 sr

Table 4.3: Dependence of the retrieved average lidar ratios from the synergy algorithm on the multiple scattering factor η for different time periods of November 30, 2016.

multiple scattering factor which corresponds to a decrease of the retrieved lidar ratio (Fig. 4.2 e). Table 4.3 summarizes the average lidar ratios for the complete time period between 16 and 18.3 UTC (last line), as well as for smaller phases within this period. It should be noted that some of these values for $\eta = 0.75$ have already been discussed in Sect. 3.6.2. The observed cloud has been divided into two parts (cf. Sect. 3.3.2): the phase between 16 and 17.2 UTC with a cloud base altitude between approximately 7 and 8 km and a larger optical thickness compared to the second period between 17.2 and 18.3 UTC where an optically thin cloud with a higher cloud base altitude has been observed. The first period is further sub-divided into the geometrically thick cloud until around 16.6 UTC, and the phase between 16.6 and 17.2 UTC where two cloud layers were present. The values reported in Table 4.3 suggest that the decrease of the lidar ratio with increasing multiple scattering factor is rather small and that the average of the retrieved lidar ratios for multiple scattering factors of $\eta = 0.5$ as well as $\eta = 1.0$ range within the standard deviation of the average lidar ratio obtained for the initially assumed multiple scattering factor of $\eta = 0.75$ for all considered time periods. As a conclusion, the impact of the multiple scattering factor on the retrieved correction factor κ (and consequently on the lidar ratio) is much smaller in the synergy algorithm than in the variation of the lidar only algorithm which is constrained by the COT derived from the transmission method. This is due to the fact that the constraint on the IWP and hence on the optical thickness is obtained from independent measurements in the synergy algorithm.

4.1.2 Influence of the Water Vapour Profile

In this section, the dependence of the retrieved microphysical properties of cirrus clouds on the assumed water vapour profile is investigated. It should be noted that the retrievals performed to analyse this impact assume a multiple scattering factor of $\eta = 0.75$ and the WASO aerosol model.

As discussed above, the profile of water vapour is obtained from the ECMWF reanalysis data introduced in Sect. 2.4.1. For November 30, 2016, the profile of 12 UTC has been shown to correspond best to the TIR radiometer measurements since radiative transfer simulations for clear sky conditions (taking into account the aerosols present in the atmosphere) using this profile reproduced the measurements under clear sky conditions fairly well. To test the influence of the water vapour profile on the retrievals obtained from the synergy algorithm, the water vapour profile from the reanalysis has been modified by adding 5 % and 10 % of the specific humidity of each individual layer to the according layer. This results in an increase of 5 % or 10 %, respectively, of the total amount of water vapour as well. It should be noted that the initial water vapour profile is characterized by a rather small total amount of water vapour of $0.622\,\mathrm{g\,cm^{-2}}$ and adding 5 % or 10 % still results in a rather dry atmosphere. For the case study of April 18, 2018, presented in Sect. 4.2, the atmospheric profile is characterized by a larger amount of moisture.

Figure 4.3 shows the measurements of channels C11 and C12 considered in the retrievals presented here together with the clear sky simulations taking into account the aerosol extinction according to the WASO aerosol model for the initial water vapour profile from the reanalysis of 12 UTC (solid lines) and the modified water vapour profiles by adding 5 % (dashed lines) and 10 % (dot-dashed lines) of the specific humidity. It is obvious that a larger amount of water vapour increases the simulated clear sky radiances for both channels. However, almost all simulated radiances are situated within the error ranges of the measurements, except for the simulation with the initial water vapour profile for channel C12 which is nevertheless very close.

The retrieved IWC profiles from the synergy algorithm taking into account the initial and modified water vapour profiles are presented in Fig. 4.4 for the two example profiles of 16.33 UTC (Fig. 4.4 a) and 18.18 UTC (Fig. 4.4 b). The retrieval performed using the initial water vapour profile (blue) results in a higher IWC in all layers for both profiles compared to the retrievals with a larger amount of water vapour in the atmospheric column. This is due to an increasing contribution of the atmospheric layers below the cloud to the simulated radiances in case of a larger amount of water vapour. Therefore, a decrease in the amount of ice is required to match the measurements. For the profile measured at 18.18 UTC the IWP is

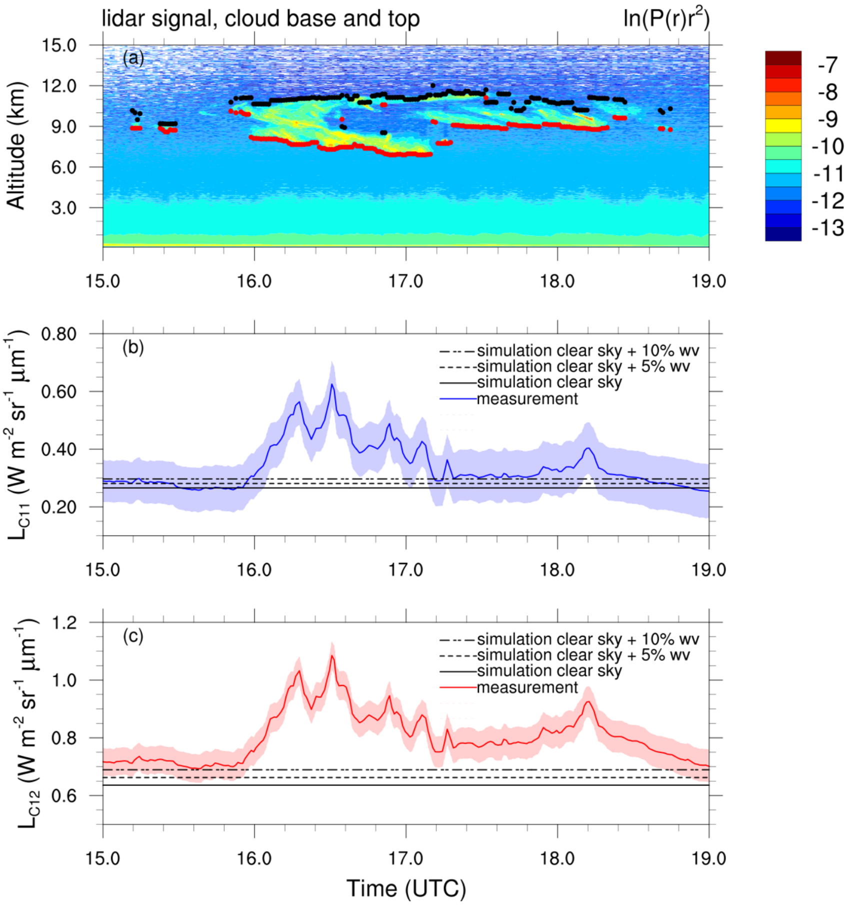

Figure 4.3: TIR radiometer measurements and clear sky simulations including aerosols (WASO) with the ECMWF reanalysis profile of 12 UTC (solid lines) and with modified amounts of water vapour by adding 5 % (dashed lines) and 10 % (dot-dashed lines) to each layer, respectively, for November 30, 2016, 15 to 19 UTC. (a) Logarithm of the range-corrected lidar signal overlaid by the cloud detection, (b) radiance of channel C11, and (c) radiance of channel C12. The shaded zones in plots (b) and (c) represent the measurement error.

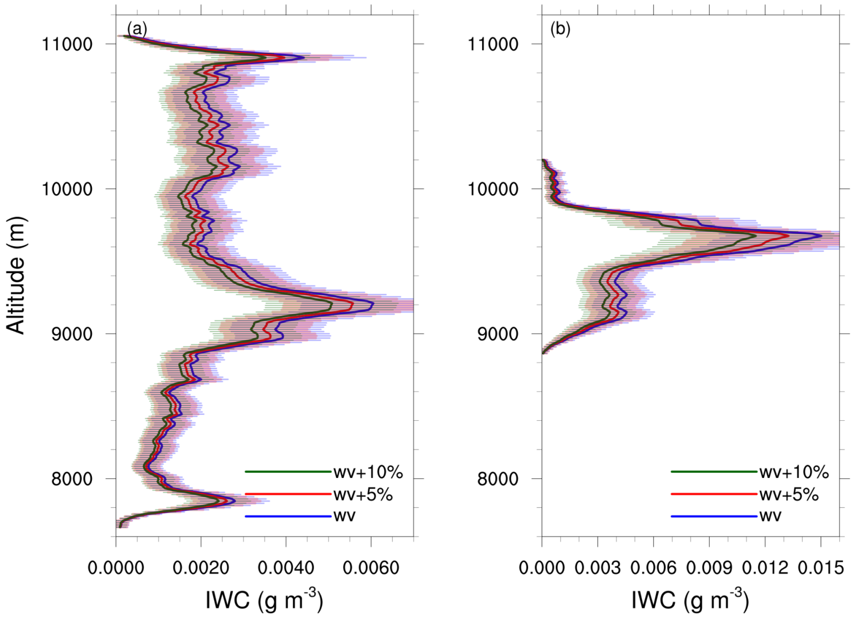

Figure 4.4: Dependence of the IWC retrieved from the synergy algorithm on the water vapour profile for the lidar profiles measured on November 30, 2016, at (a) 16.33 UTC and (b) 18.18 UTC. Shaded zones represent the error on the retrieval and the different colours stand for different water vapour profiles (blue: initial profile from ECMWF reanalysis of November 30, 2016, 12 UTC, red: 5 % have been added to each layer of the initial profile, and green: 10 % have been added to each layer of the initial profile).

reduced to $4.75 \pm 1.99\,\mathrm{g\,m^{-2}}$ for the profile where 10 % of water vapour have been added compared to $6.13 \pm 2.19\,\mathrm{g\,m^{-2}}$ for the initial profile. Similarly, the IWP for the profile measured at 16.33 UTC is reduced from $7.79 \pm 2.54\,\mathrm{g\,m^{-2}}$ obtained with the initial water vapour profile to $6.46 \pm 2.29\,\mathrm{g\,m^{-2}}$ obtained with the modified profile where 10 % of water vapour have been added. Consequently, the optical thickness is reduced as well resulting in an increasing correction factor κ since the backscatter-to-extinction ratio has to increase in order to compensate the decrease in the extinction. The retrieval results for both profiles are summarized in Tables 4.4 (for 18.18 UTC) and 4.5 (for 16.33 UTC).

Figure 4.5 presents the temporal evolution of the retrieval results of the synergy algorithm performed with $\eta = 0.75$ and assuming the WASO aerosol type, considering the initial and modified water vapour profiles for the whole case study period between 15 and 19 UTC. As indicated by the two example profiles, the retrieved IWP and COT decrease with increasing amount of water vapour in the atmospheric column. For the optically thicker cloud between 16 and 17.2 UTC this decrease in IWP and COT is smaller than for the optically very thin cloud between 17.2 and

Total water vapour ($\mathrm{g\,cm^{-2}}$)	IWP ($\mathrm{g\,m^{-2}}$)	COT	κ
0.622	6.13 ± 2.19	0.239 ± 0.085	1.48 ± 0.33
0.653	5.44 ± 2.09	0.212 ± 0.081	1.63 ± 0.41
0.684	4.75 ± 1.99	0.185 ± 0.078	1.82 ± 0.54

Table 4.4: Dependence of the retrieved quantities from the synergy algorithm on the total amount of water vapour in the atmospheric column for November 30, 2016, 18.18 UTC.

Total water vapour ($\mathrm{g\,cm^{-2}}$)	IWP ($\mathrm{g\,m^{-2}}$)	COT	κ
0.622	7.79 ± 2.54	0.304 ± 0.099	2.15 ± 0.33
0.653	7.13 ± 2.41	0.278 ± 0.094	2.30 ± 0.39
0.684	6.46 ± 2.29	0.252 ± 0.089	2.47 ± 0.48

Table 4.5: Dependence of the retrieved quantities from the synergy algorithm on the total amount of water vapour in the atmospheric column for November 30, 2016, 16.33 UTC.

18.3 UTC. Thus, the increase of the correction factor κ (and according decrease of the lidar ratio) with increasing moisture in the atmosphere is rather small for the first period. The average lidar ratio between 16 and 17.2 UTC is reduced from $35.6 \pm 4.4\,\mathrm{sr}$ to $28.2 \pm 3.3\,\mathrm{sr}$ between the initial profile and the profile where 10 % of water vapour have been added. For the second period, the influence of an increasing moisture in the atmosphere on the retrieved correction factor κ and the lidar ratio is more important resulting in an average lidar ratio of $41.4 \pm 12.5\,\mathrm{sr}$ for the modified water profile by adding 10 % compared to $52.6 \pm 15.3\,\mathrm{sr}$ for the initial water vapour profile (cf. Table 4.6). Furthermore, the retrieved correction factors κ for the phase function in backscattering direction during the second period with the optically thin cloud are shown to be rather irregular indicating that the observed cirrus may be optically too thin to reasonably retrieve the microphysical properties of the cloud, particularly with increasing moisture in the atmosphere. This is not surprising since it has been shown by Dubuisson et al. (2008) that the sensitivity of ground-based TIR radiometer data is weaker in a moist than in a dry atmosphere.

However, the error assigned to the assumed water vapour profile for the retrievals presented here has been set to 10 % as mentioned in Sect. 3.6.1. This large error has been chosen to account for the coarse spatial (0.1° x 0.1° latitude/longitude grid) and temporal (four time steps at 0, 6, 12 and 18 UTC) resolution of the reanalysis data which might not be sufficiently exact to represent local water vapour variations

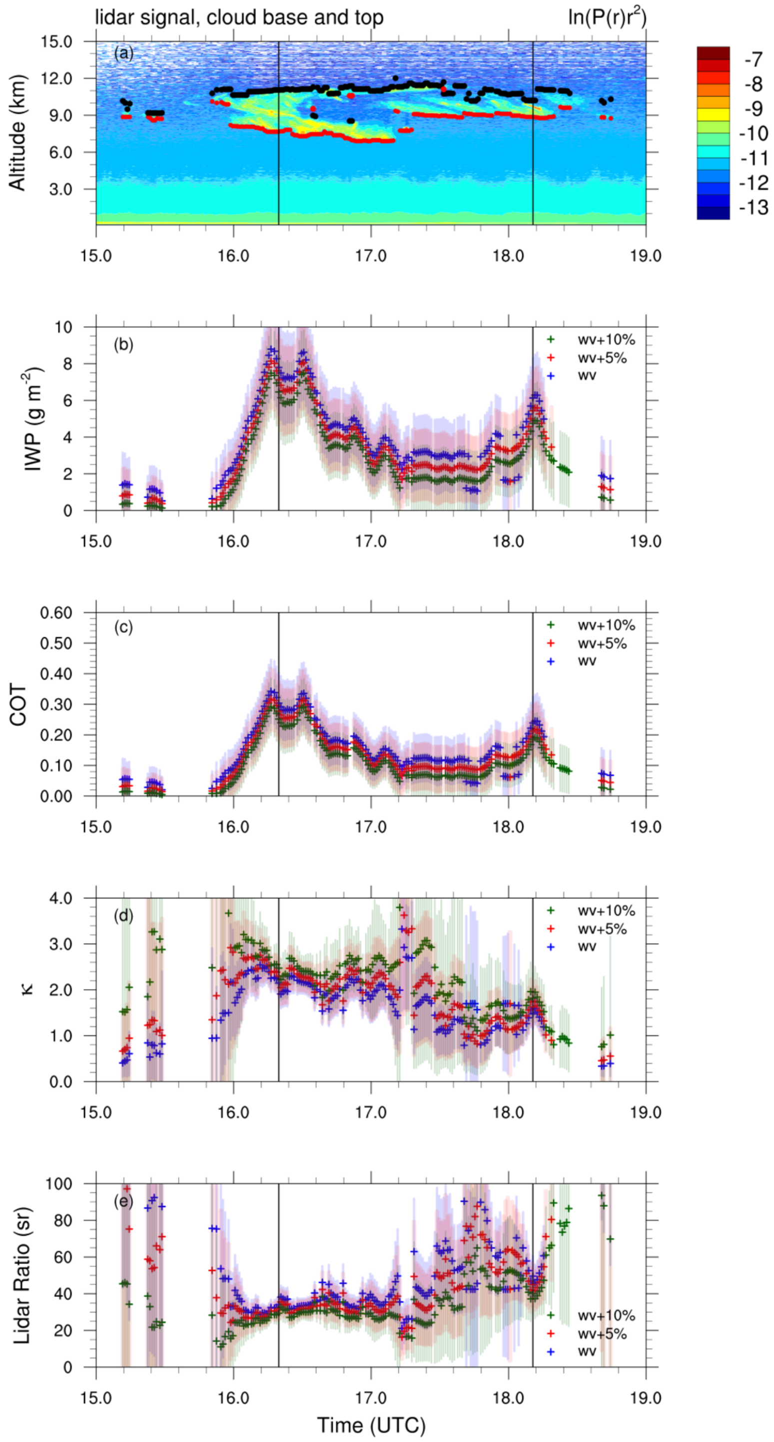

Figure 4.5: Retrieval results from the synergy algorithm for different water vapour profiles performed with $\eta = 0.75$ and considering the WASO aerosol model for November 30, 2016, 15 to 19 UTC. (a) Logarithm of the range-corrected lidar signal overlaid by the cloud detection, (b) retrieved IWP, (c) retrieved COT, (d) retrieved correction factor κ, and (e) retrieved lidar ratio (sr). Blue: initial water vapour profile from ECMWF reanalysis of November 30, 2016, 12 UTC, red and green: 5 % and 10 % water vapour have been added to each layer of the initial profile, respectively.

Time period	$\mathrm{wv} = 0.622\,\mathrm{g\,cm^{-2}}$	$\mathrm{wv} = 0.653\,\mathrm{g\,cm^{-2}}$	$\mathrm{wv} = 0.684\,\mathrm{g\,cm^{-2}}$
16.0 - 16.6 UTC	$33.5 \pm 3.3\,\mathrm{sr}$	$30.6 \pm 2.7\,\mathrm{sr}$	$27.7 \pm 3.1\,\mathrm{sr}$
16.0 - 17.2 UTC	$35.6 \pm 4.4\,\mathrm{sr}$	$32.0 \pm 3.4\,\mathrm{sr}$	$28.2 \pm 3.3\,\mathrm{sr}$
17.2 - 18.3 UTC	$52.6 \pm 15.3\,\mathrm{sr}$	$50.9 \pm 16.2\,\mathrm{sr}$	$41.4 \pm 12.5\,\mathrm{sr}$
Total	$43.2 \pm 13.6\,\mathrm{sr}$	$40.8 \pm 14.7\,\mathrm{sr}$	$34.4 \pm 11.0\,\mathrm{sr}$

Table 4.6: Dependence of the retrieved average lidar ratios from the synergy algorithm on the total amount of water vapour for different time periods of November 30, 2016.

as discussed in Sect. 3.3. Due to this large error, the error ranges of the retrieved quantities are large as well and as a consequence they overlap for the three different retrievals shown here although the retrieved values for the optically thin cloud are quite different. As a conclusion, a better characterization of the local water vapour profile during the measurement would considerably reduce the error on the retrieved quantities due to a poor knowledge of the water vapour profile and thereby enhance the quality of the retrievals.

4.1.3 Influence of the Aerosol Model

All retrievals presented in Chapter 3 have been performed applying the WASO aerosol model from the OPAC database (Hess et al., 1998b) which is supposed to represent a water soluble urban aerosol. In a first approximation, this seems to be a reasonable assumption since the measurement platform of the LOA is situated in the Lille metropolitan area (cf. Sect. 2.1). However, these aerosol characteristics are not necessarily representative for all measurement periods. This section aims to investigate the influence on the retrievals obtained from the synergy algorithm if a different aerosol type is assumed. This second aerosol model which will be tested here is the water-insoluble more absorbent INSO aerosol type introduced in Sect. 2.4.2. The retrievals presented here assume a multiple scattering factor of $\eta = 0.75$ and the original water vapour profile from the reanalysis data of 12 UTC.

Figure 3.19 presented in the previous chapter shows the influence on the clear sky simulations of taking into account the two different aerosol models. The simulated radiances under clear sky conditions are slightly larger for the INSO aerosol type (dashed lines) than for the WASO aerosol type (solid lines) since the INSO aerosol is more absorbent. Thus, it can be expected that changing the aerosol model from WASO to INSO leads to a reduction of the retrieved IWC, similarly to the impact

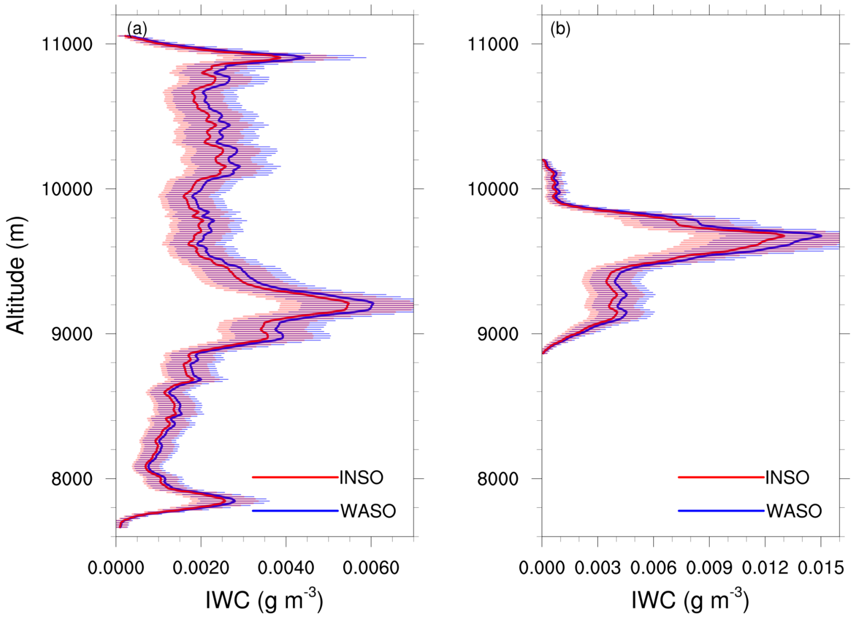

Figure 4.6: Dependence of the IWC retrieved from the synergy algorithm on the aerosol model for the lidar profiles measured on November 30, 2016 at (a) 16.33 UTC and (b) 18.18 UTC. Shaded zones represent the error on the retrieval and the different colours stand for the two aerosol models (blue: WASO, red: INSO).

of adding water vapour to the atmospheric column which has been discussed in the previous section.

This hypothesis is confirmed in Fig. 4.6 which presents the retrieved IWC profiles considering the two aerosol models for the two example profiles measured at 16.33 UTC and 18.18 UTC. In both examples, the retrieved IWC obtained assuming the INSO aerosol model (represented by the red line) is smaller in all layers compared to the retrieval result obtained assuming the WASO aerosol type (blue). The resulting IWP from the retrieval performed with the WASO aerosol model is $6.13 \pm 2.19\,\mathrm{g\,m^{-2}}$ compared to $5.34 \pm 2.06\,\mathrm{g\,m^{-2}}$ using the INSO aerosol type for the profile measured at 18.18 UTC as well as $7.79 \pm 2.54\,\mathrm{g\,m^{-2}}$ and $6.98 \pm 2.37\,\mathrm{g\,m^{-2}}$, respectively, for the profile measured at 16.33 UTC. The corresponding COT and the retrievals of the correction factor κ are presented in Tables 4.7 (for 18.18 UTC) and 4.8 (for 16.33 UTC). As discussed in the case of modifying the water vapour profile, the decrease in the retrieved IWP and COT has to be compensated by an increase of the backscatter-to-extinction ratio and hence results in an increase of the correction factor κ for the phase function in backscattering direction.

Aerosol model	IWP ($\mathrm{g\,m^{-2}}$)	COT	κ
WASO	6.13 ± 2.19	0.239 ± 0.085	1.48 ± 0.33
INSO	5.34 ± 2.06	0.208 ± 0.080	1.63 ± 0.41

Table 4.7: Dependence of the retrieved quantities from the synergy algorithm on the aerosol model for November 30, 2016, 18.18 UTC.

Aerosol model	IWP ($\mathrm{g\,m^{-2}}$)	COT	κ
WASO	7.79 ± 2.54	0.304 ± 0.099	2.15 ± 0.33
INSO	6.98 ± 2.37	0.272 ± 0.092	2.31 ± 0.39

Table 4.8: Dependence of the retrieved quantities from the synergy algorithm on the aerosol model for November 30, 2016, 16.33 UTC.

Figure 4.7 shows the comparison of the retrieval results obtained assuming $\eta = 0.75$ and considering the atmospheric profile from the ECMWF reanalysis of 12 UTC for both aerosol models for the whole time period of the case study between 15 and 19 UTC. As mentioned above, the retrieved COT and IWP are smaller for the INSO aerosol model (red) than for the WASO aerosol type (blue) and hence the correction factors κ are larger which leads to a smaller lidar ratio. Similar to the results obtained for the modified water vapour profile, this increase of κ and the corresponding decrease of the lidar ratio is rather small for the optically thicker cloud in the first half of the period. On the other hand, the retrievals for the optically thin cloud in the second half show a larger impact of changing the aerosol model together with considerably larger uncertainties on the retrieved parameters due to the small signal in the TIR radiometer measurements of the optically thin cirrus.

The average values of the retrieved lidar ratios are summarized in Table 4.9 for the different time periods for both aerosol models. By comparing these average lidar ratios to the lidar ratios reported in Table 4.6, it can be remarked that changing the aerosol model from WASO to INSO leads to a similar effect like adding 5 % of water vapour to every layer of the water vapour profile obtained from the ECMWF reanalysis of 12 UTC. Thus, it is less strong than the impact of adding 10 % of water vapour. Nevertheless, similarly to the conclusion drawn in the previous section for modifying the water vapour profile, it can be deduced here that a better characterization of the aerosols which are actually present during the measurement would help to reduce the uncertainties on the retrieved microphysics of the cirrus cloud.

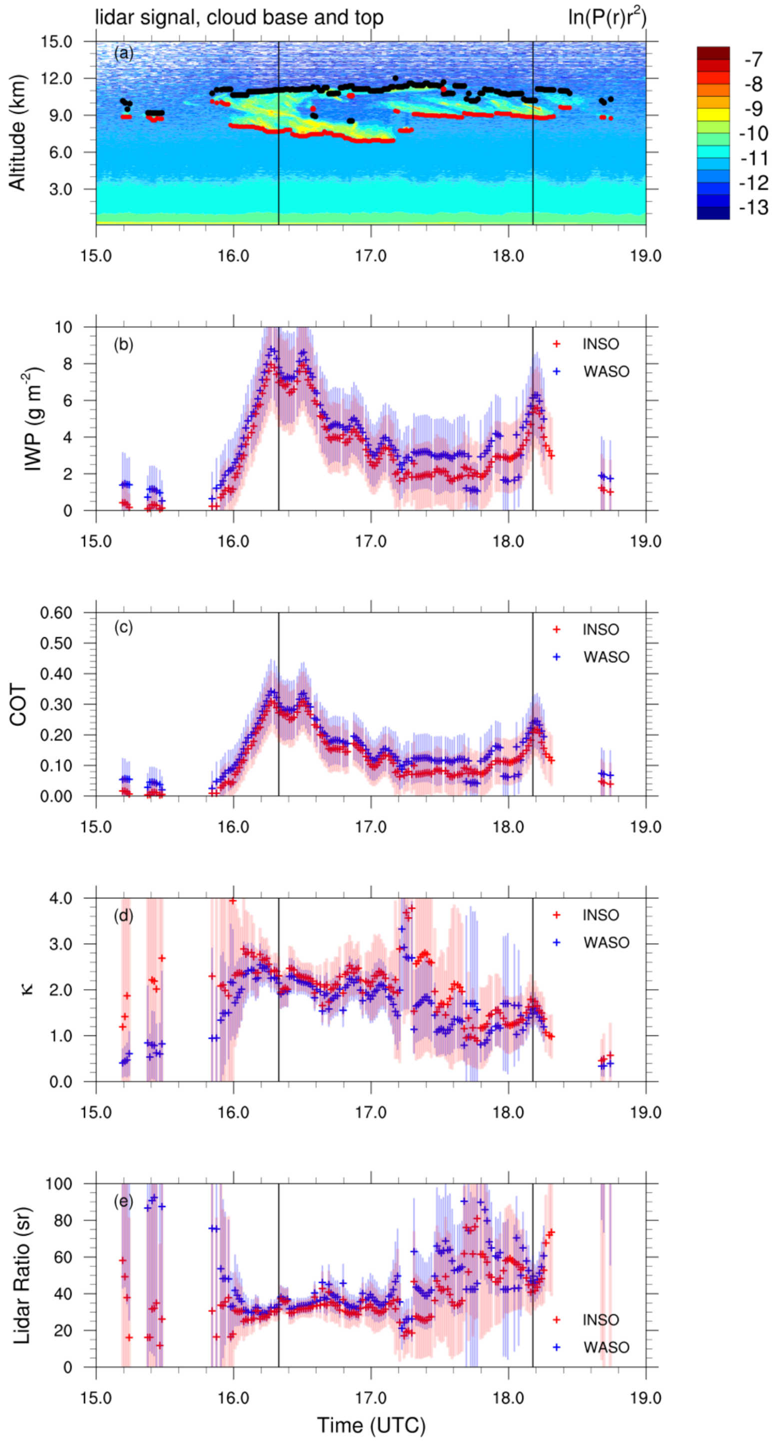

Figure 4.7: Retrieval results from the synergy algorithm for the two different aerosol models performed with $\eta = 0.75$ and considering the atmospheric profile from the ECMWF reanalysis of 12 UTC for November 30, 2016, 15 to 19 UTC. (a) Logarithm of the range-corrected lidar signal overlaid by the cloud detection, (b) retrieved IWP, (c) retrieved COT, (d) retrieved correction factor κ, and (e) retrieved lidar ratio (sr). The aerosol model WASO is represented in blue and INSO in red.

Time period	WASO	INSO
16.0 - 16.6 UTC	33.5 ± 3.3 sr	30.6 ± 3.3 sr
16.0 - 17.2 UTC	35.6 ± 4.4 sr	31.7 ± 3.6 sr
17.2 - 18.3 UTC	52.6 ± 15.3 sr	46.9 ± 15.5 sr
Total	43.2 ± 13.6 sr	38.8 ± 13.3 sr

Table 4.9: Dependence of the retrieved average lidar ratios from the synergy algorithm on the aerosol model for different time periods of November 30, 2016.

However, the case study of November 30, 2016, is characterized by a cold and dry atmosphere as well as a low aerosol optical thickness. This corresponds to favourable conditions for the application of our algorithm because under these conditions the influence of the atmosphere on the TIR radiometer measurements is small compared to the influence of the cloud. In the following, we will introduce a second case study where quite different atmospheric conditions have been observed.

4.2 The Case Study of April 18, 2018

In this section, we will present and discuss the application of our methodology developed in Chapter 3 to a cirrus cloud observed on April 18, 2018, starting around 15 UTC and lasting until 2 UTC on the following day. However, the last two hours between 0 and 2 UTC on April 19, 2018, will not be shown here for brevity reasons since the retrieval results are not changing considerably and no additional conclusions can be drawn from this period.

The case study of April 18, 2018, has several advantages. Firstly, the temperature of the cavity of the TIR radiometer during the measurement period when the cirrus cloud has been observed ranged between 18.1 °C and 33.8 °C which is closer to the cavity temperature during the calibration of the instrument (21 °C for the calibration performed in April 2018) than in case of November 30, 2016, where the instrument's temperature during the measurement varied between 2.9 °C and 10.6 °C as mentioned in Sect. 3.3.2 (the cavity temperature during the according calibration of November 2016 was 24 °C, cf. Table 2.4). Hence, the rather uncertain temperature correction due to the temperature dependence of the sensitivity of the instrument discussed in Sect. 2.2.2 has a smaller influence on the measured radiances of April 18, 2018, resulting in a lower measurement error compared to the case study of November 30, 2016. The resulting errors range between 1 % and 4 % for channel C09, between 2 % and 8 % for channel C11, as well as between 1 % and 3 % for channel C12, compared to the above-mentioned 3 % to 4 %, 7 % to 10 % and 4 % to 5 %, respectively, for November 30, 2016. Furthermore, it is worth noting that a calibration of the instrument has taken place in the beginning of April 2018. Thus, similarly as for the other case study, the measurements have been performed shortly after calibrating the instrument (cf. Table 2.4 for the applied sensitivities). Another advantage of this case study is the long period of a single-layer cirrus cloud in a quite constant altitude as well as rather stable conditions of the surrounding atmosphere. In particular, the total amount of water vapour obtained from the ECMWF reanalysis data varied little between the three time steps of 12 UTC and 18 UTC of April 18, 2018, and 0 UTC of April 19, 2018 ($1.44\,\mathrm{g\,cm^{-2}}$, $1.41\,\mathrm{g\,cm^{-2}}$ and $1.47\,\mathrm{g\,cm^{-2}}$, respectively), leading to stable clear sky simulations over the whole period.

However, this amount of water vapour is much larger (even though still considerably smaller than values of 3 - $4\,\mathrm{g\,cm^{-2}}$ that can be reached in summer) compared to the above-mentioned $0.622\,\mathrm{g\,cm^{-2}}$ during the case study of November 30, 2016, which is a disadvantage since the sensitivity of the TIR radiances to cirrus cloud properties is smaller in moist than in dry atmospheres as discussed above (Dubuisson et al., 2008). Furthermore, the aerosol load in the atmosphere, even in elevated layers, was considerably higher on April 18, 2018, leading to problems in the identification of the clear sky reference zone for the calibration of the lidar signal as will be shown below. The aerosol optical thickness retrieved from our lidar only algorithm assuming the WASO aerosol model is on average 0.212 ± 0.107 for April 18, 2018, compared to 0.035 ± 0.013 for November 30, 2016.

Figure 4.8 introduces the case study of April 18, 2018, by presenting the lidar and TIR radiometer measurements. Figure 4.8 a shows the lidar signal overlaid by the cloud detection. This plot indicates an increased noise in the lidar measurements in the cirrus altitude during day time. After sunset (around 18.75 UTC for April 18, 2018, in Lille), the lidar measurements are considerably less noisy. Thus, the retrieval results for the night-time measurements can be expected to be of better quality. The TIR radiometer measurements show an important increase in all three channels due to a relatively thick cloud between 16.5 and 19 UTC and a decrease for the very thin cloud between 19 and 20.5 UTC. However, during this period the TIR radiometer signal does not drop down to the clear sky level before the cloud (between 14 and 15 UTC). Around 20.5 UTC a short period with an enhanced signal in the TIR radiometer measurements is observed corresponding to an increase in the lidar signal. For the rather strong lidar signals after 21.5 UTC, however, the TIR radiometer signal increases in the beginning but decreases at about 23 UTC which seems to be incoherent with the lidar observations since the cloud altitude remains more or less constant (at least until 23.7 UTC) and the backscattered lidar signal shows an increase shortly after 23 UTC. We can only speculate about the reasons for the decrease in the measured TIR radiances at the same time. One possible explanation could be a change of the surrounding atmospheric conditions even though the ECMWF reanalysis profiles do not indicate such a change. However, as discussed above the reanalysis data might not represent the local variations of water vapour sufficiently exact. Another hypothesis is that parts of the cloud were not situated in the FOV of the TIR radiometer since the FOV of the lidar and the TIR radiometer are not exactly the same. A further explanation could be the presence of oriented ice crystals in a preferential plane which will be discussed in more detail below. Nevertheless, attempts to retrieve the microphysical properties of the cirrus cloud during this period from the algorithms introduced in Chapter 3 have been performed and will be presented in the following.

As discussed for the case study of November 30, 2016, before the algorithms using the TIR radiometer measurements, i.e. the TIR only algorithm and the synergy algorithm, can be applied, it is necessary to verify if the radiances measured under clear sky conditions are reproduced by the forward model (LIDORT). Figures 4.8 b to 4.8 d include the clear sky simulations without taking aerosols into account (solid lines) as well as by introducing the aerosol optical thickness obtained from the lidar assuming the WASO (dashed lines) and INSO (dot-dashed lines) aerosol models. Although the aerosol optical thickness was quite important during April 18, 2018, the simulation including the WASO aerosol type does not differ significantly from the clear sky simulation without taking aerosols into account since this aerosol type does not have a strong impact on the radiances in the TIR due to its weak absorption features. The simulation using the INSO aerosol model on the other hand shows an important increase of the simulated clear sky TIR radiances, although it should be noted that this aerosol model is an extreme model in terms of absorption and has been integrated here to study the behaviour of the algorithm rather than producing a realistic retrieval. As for the case study of November 30, 2016, the simulated radiances of channel C09 are not reproduced by the radiative transfer model while channels C11 and C12 represent the clear sky simulations without and with both aerosol models quite well considering the fluctuations in the measurements as well as the measurement error. This underlines that the measurements of channel C09 are connected with a problem that could be originating from an insufficient knowledge of the spectral filter function as has already been discussed in Sect. 3.3.2 However, currently the reason for this problem is unknown.

For the presentation of the results for the case study of April 18, 2018, the cloudy period has been divided into two parts: the period between 15 and 20 UTC and the period between 20 and 24 UTC. In a first step, the results from the TIR only algorithm are presented. To recall, the TIR only algorithm does not take aerosols into account since this information is obtained in the synergy algorithm from the lidar measurements and thus not available in the TIR only algorithm. Furthermore, it assumes a constant IWC over the whole cirrus layer. In a second step, the retrievals from the variation of the lidar only algorithm which is constrained by the COT obtained from the transmission method are shown before finally the retrieval results

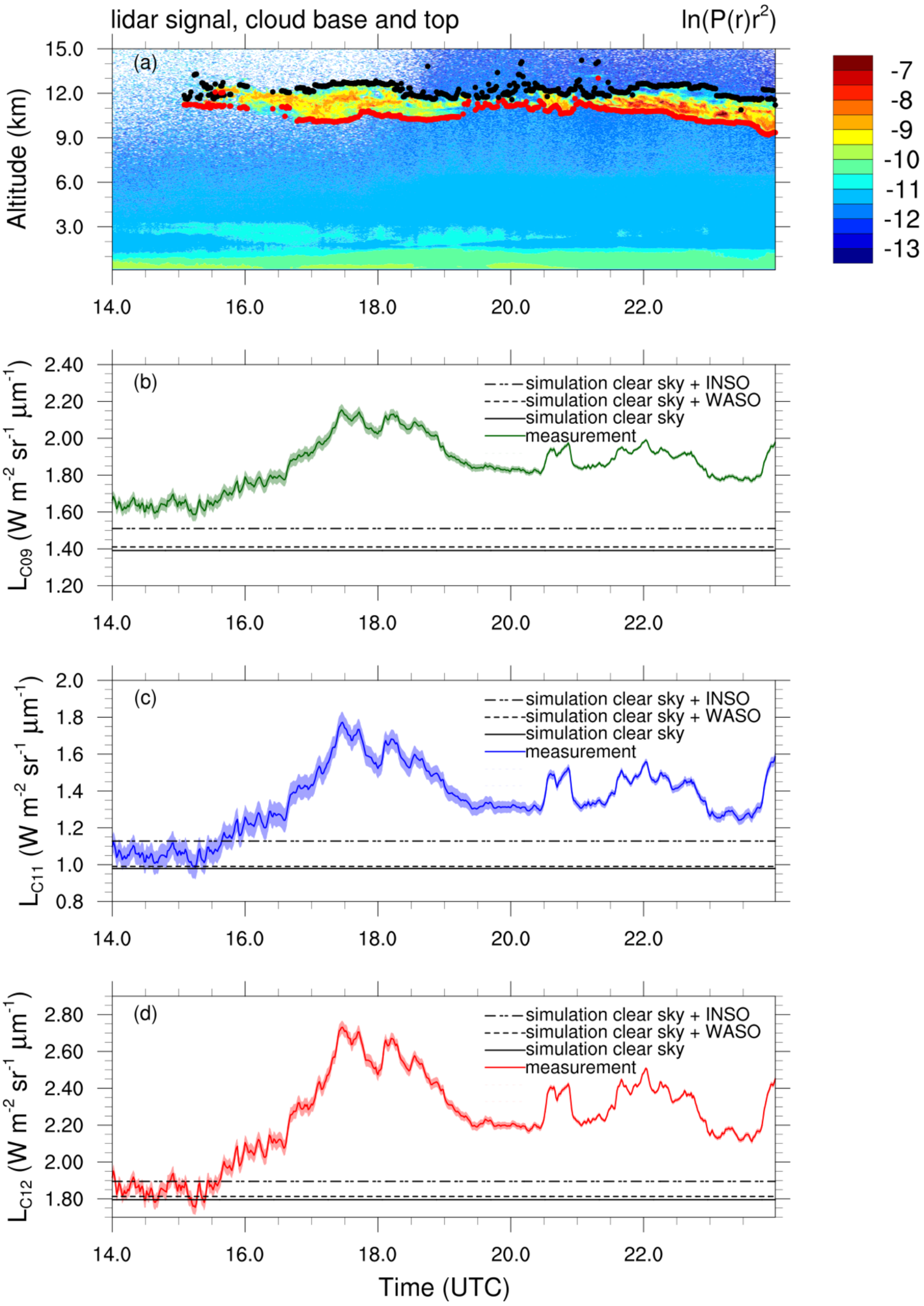

Figure 4.8: TIR radiometer measurements and clear sky simulations without aerosols (solid lines) and by taking aerosols into account (the WASO aerosol model is represented by the dashed lines and INSO by dot-dashed lines) with the ECMWF reanalysis profile of 18 UTC for April 18, 2018, 14 to 24 UTC. (a) Logarithm of the range-corrected lidar signal overlaid by the cloud detection, (b) radiance of channel C09, (c) radiance of channel C11, and (d) radiance of channel C12. The shaded zones in plots (b) to (d) represent the measurement error.

obtained from the synergy algorithm performed assuming both aerosol models are discussed.

The retrieval results obtained from the TIR only algorithm are presented for the two time periods mentioned above in Figs. 4.9 (for 15 to 20 UTC) and 4.10 (for 20 to 24 UTC). The cost function normalized by the size of the measurement vector shown in Figs. 4.9 c and 4.10 c is always smaller than unity indicating a good convergence of the TIR only algorithm for this case study. This is also confirmed by the overlapping measurement and forward model after the last iteration step for both channels considering the according error ranges illustrated in Figs. 4.9 d and 4.10 d. The retrieved IWP is presented in Figs. 4.9 b and 4.10 b. Generally, the retrieved IWP is larger where the measured lidar signal is stronger which seems to be logical. The exception is the above-mentioned period between approximately 23 and 23.7 UTC where the measured TIR radiances decrease although the cloud does not seem to change significantly during this period. It seems rather strange that the TIR radiances and hence the retrieved IWP are larger between 20 and 20.4 UTC as well as around 21 UTC where the observed cirrus cloud was obviously thinner than between 23 and 23.7 UTC. As mentioned above, we can currently not give a definite explanation for this. However, since we have a second tool consisting of the lidar measurements and the lidar only algorithm, we can compare the results of both algorithms.

Figures 4.11 and 4.12 present the retrieval results obtained from the lidar only algorithm which is constrained by the COT for the time periods of 15 to 20 UTC and 20 to 24 UTC, respectively. These retrievals have been performed assuming a multiple scattering factor of $\eta = 0.75$ for ice clouds and the WASO aerosol model. Figure 4.11 shows very few retrievals before 18 UTC. This is due to the fact that the transmission method of Young (1995) is not applicable if the lidar signal above the cloud is too noisy. As mentioned above, the day-time lidar measurements for the case study of April 18, 2018, are very noisy. However, when no optical thickness from the transmission method is available, the lidar only algorithm nevertheless tries to retrieve the cloud properties by assuming a constant correction factor $\kappa = 1.7$ which corresponds to the a priori. Hence, there are a few retrievals reported in Fig. 4.11 before 18 UTC even though no retrieval of the correction factor and the lidar ratio is presented. These retrievals, however, are very uncertain due to the strong assumption for the backscatter-to-extinction ratio and due to the noisy lidar signal. The fact that only very few retrieval results are presented before 18

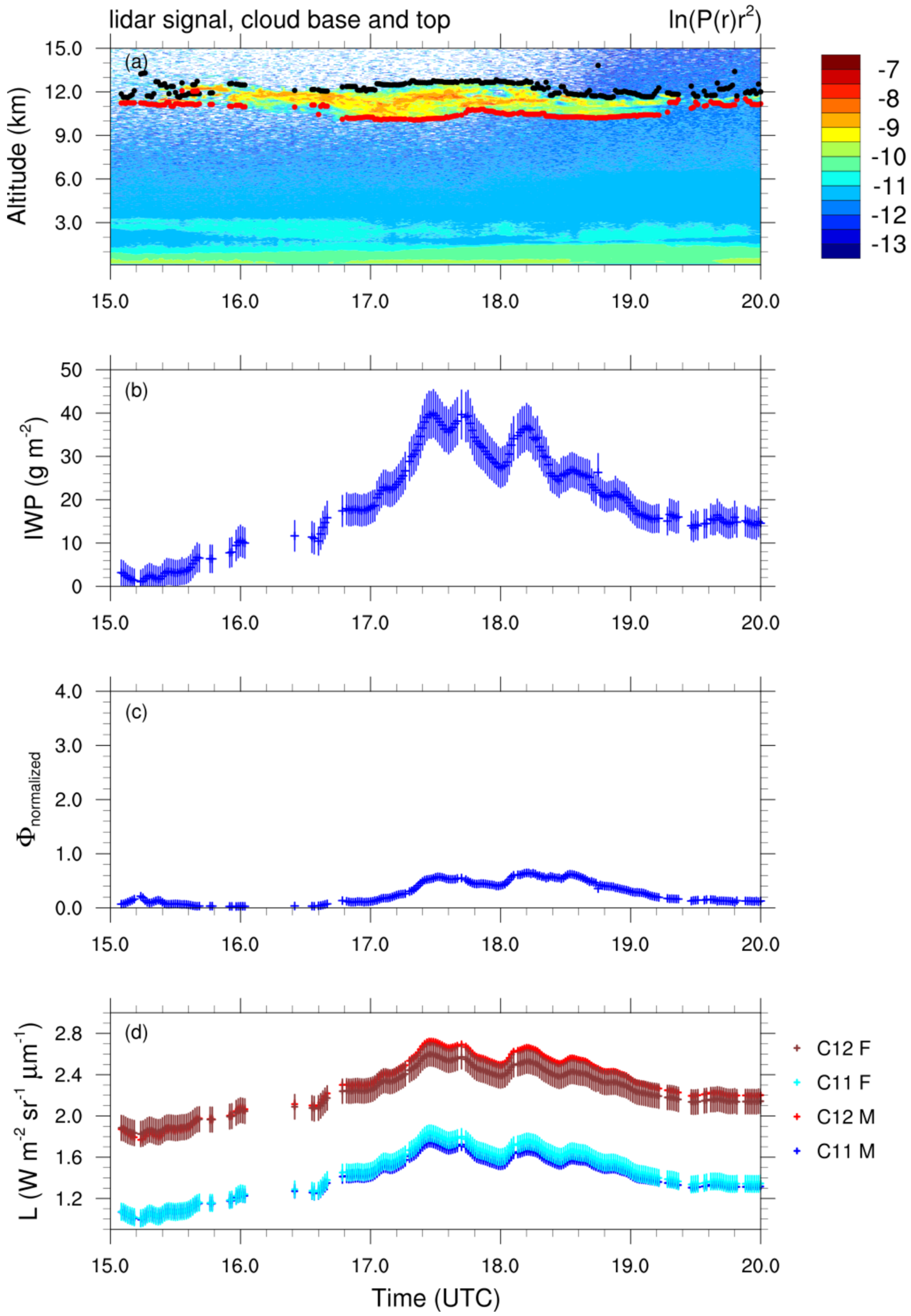

Figure 4.9: Retrieval results from the TIR only algorithm for April 18, 2018, 15 to 20 UTC. (a) Logarithm of the range-corrected lidar signal overlaid by the cloud detection, (b) retrieved IWP, (c) cost function normalized by the size of the measurement vector after the last iteration step, and (d) TIR radiometer measurements (C11 M and C12 M) and forward model after the last iteration step (C11 F and C12 F).

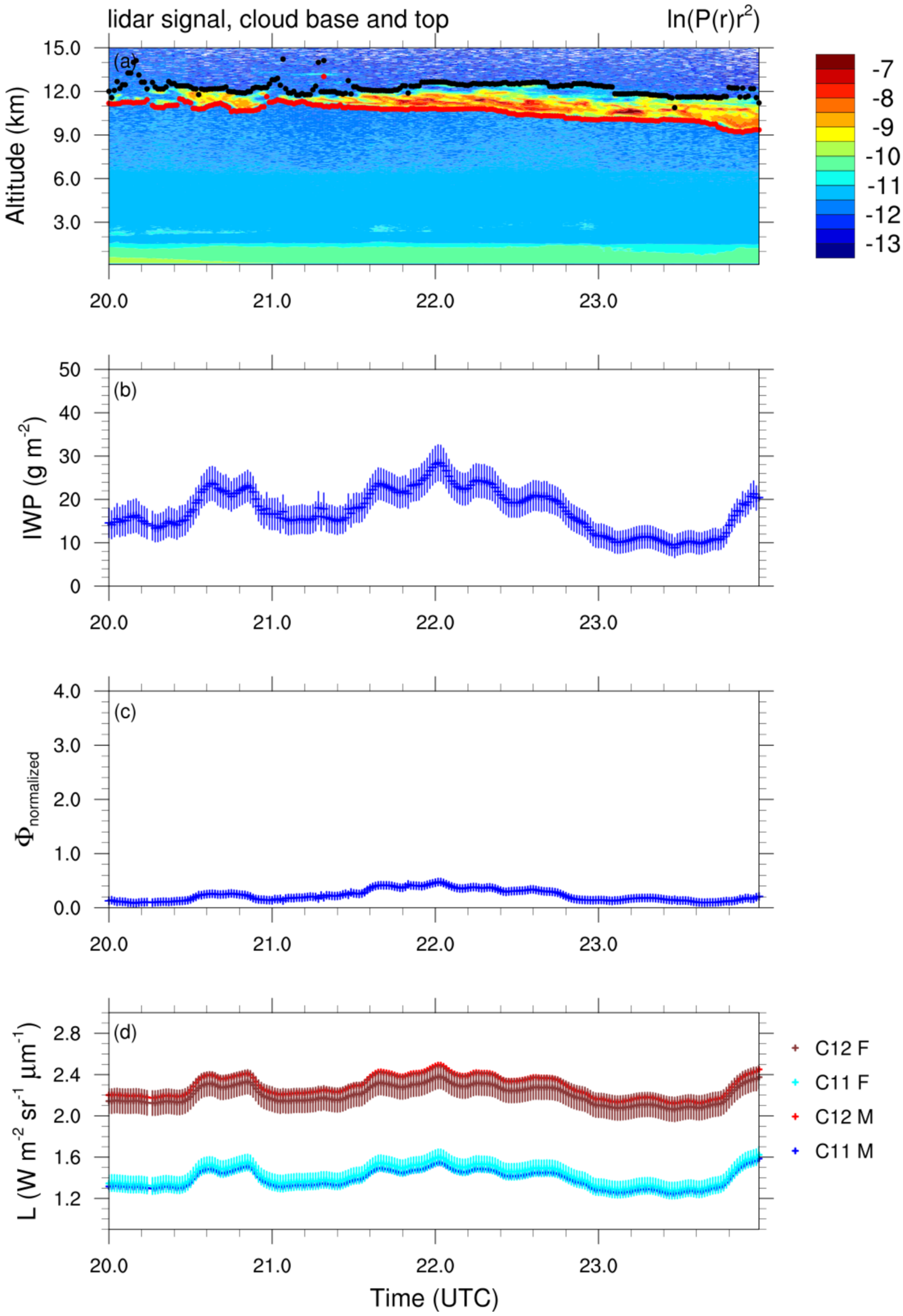

Figure 4.10: Same as Fig. 4.9 but for April 18, 2018, 20 to 24 UTC.

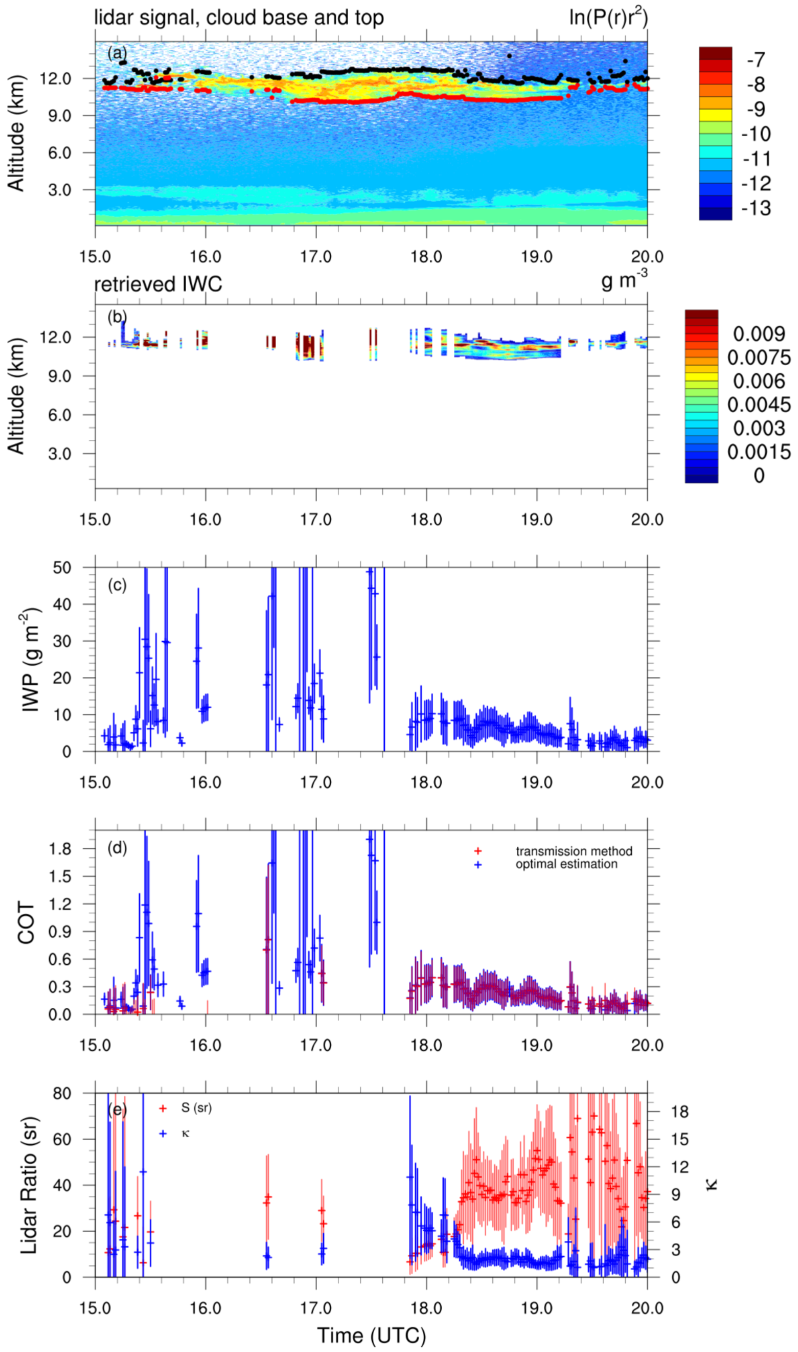

Figure 4.11: Retrieval results from the variation of the lidar only algorithm constrained by the optical thickness performed with $\eta = 0.75$ and aerosol properties corresponding to the WASO aerosol type for April 18, 2018, 15 to 20 UTC. (a) Logarithm of the range-corrected lidar signal overlaid by the cloud detection, (b) retrieved IWC profiles, (c) integrated IWC profiles (IWP), (d) cloud optical thickness from the lidar only algorithm (blue) and the transmission method introduced in Sect. 2.3.3 (red), and (e) lidar ratio (sr) on the left axis (red) and retrieved correction factor κ on the right axis (blue).

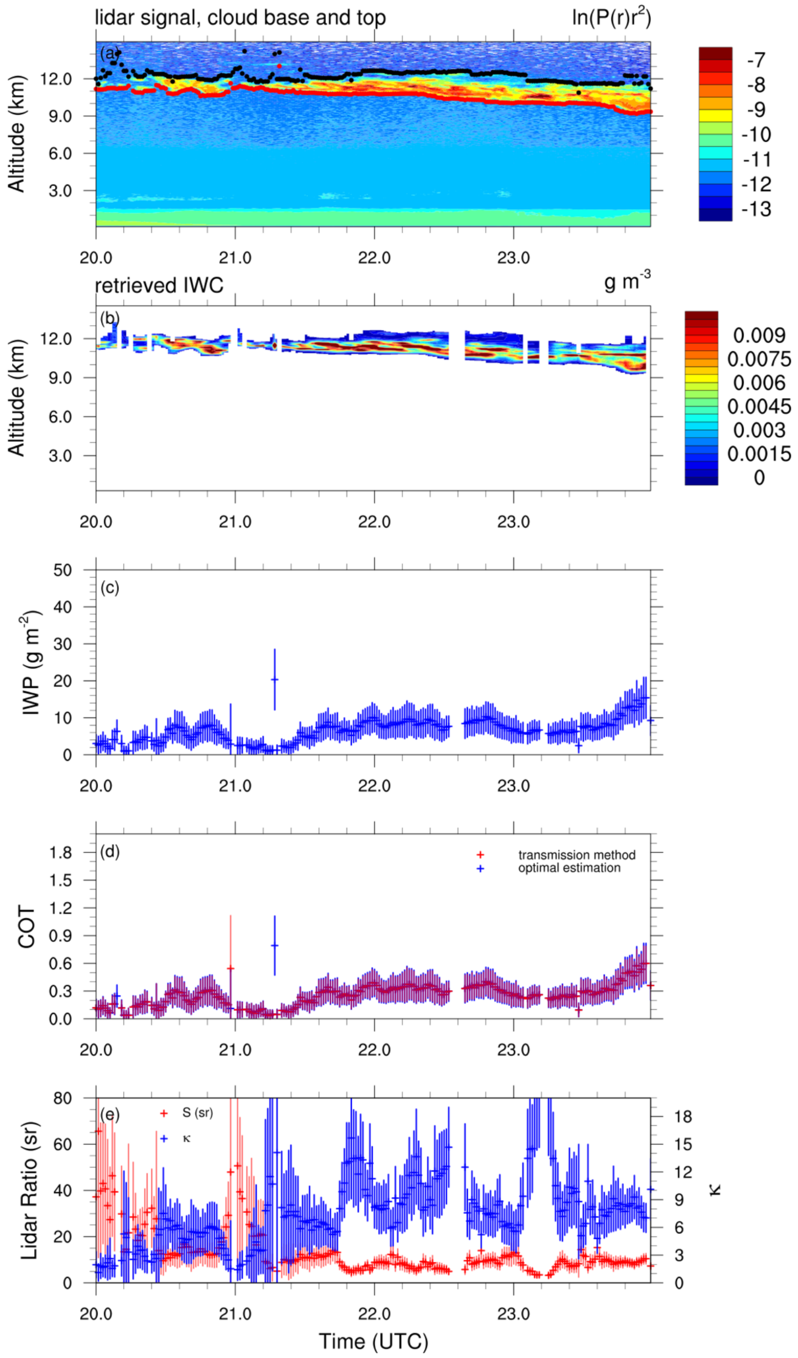

Figure 4.12: Same as Fig. 4.11 but for April 18, 2018, 20 to 24 UTC.

UTC underlines the difficulties of the lidar only algorithm to converge under these conditions. After 18.4 UTC, meaning close to sunset, the retrieval results are quite regular until the end of the presented period at 20 UTC and the retrieved lidar ratio takes reasonable values around 40 sr although the error on this lidar ratio is large because the COT from the transmission method is associated with a large error due to the noise in the lidar signal which is still important (Fig. 4.11 e). During the second period shown in Fig. 4.12, the convergence of the lidar only algorithm is considerably better indicated by the almost continuous record of presented retrievals and the coincidence of the optical thickness obtained from the transmission method (represented in red in Fig. 4.12 d) and from the lidar only algorithm (represented in blue in Fig. 4.12 d). However, the retrieved correction factors κ are large and thus the corresponding lidar ratios are very low. By comparing with Fig. 4.12 a, it seems like the lidar ratio is particularly small when a strong peak in the lidar signal is present while no significant change of the COT is observed. This is logical because the extinction is constrained by the optical thickness. Hence, to compensate the strong backscattering, the backscatter-to-extinction ratio and thus the correction factor κ have to increase. An example of such a profile is shown in Fig. 4.19 and will be discussed below in connection with the synergy algorithm. These strong peaks in the lidar signal might either be due to the presence of ice crystals with a very smooth surface since in this case the backscattering peak can be very strong as discussed in Sect. 3.4.3, or to the presence of oriented ice crystals in a preferential plane which does not correspond to the assumption of randomly oriented particles made in the BV2015 microphysical model. This preferred orientation is known to increase the particles phase function in the backscattering direction due to specular reflection (Borovoi et al., 2008; Zhou et al., 2012), and would lead to the retrieval of a large correction factor κ (and hence a low lidar ratio) to compensate the misrepresentation of the backscattering direction in the microphysical model. Another scenario which is not included in the BV2015 parametrization is the presence of supercooled liquid droplets. However, since the temperature in the cirrus altitude ranges from - 45 °C to - 55 °C for the considered case study, it is very unlikely that the strong peaks in the lidar signal are due to supercooled liquid droplets.

For both considered periods the IWP obtained from the lidar only algorithm (cf. Figs. 4.11 c and 4.12 c) is considerably smaller than the IWP retrieved from the TIR only algorithm (cf. Figs. 4.9 c and 4.10 c). Hence, it is interesting to have a look at the results obtained from the synergy algorithm which combines the information provided by both instruments. Consequently, we will finally focus on the advantage

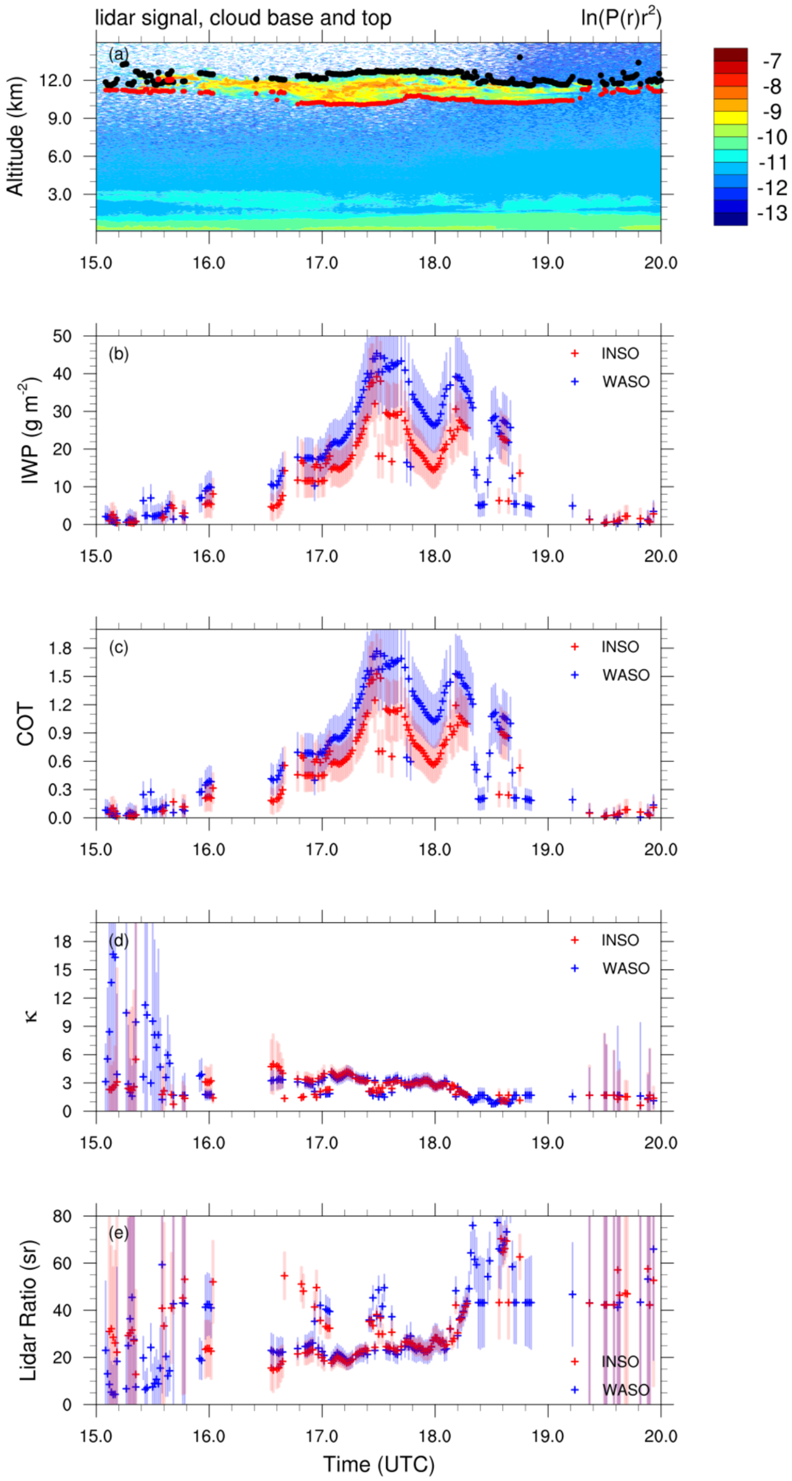

Figure 4.13: Retrieval results from the synergy algorithm for the two different aerosol models performed with $\eta = 0.75$ considering the atmospheric profile from the ECMWF reanalysis of 18 UTC for April 18, 2018, 15 to 20 UTC. (a) Logarithm of the range-corrected lidar signal overlaid by the cloud detection, (b) retrieved IWP, (c) retrieved COT, (d) retrieved correction factor κ, and (e) retrieved lidar ratio (sr). The aerosol model WASO is represented in blue and INSO in red.

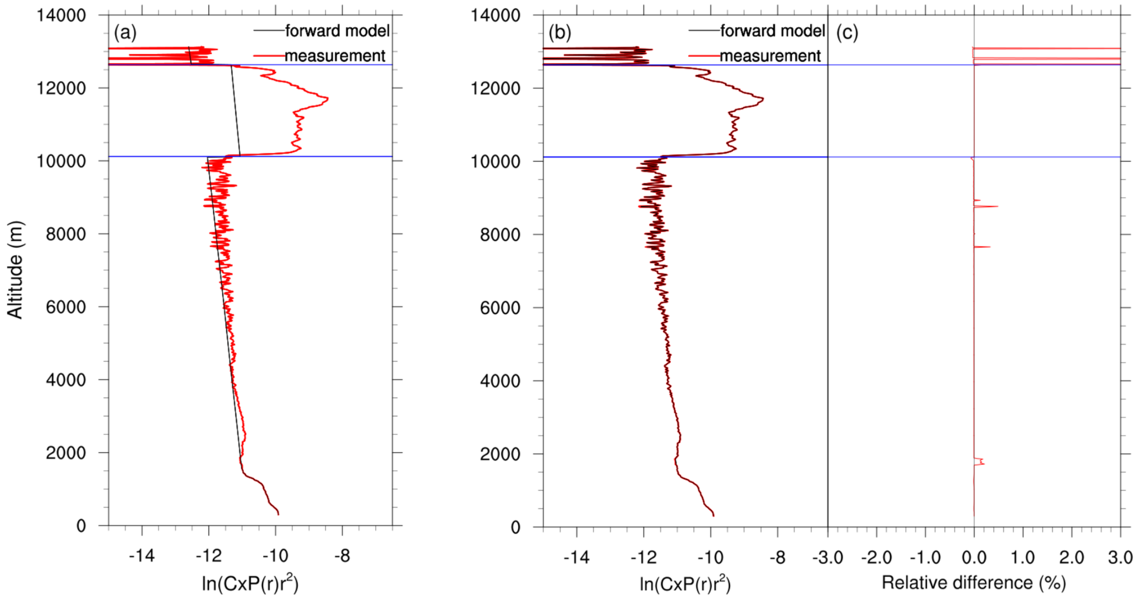

Figure 4.14: Lidar forward model of the synergy algorithm of the (a) a priori and (b) after the last iteration step (black lines) for the profile measured on April 18, 2018 at 17.4 UTC (the red lines represent the measurement, the horizontal blue lines indicate the defined cloud base and top altitudes). (c) Relative difference between the measurement and the forward model after the last iteration step.

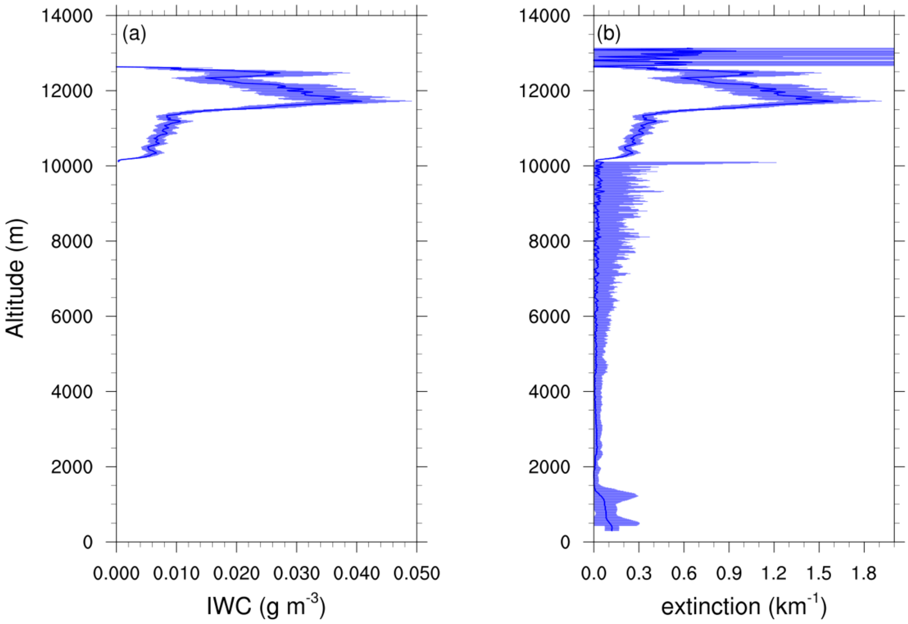

Figure 4.15: (a) Retrieved IWC and (b) extinction profiles from the synergy algorithm for the profile measured on April 18, 2018 at 17.4 UTC (cf. Fig. 4.14). Shaded areas represent the error on the retrieved parameters.

of the synergy algorithm compared to the TIR only and the lidar only algorithms. Figure 4.13 shows the retrieval results obtained from the synergy algorithm for both aerosol models (WASO in blue and INSO in red) assuming a multiple scattering factor of $\eta = 0.75$ for the time period of 15 to 20 UTC. Compared to the lidar only algorithm, the synergy algorithm converged for a considerably larger number of profiles before 18 UTC. This is due to the fact that thanks to the TIR radiometer measurements the IWP and hence the optical thickness is constrained which allows to adjust the correction factor κ for the phase function in backscattering direction (Fig. 4.13 d). By contrast, in the lidar only algorithm a constant correction factor has to be assumed when the optical thickness is not available which in this case did not allow the algorithm to converge. Figure 4.14 illustrates one profile during this period measured at 17.4 UTC indicating why the transmission method is not applicable at the high time resolution due to the low signal-to-noise ratio. The red lines in Figs. 4.14 a and 4.14 b represent the lidar measurement. It is obvious that the signal is completely attenuated above the cloud. Hence, the retrieved cloud top is an apparent cloud top where the signal is equal to the background noise not allowing the application of the transmission method which requires the signal at the cloud top (cf. Sect. 2.3.3). The synergy algorithm, however, is able to converge (cf. Figs. 4.14 b and 4.14 c) since on the one hand, the IWP is constrained by the TIR radiometer measurements and on the other hand, the error on the lidar measurements is calculated as a function of altitude (cf. Sect. 2.3.3). Thus, the large error for the altitudes above the cloud top allows to reduce the cost function. However, as a consequence the resulting errors on the retrieved extinction and IWC profiles are increasing considerably with increasing altitude as well (cf. Fig. 4.15).

Next to the noise in high altitudes, another issue concerning the lidar measurements during April 18, 2018, is the choice of the molecular reference zone for the calibration of the lidar signal. As shown in Fig. 4.14 (cf. Figs. 4.17 and 4.19 as well), the lidar signal is strongly increased due to the aerosols in the boundary layer until an altitude of about 1500 m where an abrupt decrease of the signal is observed. Between approximately 2000 m and 3500 m the signal is increasing again indicating a possible presence of aerosols in an elevated layer. As a consequence, the choice of the reference zone for the calibration of the lidar signal is challenging and our algorithm identifies the zone between approximately 1800 m and 2100 m as zone with minimal signal during this day which is a rather untypical altitude for the molecular reference zone. In comparison, the molecular reference zone for November 30, 2016, ranged between 5000 m and 6000 m (cf. Fig. 3.8).

Time period	WASO	INSO
15.0 - 20.0 UTC	$33.6 \pm 18.7\,\mathrm{sr}$	$32.1 \pm 15.7\,\mathrm{sr}$
20.0 - 24.0 UTC	$16.8 \pm 10.0\,\mathrm{sr}$	$17.8 \pm 13.4\,\mathrm{sr}$
Total	$24.8 \pm 17.0\,\mathrm{sr}$	$24.2 \pm 16.1\,\mathrm{sr}$

Table 4.10: Dependence of the retrieved average lidar ratios from the synergy algorithm on the aerosol model for different time periods of April 18, 2018.

However, as mentioned above, the synergy algorithm converged for a quite large number of profiles and the retrieved IWP for the period between 15 and 20 UTC is reported in Fig. 4.13 b. It shows for the retrievals assuming the WASO aerosol model (blue) similar values as the retrievals from the TIR only algorithm (cf. Fig. 4.9 b). This is due to the fact that the WASO aerosol type does not have a large influence on the TIR radiances as indicated in Fig. 4.8. On the other hand, when assuming the INSO aerosol type the simulated clear sky radiances below the cloud are significantly increased which leads to a considerably reduced retrieval of the IWP (represented in red in Fig. 4.13 b) since the signal due to the cloud needs to be less important in order to match the TIR radiometer measurements. Consequently, the retrieved optical thickness of the cirrus cloud is reduced considerably as well when assuming the INSO aerosol type instead of the WASO aerosol type pointing out the importance of a good characterization of the aerosol properties in the underlying layers, in particular their absorption characteristics. The influence on the retrieved correction factor κ and hence the lidar ratio, however, is rather small.

Figure 4.16 presents the retrieval results obtained from the synergy algorithm for the two aerosol models for the second period between 20 and 24 UTC of the case study of April 18, 2018. Similarly as for the first period, the retrieved IWP and COT are considerably lower when assuming the INSO aerosol type but the impact on the retrieved correction factor κ and the lidar ratio is rather small. Table 4.10 summarizes the retrieved average lidar ratios and standard deviations for both periods and both aerosol models. It underlines that the influence of the assumed aerosol model on the average values for the lidar ratio is small.

Furthermore, the same low lidar ratios as in case of the lidar only algorithm constrained by the COT are obtained from the synergy algorithm as well (cf. Fig. 4.12). The black vertical lines in Fig. 4.16 indicate the profiles measured at 23 UTC and 23.2 UTC which are presented in Figs. 4.17 and 4.19, respectively. These two figures show the convergence in case of assuming the WASO aerosol model

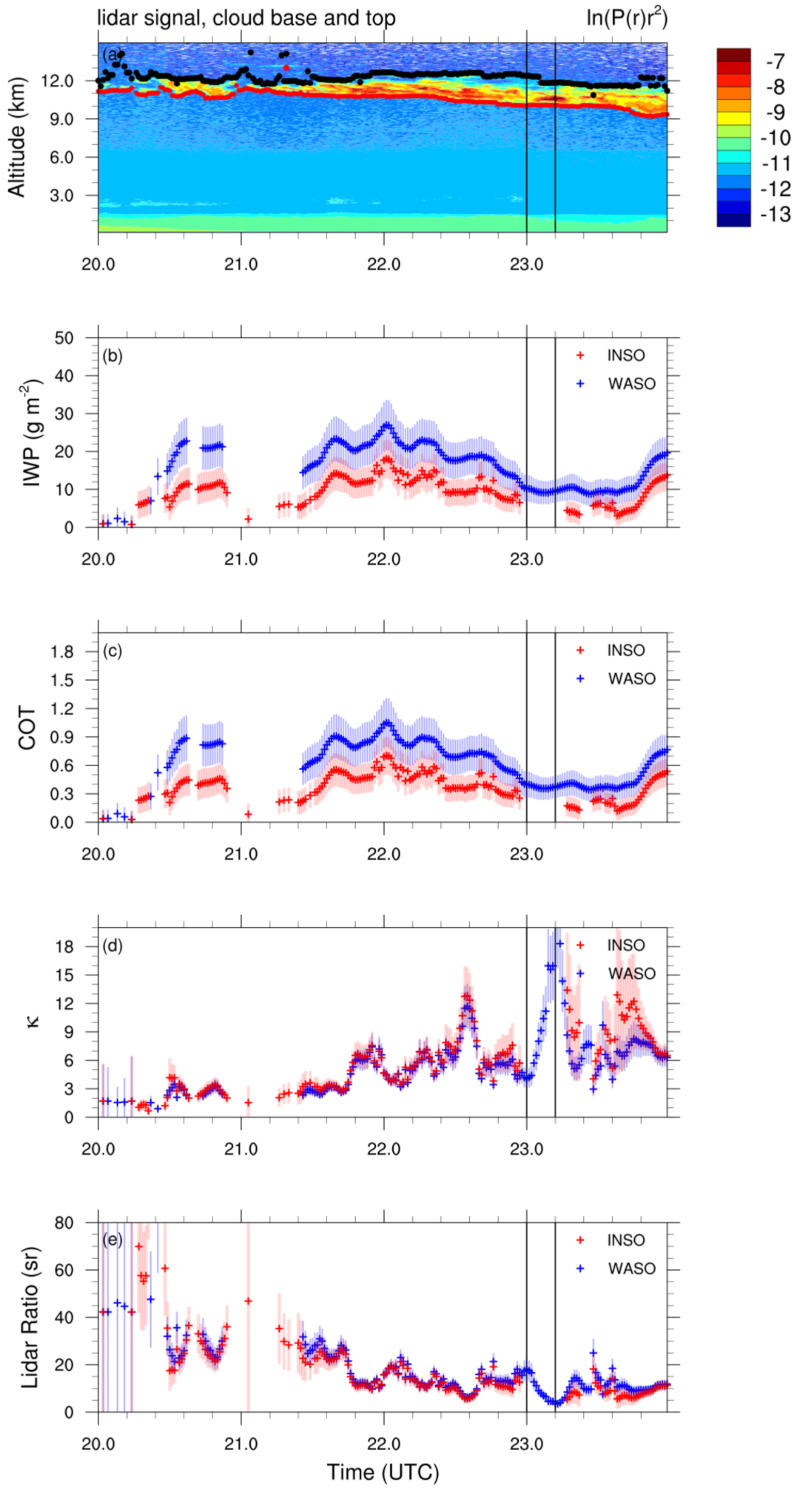

Figure 4.16: Same as Fig. 4.13 but for April 18, 2018, 20 to 24 UTC.

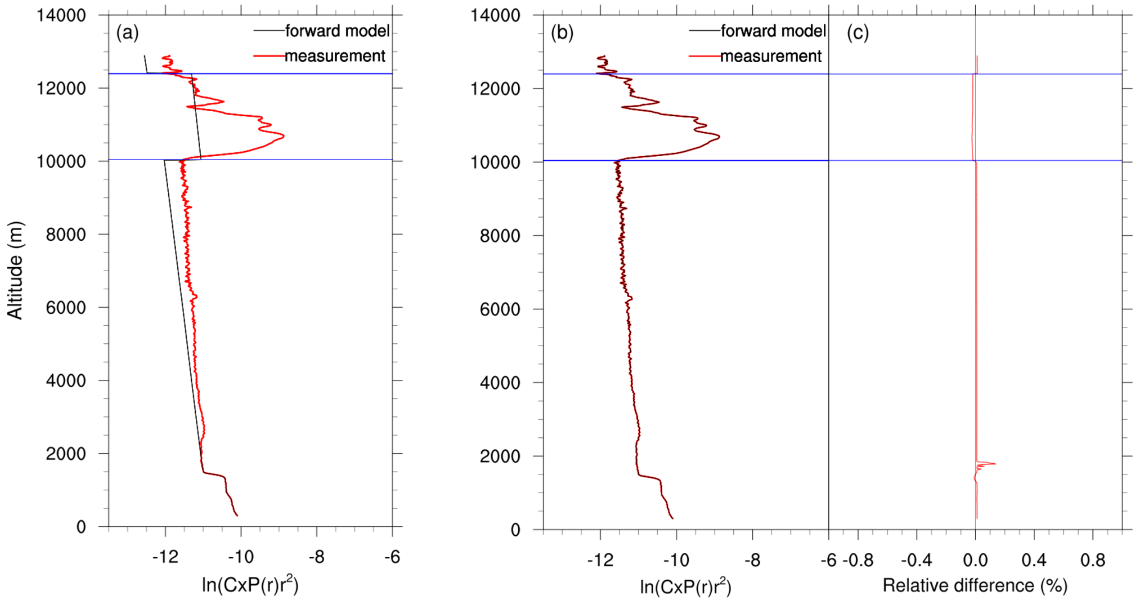

Figure 4.17: Same as 4.14 but for the profile measured on April 18, 2018 at 23 UTC.

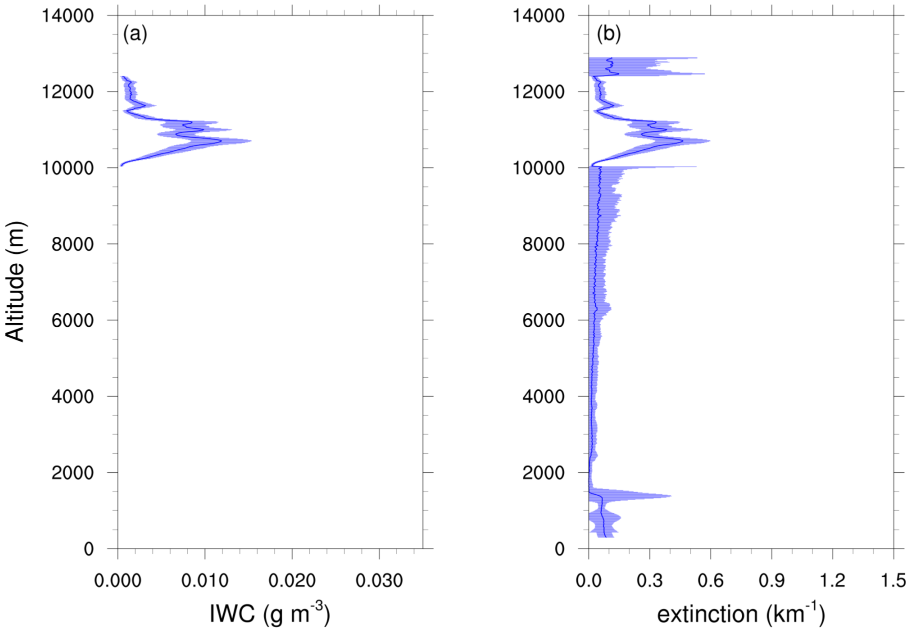

Figure 4.18: Same as Fig. 4.15 but for the lidar profile measured on April 18, 2018 at 23 UTC.

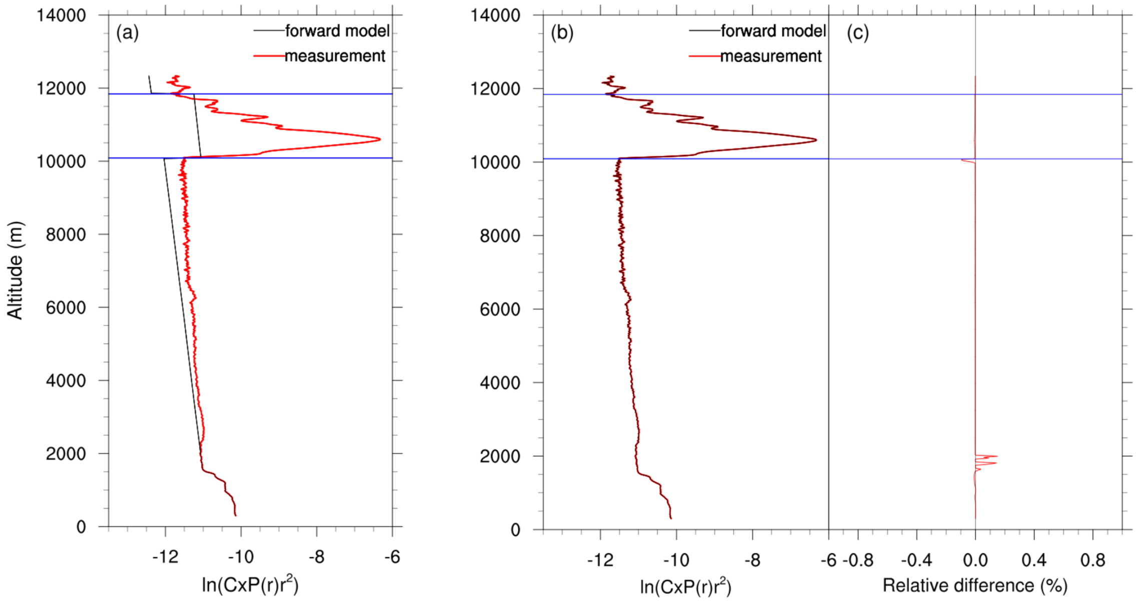

Figure 4.19: Same as 4.14 but for the profile measured on April 18, 2018 at 23.2 UTC.

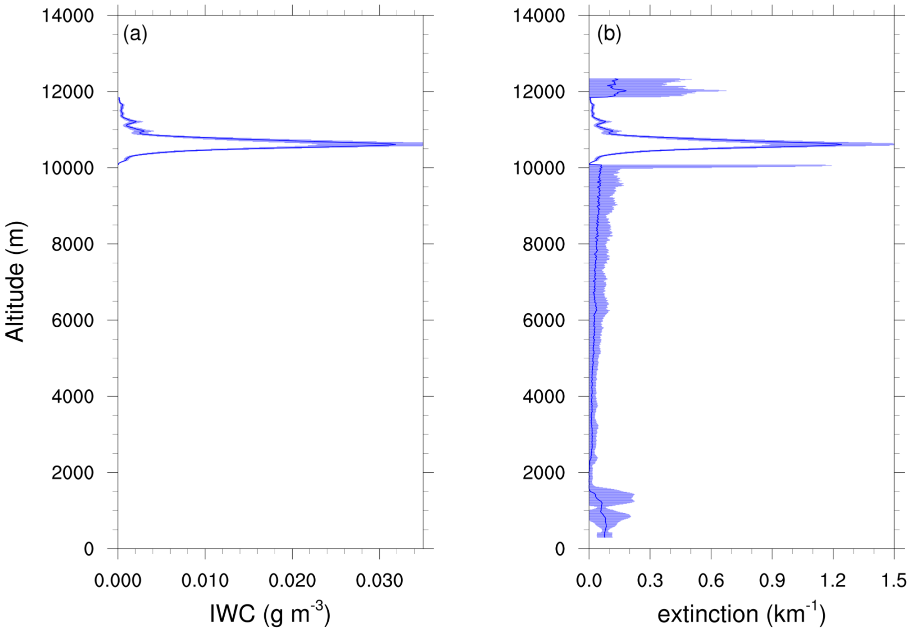

Figure 4.20: Same as Fig. 4.15 but for the lidar profile measured on April 18, 2018 at 23.2 UTC.

since assuming the INSO aerosol model did not lead to convergence for these two profiles as indicated in Fig. 4.16 by the absence of retrieval results. However, these profiles illustrate the effect of a strong peak in the lidar signal which is responsible for the very low retrieved lidar ratio at 23.2 UTC ($3.6 \pm 0.8\,\mathrm{sr}$). For 23 UTC, the measured peak is still moderate and the corresponding retrieval of the lidar ratio appears to be reasonable ($18.1 \pm 4.2\,\mathrm{sr}$). The according IWC and extinction profiles for 23 UTC are presented in Fig. 4.18. On the other hand, the profile of 23.2 UTC shows a very strong peak in the measured backscattering signal (cf. Fig. 4.19) resulting in a strong and vertically narrow peak in the retrieved IWC and extinction profiles which seems to be unnatural (cf. Fig. 4.20). As discussed above, this strong increase in the lidar backscattering signal is not observed in the TIR radiometer measurements. Consequently, the retrieved correction factor κ strongly increases to match the lidar measurements while a further increase of the total extinction and IWP, which would appear in the case of the lidar only algorithm without the COT constraint, is suppressed in order to match the TIR radiometer measurements.

Since the TIR measurements as well as the optical thickness obtained from the transmission method do not increase at the same time when the strong increase in the lidar measurements is observed, the peak in the lidar measurements is likely due to a different reason than an increase of the optical thickness of the cirrus cloud. As mentioned above, the presence of oriented ice crystals inside the cloud could be a possible explanation for this phenomenon. This case is not considered in the BV2015 microphysical model which assumes randomly oriented ice crystals. Hence, the microphysical model does not represent the phase function for preferentially oriented ice crystals which may lead to difficulties in retrieving the microphysical properties of the cirrus cloud during this case study. Another explanation could be the above-discussed presence of ice crystals with a very smooth surface which strongly increases the phase function in the backscattering direction, whereas the presence of supercooled liquid is unlikely in case of the observed cloud due to the low temperature in the cirrus altitude. However, it is important to note that these limitations of the BV2015 microphysical model exist.

To conclude, Figs. 4.21 (for 15 to 20 UTC) and 4.22 (for 20 to 24 UTC) show a comparison of the three algorithms developed during this thesis for the case study of April 18, 2018. The retrieved IWP from the TIR only algorithm is represented in blue, the retrieval from the variation of the lidar only algorithm constrained by the COT from the transmission method is represented in red, and the retrievals of

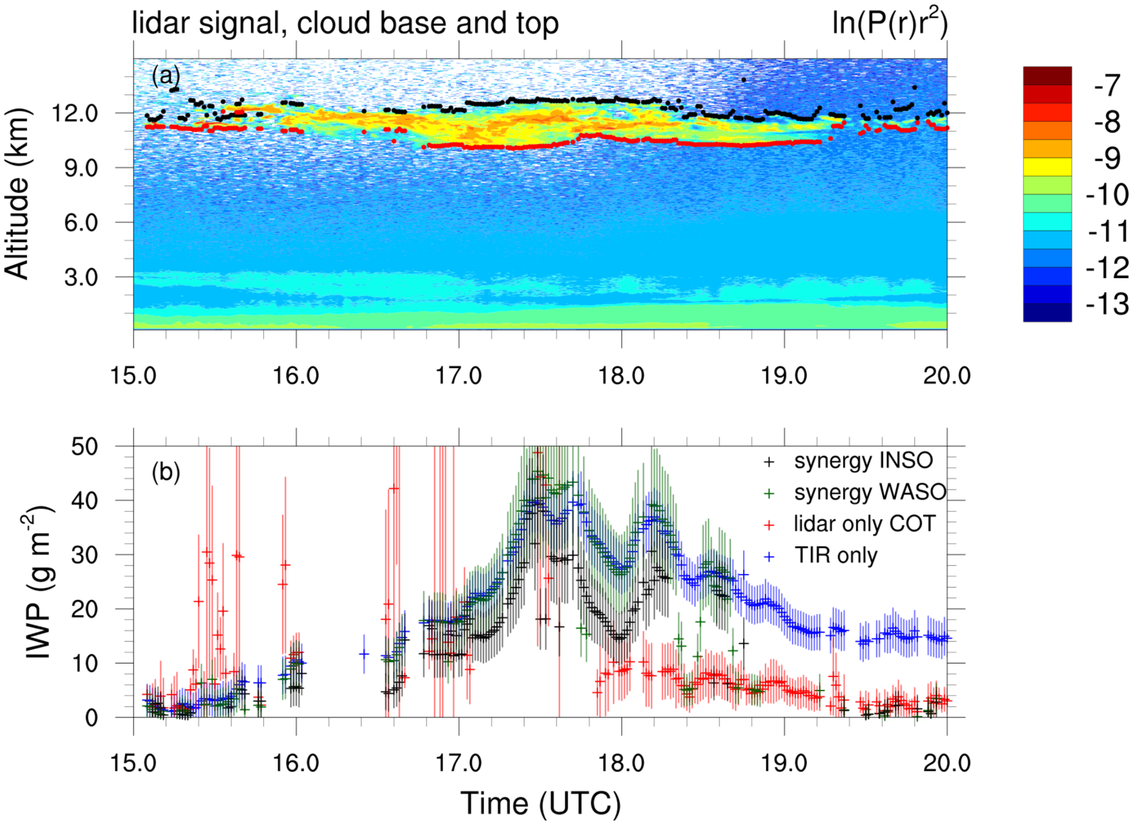

Figure 4.21: Comparison of the retrieval results from the different algorithms for April 18, 2018, 15 to 20 UTC. (a) Logarithm of the range-corrected lidar signal overlaid by the cloud detection, and (b) retrieved IWP from the different algorithms (blue: TIR only algorithm, red: lidar only algorithm constrained by the COT from the transmission method, green: synergy algorithm assuming the WASO aerosol type, black: synergy algorithm assuming the INSO aerosol type).

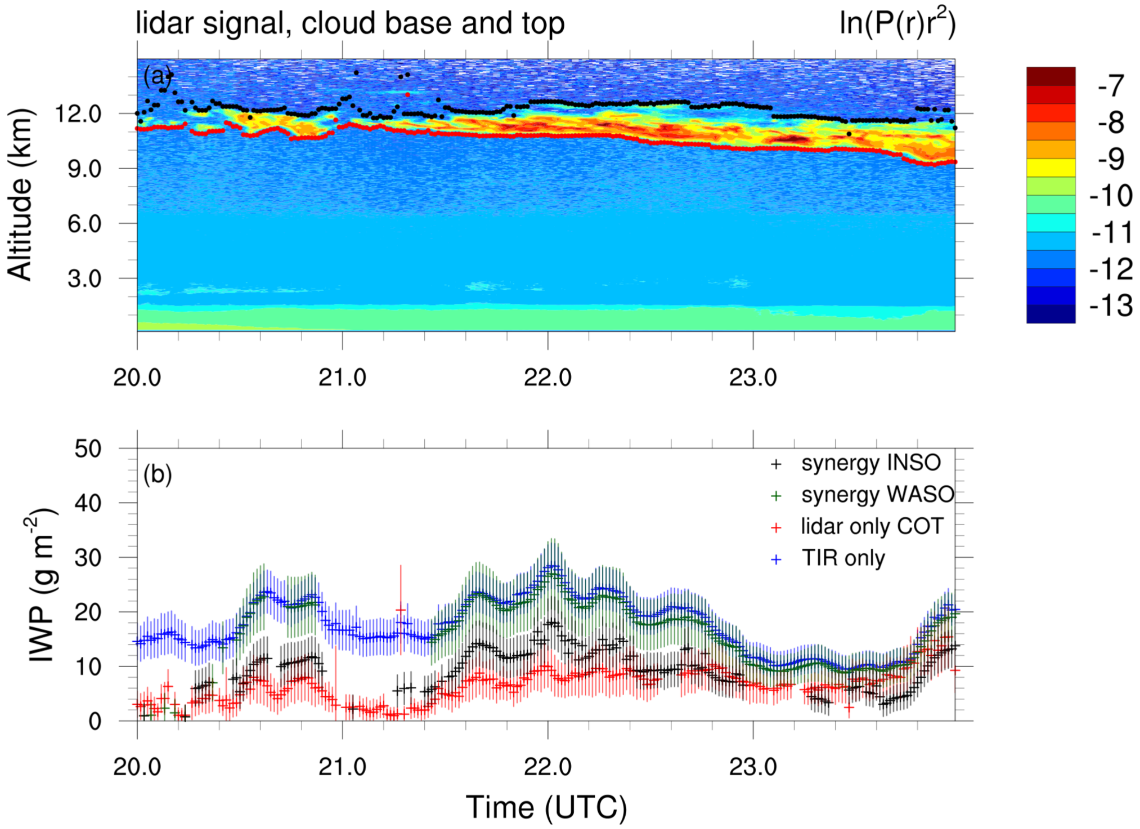

Figure 4.22: Same as Fig. 4.21 but for April 18, 2018, 20 to 24 UTC.

the synergy algorithm assuming the two different aerosol models are represented in green (WASO) and black (INSO). In contrast to the case study of November 30, 2016 (cf. Fig. 3.23), the retrieved IWP from the lidar only algorithm constrained by the COT is smaller than the IWP from the TIR only algorithm for April 18, 2018. The IWP obtained from the synergy algorithm assuming the WASO aerosol model is very close to the IWP retrieved from the TIR only algorithm since the influence of the WASO aerosol type on the TIR radiances is small (cf. Fig. 4.8). On the other hand, in case of assuming the INSO aerosol model the retrieved IWP from the synergy algorithm is considerably reduced and closer to the retrieval of the variation of the lidar only algorithm which is constrained by the COT from the transmission method of Young (1995). These results underline the importance of the choice of the aerosol characteristics in our synergy algorithm for the retrieved microphysical properties of cirrus clouds. A better characterization of the aerosols which are actually present during the measurement is thus crucial to reduce the errors on the retrieved cirrus cloud microphysics obtained from this algorithm.

4.3 Summary and Conclusions

The first part of this chapter showed sensitivity studies for the case study of November 30, 2016, discussing the influence of several non-retrieved quantities on the retrieved microphysical properties of cirrus clouds from our synergy algorithm. The investigated parameters are the multiple scattering factor, the water vapour profile and the assumed aerosol properties. The impact of the multiple scattering factor on the retrieved correction factor κ (and consequently on the lidar ratio) has been shown to be small. This is due to the fact that the TIR radiances in the synergy algorithm provide independently of the lidar measurements a constraint on the IWP and hence on the optical thickness. On the contrary, the water vapour profile has an important influence on the retrieved quantities since the TIR radiances are highly sensitive to water vapour. Thus, a good characterization of the local water vapour profile is essential to reduce the error on the retrievals due to a poor knowledge of this quantity. The choice of the aerosol model significantly influences the retrieval results as well, especially in case of a larger aerosol optical thickness. Hence, a better characterization of the aerosols present during the measurement is also important to reduce the uncertainties on the retrieved microphysics of cirrus clouds. Another non-retrieved parameter influencing the retrieval results is the temperature profile which should be investigated in future sensitivity studies. The impact of this parameter is complex because the temperature profile influences at the same time the measurements in the TIR, the molecular signal of the lidar, and the calculation of the single scattering properties from the BV2015 parametrization since they are functions of temperature and IWC.

However, the case study of November 30, 2016, for which the sensitivity studies were performed, is characterized by a cold and dry atmosphere as well as a low aerosol optical thickness. This means the conditions for the application of our algorithm are favourable because in this case the influence of the atmosphere on the TIR radiometer measurements is small compared to the influence of the cloud. Consequently, a second case study of April 18, 2018, has been introduced in the second part of this chapter where the aerosol optical thickness as well as the amount of water vapour were considerably higher. During this second case study a longer lasting cirrus cloud in a constant altitude and of quite constant geometrical thickness has been observed. We presented and compared the retrievals of all three algorithms introduced in Chapter 3 and discussed the results. It has been shown that due to the higher aerosol optical thickness, the choice of the aerosol model in the synergy algorithm is more important than in the case study of November 30, 2016, since the retrieved IWP and optical thickness are considerably reduced when applying the INSO aerosol model compared to the WASO aerosol model. Furthermore, it has been shown that in case of a noisy lidar signal during day time, the synergy algorithm is advantageous compared to the lidar only algorithm because the optical thickness from the transmission method is not available when the lidar signal is too noisy above the cloud top. Since the synergy algorithm uses the TIR measurements to constrain the IWP and hence the optical thickness, retrievals with this algorithm are still possible in case of an increased noise above the cloud top. Another strength of the synergy algorithm is that it allows to detect anomalies of the observed cirrus cloud thanks to the combination of lidar and TIR measurements as has been discussed in the context of the strong increase of the lidar signal around 23.2 UTC. At the same time, no increase of the TIR radiances was observed which led to the conclusion that the peak in the lidar measurements is not due to an increase of the optical thickness of the cirrus cloud. Hence, the possible reasons for this phenomenon that have been discussed in Sect. 4.2 include the presence of oriented ice crystals as well as the presence of particles with a smooth surface. Another imaginable reason could be the presence of supercooled water droplets although this hypothesis is unlikely in the considered case study due to the low temperature at the cirrus altitude. All three reasons are possible because the BV2015 microphysical model assumes randomly oriented ice crystals, tries to imitate the behaviour of phase functions for heterogeneous particles without backscattering peak, and does not include supercooled liquid water. These limitations of the microphysical model have to be kept in mind when applying our algorithm and future work is necessary to refine the microphysical model for cirrus.

CHAPTER 5

Conclusions and Perspectives

Since cirrus clouds occur all around the globe and in all seasons, it is without doubt that they have a large impact on the Earth-atmosphere system. Unfortunately, this impact is still badly quantified nowadays which is mainly due to the large variation of their microphysical, optical and radiative properties. Cirrus clouds are composed of ice crystals characterized by irregular shapes and considerably varying sizes. Therefore, the modelling of their single scattering properties, which are required in global climate models to estimate their impact on the climate system, is challenging. To accurately model the characteristics of cirrus clouds, a precise knowledge about the particles composing the cloud is essential. The only way to obtain this knowledge is to perform extensive observations.

The observations performed nowadays are of different types which all have advantages and disadvantages. Airborne in situ measurements are an important source of information that can provide details about the ice crystal shape, number concentration and particle size distribution. However, these measurements are performed for a specific cloud at a specific time and cannot necessarily be generalized. To obtain spatially and temporally extensive observations, remote sensing techniques are required. The global occurrence frequencies of cirrus clouds can be obtained from satellite observations. In particular, the A-Train mission including active as well as passive spaceborne sensors has significantly improved our knowledge about the global distribution and frequency of cirrus clouds in recent years. Nevertheless, the spaceborne remote sensing of cirrus is challenging because they are generally optically thin and very often semi-transparent which complicates the accurate retrieval of their microphysical properties. In contrast to satellite observations, ground-based remote sensing does not provide global coverage but the targets are situated much closer to the instrument and thus a higher accuracy can be achieved. Furthermore, the measurements at one specific site can be performed continuously allowing to observe the development and temporal variation of the cloud.

Regardless if satellite or ground-based data is considered, the development of accurate retrieval algorithms using synergistic observations and thus taking into account a maximum amount of available information is crucial for an adequate characterization of cirrus clouds. The aim of this thesis was to develop such an algorithm combining the measurements of a ground-based micropulse lidar and a TIR radiometer. These instruments have been chosen because they are relatively simple and thus not too expensive compared to advanced lidar systems. Hence, this instrumentation can readily be found at other measurement sites. For example, the measurement site of the LOA in M'Bour, Senegal, or the measurement site of the Observatoire de Physique de l'Atmosphère de La Réunion (OPAR) in Maïdo on the isle of La Réunion, are equipped with similar instrumentation. Furthermore, the CALIPSO satellite carries a TIR radiometer (IIR) and a lidar (CALIOP) as well. Thus, the algorithm developed during this thesis should be applicable to other measurement sites in different geographical regions as well as to spaceborne data.

The inversion method that has been chosen for our algorithms is based on optimal estimation theory since this method is a well-adapted tool to integrate different types of measurements in a common retrieval framework as has been discussed in the course of this work. Until the final synergy algorithm has been established, several intermediate algorithms have been developed that independently of each other provide characteristics of cirrus clouds where the common parameter obtained from all algorithms is the IWP. It has been shown that these different IWP retrievals are not always in agreement with each other.

The first algorithm that has been presented in this thesis is the TIR only algorithm to retrieve the IWP from the radiometer measurements alone. Nevertheless, this algorithm integrates the information about the cloud altitude and time period from the active lidar measurements. Since the information about the vertical profile of the cloud properties is not available from the passive TIR radiometer measurements alone, the algorithm assumes a homogeneous cloud with a constant IWC throughout the whole cloud layer. This is a common assumption in retrieval algorithms for passive sensors and has been shown to be valid for thin cirrus by Feofilov et al. (2015).

However, the backscatter profiles measured by the lidar provide an information about the vertical distribution of the particles inside the cloud. This information was used in a second step to develop an algorithm that retrieves IWC profiles of cirrus. This algorithm requires strong assumptions because there are three unknown parameters in the lidar equation (cf. Eq. 3.23): backscattering, extinction and multiple scattering. The ambiguity between these parameters arising from a combination of scattering and absorption processes in the atmosphere cannot be resolved from simple micropulse measurements alone. The lidar only algorithm presented in this thesis assumes a predefined multiple scattering factor and uses the BV2015 microphysical model for cirrus to calculate the backscatter-to-extinction ratio which is defined as product of the single scattering albedo and the phase function in the exact backscattering direction (cf. Eq. 3.26). As a consequence, the retrieval results from this algorithm strongly depend on the BV2015 parametrization which defines the single scattering properties (scattering coefficient, absorption coefficient and asymmetry parameter) as a function of IWC and in-cloud temperature. The single scattering albedo, which is obtained from the scattering and absorption coefficients, is assumed to be represented accurately enough in this microphysical model. On the contrary, the analytical phase function of Baran et al. (2001), which is parametrized from the calculated asymmetry parameter, assumes a flat ending. This assumption has been shown in recent publications to not realistically represent the exact backscattering direction (Zhou and Yang, 2015; Ding et al., 2016). When the analytical phase function is used in the definition of the backscatter-to-extinction ratio, this parameter is generally underestimated resulting in an overestimation of the retrieved IWP compared to the TIR only algorithm.

Consequently, the challenge is to constrain the backscatter-to-extinction ratio. In this thesis, we presented two strategies for this purpose: in a first step the COT obtained from the transmission method of Young (1995) has been used, and in a second step the TIR radiometer measurements have been shown to constrain the backscatter-to-extinction ratio as well by constraining the integrated IWC over the whole cloud layer (IWP). In both cases a correction factor for the backscatter-to-extinction ratio, which can be interpreted as a correction factor for the phase function in the exact backscattering direction (cf. Eq. 3.46), is retrieved together with the IWC profile. It should be noted that this correction factor is assumed to be constant over the whole cloud layer since no information about the vertical variation of this parameter is available. Nevertheless, the backscatter-to-extinction ratio varies slightly with altitude since it is calculated layer by layer from the according IWC and temperature with the BV2015 parametrization.

The lidar only algorithm which is constrained by the COT suffers from a strong dependence on the multiple scattering factor since the effective optical thickness obtained from the transmission method is divided by the multiple scattering factor to be consistent with the assumption on this parameter in the forward model of the optimal estimation algorithm. As a consequence, the retrieved IWP strongly depends on the assumed multiple scattering factor. Thus, one advantage of the final synergy algorithm developed in this thesis is that instead of a retrieval product depending on strong assumptions itself, independent measurements are used to constrain the backscatter intensity of the ice crystals. This synergy algorithm is an expansion of the original lidar only algorithm which integrates the TIR radiometer measurements in the optimal estimation framework to retrieve the above-mentioned correction factor for the analytical phase function in the exact backscattering direction. It has been shown in the sensitivity study presented in Sect. 4.1.1 that the influence of the multiple scattering factor on the retrievals from the synergy algorithm is much smaller than its influence on the retrievals from the lidar only algorithm which is constrained by the COT.

One of the most important achievements of our synergy algorithm is the integration of information from the whole atmospheric profile in the forward modelling of the TIR radiances which is accessible thanks to the active lidar measurements. Thus, it is no longer necessary to assume a homogeneous cloud and the profile of IWC can be accounted for in the radiative transfer model. Furthermore, the extinction of aerosols which may be present in the atmosphere is included in the TIR forward model. It is worth noting that the high vertical resolution of the radiative transfer calculations in the TIR forward model is possible thanks to the numerical efficiency of the radiative transfer model LIDORT which allows to obtain the radiances and Jacobians for different atmospheric parameters from a single simulation.

However, there are limits of this algorithm which have been discussed in the last chapter of this thesis. Firstly, the optical thickness of the cloud has to be sufficiently large to obtain a measurable signal in the TIR. In case of optically very thin clouds, the uncertainties of our retrievals are very large which seems, however, to be rather logical. Sassen and Comstock (2001) quantified the minimum COT for the application of their LIRAD method to 0.05. This minimum value is valid for dry atmospheres and strongly depends on the atmospheric conditions. If the amount of water vapour in the atmosphere is large, the optical thickness of the cirrus cloud has to be larger because the water vapour is also producing an important signal in the TIR radiometer measurements as expected from Dubuisson et al. (2008).

Unfortunately, the water vapour profile is one of the most uncertain non-retrieved parameters in our method. It is obtained from the ECMWF reanalysis provided on a rather coarse spatial ($0.1° \text{x} 0.1°$ latitude/longitude grid) and temporal (four time steps at 0, 6, 12 and 18 UTC) resolution which is not accurately enough to represent local water vapour variations. As a consequence, a large error of 10 % for each layer has been assigned to the water vapour profile. The sensitivity study presented in Sect. 4.1.2 where 10 % of water vapour have been added to each layer of the atmospheric profile shows that the influence of this operation on the retrieved quantities is far more important than the influence of changing the assumed multiple scattering factor. However, due to the large error which has been assigned to the water vapour profile, the error on the retrieved quantities is large as well. Hence, one improvement of our method would be to better characterize the local water vapour profile during the measurement because this would considerably reduce the error on the retrieved quantities. A better characterization of the water vapour profile could be obtained for example with the help of a micro-wave radiometer. Such an instrument is planned to be installed on the measurement platform of the LOA in the near future.

Another large uncertainty on the retrievals of the synergy algorithm is arising from strong assumptions on the aerosol properties. Especially the second case study of April 18, 2018, presented in Sect. 4.2 shows that the choice of the aerosol model strongly influences the retrieved microphysics of the cloud. Furthermore, it has been shown that a strong aerosol extinction as well as elevated layers of aerosols may create problems for the calibration of the lidar signal. In a first approximation, two aerosol models from the OPAC database have been tested in this thesis. However, it is certain that a better characterization of the aerosols which are actually present during the measurement, for example obtained with the help of depolarization measurements, would reduce the uncertainties on the retrieved microphysics of the cirrus cloud.

Furthermore, the quality of the measurements from the lidar as well as from the TIR radiometer plays a crucial role. The second case study of April 18, 2018, showed that the micro-pulse lidar measurements can be very noisy in the cirrus altitude during daytime not allowing the application of the transmission method of Young (1995). Thus, it could be interesting to test our method with a more powerful lidar system. Concerning the TIR radiometer measurements, it has been demonstrated that for both case studies presented in this thesis it was not possible to reproduce the measurements of channel C09 under clear sky conditions with the radiative transfer model while the measurements of channels C11 and C12 were reproduced by the simulations assuming the atmospheric profiles from the reanalysis. This behaviour of channel C09 was confirmed when analysing the other days summarized in Table 2.6 revealing a systematic bias of this channel. As a consequence, channel C09 was excluded in the retrievals performed during this thesis. The reason for the problem with this channel is currently unknown. It may be related to an insufficient knowledge of the spectral response function of this channel. Further studies are required to understand this problem and eventually find a solution. In this context, it could be useful to investigate for a larger amount of data the response of the different channels with respect to changes of the water vapour profile, for example by comparing field measurements and simulations as a function of the integrated water vapour under clear sky conditions as well as in the presence of low and optically thick clouds.

Another problem connected with the TIR radiometer measurements is the fact that the sensitivity of the instrument depends on the temperature of the instruments cavity. This temperature dependence is related to a large uncertainty as has been discussed in Sect. 2.2.2. Especially for the case study of November 30, 2016, the temperature correction resulted in a large measurement error since the atmospheric temperature during this day was low. As a consequence, the cavity temperature during the measurement which varied between 2.9 °C and 10.6 °C was considerably colder than the temperature during the calibration (24 °C). Thus, another improvement of our method would be to isolate the instrument from atmospheric temperature influences to keep the cavity temperature constant during the measurement and preferably close to the temperature during the calibration.

Next to technical improvements such as isolating the instrument from temperature influences and improving the characterization of the aerosols as well as the atmospheric water vapour profile during the measurement, the perspectives related to this newly developed synergy algorithm are diverse. One important aspect is the application of the algorithm to all available data for the measurement site of the LOA in Lille but also for other measurement sites equipped with the same instrumentation, e.g. the site in M'Bour, Senegal, or the OPAR site of La Réunion. The advantage of the latter is that it is situated in 2200 m altitude and hence the atmosphere is very clean. This means the influence of aerosols and water vapour, which are important sources of uncertainty in our algorithm as discussed above, is small at this measurement site. The planning of a campaign dedicated to simultaneous TIR radiometer and lidar measurements in La Réunion is ongoing. The application of our algorithm to data measured under these conditions would allow to test and improve existing microphysical ice cloud models, in particular the BV2015 model and its original representation of bulk optical properties as a function of the in-cloud temperature and IWC. It has been shown in this thesis that the coherence of this model is overall quite good but that there are limitations, especially due to the poor representation of the exact backscattering characteristics of the bulk ice.

However, in this thesis the analytical phase function of Baran et al. (2001) has been used which could be replaced by the exact phase function from the ensemble model (Baran and Labonnote, 2007). Furthermore, one should be aware that the microphysical model used here is based on a large database of in situ measurements performed in the tropics and the mid-latitudes. Hence, it represents a mixture of ice clouds with very different formation mechanisms and characteristics. This is reasonable from a statistical point of view when regarding global trends, especially with model studies, but might not be representative for the retrieval of the microphysical properties of a specific cirrus cloud in the mid-latitudes. In addition, contrail induced cirrus clouds which are frequently observed in the mid-latitudes are not included in this model. Another limitation is due to the assumption of randomly oriented particles not taking into account that the ice crystals might be oriented in a preferential plane as discussed in Sect. 4.2 in the context of the case study of April 18, 2018. Finally, the presence of supercooled liquid droplets is not considered in the microphysical model although it cannot be excluded in our algorithm since our definition of high-level clouds allows the presence of supercooled water. However, with the current set of measurements no information about the cloud phase can be obtained. This information would be available from a lidar that includes depolarization channels.

Since data from several measurement sites are available, one important perspective is the establishment of climatologies and the comparison of the retrieved cirrus cloud properties for different geographical regions. Finally, as indicated above, an interesting project could be to apply this algorithm to satellite data from the CALIPSO mission, i.e. the CALIOP lidar and the IIR radiometer. This would allow to retrieve the cloud properties on a global scale and to compare the IWP from our method to the operational CALIPSO algorithms.

Bibliography

Abercromby, R., 1887: Suggestions for an international nomenclature of clouds. *Quart. J. Roy. Meteor. Soc.*, **13**, 154–166.

Ansmann, A., M. Riebesell, and C. Weitkamp, 1990: Measurement of atmospheric aerosol extinction profiles with a Raman lidar. *Opt. Lett.*, **15 (13)**, 746–748, doi:10.1364/OL.15.000746.

Ansmann, A., U. Wandinger, M. Riebesell, C. Weitkamp, and W. Michaelis, 1992: Independent measurement of extinction and backscatter profiles in cirrus clouds by using a combined Raman elastic-backscatter lidar. *Appl. Opt.*, **31 (33)**, 7113–7131, doi:10.1364/AO.31.007113.

Ansmann, A., et al., 1993: Lidar network observations of cirrus morphological and scattering properties during the International Cirrus Experiment 1989: The 18 october 1989 case study and statistical analysis. *J. Appl. Meteor.*, **32**, 1608–1622, doi:10.1175/1520-0450(1993)032<1608:LNOOCM>2.0.CO;2.

Baran, A. J., 2007: *On the remote sensing and radiative properties of cirrus.* doi:10.1007/978-3-540-68435-0_2, in Light Scattering Reviews 2: Remote Sensing and Inverse Problems, pp. 59-95, A. A. Kokhanovsky (ed). Praxis Publishing Ltd: Chichester, UK.

Baran, A. J., 2009: A review of the light scattering properties of cirrus. *J. Quant. Spectrosc. Rad. Trans.*, **110**, 1239–1260, doi:10.1016/j.jqsrt.2009.02.026.

Baran, A. J., P. J. Connolly, A. J. Heymsfield, and A. Bansemer, 2011: Using in situ estimates of ice water content, volume extinction coefficient, and the total solar optical depth obtained during the tropical ACTIVE campaign to test an ensemble model of cirrus ice crystals. *Quart. J. Roy. Meteor. Soc.*, **137**, 199–218, doi:10.1002/qj.731.

Baran, A. J., R. Cotton, K. Furtado, S. Havemann, L. C. Labonnote, F. Marenco, A. Smith, and J.-C. Thelen, 2014a: A self-consistent scattering model for cirrus. II: The high and low frequencies. *Quart. J. Roy. Meteor. Soc.*, **140**, 1039–1057, doi:10.1002/qj.2193.

Baran, A. J. and P. N. Francis, 2004: On the radiative properties of cirrus cloud at solar and thermal wavelengths: A test of model consistency using high-resolution airborne radiance measurements. *J. Quant. Spectrosc. Rad. Trans.*, **130**, 763–778, doi:10.1256/qj.03.151.

Baran, A. J., P. N. Francis, L. C. Labonnote, and M. Doutriaux-Boucher, 2001: A scattering phase function for ice cloud: Tests of applicability using aircraft and satellite multi-angle multi-wavelength radiance measurements of cirrus. *Quart. J. Roy. Meteor. Soc.*, **127**, 2395–2416, doi:10.1002/qj.49712757711.

Baran, A. J., P. Hill, K. Furtado, P. Field, and J. Manners, 2014b: A coupled cloud physics-radiation parameterization of the bulk optical properties of cirrus and its impact on the Met Office Unified Model Global Atmosphere 5.0 configuration. *J. Climate*, **27**, 7725–7752, doi:10.1175/JCLI-D-13-00700.1.

Baran, A. J. and L. C. Labonnote, 2006: On the reflection and polarisation properties of ice cloud. *J. Quant. Spectrosc. Rad. Trans.*, **100**, 41–54, doi:10.1016/j.jqsrt.2005.11.062.

Baran, A. J. and L. C. Labonnote, 2007: A self-consistent scattering model for cirrus. I: The solar region. *Quart. J. Roy. Meteor. Soc.*, **133**, 1899–1912, doi:10.1002/qj.164.

Baum, B. A., A. J. Heymsfield, P. Yang, and S. T. Bedka, 2005: Bulk scattering properties for the remote sensing of ice clouds. Part I: Microphysical data and models. *J. Appl. Meteor.*, **44**, 1885–1895, doi:10.1175/JAM2308.1.

Berthier, S., P. Chazette, J. Pelon, and B. Baum, 2008: Comparison of cloud statistics from spaceborne lidar systems. *Atmos. Chem. Phys.*, **8**, 6965–6977, doi:10.5194/acp-8-6965-2008.

Blanchard, Y., A. Royer, N. T. O'Neill, D. D. Turner, and E. W. Eloranta, 2017: Thin ice clouds in the Arctic: Cloud optical depth and particle size retrieved from ground-based thermal infrared radiometry. *Atmos. Meas. Tech.*, **10**, 2129–2147, doi:10.5194/amt-10-2129-2017.

Borovoi, A., V. Galileiskii, A. Morozov, and A. Cohen, 2008: Detection of ice crystal particles preferably oriented in the atmosphere by use of the specular component of scattered light. **16 (11)**, 7625–7633, doi:10.1364/OE.16.007625.

Boucher, O., 1999: Air traffic may increase cirrus cloudiness. *Nature*, **397**, 30–31.

Boucher, O., et al., 2013: Clouds and Aerosols. In: Climate Change 2013: The Physical Science Basis. Contribution of Working Group I to the Fifth Assessment Report of the Intergovernmental Panel on Climate Change [Stocker, T.F., D. Qin, G.-K. Plattner, M. Tignor, S.K. Allen, J. Boschung, A. Nauels, Y. Xia, V. Bex and P.M. Midgley (eds.)], Cambridge University Press, Cambridge, United Kingdom and New York, NY, USA.

Brogniez, G., C. Pietras, M. Legrand, P. Dubuisson, and M. Haeffelin, 2003: A high-accuracy multiwavelength radiometer for in situ measurements in the thermal infrared. Part II: Behavior in field experiments. *J. Atmos. Oceanic Technol.*, **20**, 1023–1033, doi:10.1175/1520-0426(2003)20<1023:AHMRFI>2.0.CO;2.

Brogniez, G., et al., 2004: Determination of cirrus radiative parameters from combination between active and passive remote sensing measurements during FRENCH/DIRAC 2001. *Atmos. Res.*, **72**, 425–452, doi:10.1016/j.atmosres.2004.03.026.

C.-Labonnote, L., G. Brogniez, J.-C. Buriez, M. Doutriaux-Boucher, J.-F. Gayet, and A. Macke, 2001: Polarized light scattering by inhomogeneous hexagonal monocrystals: Validation with ADEOS-POLDER measurements. *J. Geophys. Res.*, **106 (D11)**, 12 139–12 153, doi:10.1029/2000JD900642.

Campbell, J. R., S. Lolli, J. R. Lewis, Y. Gu, and E. J. Welton, 2016: Daytime cirrus cloud top-of-the-atmosphere radiative forcing properties at a midlatitude site and their global consequences. *J. Appl. Meteor. Climatol.*, **55**, 1667–1679, doi:10.1175/JAMC-D-15-0217.1.

Campbell, J. R., M. A. Vaughan, M. Oo, R. E. Holz, J. R. Lewis, and E. J. Welton, 2015: Distinguishing cirrus cloud presence in autonomous lidar measurements. *Atmos. Meas. Tech.*, **8**, 435–449, doi:10.5194/amt-8-435-2015.

Chahine, M. T., et al., 2006: Airs: Improving weather forecasting and providing new data on greenhouse gases. *Bull. Amer. Meteor. Soc.*, **87 (7)**, 911–926, doi:10.1175/BAMS-87-7-911.

Chaikovsky, A., et al., 2016: Lidar-Radiometer Inversion Code (LIRIC) for the retrieval of vertical aerosol properties from combined lidar/radiometer data: Development and distribution in EARLINET. *Atmos. Meas. Tech.*, **9**, 1181–1205, doi:10.5194/amt-9-1181-2016.

Chen, W.-N., C.-W. Chiang, and J.-B. Nee, 2002: Lidar ratio and depolarization ratio for cirrus clouds. *Appl. Opt.*, **41 (30)**, 6470–6476, doi:10.1364/AO.41.006470.

Chen, Y., P. J. DeMott, S. M. Kreidenweis, D. C. Rogers, and D. E. Sherman, 2000: Ice formation by sulfate and sulfuric acid aerosol particles under upper-tropospheric conditions. *J. Atmos. Sci.*, **57 (22)**, 3752–3766, doi:10.1175/1520-0469(2000)057<3752:IFBSAS>2.0.CO;2.

Chiriaco, M., H. Chepfer, V. Noel, A. Delaval, M. Haeffelin, P. Dubuisson, and P. Yang, 2004: Improving retrievals of cirrus cloud particle size coupling lidar and three-channel radiometric techniques. *Mon. Wea. Rev.*, **132**, 1648–1700, doi:10.1175/1520-0493(2004)132<1684:IROCCP>2.0.CO;2.

Clerbaux, C., et al., 2009: Monitoring of atmospheric composition using the thermal infrared IASI/MetOp sounder. *Atmos. Chem. Phys.*, **9 (16)**, 6041–6054, doi:10.5194/acp-9-6041-2009.

Comstock, J. M. and K. Sassen, 2001: Retrieval of cirrus cloud radiative and backscattering properties using combined lidar and infrared radiometer (LIRAD) measurements. *J. Atmos. Oceanic Technol.*, **18**, 1658–1673, doi:10.1175/1520-0426(2001)018<1658:ROCCRA>2.0.CO;2.

Córdoba-Jabonero, C., F. J. S. Lopes, E. Landulfo, E. Cuevas, H. Ochoa, and M. Gil-Ojeda, 2017: Diversity on subtropical and polar cirrus clouds properties as derived from both ground-based lidars and CALIPSO/CALIOP measurements. *Atmos. Res.*, **183**, 151–165, doi:10.1016/j.atmosres.2016.08.015.

Cox, S. K., 1971: Cirrus clouds and climate. *J. Atmos. Sci.*, **28**, 1513–1515, doi:10.1175/1520-0469(1971)028<1513:CCATC>2.0.CO;2.

Cox, S. K., D. S. McDougal, D. A. Randall, and R. A. Schiffer, 1987: FIRE - The First ISCCP Regional Experiment. *Bull. Amer. Meteor. Soc.*, **68 (2)**, 114–118, doi:10.1175/1520-0477(1987)068<0114:FFIRE>2.0.CO;2.

Davis, S., et al., 2010: In situ and lidar observations of tropopause subvisible cirrus clouds during TC4. *J. Geophys. Res.*, **115**, D00J17, doi:10.1029/2009JD013093.

Delanoë, J. and R. J. Hogan, 2008: A variational scheme for retrieving ice cloud properties from combined radar, lidar, and infrared radiometer. *J. Geophys. Res.*, **113**, D07 204, doi:10.1029/2007JD009000.

Delanoë, J. and R. J. Hogan, 2010: Combined CloudSat-CALIPSO-MODIS retrievals of the properties of ice clouds. *J. Geophys. Res.*, **115**, D00H29, doi:10.1029/2009JD012346.

DeMott, P. J., D. J. Cziczo, A. J. Prenni, D. M. Murphy, S. M. Kreidenweis, D. S. Thomson, R. Borys, and D. C. Rogers, 2003: Measurements of the concentration and composition of nuclei for cirrus formation. *Proc. Nat. Acad. Sci.*, **100 (25)**, 14 655–14 660, doi:10.1073/pnas.2532677100.

DeMott, P. J., D. C. Rogers, and S. M. Kreidenweis, 1997: The susceptibility of ice formation in upper tropospheric clouds to insoluble aerosol components. *J. Geophys. Res.*, **102 (D16)**, 19 575–19 584, doi:10.1029/97JD01138.

DeMott, P. J., et al., 2010: Predicting global atmospheric ice nuclei distributions and their impacts on climate. *Proc. Nat. Acad. Sci.*, **107 (25)**, 11 217–11 222, doi:10.1073/pnas.0910818107.

Deschamps, P.-Y., F.-M. Bréon, M. Leroy, A. Podaire, A. Bricaud, J.-C. Buriez, and G. Sèze, 1994: The POLDER mission: Instrument characteristics and scientific objectives. *IEEE Trans. Geosci. Remote Sensing*, **32 (3)**, 598–615, doi:10.1109/36.297978.

Dessler, A. E., S. P. Palm, W. D. Hart, and J. D. Spinhirne, 2006: Tropopause-level thin cirrus coverage revealed by ICESat/Geoscience Laser Altimeter System. *J. Geophys. Res.*, **111**, D08 203, doi:10.1029/2005JD006586.

Ding, J., P. Yang, R. E. Holz, S. Platnick, K. G. Meyer, M. A. Vaughan, Y. Hu, and M. D. King, 2016: Ice cloud backscatter study and comparison with CALIPSO and MODIS satellite data. *Optics Express*, **24 (1)**, 620–636, doi:10.1364/OE.24.000620.

Dinh, T., A. Podglajen, A. Hertzog, B. Legras, and R. Plougonven, 2016: Effect of gravity wave temperature fluctuations on homogeneous ice nucleation in the tropical tropopause layer. *Atmos. Chem. Phys.*, **16**, 35–46, doi:10.5194/acp-16-35-2016.

Donovan, D. P. and A. C. A. P. van Lammeren, 2001: Cloud effective particle size and water content profile retrievals using combined lidar and radar observations: 1. Theory and examples. *J. Geophys. Res.*, **106 (D21)**, 27 425–27 448, doi:10.1029/2001JD900243.

Dowling, D. R. and L. F. Radke, 1990: A summary of the physical properties of cirrus clouds. *J. Appl. Meteor.*, **29**, 970–978, doi:10.1175/1520-0450(1990)029<0970:ASOTPP>2.0.CO;2.

Dubuisson, P., V. Giraud, J. Pelon, B. Cadet, and P. Yang, 2008: Sensitivity of thermal infrared radiation at the top of the atmosphere and the surface to ice cloud microphysics. *J. Appl. Meteor. Climatol.*, **47**, 2545–2560, doi:10.1175/2008JAMC1805.1.

Elouragini, S. and P. H. Flamant, 1996: Iterative method to determine an averaged backscatter-to-extinction ratio in cirrus clouds. *Appl. Opt.*, **35 (9)**, 1512–1518, doi:10.1364/AO.35.001512.

Feofilov, A. G., C. J. Stubenrauch, and J. Delanoë, 2015: Ice water content vertical profiles of high-level clouds: Classification and impact on radiative fluxes. *Atmos. Chem. Phys.*, **15**, 12 327–12 344, doi:10.5194/acp-15-12327-2015.

Fernald, F. G., 1984: Analysis of atmospheric lidar observations: some comments. *Appl. Opt.*, **23 (5)**, 652–653, doi:10.1364/AO.23.000652.

Field, P. R., A. J. Heymsfield, and A. Bansemer, 2007: Snow size distribution parameterization for midlatitude and tropical ice clouds. *J. Atmos. Sci.*, **64**, 4346–4365, doi:10.1175/2007JAS2344.1.

Field, P. R., R. J. Hogan, P. R. A. Brown, A. J. Illingworth, T. W. Choularton, and R. J. Cotton, 2005: Parametrization of ice-particle size distributions for mid-latitude stratiform cloud. *Quart. J. Roy. Meteor. Soc.*, **131**, 1997–2017, doi:10.1256/qj.04.134.

Field, P. R., R. Wood, P. R. A. Brown, P. H. Kaye, E. Hirst, R. Greenaway, and J. A. Smith, 2003: Ice particle interarrival times measured with a fast FSSP. *J. Atmos. Oceanic Technol.*, **20**, 249–261, doi:10.1175/1520-0426(2003)020<0249:ipitmw>2.0.co;2.

Flamant, P. H., 2008: Lidars atmosphériques et météorologiques - Principes fondamentaux. *Techniques de l'Ingénieur*, **e4310**.

Garnier, A., J. Pelon, P. Dubuisson, M. Faivre, O. Chomette, N. Pascal, and D. P. Kratz, 2012: Retrieval of cloud properties using CALIPSO Imaging Infrared Radiometer. Part I: Effective emissivity and optical depth. *J. Appl. Meteor. Climatol.*, **51**, 1407–1425, doi:10.1175/JAMC-D-11-0220.1.

Garnier, A., J. Pelon, M. A. Vaughan, D. M. Winker, C. R. Trepte, and P. Dubuisson, 2015: Lidar multiple scattering factors inferred from CALIPSO lidar and

IIR retrievals of semi-transparent cirrus cloud optical depths over oceans. *Atmos. Meas. Tech.*, **8**, 2759–2774, doi:10.5194/amt-8-2759-2015.

Garnier, A., et al., 2013: Retrieval of cloud properties using CALIPSO Imaging Infrared Radiometer. Part II: Effective diameter and ice water path. *J. Appl. Meteor. Climatol.*, **52**, 2582–2599, doi:10.1175/JAMC-D-12-0328.1.

Giannakaki, E., D. S. Balis, V. Amiridis, and S. Kazadzis, 2007: Optical and geometrical characteristics of cirrus clouds over a Southern European lidar station. *Atmos. Chem. Phys.*, **7**, 5519–5530, doi:10.5194/acp-7-5519-2007.

Godin, S., G. Mégie, and J. Pelon, 1989: Systematic lidar measurements of the stratospheric ozone vertical distribution. *Geophys. Res. Lett.*, **16 (6)**, 547–550, doi:10.1029/GL016i006p00547.

Goldfarb, L., P. Keckhut, M.-L. Chanin, and A. Hauchecorne, 2001: Cirrus climatological results from lidar measurements at OHP (44 °N, 6 °E). *Geophys. Res. Lett.*, **28 (9)**, 1687–1690, doi:10.1029/2000GL012701.

Grund, C. J. and E. W. Eloranta, 1990: The 27-28 October 1986 FIRE IFO Cirrus Case Study: Cloud optical properties determined by high spectral resolution lidar. *Mon. Wea. Rev.*, **118 (11)**, 2344–2355, doi:10.1175/1520-0493(1990)118<2344:TOFICC>2.0.CO;2.

Guignard, A., C. J. Stubenrauch, A. J. Baran, and R. Armante, 2012: Bulk microphysical properties of semi-transparent cirrus from AIRS: a six year global climatology and statistical analysis in synergy with geometrical profiling data from CloudSat-CALIPSO. *Atmos. Chem. Phys.*, **12 (1)**, 503–525, doi:10.5194/acp-12-503-2012.

Hartmann, D. L., M. E. Ockert-Bell, and M. L. Michelsen, 1992: The effect of cloud type on Earth's energy balance: Global analysis. *J. Climate*, **5 (11)**, 1281–1304, doi:10.1175/1520-0442(1992)005<1281:TEOCTO>2.0.CO;2.

Henyey, L. G. and J. L. Greenstein, 1941: Diffuse radiation in the Galaxy. *Astrophys. Journal*, **93**, 70–83, doi:10.1086/144246.

Hess, M., R. B. A. Koelemeijer, and P. Stammes, 1998a: Scattering matrices of imperfect hexagonal ice crystals. *J. Quant. Spectrosc. Rad. Trans.*, **60 (3)**, 301–308, doi:10.1016/S0022-4073(98)00007-7.

Hess, M., P. Koepke, and I. Schult, 1998b: Optical properties of aerosols and clouds: The software package OPAC. *Bull. Amer. Meteor. Soc.*, **79 (5)**, 831–844, doi:10.1175/1520-0477(1998)079<0831:OPOAAC>2.0.CO;2.

Heymsfield, A., 1975a: Cirrus uncinus generating cells and the evolution of cirriform clouds. Part I: Aircraft observations of the growth of the ice phase. *J. Atmos. Sci.*, **32 (4)**, 799–808, doi:10.1175/1520-0469(1975)032<0799:CUGCAT>2.0.CO;2.

Heymsfield, A., 1975b: Cirrus uncinus generating cells and the evolution of cirriform clouds. Part II: The structure and circulations of the cirrus uncinus generating head. *J. Atmos. Sci.*, **32 (4)**, 809–819, doi:10.1175/1520-0469(1975)032<0809:CUGCAT>2.0.CO;2.

Heymsfield, A., 1975c: Cirrus uncinus generating cells and the evolution of cirriform clouds. Part III: Numerical computations of the growth of the ice phase. *J. Atmos. Sci.*, **32 (4)**, 820–830, doi:10.1175/1520-0469(1975)032<0820:CUGCAT>2.0.CO;2.

Heymsfield, A. J. and J. Iaquinta, 2000: Cirrus crystal terminal velocities. *J. Atmos. Sci.*, **57**, 916–938, doi:10.1175/1520-0469(2000)057<0916:CCTV>2.0.CO;2.

Heymsfield, A. J. and L. M. Miloshevich, 1993: Homogeneous ice nucleation and supercooled liquid water in orographic wave clouds. *J. Atmos. Sci.*, **50 (15)**, 2335–2353, doi:10.1175/1520-0469(1993)050<2335:HINASL>2.0.CO;2.

Heymsfield, A. J. and L. M. Miloshevich, 2003: Parameterizations for the cross-sectional area and extinction of cirrus and stratiform ice cloud particles. *J. Atmos. Sci.*, **60 (7)**, 936–956, doi:10.1175/1520-0469(2003)060<0936:PFTCSA>2.0.CO;2.

Heymsfield, A. J. and C. M. R. Platt, 1984: A parameterization of the particle size spectrum of ice clouds in terms of the ambient temperature and the ice water content. *J. Atmos. Sci.*, **41 (5)**, 846–855, doi:10.1175/1520-0469(1984)041<0846:APOTPS>2.0.CO;2.

Hildebrandsson, H., 1887: Remarks concerning the nomenclature of clouds for ordinary use. *Quart. J. Roy. Meteor. Soc.*, **13**, 148–154.

Hoareau, C., P. Keckhut, V. Noel, H. Chepfer, and J.-L. Baray, 2013: A decadal cirrus clouds climatology from ground-based and spaceborne lidars above the south of France (43.9 °N - 5.7 °E). *Atmos. Chem. Phys.*, **13 (14)**, 6951–6963, doi:10.5194/acp-13-6951-2013.

Hong, Y., G. Liu, and J.-L. F. Li, 2016: Assessing the radiative effects of global ice clouds based on CloudSat and CALIPSO measurements. *J. Climate*, **29**, 7651–7674, doi:10.1175/JCLI-D-15-0799.1.

Hoose, C. and O. Möhler, 2012: Heterogeneous ice nucleation on atmospheric aerosols: A review of results from laboratory experiments. *Atmos. Chem. Phys.*, **12**, 9817–9854, doi:10.5194/acp-12-9817-2012.

Howard, L., 1803: On the modifications of clouds, and on the principles of their production, suspension and destruction; being the substance of an essay read before the Askesian Society in the session 1802-3. *Philosophical Magazine*, **16**, 97–107 and 344–357, and *Philosophical Magazine*, **17**, 5-11. Reprinted in: Neudrücke von Schriften und Karten über Meteorologie und Erdmagnetismus, **3**, Berlin, 1894.

Inoue, T., 1985: On the temperature and effective emissivity determination of semi-transparent cirrus clouds by bi-spectral measurements in the 10 μm window region. *J. Meteor. Soc. Japan*, **63 (1)**, 88–99, doi:10.2151/jmsj1965.63.1_88.

Inoue, T., 1987: A cloud type classification with NOAA 7 split-window measurements. *J. Geophys. Res.*, **92 (D4)**, 3991–4000, doi:10.1029/JD092iD04p03991.

Jensen, E. J., et al., 2013: Ice nucleation and dehydration in the tropical tropopause layer. *Proc. Nat. Acad. Sci.*, **110 (6)**, 2041–2046, doi:10.1073/pnas.1217104110.

Josset, D., J. Pelon, A. Garnier, Y. Hu, M. Vaughan, P.-W. Zhai, R. Kuehn, and P. Lucker, 2012: Cirrus optical depth and lidar ratio retrieval from combined CALIPSO-CloudSat observations using ocean surface echo. *J. Geophys. Res.*, **117**, D05 207, doi:10.1029/2011JD016959.

Järvinen, E., et al., 2018: Additional global climate cooling by clouds due to ice crystal complexity. *Atmos. Chem. Phys.*, **18**, 15 767–15 781, doi:10.5194/acp-18-15767-2018.

Kärcher, B. and U. Lohmann, 2002a: A parameterization of cirrus cloud formation: Homogeneous freezing including effects of aerosol size. *J. Geophys. Res.*, **107 (D23)**, 4698, doi:10.1029/2001JD001429.

Kärcher, B. and U. Lohmann, 2002b: A parameterization of cirrus cloud formation: Homogeneous freezing of supercooled aerosols. *J. Geophys. Res.*, **107 (D2)**, 4010, doi:10.1029/2001JD000470.

Keckhut, P., F. Borchi, S. Bekki, A. Hauchecorne, and M. Silaouina, 2006: Cirrus classification at midlatitude from systematic lidar observations. *J. Appl. Meteor. Climatol.*, **45**, 249–258, doi:10.1175/JAM2348.1.

King, M. D., Y. J. Kaufman, W. P. Menzel, and D. Tanré, 1992: Remote sensing of cloud, aerosol, and water vapor properties from the Moderate Resolution Imaging Spectrometer (MODIS). *IEEE Trans. Geosci. Remote Sensing*, **30 (1)**, 2–27, doi:10.1109/36.124212.

King, M. D., et al., 2003: Cloud and aerosol properties, precipitable water, and profiles of temperature and water vapor from MODIS. *IEEE Trans. Geosci. Remote Sensing*, **41 (2)**, 442–458, doi:10.1109/TGRS.2002.808226.

Klett, J. D., 1981: Stable analytical inversion solution for processing lidar returns. *Appl. Opt.*, **20 (2)**, 211–220, doi:10.1364/AO.20.000211.

Klett, J. D., 1985: Lidar inversion with variable backscatter/extinction ratios. *Appl. Opt.*, **24 (11)**, 1638–1643, doi:10.1364/AO.24.001638.

Koop, T., B. Luo, A. Tsias, and T. Peter, 2000: Water activity as the determinant for homogeneous ice nucleation in aqueous solutions. *Letters to Nature*, **406**, 611–614.

Korolev, A., G. A. Isaac, and J. Hallett, 2000: Ice particle habits in stratiform clouds. *Quart. J. Roy. Meteor. Soc.*, **126**, 2873–2902, doi:10.1002/qj.49712656913.

Krämer, M., et al., 2009: Ice supersaturations and cirrus cloud crystal numbers. *Atmos. Chem. Phys.*, **9**, 3505–3522, doi:10.5194/acp-9-3505-2009.

Krämer, M., et al., 2016: A microphysics guide to cirrus clouds – Part 1: Cirrus types. *Atmos. Chem. Phys.*, **16**, 3463–3483, doi:10.5194/acp-16-3463-2016.

Lamarck, J.-B., 1802: Sur la forme des nuages. *Annuaire Météorologique pour l'an X de l'ère de la République Française*, **3**, 149–164.

Lawson, R. P., 2011: Effects of ice particles shattering on the 2D-S probe. *Atmos. Meas. Tech.*, **4**, 1361–1381, doi:10.5194/amt-4-1361-2011.

Legrand, M., C. Pietras, G. Brogniez, M. Haeffelin, N. K. Abuhassan, and M. Sicard, 2000: A high-accuracy multiwavelength radiometer for in situ measurements in the thermal infrared. Part I: Characterization of the instrument. *J. Atmos. Oceanic Technol.*, **17**, 1203–1214, doi:10.1175/1520-0426(2000)017<1203:AHAMRF>2.0.CO;2.

Levenberg, K., 1944: A method for the solution of certain non-linear problems in least squares. *Quart. Appl. Math.*, **2**, 164–168, doi:10.1090/qam/10666.

Liou, K.-N., 1974: On the radiative properties of cirrus in the window region and their influence on remote sensing of the atmosphere. *J. Atmos. Sci.*, **31**, 522–532, doi:10.1175/1520-0469(1974)031<0522:OTRPOC>2.0.CO;2.

Liou, K.-N., 1986: Review: Influence of cirrus clouds on weather and climate processes: A global perspective. *Mon. Wea. Rev.*, **114**, 1167–1199, doi:10.1175/1520-0493(1986)114<1167:IOCCOW>2.0.CO;2.

Liu, J. J., Z. Q. Li, Y. F. Zheng, and M. Cribb, 2015: Cloud-base distribution and cirrus properties based on micropulse lidar measurements at a site in southeastern China. *Adv. Atmos. Sci.*, **32 (7)**, 991–1004, doi:10.1007/s00376-014-4176-2.

Lohmann, U. and B. Gasparini, 2017: A cirrus cloud climate dial? *Science*, **357**, 248–249, doi:10.1126/science.aan3325.

Lopatin, A., O. Dubovik, A. Chaikovsky, P. Goloub, T. Lapyonok, D. Tanré, and P. Litvinov, 2013: Enhancement of aerosol characterization using synergy of lidar and sun-photometer coincident observations: the GARRLiC algorithm. *Atmos. Meas. Tech.*, **6**, 2065–2088, doi:10.5194/amt-6-2065-2013.

Lynch, D. K., K. Sassen, D. O'C. Starr, and G. Stephens, 2002: *Cirrus*. Oxford University Press, Cambridge New York (N.Y.) Paris.

Mace, G. G., O'C. Starr, T. P. Ackerman, and P. Minnis, 1995: Examination of coupling between an upper-tropospheric cloud system and synoptic-scale dynamics diagnosed from wind profiler and radiosonde data. *J. Atmos. Sci.*, **52 (23)**, 4094–4127, doi:10.1175/1520-0469(1995)052<4094:EOCBAU>2.0.CO;2.

Macke, A., J. Mueller, and E. Raschke, 1996: Single scattering properties of atmospheric ice crystals. *J. Atmos. Sci.*, **53 (19)**, 2813–2825, doi:10.1175/1520-0469(1996)053<2813:SSPOAI>2.0.CO;2.

Marquardt, D. W., 1963: An algorithm for least-squares estimation of nonlinear parameters. *J. Soc. Indust. Appl. Math.*, **11 (2)**, 431–441, doi:10.1137/0111030.

McDonald, J. E., 1953: Homogeneous nucleation of supercooled water drops. *J. Meteor.*, **10**, 416–433, doi:10.1175/1520-0469(1953)010<0416:HNOSWD>2.0.CO;2.

McFarquhar, G. M. and A. J. Heymsfield, 1998: The definition and significance of an effective radius for ice clouds. *J. Atmos. Sci.*, **55 (11)**, 2039–2052, doi:10.1175/1520-0469(1998)055<2039:TDASOA>2.0.CO;2.

McFarquhar, G. M., A. J. Heymsfield, A. Macke, J. Iaquinta, and S. M. Aulenbach, 1999: Use of observed ice crystal sizes and shapes to calculate mean-scattering properties and multispectral radiances: CEPEX April 4, 1993, case study. *J. Geophys. Res.*, **104 (D24)**, 31 763–31 779, doi:10.1029/1999JD900802.

McFarquhar, G. M., A. J. Heymsfield, J. Spinhirne, and B. Hart, 2000: Thin and subvisual tropopause tropical cirrus: Observations and radiative impacts. *J. Atmos. Sci.*, **57 (12)**, 1841–1853, doi:10.1175/1520-0469(2000)057<1841:TASTTC>2.0.CO;2.

Mishchenko, M. I., L. D. Travis, R. A. Kahn, and R. A. West, 1997: Modeling phase functions for dustlike tropospheric aerosols using a shape mixture of randomly oriented polydisperse spheroids. *J. Geophys. Res.*, **102 (D14)**, 16 831–16 847, doi:10.1029/96JD02110.

Mitchell, D. L., 2002: Effective diameter in radiation transfer: General definition, applications, and limitations. *J. Atmos. Sci.*, **59 (15)**, 2330–2346, doi:10.1175/1520-0469(2002)059<2330:EDIRTG>2.0.CO;2.

Mortier, A., 2013: Tendances et variabilités de l'aérosol atmosphérique à l'aide du couplage Lidar/Photomètre sur les sites de Lille et Dakar. Ph.D. thesis, Université de Lille 1 Sciences et Technologies, Ecole Doctorale: Sciences de la Matière, du Rayonnement et de l'Environnement.

Nohra, R., 2016: Étude des propriétés macrophysique et optiques de cirrus à l'aide d'un micro-lidar sur le site de Lille. Ph.D. thesis, Université de Lille 1 Sciences et Technologies, Ecole Doctorale: Sciences de la Matière, du Rayonnement et de l'Environnement.

Pal, S. R., W. Steinbrecht, and A. I. Carswell, 1992: Automated method for lidar determination of cloud-base height and vertical extent. *Appl. Opt.*, **31 (10)**, 1488–1494, doi:10.1364/AO.31.001488.

Pandit, A. K., H. S. Gadhavi, M. Venkat Ratnam, K. Raghunath, S. V. B. Rao, and A. Jayaraman, 2015: Long-term trend analysis and climatology of tropical cirrus clouds using 16 years of lidar data set over Southern India. *Atmos. Chem. Phys.*, **15**, 13 833–13 848, doi:10.5194/acp-15-13833-2015.

Parol, F., J. C. Buriez, G. Brogniez, and Y. Fouquart, 1991: Information content of AVHRR channels 4 and 5 with respect to the effective radius of cirrus cloud particles. *J. Appl. Meteor.*, **30**, 973–984, doi:10.1175/1520-0450-30.7.973.

Platt, C. M., et al., 1994: The Experimental Cloud Lidar Pilot Study (ECLIPS) for cloud-radiation research. *Bull. Amer. Meteor. Soc.*, **75 (9)**, 1635–1654, doi:10.1175/1520-0477(1994)075<1635:TECLPS>2.0.CO;2.

Platt, C. M. R., 1973: Lidar and radiometric observations of cirrus clouds. *J. Atmos. Sci.*, **30**, 1191–1204, doi:10.1175/1520-0469(1973)030<1191:LAROOC>2.0.CO;2.

Platt, C. M. R., 1979: Remote sounding of high clouds: I. Calculation of visible and infrared optical properties from lidar and radiometer measurements. *J. Appl. Meteor.*, **18**, 1130–1143, doi:10.1175/1520-0450(1979)018<1130:RSOHCI>2.0.CO;2.

Platt, C. M. R. and A. C. Dilley, 1981: Remote sounding of high clouds. IV: Observed temperature variations in cirrus optical properties. *J. Atmos. Sci.*, **38**, 1069–1082, doi:10.1175/1520-0469(1981)038<1069:RSOHCI>2.0.CO;2.

Platt, C. M. R., J. C. Scott, and A. C. Dilley, 1987: Remote sounding of high clouds. Part VI: Optical properties of midlatitude and tropical cirrus. *J. Atmos. Sci.*, **44 (4)**, 729–747, doi:10.1175/1520-0469(1987)044<0729:RSOHCP>2.0.CO;2.

Platt, C. M. R., D. M. Winker, M. A. Vaughan, and S. D. Miller, 1999: Backscatter-to-extinction ratios in the top layers of Tropical Mesoscale Convective Systems and in isolated cirrus from LITE observations. *J. Appl. Meteor.*, **38 (9)**, 1330–1345, doi:10.1175/1520-0450(1999)038<1330:BTERIT>2.0.CO;2.

Platt, C. M. R., S. A. Young, R. T. Austin, G. R. Patterson, D. L. Mitchell, and S. D. Miller, 2002: LIRAD observations of tropical cirrus clouds in MCTEX. Part

I: Optical properties and detection of small particles in cold cirrus. *J. Atmos. Sci.*, **59 (22)**, 3145–3162, doi:10.1175/1520-0469(2002)059<3145:LOOTCC>2.0.CO;2.

Pruppacher, H. and J. D. Klett, 1997: *Microphysics of Clouds and Precipitation*. Atmospheric and Oceanographic Sciences Library, Kluwer Academic Publishers, Dordrecht, the Netherlands.

Pruppacher, H. R., 1995: A new look at homogeneous ice nucleation in supercooled water drops. *J. Atmos. Sci.*, **52 (11)**, 1924–1933, doi:10.1175/1520-0469(1995)052<1924:ANLAHI>2.0.CO;2.

Rodgers, C. D., 1976: Retrieval of atmospheric temperature and composition from remote measurements of thermal radiation. *Rev. Geophys. Space Phys.*, **14 (4)**, 609–624, doi:10.1029/RG014i004p00609.

Rodgers, C. D., 1990: Characterization and error analysis of profiles retrieved from remote sounding measurements. *J. Geophys. Res.*, **95 (D5)**, 5587–5595, doi:10.1029/JD095iD05p05587.

Rodgers, C. D., 2000: *Inverse Methods for Atmospheric Sounding: Theory and Practice*. World Scientific Pub. Co. Inc.

Saito, M., H. Iwabuchi, P. Yang, G. Tang, M. D. King, and M. Sekiguchi, 2017: Ice particle morphology and microphysical properties of cirrus clouds inferred from combined CALIOP-IIR measurements. *J. Geophys. Res. Atmos.*, **122**, 4440–4462, doi:10.1002/2016JD026080.

Sassen, K., 1991: The polarization lidar technique for cloud research: A review and current assessment. *Bull. Amer. Meteor. Soc.*, **72 (12)**, 1848–1866, doi:10.1175/1520-0477(1991)072<1848:TPLTFC>2.0.CO;2.

Sassen, K. and S. Benson, 2001: A midlatitude cirrus cloud climatology from the facility for atmospheric remote sensing. Part II: Microphysical properties derived from lidar depolarization. *J. Atmos. Sci.*, **58**, 2103–2112, doi:10.1175/1520-0469(2001)058<2103:AMCCCF>2.0.CO;2.

Sassen, K. and J. R. Campbell, 2001: A midlatitude cirrus cloud climatology from the facility for atmospheric remote sensing. Part I: Macrophysical and synoptic properties. *J. Atmos. Sci.*, **58**, 481–496, doi:10.1175/1520-0469(2001)058<0481:AMCCCF>2.0.CO;2.

Sassen, K. and B. S. Cho, 1992: Subvisual-thin cirrus lidar dataset for satellite verification and climatological research. *J. Appl. Meteor.*, **31**, 1275–1285, doi:10.1175/1520-0450(1992)031<1275:STCLDF>2.0.CO;2.

Sassen, K. and J. M. Comstock, 2001: A midlatitude cirrus cloud climatology from the facility for atmospheric remote sensing. Part III: Radiative properties. *J. Atmos. Sci.*, **58**, 2113–2127, doi:10.1175/1520-0469(2001)058<2113:AMCCCF>2.0.CO;2.

Sassen, K., Z. Wang, and D. Liu, 2008: Global distribution of cirrus clouds from CloudSat/Cloud-Aerosol Lidar and Infrared Pathfinder Satellite Observations (CALIPSO) measurements. *J. Geophys. Res.*, **113**, D00A12, doi:10.1029/2008JD009972.

Schiffer, R. A. and W. B. Rossow, 1983: The International Satellite Cloud Climatology Project (ISCCP): The first project of the World Climate Research Programme. *Bull. Amer. Meteor. Soc.*, **64 (7)**, 779–784, doi:10.1175/1520-0477-64.7.779.

Seifert, P., A. Ansmann, D. Müller, U. Wandinger, D. Althausen, A. J. Heymsfield, S. T. Massie, and C. Schmitt, 2007: Cirrus optical properties observed with lidar, radiosonde, and satellite over the tropical Indian Ocean during the aerosol-polluted northeast and clean maritime southwest monsoon. *J. Geophys. Res.*, **112**, D17 205, doi:10.1029/2006JD008352.

Sicard, M., P. R. Spyak, G. Brogniez, M. Legrand, N. K. Abuhassan, C. Pietras, and J.-P. Buis, 1999: Thermal-infrared field radiometer for vicarious cross-calibration: characterization and comparisons with other field instruments. *Opt. Eng.*, **38 (2)**, 345–356, doi:10.1117/1.602094.

Sourdeval, O., L. C. Labonnote, A. J. Baran, and G. Brogniez, 2015: A methodology for simultaneous retrieval of ice and liquid water cloud properties. Part I: Information content and case study. *Quart. J. Roy. Meteor. Soc.*, **141 (688)**, 870–882, doi:10.1002/qj.2405.

Sourdeval, O., L. C. Labonnote, A. J. Baran, J. Mülmenstädt, and G. Brogniez, 2016: A methodology for simultaneous retrieval of ice and liquid water cloud properties. Part 2: Near-global retrievals and evaluation against A-Train products. *Quart. J. Roy. Meteor. Soc.*, **142**, 3063–3081, doi:10.1002/qj.2889.

Sourdeval, O., L. C. Labonnote, G. Brogniez, O. Jourdan, J. Pelon, and A. Garnier, 2013: A variational approach for retrieving ice cloud properties from infrared measurements: Application in the context of two IIR validation campaigns. *Atmos. Chem. Phys.*, **13**, 8229–8244, doi:10.5194/acp-13-8229-2013.

Sourdeval, O., et al., 2012: Validation of IIR/CALIPSO Level 1 measurements by comparison with collocated airborne observations during CIRCLE-2 and Biscay '08 campaigns. *J. Atmos. Oceanic Technol.*, **29**, 653–667, doi:10.1175/JTECH-D-11-00143.1.

Spichtinger, P. and M. Krämer, 2013: Tropical tropopause ice clouds: a dynamic approach to the mystery of low crystal numbers. *Atmos. Chem. Phys.*, **13**, 9801–9818, doi:10.5194/acp-13-9801-2013.

Spurr, R. J. D., 2012: *User's Guide: LIDORT Version 3.6*. RT Solutions, Inc., Cambridge, USA.

Spurr, R. J. D., T. P. Kurosu, and K. V. Chance, 2001: A linearized discrete ordinate radiative transfer model for atmospheric remote-sensing retrieval. *J. Quant. Spectrosc. Rad. Trans.*, **68**, 689–735, doi:10.1016/S0022-4073(00)00055-8.

Stephens, G. L., R. J. Engelen, M. Vaughan, and T. L. Anderson, 2001: Toward retrieving properties of the tenuous atmosphere using space-based lidar measurements. *J. Geophys. Res.*, **106 (D22)**, 28 143–28 157, doi:10.1029/2001JD000632.

Stephens, G. L. and P. J. Webster, 1981: Clouds and climate: Sensitivity of simple systems. *J. Atmos. Sci.*, **38**, 235–247, doi:10.1175/1520-0469(1981)038<0235:CACSOS>2.0.CO;2.

Stephens, G. L., et al., 2002: The CloudSat mission and the A-Train: A new dimension of space-based observations of clouds and precipitation. *Bull. Amer. Meteor. Soc.*, **83**, 1771–1790, doi:10.1175/BAMS-83-12-1771.

Stephens, G. L., et al., 2008: CloudSat mission: Performance and early science after the first year of operation. *J. Geophys. Res.*, **113**, D00A18, doi:10.1029/2008JD009982.

Stephens, G. L., et al., 2012: An update on Earth's energy balance in light of the latest global observations. *Nature Geoscience*, **5**, 691–696, doi:10.1038/NGEO1580.

Strapp, J. W., F. Albers, A. Reuter, A. V. Korolev, U. Maixner, E. Rashke, and Z. Vukovic, 2001: Laboratory measurements of the response of a PMS OAP-2DC. *J. Atmos. Oceanic Technol.*, **18**, 1150–1170, doi:10.1175/1520-0426(2001)018<1150:LMOTRO>2.0.CO;2.

Stubenrauch, C. J., A. Chédin, R. Armante, and N. A. Scott, 1999: Clouds as seen by satellite sounders (3I) and imagers (ISCCP). Part II: A new approach for cloud parameter determination in the 3I algorithms. *J. Climate*, **12 (8)**, 2214–2223, doi:10.1175/1520-0442(1999)012<2214:CASBSS>2.0.CO;2.

Stubenrauch, C. J., S. Cros, A. Guignard, and N. Lamquin, 2010: A 6-year global cloud climatology from the Atmospheric InfraRed Sounder AIRS and a statistical analysis in synergy with CALIPSO and CloudSat. *Atmos. Chem. Phys.*, **10 (15)**, 7197–7214, doi:10.5194/acp-10-7197-2010.

Stubenrauch, C. J., S. Cros, N. Lamquin, R. Armante, A. Chédin, C. Crevoisier, and N. A. Scott, 2008: Cloud properties from Atmospheric Infrared Sounder and evaluation with Cloud-Aerosol Lidar and Infrared Pathfinder Satellite Observations. *J. Geophys. Res. Atmos.*, **113 (D8)**, doi:10.1029/2008JD009928.

Stubenrauch, C. J., A. G. Feofilov, S. E. Protopapadaki, and R. Armante, 2017: Cloud climatologies from the infrared sounders AIRS and IASI: Strengths and applications. *Atmos. Chem. Phys.*, **17 (22)**, 13 625–13 644, doi:10.5194/acp-17-13625-2017.

Tabazadeh, A., S. T. Martin, and J.-S. Lin, 2000: The effect of particle size and nitric acid uptake on the homogeneous freezing of aqueous sulfuric acid particles. *Geophys. Res. Lett.*, **27 (8)**, 1111–1114, doi:10.1029/1999GL010966.

Takano, Y. and K. N. Liou, 1989: Solar radiative transfer in cirrus clouds. Part I: Single-scattering and optical properties of hexagonal ice crystals. *J. Atmos. Sci.*, **46 (1)**, 3–19, doi:10.1175/1520-0469(1989)046<0003:SRTICC>2.0.CO;2.

Turner, D. D. and E. W. Eloranta, 2008: Validating mixed-phase cloud optical depth retrieved from infrared observations with high spectral resolution lidar. *IEEE Geosci. Remote Sens. Lett.*, **5 (2)**, 285–288, doi:10.1109/LGRS.2008.915940.

van de Hulst, H. C., 1957: *Light Scattering by Small Particles.* John Wiley & Sons, Inc., New York.

Vidot, J., A. J. Baran, and P. Brunel, 2015: A new ice cloud parameterization for infrared radiative transfer simulation of cloudy radiances: Evaluation and optimization with IIR observations and ice cloud profile retrieval products. *J. Geophys. Res. Atmos.*, **120**, 6937–6951, doi:10.1002/2015JD023462.

Wang, T. and A. E. Dessler, 2012: Analysis of cirrus in the tropical tropopause layer from CALIPSO and MLS data: A water perspective. *J. Geophys. Res.*, **117**, D04 211, doi:10.1029/2011JD016442.

Webster, E. W., 1931: *Meteorology.* Translation of Aristotle's Meteorologica, in: The Works of Aristotle (ed. W. D. Ross), 12 vols, Oxford (1908-1952), Vol.3 (1931), Clarendon Press, Oxford.

Weickmann, H. K., 1945: Formen und Bildung atmosphärischer Eiskristalle. *Beitr. Phys. Atmos.*, **28**, 12–52.

Weickmann, H. K., 1949: *Die Eisphase in der Atmosphäre.* Dt. Wetterdienst in der US-Zone.

Wielicki, B. A., R. D. Cess, M. D. King, D. A. Randall, and E. F. Harrison, 1995: Mission to planet Earth: Role of clouds and radiation in climate. *Bull. Amer. Meteor. Soc.*, **76 (11)**, 2125–2153, doi:10.1175/1520-0477(1995)076<2125:MTPERO>2.0.CO;2.

Winker, D. M., R. H. Couch, and M. P. McCormick, 1996: An overview of LITE: NASA's Lidar In-space Technology Experiment. *Proceedings of the IEEE*, **84 (2)**, 164–180, doi:10.1109/5.482227.

Winker, D. M., J. R. Pelon, and M. P. McCormick, 2003: The CALIPSO mission: spaceborne lidar for observation of aerosols and clouds. *Proc. SPIE*, **4893**, Lidar Remote Sensing for Industry and Environment Monitoring III (21 March 2003), doi:10.1117/12.466539.

Winker, D. M., M. A. Vaughan, A. Omar, Y. Hu, K. A. Powell, Z. Liu, W. H. Hunt, and S. A. Young, 2009: Overview of the CALIPSO mission and CALIOP data processing algorithms. *J. Atmos. Oceanic Technol.*, **26**, 2310–2323, doi:10.1175/2009JTECHA1281.1.

Winker, D. M., et al., 2010: The CALIPSO mission: A global 3D view of aerosols and clouds. *Bull. Amer. Meteor. Soc.*, **91**, 1211–1230, doi:10.1175/2010BAMS3009.1.

WMO, 2017: *International Cloud Atlas*. published online by the World Meteorological Organization (WMO), URL `https://cloudatlas.wmo.int/home.html`.

Wu, M.-L. C., 1987: A method for remote sensing the emissivity, fractional cloud cover and cloud top temperature of high-level, thin clouds. *J. Climate Appl. Meteor.*, **26 (2)**, 225–233, doi:10.1175/1520-0450(1987)026<0225:AMFRST>2.0.CO;2.

Wylie, D. P., W. P. Menzel, H. M. Woolf, and K. I. Strabala, 1994: Four years of global cirrus cloud statistics using HIRS. *J. Climate*, **7 (12)**, 1972–1986, doi:10.1175/1520-0442(1994)007<1972:FYOGCC>2.0.CO;2.

Yang, P., B. A. Baum, A. J. Heymsfield, Y. X. Hu, H.-L. Huang, S.-C. Tsay, and S. Ackerman, 2003: Single-scattering properties of droxtals. *J. Quant. Spectrosc. Rad. Trans.*, **79-80**, 1159–1169, doi:10.1016/S0022-4073(02)00347-3.

Yang, P. and K. N. Liou, 1998: Single-scattering properties of complex ice crystals in terrestrial atmosphere. *Contr. Atmos. Phys.*, **71 (2)**, 223–248, doi:10.1364/AO.44.005512.

Young, S. A., 1995: Analysis of lidar backscatter profiles in optically thin clouds. *Appl. Opt.*, **34 (30)**, 7019–7031, doi:10.1364/AO.34.007019.

Zhang, Y., A. Macke, and F. Albers, 1999: Effect of crystal size spectrum and crystal shape on stratiform cirrus radiative forcing. *Atmos. Res.*, **52**, 59–75, doi:10.1016/S0169-8095(99)00026-5.

Zhou, C. and P. Yang, 2015: Backscattering peak of ice cloud particles. *Optics Express*, **23 (9)**, 11 995–12 003, doi:10.1364/OE.23.011995.

Zhou, C., P. Yang, A. E. Dessler, Y. Hu, and B. A. Baum, 2012: Study of horizontally oriented ice crystals with CALIPSO observations and comparison with Monte Carlo radiative transfer simulations. *J. Appl. Meteor. Climatol.*, **51 (7)**, 1426–1439, doi:10.1175/JAMC-D-11-0265.1.

List of Figures

List of Tables